



# **Silicon Nanowire based Sensor for Highly Sensitive and Selective Detection of Ammonia**

Dissertation  
zur Erlangung des akademischen Grades  
Doktoringenieur  
(Dr.-Ing.)

vorgelegt von

Cindy Schmädicke  
geboren am 21. November 1987 in Dresden

Technische Universität Dresden  
Fakultät Maschinenwesen  
Institut für Werkstoffwissenschaft  
Lehrstuhl für Materialwissenschaft und Nanotechnik  
2015

Tag der Einreichung: 22.01.2015

Tag der Verteidigung: 07.04.2015

1. Gutachter: Prof. Dr. Gianaurelio Cuniberti, TU Dresden
2. Gutachter: Prof. Dr. Timothy M. Swager, Massachusetts Institute of Technology
3. Gutachter: Prof. Dr. Andrés F. Lasagni, TU Dresden



## **Erklärung**

a) Hiermit versichere ich, dass ich die vorliegende Arbeit ohne unzulässige Hilfe Dritter und ohne Benutzung anderer als der angegebenen Hilfsmittel angefertigt habe; die aus fremden Quellen direkt oder indirekt übernommenen Gedanken sind als solche kenntlich gemacht.

b) Bei der Auswahl und Auswertung des Materials sowie bei der Herstellung des Manuskripts habe ich Unterstützungsleistungen von folgenden Personen erhalten:

Markus Pötschke (Unterkapitel 3.3 und 3.5)

Manfred Bobeth (Unterkapitel 3.3 und 3.5)

Sebastian Pregl (Unterkapitel 4.1)

Andreas Gang (Unterkapitel 4.4 und 4.5)

Felix Zörgiebel (MATLAB-Programmierung)

Jan Voigt (Unterkapitel 5.3)

Gero Wiemann (Unterkapitel 5.3)

Weitere Personen waren an der geistigen Herstellung der vorliegenden Arbeit nicht beteiligt. Insbesondere habe ich nicht die Hilfe eines kommerziellen Promotionsberaters in Anspruch genommen. Dritte haben von mir keine geldwerten Leistungen für Arbeiten erhalten, die in Zusammenhang mit dem Inhalt der vorgelegten Dissertation stehen.

c) Die Arbeit wurde bisher weder im Inland noch im Ausland in gleicher oder ähnlicher Form einer anderen Prüfungsbehörde vorgelegt und ist auch noch nicht veröffentlicht worden.

d) Die Promotionsordnung der Fakultät Maschinenwesen an der TU Dresden vom 01.07.2001 wird anerkannt.



## Abstract

The precise determination of the type and concentration of gases is of increasing importance in numerous applications. Despite the diverse operating principles of today's gas sensors, technological trends can be summarized with the keyword miniaturization, because of the resulting benefits such as integrability and energy efficiency.

This work deals with the development and fabrication of novel nanowire based gas sensors, which in comparison to conventional devices have an advantageous combination of high sensitivity and selectivity with low power consumption and small size. On the basis of grown silicon nanowires, sensors based on the functional principle of classical Schottky barrier field effect transistors with abrupt metal-semiconductor contacts are fabricated. The sensing performance of the devices is investigated with respect to the detection of ammonia. Ammonia concentrations down to 170 ppb ( $120 \mu\text{g}/\text{m}^3$ ) are measured with a sensor response of more than 160 % and a theoretical limit of detection of 20 ppb is determined. Selectivity investigations show that no cross sensitivity to most common solvents occurring in living spaces exists. Moisture influences on the device are studied and reveal that the sensor responds within seconds, making it potentially suitable as humidity sensor. Moreover, it is shown that a higher relative humidity and higher temperatures decrease the sensor sensitivity. In terms of possible applications, it is a great advantage that the maximum sensitivity is achieved at 25 °C.

With respect to sensitivity and selectivity an enhancement is demonstrated compared to most nanosensors known from the literature. Hence, the technology offers the potential to complement conventional measurement systems in future sensor technology especially in portable applications.

## Kurzfassung

Die präzise Bestimmung der Art und Konzentration von Gasen erlangt in zahlreichen Anwendungsgebieten zunehmend an Bedeutung. Trotz der vielfältigen Wirkprinzipien heutiger Gassensoren lassen sich die technologischen Trends mit dem Schlagwort Miniaturisierung zusammenfassen, da sich daraus entscheidende Vorteile wie Integrierbarkeit und Energieeffizienz ergeben.

Diese Arbeit beschäftigt sich mit der Entwicklung und Herstellung neuartiger nanodrahtbasierter Gassensoren, welche im Vergleich zu klassischen Sensoren eine vorteilhafte Kombination von hoher Sensitivität und Selektivität bei geringem Stromverbrauch und geringer Größe aufweisen. Auf der Grundlage gewachsener Silizium-Nanodrähte werden Sensoren mit abrupten Metall-Halbleiter-Kontakten hergestellt, welche auf dem Funktionsprinzip klassischer Schottkybarrieren-Feldeffekttransistoren beruhen. Die Eignung der Sensoren wird in Bezug auf die Detektion von Ammoniak untersucht. Dabei kann eine minimale Ammoniakkonzentration von 170 ppb ( $120 \mu\text{g}/\text{m}^3$ ) mit einer Signaländerung von mehr als 160 % gemessen werden, wobei die theoretische Nachweisgrenze mit 20 ppb ermittelt wird. Selektivitätsuntersuchungen zeigen, dass keine Querempfindlichkeit gegenüber den am häufigsten in Wohnräumen vorkommenden Lösungsmitteln besteht. Feuchtigkeitseinflüsse auf den Sensor werden untersucht und es wird nachgewiesen, dass der Sensor Ansprechzeiten im Sekundenbereich besitzt, was ihn zu einem potenziell geeigneten Feuchtigkeitssensor macht. Darüber hinaus wird gezeigt, dass eine höhere relative Luftfeuchtigkeit und höhere Umgebungstemperaturen die Sensorsensitivität verringern. In Bezug auf mögliche Einsatzgebiete stellt die maximale Empfindlichkeit bei 25 °C einen großen Vorteil da.

Bezogen auf Sensitivität und Selektivität wird somit eine Verbesserung im Vergleich zu den meisten aus der Literatur bekannten Nanosensoren demonstriert. Damit bietet die Technologie das Potential, konventionelle Messsysteme in zukünftiger Sensorik vor allem in portablen Anwendungen zu ergänzen.

# Content

<b>List of Figures</b> .....	<b>XI</b>
<b>List of Tables</b> .....	<b>XV</b>
<b>Constants, Symbols, and Abbreviations</b> .....	<b>XVII</b>
<b>1 Introduction</b> .....	<b>1</b>
1.1 Motivation .....	1
1.2 State of the Art.....	3
1.3 Scope of this Thesis .....	6
<b>2 Fundamentals</b> .....	<b>9</b>
2.1 Introduction to Gas Sensors .....	9
2.1.1 History of Gas Sensor Development .....	11
2.1.2 Gas Sensor Classification .....	12
2.2 Semiconductor Gas Sensor Technology .....	18
2.3 Gas Sensing Properties .....	22
2.3.1 Response, Response Time, and Recovery Time .....	22
2.3.2 Sensitivity and Limit of Detection.....	23
2.3.3 Selectivity.....	24
2.3.4 Long-term Stability .....	25
2.4 Nanoscale Gas Sensors .....	25
2.5 Silicon Nanowire Based Gas Sensors .....	27
2.5.1 Fabrication Methods.....	28
2.5.2 Metal-Semiconductor Contact.....	30
2.5.3 Working Principle: Resistor versus Field Effect Transistor.....	33
2.5.4 Sensing Mechanism.....	34
2.6 Ammonia and its Sensing Applications .....	35
2.6.1 Chemical and Toxicological Properties.....	36
2.6.2 Application Areas of Ammonia Sensors.....	37
2.6.3 Ammonia Sensing Principles .....	39
2.7 Summary.....	41
<b>3 Copper Nanowire Synthesis</b> .....	<b>43</b>
3.1 Directed Electrochemical Nanowire Assembly .....	43

---

3.2	Growth Process and Tip-Probe Station .....	44
3.3	Theory .....	46
3.4	Nanowire Growth with DENA.....	47
3.4.1	Effect of Salt Concentration .....	49
3.4.2	Effect of voltage amplitude .....	50
3.4.3	Effect of Frequency.....	51
3.4.4	Electrical Properties.....	51
3.5	Discussion .....	53
3.6	Summary.....	56
<b>4</b>	<b>Technology for the Fabrication of Silicon Nanowire based Sensors .....</b>	<b>59</b>
4.1	Nanowire Synthesis.....	60
4.2	Nanowire Transfer and Oxidation .....	62
4.3	Sensor Design .....	63
4.4	Fabrication of Contact Electrodes .....	64
4.4.1	Lithography .....	65
4.4.2	Oxide Etching.....	66
4.4.3	Nickel Deposition .....	66
4.5	Fabrication of Schottky Contacts within a Nanowire.....	67
4.6	Summary.....	67
<b>5</b>	<b>Measurement Setup and Implementation .....</b>	<b>69</b>
5.1	State of the Art.....	69
5.2	Requirements of a Test System for Gas Sensors .....	70
5.3	Apparatus .....	71
5.3.1	Gas Delivery System.....	72
5.3.2	Exposure Chamber.....	72
5.3.3	Control and Read-out Electronics .....	75
5.3.4	Temperature Control .....	77
5.4	Measurement Procedure.....	79
5.4.1	Gas Mixing .....	79
5.4.2	Gas Measurement Protocol.....	81
5.5	Summary.....	82
<b>6</b>	<b>Characterization of Silicon Nanowire based Sensors .....</b>	<b>83</b>
6.1	Electrical Characterization of the Sensors.....	83
6.2	Sensor Requirements and Typical Diagrams of Gas Sensing.....	86



---

6.3 Resistance Response of the Devices towards Ammonia.....	88
6.4 Measurements at the Drägerwerk AG & Co. KGaA .....	90
6.5 Gas Sensing Performance of Native Oxide Shell Silicon Nanowires .....	92
6.5.1 Drift Investigation .....	93
6.5.2 Response and Recovery Time .....	94
6.5.3 Repeatability .....	98
6.5.4 Calibration Curve and Limit of Detection .....	99
6.5.5 Effect of Humidity .....	103
6.5.6 Influence of Temperature .....	109
6.5.7 Selectivity.....	112
6.5.8 Sensor-to-Sensor Reproducibility.....	113
6.5.9 Long-term Stability .....	114
6.6 Sensors based on Silicon Nanowires with a Thermally Grown Oxide Shell.....	116
6.6.1 Drift Investigation .....	117
6.6.2 Influence of Ammonia, Humidity, and Temperature .....	118
6.7 Comparison of the Performances of Native and Thermal Oxide Shell Silicon Nanowire based Sensors .....	121
6.8 Summary.....	123
<b>7 Conclusions and Outlook .....</b>	<b>125</b>
7.1 Conclusions .....	125
7.2 Outlook.....	127
<b>Bibliography .....</b>	<b>129</b>
<b>Appendix.....</b>	<b>155</b>
<b>Publications and Conferences .....</b>	<b>159</b>
<b>Patent Filing.....</b>	<b>161</b>
<b>Acknowledgements .....</b>	<b>163</b>



## List of Figures

Fig. 1.1: Signal processing in living organisms and in technical systems .....	2
Fig. 1.2: Composition of clean air. ....	3
Fig. 1.3: Vertical SiNW array based $\text{NH}_3$ sensor.....	6
Fig. 2.1: Schematic illustration of a typical gas sensor system. ....	10
Fig. 2.2: Former gas sensors and measuring setup.....	12
Fig. 2.3: Optical gas sensor.....	13
Fig. 2.4: Schematic diagrams of mass-sensitive gas sensors.....	16
Fig. 2.5: Principles of gas sensing via magnetic and thermal detection mechanisms. ....	17
Fig. 2.6: $\text{SnO}_2$ based gas sensor. ....	20
Fig. 2.7: Schematic representations of CNT based gas detection.....	21
Fig. 2.8: Gas sensor block diagram (center), example of a possible sensor output (right) due to a step change in the concentration of an analyte (left).....	22
Fig. 2.9: Vertical standing SiNWs. ....	29
Fig. 2.10: The Schottky contact.....	31
Fig. 2.11: Charge carrier injection mechanisms for electrons at a Schottky barrier.....	32
Fig. 2.12: Schematic illustration of SiNW based sensor principles.....	34
Fig. 2.13: P-type SiNW based sensing mechanism of $\text{NH}_3$ . ....	35
Fig. 2.14: Global ( $1^\circ \times 1^\circ$ ) estimates of atmospheric ammonia concentrations .....	36
Fig. 3.1: Schematic representation of a sensor layout and copper nanowire synthesis. ....	44
Fig. 3.2: Setup of copper nanowire growth experiments, which comprises the tip-probe station and electrical measuring equipment.....	46
Fig. 3.3: EDX analysis of a grown nanowire. ....	49
Fig. 3.4: SEM images of copper nanowires grown at concentrations of 0.05 (a), 0.1 (b), 0.5 (c), 1.0 (d), and 2.0 mM (e).....	50
Fig. 3.5: SEM images of copper nanowires grown at peak-to-peak voltages $V_{pp}$ of 6 (a), 8 (b), 10 (c), and 20 V (d), a concentration of 1 mM, and a frequency of 250 kHz. ...	50
Fig. 3.6: SEM images of copper nanowires grown at frequencies of 50 (a), 150 (b), 250 (c), 400 (d), 500 (e), and 750 kHz (f). ....	51
Fig. 3.7: Electrical characterization of a contacted copper nanowire with a diameter of around 500 nm. ....	52
Fig. 3.8: Measurement of the resistance over time for an exemplary copper nanowire. ....	53
Fig. 3.9: Simultaneously grown copper nanowires. ....	53

Fig. 4.1: Process steps for the silicon nanowire based sensor fabrication. ....	60
Fig. 4.2: Si nanowire synthesis.....	61
Fig. 4.3: Contact printing of NWs. ....	63
Fig. 4.4: Sensor design.....	64
Fig. 4.5: SEM image of contacted NWs with NiSi <sub>2</sub> interfaces.....	67
Fig. 5.1: Schematic configuration of the developed gas flow apparatus with a small volume gas chamber equipped with read-out electronics for the sensor measurements. .	71
Fig. 5.2: CAD model of the gas measurement chamber.....	73
Fig. 5.3: Apparatus with exposure chamber (left). Stainless steel 6-way-cross with six ports, with different functions, like gas inlet, gas outlet, and viewports, respectively (right). ....	74
Fig. 5.4: Components inside the gas exposure chamber.....	75
Fig. 5.5: Proceeding of the data readout.....	76
Fig. 5.6: Schematic representation of the control and read-out electronics. ....	78
Fig. 5.7: Schematics of the temperature control. ....	79
Fig. 5.8: Schema of the gas mixing method. ....	80
Fig. 5.9: Characteristic process steps of gas measurements with several measurement cycles. ....	82
Fig. 6.1: Schematic representation of a nanowire sensor with nickel silicide contacts. ....	84
Fig. 6.2: Transfer characteristics of typical SiNW based sensors.....	85
Fig. 6.3: Gate current $I_G$ in dependence of gate voltage $V_G$ for devices based on (a) NWs with a native SiO <sub>2</sub> shell and (b) NWs with a thermally grown SiO <sub>2</sub> shell. ....	86
Fig. 6.4: Operating principles for SiNW based gas sensors and recorded sensor signals. ..	88
Fig. 6.5: Response towards N <sub>2</sub> flow rate change of 2, 1, and 0.2 l/min. ....	89
Fig. 6.6: Sensing response of SiNW based resistors to 20, 10, 5, 2.5, 1, and 0.5 ppm NH <sub>3</sub>	90
Fig. 6.7: Schematic structure of the measuring apparatus at the Drägerwerk AG & Co. KGaA. ....	91
Fig. 6.8: PMMA adapter and sample holder ....	92
Fig. 6.9: Threshold voltage drift over a period of 3 h.....	93
Fig. 6.10: Response and recovery time of the sensors for different NH <sub>3</sub> concentrations.....	95
Fig. 6.11: Sensor repeatability.. ....	98
Fig. 6.12: Sensor repeatability determined from three consecutive measurements of 680 ppb NH <sub>3</sub> . ....	99
Fig. 6.13: Change of the $I_{DS}-V_G$ characteristics under exposure to different NH <sub>3</sub> concentrations at 57 % RH and 25 °C. ....	100

---

Fig. 6.14: Influence of $\text{NH}_3$ on the hysteresis of the signal.....	101
Fig. 6.15: Calibration curve of the SiNW based $\text{NH}_3$ sensor.....	102
Fig. 6.16: Sensor response towards relative humidity changes in the range 17.5–69.5 %.	106
Fig. 6.17: Sensor response towards 0 % RH. ....	107
Fig. 6.18: Sensing responses of the SiNWs based sensor upon exposure to 680 ppb $\text{NH}_3$ at different humidity. ....	108
Fig. 6.19: Sensor response towards temperature changes in the range 30–50 °C. ....	110
Fig. 6.20: Sensing responses of the SiNWs based sensor device at different temperatures upon exposure to 680 ppb $\text{NH}_3$ .....	111
Fig. 6.21: Sensing properties of a SiNW sensor for various substances.....	113
Fig. 6.22: Response towards $\text{NH}_3$ gas of three SiNW based sensors prepared according to the same fabrication procedure. ....	114
Fig. 6.23: Comparison of the 680 ppb $\text{NH}_3$ detection of a fresh and an aged sensor.....	116
Fig. 6.24: Threshold voltage drift over a period of 3 h.....	118
Fig. 6.25: $I_{DS}-V_G$ characteristics before and after exposure to $\text{NH}_3$ with concentrations of 680 ppb and 1.36 ppm at 17.5 % RH at 25 °C for 10 min, respectively. ....	119
Fig. 6.26: Influence of humidity on the devices based on thermally grown $\text{SiO}_2$ shell nanowires.....	120
Fig. 6.27: Sensor response of a thermally grown oxide SiNW based device towards temperature changes in the range 30–50 °C.....	121



## List of Tables

Table 1.1: Overview of SiNW based sensors for the detection of ammonia. ....	4
Table 2.1: Summary of potential occurring effects in dependence of the NH <sub>3</sub> concentration [169, 170]. ....	37
Table 6.1: Requirements on gas sensors. ....	87
Table 6.2: Tested substances with corresponding concentrations and occupational exposure limits.....	112
Table 6.3: Comparison between sensing performances of natively and thermally grown oxide SiNW based devices.....	122





## Constants, Symbols, and Abbreviations

### List of Constants

$e$	Euler number	2.718281828459045235
$F$	Faraday constant	96 485.3365 C · mol <sup>-1</sup>
$k_B$	Boltzmann constant	8.617 343 · 10 <sup>-5</sup> eV · K <sup>-1</sup>
$R$	Universal gas constant	8.314 462 1 J · mol <sup>-1</sup> · K <sup>-1</sup>

### List of Symbols

$a$	Activity of the anion
$a_+$	Activity of the cation
$A$	Constant specific for a given film composition
$A$	Pre-exponential factor
$c$	Concentration
$c_A$	Analyte concentration
$c_{ox}$	Concentration of oxidant
$c_{red}$	Concentration of reductive
$C_{Tot}$	Total capacitance
$d_T$	tunneling distance
$d_{T,Si}$	Tunneling distance in unstrained bulk silicon
$E$	Electrode potential
$E_a$	Activation energy of adsorption
$E_A$	Activation energy
$E_C$	Conduction band (energy)
$E_d$	Activation energy of desorption
$E_{eq.}$	Equilibrium potential
$E_{eq.}^\circ$	Electrode potential
$E_{F,me}$	Fermi energy for metal
$E_G$	Band gap
$E_i$	Fermi level of intrinsic semiconductors
$E_n$	Electron energy

$E_V$	Valence band (energy)
$E_{vac}$	Vacuum energy level
$f$	Frequency
$I$	Current
$I_{DS}$	Drain-source current
$I_G$	Gate current
$j$	Charge current density
$j_0$	Exchange current density
$J$	Current density
$J_S$	Saturation current density
$J_{SB}$	Current density of the Schottky barrier
$J_{Th}$	Thermionic current density
$J_T$	Tunneling current density
$k$	Numerical factor
$K$	Adsorption rate constant
$K'$	Desorption rate constant
$k_0$	Reaction rate constant
$L$	Effective channel length
$L_d$	Debye length
MSD	Mean squared displacement
$q$	Electrical charge
$Q_D$	Charge of depletion layer
$R$	Resistance
$r_a$	Rate of adsorption
$R_{analyte}$	Resistance when exposed to the analyte
$R_{carrier}$	Resistance when exposed to the carrier gas
$r_d$	rate of desorption
$R_S$	Sensor resistance
$r_{tip}$	Tip radius
$S$	Sensitivity
$s_{bi}$	Standard deviation of the blank measures
$t$	Time
$T$	Temperature
$t_E$	End time

$t_s$	Start time
$V$	Voltage
$\dot{V}$	Volumetric flow rate
$V_{BG}$	Back-gate potential
$V_{DS}$	Drain-source voltage
$V_G$	Gate voltage
$V_{pp}$	Peak-to-peak voltage
$V_{th}$	Threshold voltage
$W$	Effective channel width
$W_A$	Work function
$\bar{x}_{bi}$	Mean value of the blank measures
$x_L$	Limit of detection
$y$	Sensor output
$z$	Ion charge number
$\alpha$	Characteristic slope of resistance curve for a material and gas
$\alpha_a$	Anodic transfer coefficient
$\alpha_c$	Cathodic transfer coefficient
$\epsilon_r$	Relative permittivity
$\epsilon_{SiO_2}$	Permittivity of silicon dioxide
$\eta$	Ideality factor
$\theta$	Fraction of the surface occupancy
$\lambda$	Wavelength
$\mu$	Charge carrier mobility
$\sigma$	Noise fluctuations
$\tau_{10}$	Recovery time
$\tau_{50}$	Recovery time
$\tau_{90}$	Response time
$\phi_{B,n}$	Potential barrier for electrons
$\phi_{B,p}$	Potential barrier for holes
$\phi_{eff}^*$	Effective barrier height
$\phi_{me}$	Potential difference between vacuum and Fermi potential
$\phi_{SB}$	Schottky barrier
$\chi$	Electron affinity
$\Psi_F$	Fermi energy

## List of Abbreviations

AC	Alternating current
AGW	Arbeitsplatzgrenzwert
ASCII	American standard code for information interchange
BNC	Bayonet Neill–Concelman
CAD	Computer-aided design
CMOS	Complementary metal-oxide-semiconductor
CMS	Chip Measurement System
CNT	Carbon nanotube
CVD	Chemical vapor deposition
DC	Direct current
DENA	Directed electrochemical nanowire assembly
EDX	Energy dispersive X-ray spectrometry
HF	High frequency
I <sup>2</sup> C	Inter-integrated circuit
I/O	Input and output
IR	Infrared
FE	Floating electrode
FET	Field-effect transistor
LCD	Liquid crystal display
LED	Light-emitting diode
LOD	Limit of detection
LPCVD	Low pressure chemical vapor deposition
MBE	Molecular beam epitaxy
MFC	Mass flow controller
MOCVD	Metal organic chemical vapor deposition
MOS	Metal oxide semiconductor
MOSFET	Metal-oxide-semiconductor field-effect transistor
MWCNT	Multiwall carbon nanotube
NBR	Acrylonitrile butadiene rubber
NDIR	Nondispersive infrared
NW	Nanowire
PCB	Printed circuit board

PECVD	Plasma-enhanced chemical vapor deposition
PVD	Physical vapor deposition
QCM	Quartz crystal microbalance
RH	Relative humidity
RIE	Reactive ion etching
RT	Room temperature
RTD	Resistive temperature detector
RTP	Rapid thermal processing
SAW	Surface acoustic wave
SBFET	Schottky-barrier field-effect transistor
SCR	Selective catalytic reduction
SEM	Scanning electron microscopy
SiNW	Silicon nanowire
SMT	Surface-mount technology
SNR	Signal-to-noise ratio
SOI	Silicon-on-insulator
SPR	Surface plasmon resonance
SWCNT	Single walled carbon nanotubes
TEM	Transmission electron microscopy
TGS	Taguchi gas sensor
TRGS	Technische Regeln für Gefahrstoffe
UART	Universal asynchronous receiver/transmitter
USI	Universal serial interface
UV	Ultraviolet
VLS	Vapor-liquid-solid process
VLSI	Very large scale integration
VOC	Volatile organic compound



# 1 Introduction

## 1.1 Motivation

To date, over 1000 different compounds have been identified in human breath [1]. Many of those molecules have been correlated to various diseases and metabolic processes. For example, during the last decade approximately 115 volatile biomarkers appearing in exhaled breath have been determined being related to cancer [2]. Breath analysis permits the use of non-invasive, real-time, and thus cost-effective methods for the diagnosis of a wide variety of diseases, including neonatal screening, asthma, renal and liver diseases, lung cancer, chronic obstructive pulmonary disease, inflammatory lung disease, or metabolic disorders [3, 4].

One approach in the exploitation of exhaled air for diagnostic purposes is the use of dogs. Those can be trained to e.g. identify people with bladder cancer on the basis of urine odor [5]. However, it is considered disadvantageous that the mean success rate for olfactory detection by dogs is around 40 %, which is relatively low compared to about 15 % expected by chance alone [5]. Additionally, using dogs only allows a qualitative estimation, but no quantitative evaluation of the composition of exhaled breath, which is however required for a rapid and enhanced diagnosis of diseases. It remains impressive that dogs can smell molecule concentrations range from tens of parts per billion (ppb) to 500 parts per trillion (ppt) [6] by their good olfactory sense. When smelling is defined as the result of a chemical analysis of the surrounding atmosphere, the way of signal processing between biological and artificial systems can be compared as shown in Fig. 1.1. Despite many research activities in recent years, the target of developing an artificial nose, also called electronic nose, that can compete with a biological olfactory system has not been reached. The challenges to create sophisticated electronic noses are twofold, because olfaction exhibits both high sensitivity for odors and clear discrimination between them [7]. Firstly, mammalian olfactory systems exhibit a very large chemical diversity and massive parallelism allowing discriminating 10,000 or more distinct odors [8]. This is the result of interaction of more than 400 different types of sensing cells in the human nose, where each type is replicated over 100,000 times, for a total of around forty million cells overall [9]. In addition, the olfactory system makes use of feature detection using broadly tuned receptor cells organized in a convergent neurone pathway [10]. Much effort lies ahead of the microelectronic technology to fabricate such a

sensor array with regard to the scale and chemical diversity. This is particularly important when the diverse composition of even clean air is considered (Fig. 1.2). Secondly, electronic nano- and microscale chemical sensing devices are normally not as sensitive as their counterparts of biological olfactory systems. For instance, not only dog but also human noses can perceive gases down to tens of ppb [11], which is lower than the detection limit of most of the current nano- and microsensors.

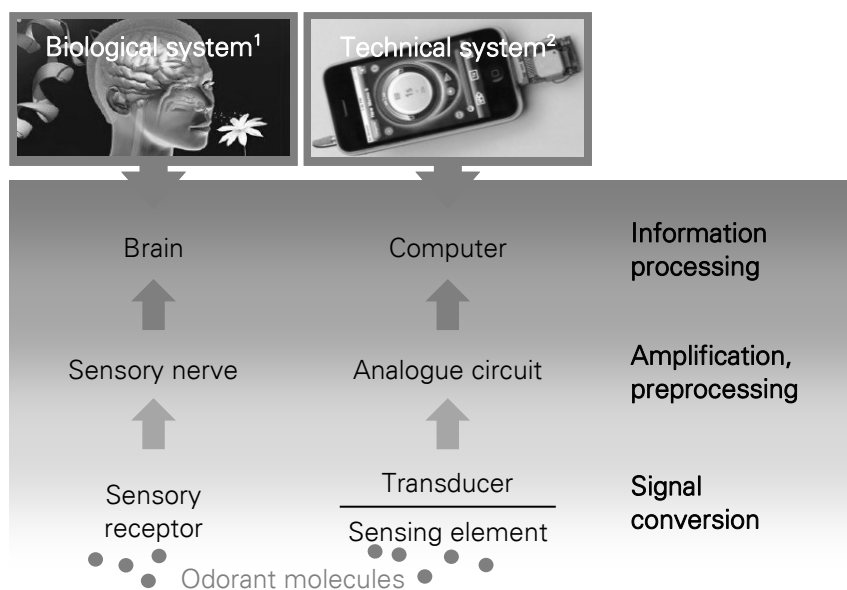


**Fig. 1.1:** Signal processing in living organisms and in technical systems (adapted from [12]).

<sup>1</sup> Picture from: <http://de.slideshare.net/SummerT23/olfaction-12941623>, 03.11.2014

<sup>2</sup> Picture from: <http://iphoneroot.com/wp-content/uploads/2009/11/chemical-sensor.jpg>, 03.11.2014

In addition to the use of gas sensors in medical applications, there is a great need for developing highly sensitive sensors for various application areas, like environmental monitoring, air quality control, and detection of explosive and toxic gases. Those developments to control hazardous gases, offensive odors, volatile organic compounds (VOCs), and other air pollutants are supported by various laws and directives around the whole globe, like the Offensive Odor Control Law in Japan, Occupational Safety and Health Act in the US, and the Air Quality Directive 2008/50/EC in Europe to name a few examples [13-15]. However, the need for highly sophisticated gas sensors is not only recognized by politics, but also by the industry, which reacts to this demand. This can be seen, because the global sensor market reached \$68.2 billion in 2012 and is expected to continue to grow, so that \$116.1 billion will be reached by 2019 [16].



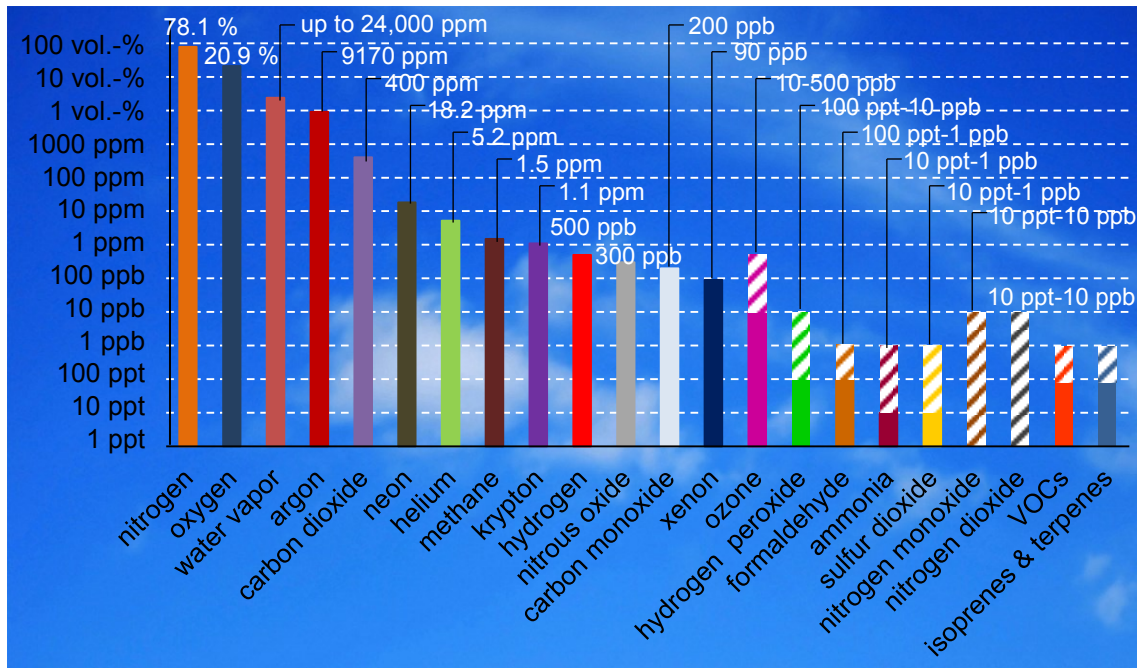


**Fig. 1.2:** Composition of clean air. VOCs include benzene, toluene, hexenal, C9-benzene, C10-benzene, acetonitrile, and ethylvinylketone.

In this market, semiconductor based sensors fabricated using mature microfabrication methods or novel nanotechnology are among the most important competitors. Silicon turns out to be advantageous in the field of semiconducting sensor materials due to reasons like low cost, reproducibility, controllable electronic behavior, and the abundant data for chemical treatments on silicon oxide. In particular silicon nanowires are considered to be a next generation building block for chemical sensing systems, because of their high surface-to-volume ratio, which is favorable to reach high sensitivities. Special interest is in the detection of ammonia ( $\text{NH}_3$ ), because it is not only one of the most common gases found in production processes in manufacturing plants, it is also one of the most dangerous. Apart from the wide spread use of ammonia sensors in leak detection in various industries particularly in the chemical industry, such as production of fertilizers, pharmaceuticals, fabrics, and dyes, the need for the detection of  $\text{NH}_3$  is also present in other areas. Especially low concentration measuring ranges dominate in medical applications for the diagnosis of certain diseases, like kidney disorder and ulcers [17, 18].

## 1.2 State of the Art

In the following, the state of the art related to silicon nanowire based sensors for the detection of ammonia is discussed. In recent years, silicon nanowires (SiNWs) have attracted

much attention as promising components for future nanoscale devices, especially for the detection of ammonia. In 2003, Zhou et al. studied the electrical resistance change of SiNW bundles upon exposure to  $\text{NH}_3$  [19]. This work firstly demonstrated the ability of SiNWs in an electrical sensor device for gas sensing applications. It has to be pointed out that in this study bundles of oxide-assisted grown SiNWs were used, instead of single wires. Those NWs were prepared by pressing them of about 0.4 mg in weight onto a glass surface. By applying silver glue at the two ends of each bundle of SiNWs, two electrodes were fabricated with a gap of 5 mm. Non-etched wires hardly showed any change in electrical resistance to a  $\text{NH}_3$  concentration of 1000 ppm, whereas the relative resistance of etched SiNWs with a native oxide shell changed in the order of 10,000.

Since then, several research groups have focused on the development and improvement of sensing devices composed of SiNWs. Table 1.1 gives an overview of SiNWs based sensors investigated upon  $\text{NH}_3$  exposure. Nanowires that have not been functionalized are referred to as bare.

**Table 1.1:** Overview of SiNW based sensors for the detection of ammonia.

Year	Approach <sup>a</sup>	SiNW size <sup>b</sup>	Functionalization	Principle	Measured concentration	Ref.
2003	BU (n)	~20 nm (d) 5 mm (g)	Si-H (via HF etch)	Resistor	1000 ppm	[19]
2006	TD (p)	76 ± 5 nm (d) 4 μm (g)	Bare	FET	No data	[20]
2006	BU (p)	76 ± 5 nm (d) 4 μm (g)	Bare	Resistor	Sat. con. <sup>1</sup>	[21]
2008	TD (p)	16 nm (w) 5 μm (l)	Peptides	Resistor	100 ppm	[22]
2009	TD (p)	75, 130 nm (w) 20 μm (l)	Bare	Resistor	250 ppm	[23]
2011	TD (p)	~200 nm (d) 4-6 μm (l)	PTE from metal <sup>2</sup>	Resistor	500 ppb	[24]
2012	BU (n)	100 nm (d) 20 μm (l)	Bare	Resistor	Pure	[25]
	TD (n)	100 nm (d) 10 μm (l)				
2012	BU (n)	150 nm (d) >20 μm (l)	Bare	Resistor	175-700 ppm	[26]
2013	BU <sup>3</sup>	50 nm (d)	Te nanoparticles	Resistor	10-400 ppm	[27]

<sup>a</sup> TD: top-down, BU: bottom-up, p: positive type doping, n: negative type doping

<sup>b</sup> w: width, l: length, d: diameter, g: gap between electrode contacts

<sup>1</sup> Sat. con.: saturated concentration

<sup>2</sup> PTE: porous top electrode

<sup>3</sup> non-doped

In the literature, several works report on the sensing response to  $\text{NH}_3$  of devices based on SiNWs without any chemical functionalization. Kamins and co-workers presented metal-catalyzed bridging SiNWs grown between silicon electrodes and exposed to a saturated vapor of  $\text{NH}_3$  at reduced pressure [21]. This led to a decrease of the conductance within 2 % for the p-type nanowires. Additional nanowire structures protected from the analyte were used as reference devices. The group of Rokad demonstrated a field-effect transistor (FET) with dense SiNWs arrays, fabricated by a top-down technique based on nanoimprint lithography [20]. The operation of the array as a FET was realized by metallic contacts and a bottom gate. When  $\text{NH}_3$  is adsorbed, the threshold voltage is shifted proportional to the concentration. In a further approach, the fabrication of SiNW sensors by SU8/ $\text{SiO}_2$ /PMMA trilayer nanoimprint was based on a silicon on insulator (SOI) substrate, which was doped by boron [23]. The devices were used for detecting 250 ppm  $\text{NH}_3$ . Different line widths of the nanowires were tested and the highest sensitivity of 19.7 % was determined for a width of 75 nm. In 2012, two types of resistors for  $\text{NH}_3$  detection were represented with on the one hand, non-intentionally doped SiNWs fabricated by the vapor-liquid-solid (VLS) growth method (bottom-up approach) and on the other hand, the so-called sidewall spacer method (top-down approach), respectively [25]. Pure  $\text{NH}_3$  exposure resulted in a relative response of  $\sim 20$  for VLS SiNWs based resistors and  $\sim 1000$  for polysilicon SiNWs based resistors. The VLS SiNWs based resistor type was further examined regarding different electrode structures [26]. Measurements under exposure to a range of  $\text{NH}_3$  concentration from 175 ppm to 700 ppm were performed with comb-shaped and V-shaped groove structures, respectively. The detection response was determined to be around 10 for both structures at a concentration of 175 ppm, but the V-shaped groove based resistor is more compatible with integration into planar technologies.

To find a way for selective detection of ammonia, McAlpine et al. explored the possibilities of linking peptides to SiNW sensors [22]. The surface of the nanowires was passivated with peptides using amide-coupling chemistry. Upon exposure to  $\text{NH}_3$  and acetic acid vapors, the peptide/nanowire sensors demonstrated the ability to discriminate analyte molecules at a concentration of 100 ppm from chemical mixtures. It was concluded that the results serve as a model platform for what can be realized in terms of selective and sensitive electronic noses.

In et al. reported a novel fabrication method based on two separate nanosphere lithography steps in order to achieve high sensitivity in ammonia sensing [24]. Arrays of vertically aligned SiNWs topped with a periodically porous top electrode enabled to greatly increase the sensitivity of the sensor (500 ppb  $\text{NH}_3$ ), while the pores in the top electrode layer significantly

enhanced sensing response times of approximately 6 min for  $\text{NH}_3$  by allowing target gases to pass through freely (Fig. 1.3).

A recent study showed SiNWs modified with tellurium nanoparticles by the reduction of  $\text{Na}_2\text{TeO}_3$  [27]. These devices detected  $\text{NH}_3$  in the range 10-400 ppm with response times of 5 s and the recovery times of 8 s. Ammonia reduces the tellurium oxide, which is present on the surface of Te nanoparticles. Thus, the majority carrier density in the Te is decreased, which in turn reduces the conductivity of the sensor.

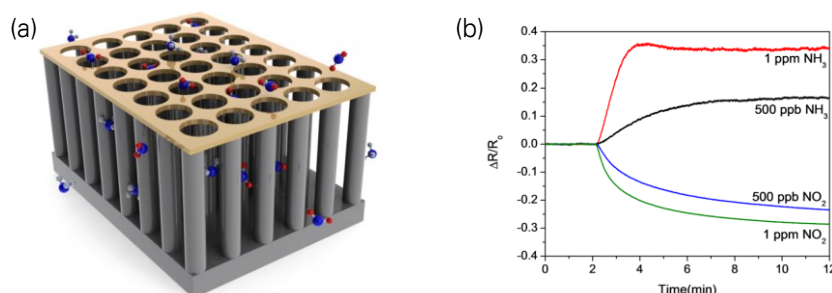


**Fig. 1.3:** Vertical SiNW array based  $\text{NH}_3$  sensor. (a) Schematic representation of the periodically porous top electrode nanowire array sensor concept. (b) Sensor response to various concentrations of  $\text{NO}_2$  and  $\text{NH}_3$  following 2 min of clean air at a constant temperature of  $40\text{ }^\circ\text{C}$  and relative humidity of 30 % [24].

### 1.3 Scope of this Thesis

The aim of this work is to develop and fabricate a gas sensor for the selective detection of low ammonia concentrations. To reach this goal, the fabrication of nanowires as reliable and reproducible components is required. For the simplification of the synthesis process copper nanowires are electrochemically prepared and parameters affecting the morphology of the wires are analyzed. The use of silicon nanowires represents an enhancement. A further required task on the way to achieve the main objective of this work is the design and assembling of an electrical measurement system, which allows the parallel evaluation of multiple sensors under a defined gas atmosphere. Moreover, this thesis intends to explain the basis of gas detection mechanisms of silicon nanowire based sensors. The studied sensing devices consist of undoped, monocrystalline silicon nanowires as recognition element. The peculiarity of these sensors is the abrupt metal-semiconductor interface achieved by silicidation. To determine the mechanisms that take place during ammonia exposure is the focus of interest of this study.

The thesis is composed of six further chapters after the introduction.

In the second chapter, different sensor types are reviewed with a particular focus on semiconductor sensor concepts. The introduced detection techniques are compared with each

other in order to show their individual advantages and limitations for the measuring of ammonia. In particular, the characteristics of nanoscale gas sensors are compared to bulk materials leading to silicon nanowire structures, which are motivated with respect to their use in gas sensors. Finally, the importance of the detection of ammonia is explained.

Chapter 3 presents an electrochemical synthesis method for copper nanowires. Special attention is dedicated to the parameters, which affect the wire morphology. These effects are relevant for the controlled nanowire growth. Lastly, the experimental results are discussed based on the theoretical background resulting in guidelines for the formation of copper nanowires.

Chapter 4 describes the details of the experimental techniques used to fabricate silicon nanowire based ammonia sensors. The focus is on the nanowire transfer and oxidation, sensor design, fabrication of contact electrodes, and the fabrication of Schottky contacts within a nanowire.

Chapter 5 is focused on the developed gas exposure apparatus. After discussing the state of the art and determining the requirements of those test systems, the technical implementation of the device used in this work is introduced. The four main parts are described in detail in order to demonstrate, how exactly the system works. Subsequently, the operational procedure of the gas measurements is presented.

In chapter 6, two different kinds of sensors are characterized electrically and with respect to their sensing performance towards ammonia. Introductory, necessary conditions for a high sensor quality are defined, which are the basis for the subsequent analyses of the conducted measurements. Firstly, the results of the sensing behavior of devices based on native SiO<sub>2</sub> shell SiNWs towards ammonia and interfering influences, such as humidity and temperature variations, are demonstrated and discussed. Secondly, the sensing behavior of a device with thermally grown SiO<sub>2</sub> layer silicon nanowires is studied. Finally, the results of both sensor types are compared.

Chapter 7 summarizes the main results of this work, draws the conclusions and shows perspectives for future projects with regard to the continuation of the research topics opened during this thesis.



## 2 Fundamentals

The purpose of this chapter is to give an overview of alternative sensor concepts and to present the state of the art in the field of gas sensing, in particular of ammonia ( $\text{NH}_3$ ) detection. First, some terminology is presented to provide a common knowledge base in the field of gas sensing followed by a historical outline. In the next section, classes of gas sensors divided into optical, electrochemical, electrical, mass-sensitive, magnetic, and thermometric mechanisms are described. Some key points concerning semiconductor gas sensor technology and their gas sensing properties are subsequently discussed. This leads to nanoscale gas sensors and especially silicon nanowire based sensing devices. Finally, potential application areas of ammonia sensors and already existing sensing principles are presented, explaining why the focus in this work is on ammonia sensing. The chapter is concluded with a short summary.

### 2.1 Introduction to Gas Sensors

Ambient air is composed of many different kinds of chemical species, natural and artificial, some of those are vital while many others are more or less harmful [13]. Therefore, the accurate determination of gas concentrations is important for many areas of application. This is usually accomplished by sensors. The term “sensor” still has no generally accepted definition. Therefore, it is necessary to define how it will be used in this work. The word “sensor” describes the whole device, following the Oxford English Dictionary definition, e.g. “a device which detects or measures a physical property and records, indicates, or otherwise responds to it”. A gas sensor is a sensor for detecting gaseous substances and is thus a chemical sensor. In the literature various definitions of chemical sensors can be found. Here, a suitable definition by Wolfbeis was considered appropriate: “Chemical sensors are small-sized devices comprising a recognition element, a transduction element, and a signal processor capable of continuously and reversibly reporting a chemical concentration.” [28]. Generally, accepted properties of such sensors comprise that sensors should [12]:

- Transform chemical quantities into electrical signals,
- Respond rapidly,
- Maintain their activity over a long time period,
- Be small,

- Be cheap,
- Be specific, i.e. they should respond exclusively to one analyte, or at least be selective to a group of analytes.

These characteristics should additionally include a high sensitivity, which allows the sensor to detect low concentrations. In order to meet the above mentioned requirements, a gas sensor usually consists of a recognition element (receptor) and a transducer connected in series, see Fig. 2.1. In the majority of gas sensors, the working principle is based on the interaction of the recognition element with the analyte molecules resulting in a change of the physical properties in such a way that the connected transducer can gain an electrical signal. Other possibilities are that either one component acts as receptor and transducer or additional elements are necessary units for signal amplification and conditioning [12]. A gas sensor detects gases, which are called analytes and commonly used units to express gas concentrations are parts per million (ppm), parts per billion (ppb), and parts per trillion (ppt). All of these values define the molar concentrations of the analyte within the tested gas sample.

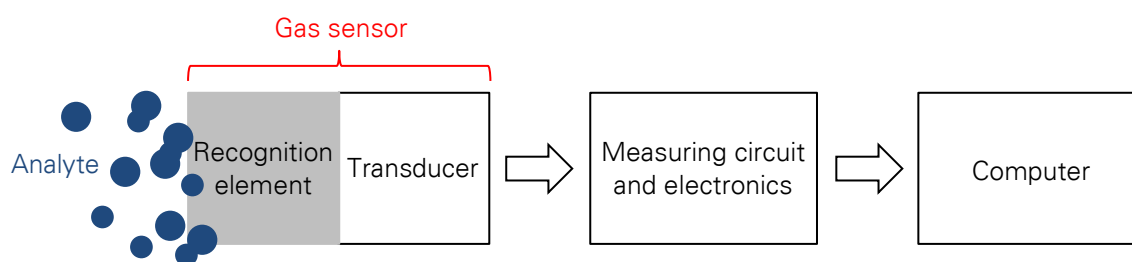


**Fig. 2.1:** Schematic illustration of a typical gas sensor system. The analyte interacts with the receptor, which changes its physical properties. This results for instance in a current variation of the transducer. The electronics is responsible for signal amplification etc. and the computer for the data analysis.

Sensors for the detection of gases incorporate versatile and partially lifesaving functions, nevertheless they are employed mostly inconspicuous. They are applied to monitor the environment, in industrial processes as well as in everyday life, and health of people. Some examples of application include exhaust gas sensor systems for efficient emission reduction [29], monitoring of carbon dioxide in the environment [30], and cancer identification by the analysis of breath [31]. Significant progress has been made in recent years and the literature is full of interesting developments. Lately developments contain a wide range of technologies, including improved surveillance systems for security applications and miniaturization of systems that were only used in laboratories.

Further developments in the field of gas sensing technology are expected also in the future, because the demand for small and inexpensive gas sensors is huge: Methane sensors could



sound the alarm when gas leaking from broken pipes in households occurs. Oxygen meters might optimize the combustion in heating systems, engines and power plants. In air-conditioned buildings or car interiors sensors for carbon dioxide would be able to draw attention to impending fatigue. Joggers could check with ozone measuring instruments whether they should postpone their run, and some diseases can be detected by means of trace gases in the exhaled air [32].

### **2.1.1 History of Gas Sensor Development**

People have worked in toxic environments since before recorded history, such as carbon monoxide sources from open flame of pre-historic cave painters. The first attempts to detect hazardous gases were performed in coal mines. With the beginning of the Industrial Revolution, coal as fossil fuel became very important. Coal is mined in mines, where methane appears naturally from the ground. This gas is especially dangerous, because it can neither be seen nor smelled and can be fatal. The first method involved using humans, where one person, before the shift started, wore a wet blanket over his shoulders and head carrying a long wick with its end lit on fire. The methane gas ignited, when the person encounters it. To protect the life of humans, the next method of detection was to use canaries in mines in the early 20th century [33]. The concept was to carry the bird in its cage into the mine and it would exhibit the effects of the toxic atmosphere before they became injurious to humans. A further development of gas detection was the flame light, which contained the flame inside a glass barrel and was encapsulated in a flame-arrestor shell so that there was no way the flame could ignite the outside atmosphere. By means of graduation marks on the glass, it could be determined, whether oxygen is absent or a combustible gas is present. While this method improved the safety compared to the lighted wick and provided light, an accidentally dropped lamp could still ignite the atmosphere if methane was present.

Only since the 1960s, gas sensors were introduced for non-professional use. Before that, some gas sensing methods just for limited fields were developed. Examples are two technologies for detecting combustible gases in the 1920s, one based on light-wave interference and the other one using a platinum catalyst in a Wheatstone bridge electronic circuit [34, 35]. In 1953, Brattain and Bardeen demonstrated that a gas can affect the electrical properties of a material by the change of the semiconducting properties of germanium with a variation of the partial pressure of oxygen in the environment [36].

It was only in 1962 that the first resistive sensor for detecting inflammable gases using oxide semiconductor (ZnO) was reported by Seiyama et al. [37]. A prototype ZnO gas sensor is

shown in Fig. 2.2a. In the same year, Taguchi invented independently the same type device based on  $\text{SnO}_2$  (Fig. 2.2b) and pioneered the application of metal oxide semiconductors to gas sensing [38]. Devices based on this technology are called Taguchi gas sensors (TGS). Fig. 2.2c shows an experimental setup, where a Japanese sake bottle was used as gas chamber.

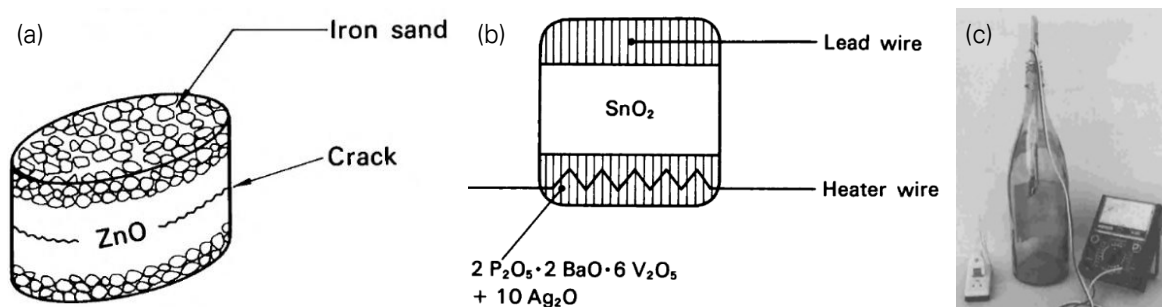


**Fig. 2.2:** Former gas sensors and measuring setup. (a) Design of a tabled-shaped gas sensor, in which  $\text{ZnO}$  was held by iron sand at both sides and pressed. The sensor cracked with repeated heat cycles, because the expansion coefficient of the both materials was quite different. (b)  $\text{SnO}_2$  gas sensor devised by Taguchi. Commercially available  $\text{SnO}_2$  was pressed and a Nichrom wire was used as a heater. A semiconductor glass mixed with equivalent  $\text{Ag}_2\text{O}$  was used as junction between  $\text{SnO}_2$  and the heater and electrode to increase the conductivity. (c) Japanese sake bottle used as gas chamber. [39]

The semiconductor gas sensors were further developed including the addition of catalyst materials, which are e.g. noble metals like Pd, before being commercialized for non-professional uses in the 1970s. Gas sensor technology expanded largely since 1980s and in recent years, a variety of further technologies was developed for gas detection. In the following, some of these technologies are discussed.

### 2.1.2 Gas Sensor Classification

Here, a brief overview of the more common methods of gas detection currently in use is given. It is important to point out that this summary is not comprehensive. Many different methods based on different materials and operating on diverse principles have been developed for detection over the years and may be used in very specific areas of detection. Additionally, variants of the approaches described here can also be employed. Six general categories of sensors are prevalently distinguished, considering signal transduction mechanisms [40]:

- (1) Optical sensors,
- (2) Electrochemical sensors,
- (3) Electrical sensors,

- (4) Mass-sensitive sensors,
- (5) Magnetic sensors,
- (6) Thermometric sensors.

In the following, the six types of sensors are introduced to get an insight and understanding of the different existing working principles of gas detection.

### *Optical sensors*

Optical gas sensors detect the modulation of some properties of the radiation that result from the interactions between various forms of light or electromagnetic waves and the analyte. Most gases can absorb infrared (IR) light at wavelengths, which are characteristic of the bonds present. For these gases, the absorbance of the gas is proportional to the concentration. Most small portable systems employing this technology use Nondispersive IR (NDIR), where a polychromatic light source is used to pass electromagnetic energy through a gas sample (Fig. 2.3a). An optical filter in front of the light detector allows limiting the incoming light to only particular wavelengths [41].

In another approach the light is transmitted through an optical waveguide, whose surface is coated with a sensitive layer. A fiber optic sensor typically includes three parts, a source of incident light, an optrode, and a transducer to convert the changing photonic signal to an electrical signal [41]. The optrode contains the reagent phase membrane or indicator, which influences the intensity or spectrum of the guided light inside the fiber affected by the analyte [42]. The location of the reagent varies with different sensor types, so also the end of the fiber can be coated (Fig. 2.3b).

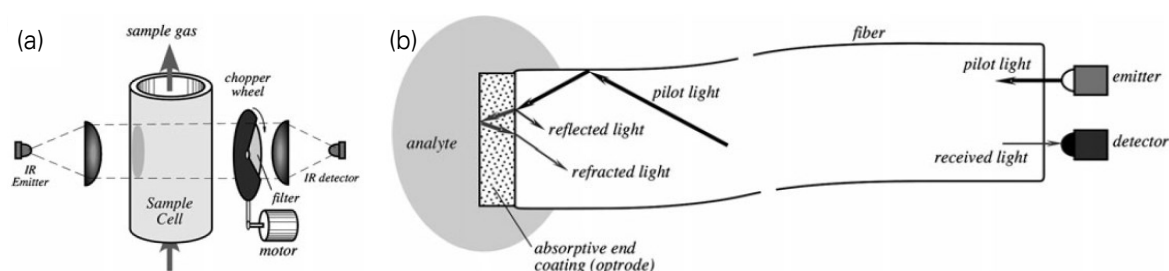


**Fig. 2.3:** Optical gas sensor. (a) Nondispersive infrared and (b) fiber optic based gas detection [41].

A special type of optical sensors operates with surface plasmon resonance (SPR). In the SPR method, the resonance angle is very sensitive to the refractive index of the medium outside the metal thin film and thus the measurement of this angle can be used to detect gas concentrations [43]. When monochromatic light is incident on a surface of an optically dense to an optically thin medium at a smaller angle than total reflection, the entire light is indeed

reflected, but it still forms an electric field in the optically thinner medium. This decreases exponentially with the distance from the surface. If this surface is now coated with a very thin non-magnetic metal, the electric field penetrates the conductive layer and surface plasmons are generated. Only if these plasmons are in resonance with the photons, a reflection now occurs. The resonance is dependent on the wavelength, the angle of incidence of light and also highly sensitive to the refractive index at the surface of the interface. The reflection angle is consequently very sensitive to the change of the refractive index of a gas sensitive layer [44].

### *Electrochemical sensors*

Gas sensors based on electrochemical cells are made of two or more electrodes, which are connected by an electrolyte, in which gas can diffuse through a membrane into the reaction chamber. Similar to a battery cell, a chemical reaction takes place under the influence of the measured gas, which leads to a voltage (potentiometric measuring principle), an electric current (amperometric measuring principle), or conductivity (conductometric measuring principle) depending on the operating mode of the sensor [41]. The reagents in the electrolyte, the electrode material, and the membrane determine the characteristics of the sensor. The electrodes are often made of catalytic metals, like platinum or palladium, or they can be carbon coated metals and have a high-surface area to react with as much of the analyte as possible for a high sensing signal. Additionally, they can be modified to enhance their reaction rates and extend their lifetime. The reactions that can occur are limited by the electrolyte, because this medium carries charges using ions instead of electrons, which contributes to the selectivity of the sensor. Electrochemical gas sensors generally have a greater selectivity than semiconductor gas sensors. They are suitable for quantitative measurements, though the area of application is preferably in the lower concentration range in favor of a longer working life span (due to the lower material conversion). At some point, however, the electrolytes are spent and then the sensor needs to be replaced. Thus, this technology is not suitable for maintenance-free devices. Their use is mainly in the industrial sector, like in the monitoring or in test equipment that are maintained at regular intervals.

### *Electrical sensors*

Electrical sensors cover a large group of gas sensors that operate due to a surface interaction with the target gas and measure the effect of the analyte on the electrical properties of another material. Usually, these sensors are the least expensive commercially available devices. The detection can be either reversible or destructive irreversible leading to analyte

decomposition. Important advantages are that the devices and supporting electronics are often simple in design, can be miniaturized, and resulting products can often be used in rough environments. Sensors in this class include polymer, metal, metal oxide, semiconductor conductometric sensors, capacitance sensors, work-function-type-, Schottky barrier-, MOS-, and FET-based sensors [45]. Due to the variety of different types, not all of them can be analyzed within this chapter. The most important electrical sensor types for this work are discussed in section 2.2 and 2.5. More detailed information about these sensors can be found in [45].

### *Mass-sensitive sensors*

Mass-sensitive gas sensors, such as microcantilever, quartz crystal microbalance (QCM), and surface acoustic wave (SAW) based sensors are sensitive to mass changes of the surface during interaction with gases [46].

The cantilever based sensor technology is derived from the atomic force microscopy technique, which works by scanning a surface with very tiny tip controlled by a feedback loop, e.g. the force between tip and surface is kept constant by a feedback loop. For the application in gas detection, neither a tip nor a feedback loop is necessary. A free-standing microcantilever is coated by a sensing layer to achieve chemical functionality. When a specific mass of analyte is adsorbed, the mechanical response in either, the static mode (deflection) or the dynamic mode (shift of resonance frequency) is measured under exposure to a gas without resorting to a feedback loop [47], see Fig. 2.4a.

The QCM technique is based on a quartz resonator, which itself is typically used as an oscillator with its stable frequency and a mass change causes a shift in its resonance frequency. The amount of this frequency shift is proportional to the mass change and this correlation is known as mass loading effect [48]. The structure of a QCM based gas sensor is shown in Fig. 2.4b. The quartz resonator comprises a quartz plate and electrodes deposited on both sides. It can be operated as a gas sensor, when the electrodes are coated with a sensing layer. The resonator is connected to an oscillator circuit and a frequency counter measures the shift in oscillation frequency [49].

SAW based sensors enable to distinguish masses up to the femtogram range [50]. The working method is indicated in Fig. 2.4c. A pair of interdigitated electrodes is patterned on the piezoelectric substrate. By applying a high frequency (HF) signal between the transmitter and receiver electrodes, a seismic wave (Rayleigh wave) is formed on the circuit. The interaction of a gas-sensitive layer coated on the substrate with the ambient air leads to frequen-

cy changes that serve the quantification of the analyte concentration. The selectivity is determined by the chemically sensitive layer.

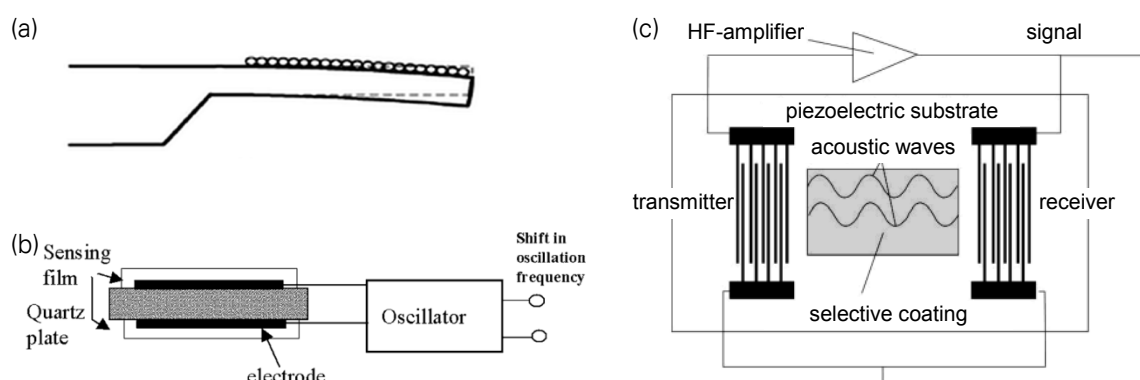


**Fig. 2.4:** Schematic diagrams of mass-sensitive gas sensors. (a) Microcantilever that bends owing to adsorption of target molecules and change of surface stress [47]. (b) Quartz crystal microbalance (QCM) device [49]. (c) Surface acoustic wave (SAW) gas sensor, adapted from [50].

### *Magnetic sensors*

The principle of magnetic sensors is based on the change of the magnetic properties of the analyte. Those sensors are represented by certain types of oxygen monitors [51]. It was found that oxygen is strongly susceptible to interaction with an external magnetic field, thus it has a high magnetic susceptibility compared to other gases [52]. Additionally, oxygen molecules have strong paramagnetic properties (positive value of the magnetic susceptibility), whereas almost all technically important gases (exception: nitrogen oxides) are diamagnetic. Therefore, a sensor principle for oxygen can be built with only minor cross sensitivities.

In the following, the measuring principle of the acousto-magnetic spectroscopy is presented, which is, in addition to e.g. the Munday-cell, widely used in oxygen monitoring. The oxygen sensor consists of two major parts: an electromagnet and an air chamber as shown in Fig. 2.5a. When a gas flows through a magnetic field, it absorbs energy resulting in the increase in volume of the gas. Thereby, in a pulsating magnetic field, periodic pressure changes arise, which can be detected as sound waves with a sensitive differential pressure transducer (microphone). The amplitude of the signal is directly proportional to the current  $O_2$  partial pressure of the measured gas. To increase the measurement accuracy, the pressure change in the measured gas is compared to the pressure change in the oxygen-free reference gas (or a gas with known oxygen content).

### Thermometric sensors

In thermometric (calorimetric) sensors chemical reactions cause temperature changes, which are converted into electrical signals, such as the change of the resistance, current, and voltage. These sensors operate with a temperature probe that is coated with a chemically selective layer. The device detects a transfer of heat during the reaction between the gas and the coating upon exposure to the analyte [41]. This catalytic reaction takes place at the surface of the sensor and has the effect that heat is evolved. Inside the device the related temperature changes and is measured. A simplified drawing of such a sensor is shown in Fig. 2.5b.

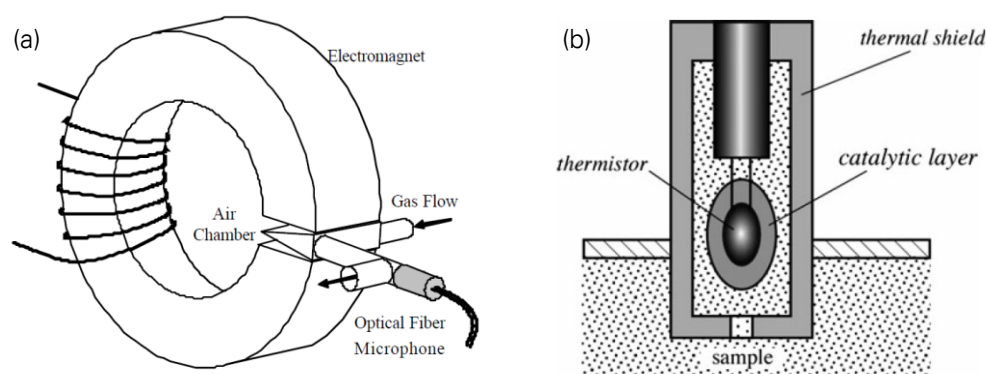


**Fig. 2.5:** Principles of gas sensing via magnetic and thermal detection mechanisms. (a) The basic measuring cell configuration of an acousto-magnetic oxygen gas sensor [52]. (b) Schematic representation of a thermal gas sensor. The thermal shield reduces the heat loss to the environment and the thermistor is coated by a catalytic layer [41].

Catalytic sensors, often referred to as pellistors, are a widely used type of such gas sensing devices and have been designed specifically to detect low concentrations of flammable gases in air [53, 54]. In those sensors the thermistor includes a platinum coil, which is embedded in a porous ceramic pellet covered with a catalytic metal like palladium or platinum. The coil operates as heater as well as the resistive temperature detector (RTD). Other kinds of heating elements and temperature sensors can also be used. When the target gas reacts at the catalytic surface, the heat liberated from the reaction increases the temperature of the pellet and coil, thus its resistance raises [41]. The sensor can be operated in two possible modes. In the isothermal mode, the temperature is kept constant while an electronic circuit controls the current through the coil. The other mode is nonisothermal, where the sensor is connected to a Wheatstone bridge whose output voltage is related to the gas concentration.

## 2.2 Semiconductor Gas Sensor Technology

A semiconductor gas sensor can be defined as a sensor into which a semiconductor material is incorporated and thus is based on a reaction between the semiconductor and the gases in the atmosphere, which leads to a change in semiconductor conductance [55]. This technology includes numerous methods of varying structures, different materials, and various working principles. Methods based on different materials can be classified in metal oxide semiconductors, polymers, carbon nanotubes, and moisture absorbing material [56]. Silicon based gas sensors can also be classified in the semiconductor technology, but are discussed in detail in section 2.5. Here, the emphasis is on the general processes occurring on the gas/semiconducting interface. Particularly, the two most competing technologies, metal oxide and carbon nanotubes (CNTs) based gas sensors, will be considered. This is essential in order to carry out a comparative evaluation of the silicon based technology. Furthermore, most of the surface processes described in this section are generally important on semiconductor gas sensors.

The adsorption of molecular species on the recognition element can take place either physical or chemical. Physisorption is a weak adsorption process that occurs due to the presence of the van der Waals forces of attraction having a low binding energy ( $\sim$  meV for small gas molecules and  $\sim$  few eV for large gas molecules) [57]. The process is usually connected to a dipole-dipole interaction between the gas and the adsorbent [55], where the electronic and chemical structure of gas molecules and surface does not change. Further, low binding energies lead to a complete desorption of gas molecules, which enables a full and fast sensor recovery. However, as physisorption is not specific, it results in low sensitivity and selectivity of the sensors. Chemisorption comprises the formation of chemical bonds between the sensing element and the gas molecules. Normally, a gaseous molecule dissociates into atoms and this leads to high binding energies  $\sim$  several eV [58]. This is favored for fabrication of gas sensors with a high selectivity, even though molecular desorption is quite low for chemisorbed molecules resulting in slow recovery [57]. Both adsorption types depend on the temperature and partial pressure of oxygen in the environment [59].

For a temperature range required for chemiresistive metal oxide gas sensor operation, oxygen is ionosorbed on the metal oxide surface. In ionosorption, there is no local adsorbate to surface atom bonding, but oxygen acts as a surface state, capturing an electron or hole depending on the semiconductor (n-type or p-type) [55]. Oxygen is attached to the surface by electrostatic attraction. In n-type semiconductors, ionosorbed oxygen atoms act as surface acceptors by binding electrons. This results in an increase of the surface resistance of the



material. Oxygen can be ionosorbed onto the metal oxide surface in several forms in dependence of the temperature. This means that at lower temperatures (150-200 °C), oxygen does not dissociate and adsorbs in a molecular form as either neutral  $O_2$  or charged  $O_2^-$ , whereas at temperatures higher than 200 °C, oxygen dissociates and adsorbs as  $O^-$  ions [59].

In metal oxide gas sensors, the change in the electrical conductivity of semiconducting metal oxides (such as  $SnO_2$ ,  $ZnO$ ,  $TiO_2$ ,  $ZrO_2$ ,  $CeO_2$ ,  $WO_3$ ,  $Fe_2O_3$ ,  $In_2O_3$ , and  $CuO$ ) upon exposure to gases is used as sensor effect. Many different metal oxides have been investigated as sensing materials [60], however tin dioxide ( $SnO_2$ ) has remained the most commonly used gas sensing material [56] and is the best understood material in the basic studies of the gas sensing mechanism [61-63]. Therefore, in the following the mechanism of gas detection is discussed more in detail on the example of a  $SnO_2$  sensor. This type belongs to the n-type semiconductors, which have always a certain number of oxygen vacancies. Some of the metal atoms thus cannot replace its outer atoms with the  $O_2$  atoms. These outer electrons are available as free electrons in the conduction band of the semiconductor for the electrical conduction. In dependence of the  $O_2$  partial pressure at the metal oxide surface, the concentration of the oxygen vacancies changes. At temperatures between 200-500 °C a stable  $O_2$  vacancy concentration inside the metal oxide is formed as function of the  $O_2$  partial pressure, so there is a direct dependence of the conduction electron concentration or the electrical conductivity and the  $O_2$  partial pressure. In addition to pure oxygen also oxidizing gases (such as e.g.  $N_2O$ ) reduce the number of  $O_2$  vacancies, so that even in presence of such gases, the number of free electrons in the conduction band decreases and the specific resistance increases according to the relationship empirically found [41]:

$$R_S = A [c]^{-\alpha}, \quad (2.1)$$

where  $R_S$  is the sensor electrical resistance,  $A$  is a constant specific for a given film composition,  $c$  is the gas concentration, and  $\alpha$  is the characteristic slope of  $R_S$  curve for that material and expected gas [10].

Reducing gases such as  $H_2$  or  $CO$  react in the presence of  $O_2$  to  $H_2O$  and  $CO_2$ . On the surface of a metal oxide they react with the oxygen and thus increase the number of  $O_2$  vacancies. This effect can be used at a constant  $O_2$  partial pressure for measuring the concentration of reducing gases [64]. The increase in the  $O_2$  vacancies increases the number of available free electrons in the conduction band, conductivity of the metal oxide layer rises.

Fig. 2.6a shows a scanning electron microscope (SEM) picture of a  $\text{SnO}_2$  layer. Metal oxides are typically fabricated as thin layers (nm- $\mu\text{m}$  range) on an interdigitated electrode structure. Sensitivity and selectivity can be increased by adding a catalyst, such as platinum (Pt). Due to the high specific resistance of the metal oxide, the metal contact layer is formed as a comb structure (interdigitated structure), so that a suitable total resistance signal for the processing results. To achieve the required operating temperature a Pt heater is placed on the backside of the substrate. In Fig. 2.6b a schematic of an exemplary  $\text{SnO}_2$  based sensor is shown.

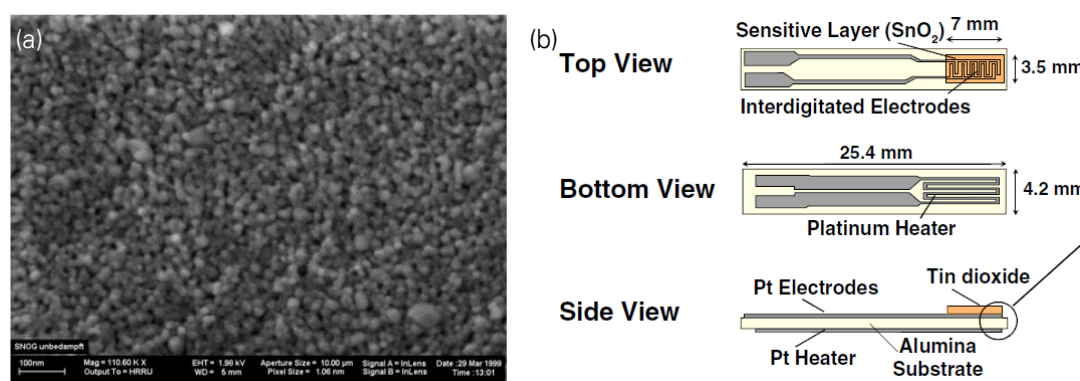


**Fig. 2.6:**  $\text{SnO}_2$  based gas sensor. (a) SEM picture of the  $\text{SnO}_2$  sensing layer. (b) Layout of the planar alumina substrate with the  $\text{SnO}_2$  layer printed on top of the interdigitated Pt electrodes and the Pt heater. The heater on the back controls the operational temperature of the sensor. [65]

The main disadvantage of gas sensors based on metal oxide semiconductors is the poor sensitivity at room temperature. However, carbon nanotubes have become a promising material for high-sensitive gas sensors, because of their unique properties, like e.g. high mechanical and thermal stability, high surface-to-volume ratio, and semiconducting character. CNTs are seamless cylinders formed by rolling-up of a graphene stripe. CNT based gas sensors show a high sensitivity towards various gases, such as ammonia ( $\text{NH}_3$ ) [66], carbon dioxide ( $\text{CO}_2$ ) [67], nitrogen oxide ( $\text{NO}_x$ ) [68, 69], ethylene [70], and organic vapors [71] at room temperature and thus cover a large scope of application. In general, CNTs can be categorized into single-walled carbon nanotubes (SWCNTs) and multiwall carbon nanotubes (MWCNTs). Both types are used for gas sensing [56]. Although, there are several different designs of CNT based gas sensors, like chemicapacitive [72] and field-effect transistor (FET) [73, 74], chemiresistive sensors based on a resistance change as output are the most commonly used architecture in the design of CNTs gas sensors, because they are easy to fabricate, have a simple structure, and a low power consumption [75]. The illustration in Fig. 2.7a shows an exemplary design of a CNT based chemiresistive gas sensor. When a particular gas is adsorbed on the surface of carbon nanotubes from the surroundings, charge transfer

occurs between the CNTs and gas molecules. Adsorption is a surface phenomenon, thus atoms from the outermost layer in CNTs are of main interest. In SWCNTs all the atoms act as surface atoms [76, 77], whereas for MWCNTs just the atoms located in the topmost layer are responsible for the sensing response [78]. Pristine CNTs exhibit p-type majority charge carriers, because of oxygen impurity [79]. Gas molecules adsorb on CNTs and can be either charge donors or acceptors to the nanotubes [80]. When the CNT surface is exposed to reducing gases, the electrical resistance increases due to the recombination of free electrons transferred from the gas molecules to the CNT and holes existent in the CNTs. On the other hand, oxidizing gases withdraw electrons from CNTs when adsorbed on their surface. This generates more holes on the surface of p-type semiconductor CNTs and thus decreasing the resistance [81]. Fig. 2.7b demonstrates the electron transfer mechanism between CNTs and adsorbed oxidizing as well as reducing gases.

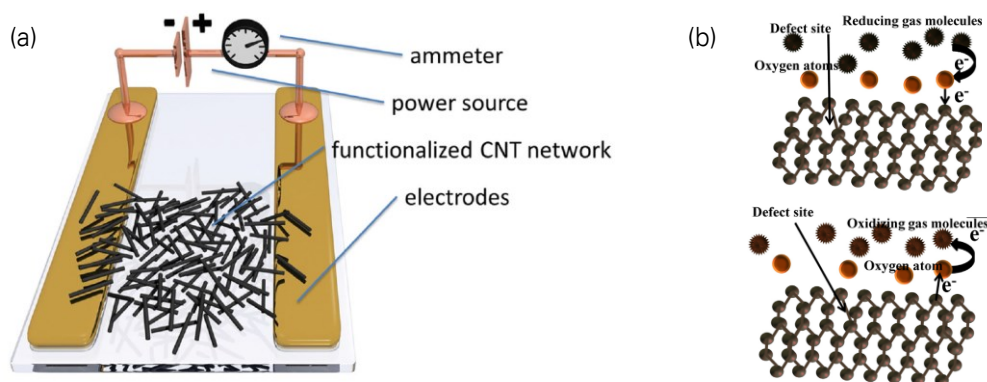


**Fig. 2.7:** Schematic representations of CNT based gas detection. (a) Resistivity based SWCNTs gas sensor [82]. (b) Electron transfer into/out of pristine carbon nanotubes, (top) reducing gas molecules are adsorbed on CNT surface and transfer electrons to CNT through defects and oxygen atoms present on surface due to chemical processes, (below) oxidizing gas molecules are adsorbed on CNT surface and withdraw electrons from CNT [57].

One possibility to enhance the sensitivity and selectivity of CNTs is chemical functionalization of the nanotubes as functional groups present on the CNT surface make them well soluble, which allows both a more extensive characterization and subsequent chemical reactivity. Hirsch summarized the surface activation routes for CNTs through different functionalization approaches [83]. Usual groups used to functionalize CNTs are hydroxyl ( $-\text{OH}$ ), carboxyl ( $-\text{COOH}$ ), carbonyl ( $-\text{C}=\text{O}$ ), and amino ( $-\text{NH}_2$ ) [84-87]. In terms of improving sensitivity, pure CNTs show no response to hydrogen due to the weak binding energy [88], but the decoration of CNTs with Pt or Pd, which act as a catalyst for the adsorption of  $\text{H}_2$ , CNTs become sensitive to  $\text{H}_2$  [89]. To enhance the selectivity to certain gases, silane binders are mixed in

CNT solution [90]. However, functionalization results in the degradation of the electrical properties of CNTs, because it introduces defects and impurities in CNTs [57].

Another interesting development in sensing materials based on carbon is the use of gas sensors with graphene. Those showed good gas sensing characteristics, because their whole volume is exposed to the analyte and they have few crystal defects, which maximizes the signal-to-noise ratio to a level sufficient for detecting variations of gas concentrations at room temperature [91]. It can be expected that novel materials, such as CNTs and graphene, will achieve increasingly attention as gas sensing materials in the future.

## 2.3 Gas Sensing Properties

In order to be used in practice, gas sensors have to meet diverse requirements depending on the area of application. Several terms are used to describe those requirements, which is fundamental to determine the performance of a gas sensor. They include ways to clearly characterize response, response and recovery time, sensitivity, selectivity, long-term stability, signal-to-noise ratio (SNR), and additional properties that are not considered further here. The explanations of selected parameters describing sensor characteristics are considered here for the sensor system as shown in Fig. 2.8.

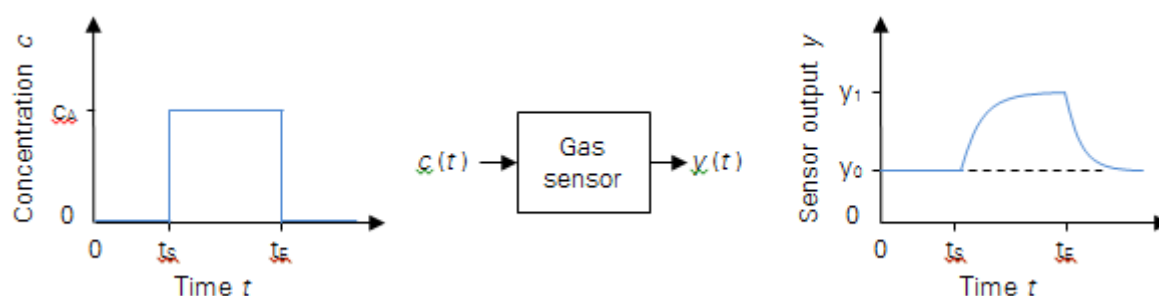


**Fig. 2.8:** Gas sensor block diagram (center), example of a possible sensor output (right) due to a step change in the concentration of an analyte (left).

### 2.3.1 Response, Response Time, and Recovery Time

The sensor output signal represents a reference or baseline value  $y_0$  under influence of the carrier gas with constant conditions, such as constant flow rate, humidity, and temperature, before exposure to the target gas ( $c = 0$ ). When the sensor is exposed (at time  $t_s$ ) to an analyte concentration  $c_A$ , the change of the sensor signal is related to the baseline and the relation  $\Delta y = y_1 - y_0$  is empirically defined as the response.

The time between the beginning of the exposure and a response of a certain percentage of the final change in the sensor signal is defined as the response time, e.g.  $\tau_{90}$  is defined as the time to reach 90 % of the final sensor signal [92]. If a device is sensitive to an analyte, a response is observed under exposure. After the end of exposure (at time  $t_E$ ), the sensor signal will return to its baseline value, if it is reversible. The time that the sensor output needs to go back to the baseline condition or to a certain percentage of it, is called recovery time. This typically depends on both, the analyte concentration within the carrier gas and the duration of the exposure. Small values of response and recovery time are indicative of a good sensor.

### 2.3.2 Sensitivity and Limit of Detection

The sensitivity  $S$  of a sensor describes the order of magnitude of the response to a particular analyte. Here semiconductor gas sensors are considered, which is why the sensor signal corresponds to the resistance behavior under gas exposure. The often used definitions are the following. Sensitivity represents the ratio of resistance in the carrier gas to that in the target gas [92], i.e.

$$S = \frac{R_{carrier}}{R_{analyte}}, \quad (2.2)$$

where  $R_{carrier}$  is the resistance value of the sensor in the carrier gas and  $R_{analyte}$  the resistance when exposed to the analyte.

The sensitivity as a percentage value is the ratio of the resistance change under gas exposure to the resistance in the carrier gas and can be determined by the equation [34]:

$$S (\%) = \frac{R_{carrier} - R_{analyte}}{R_{carrier}} \cdot 100. \quad (2.3)$$

A positive value of  $S$  means that the resistance decreases on gas exposure and vice versa. For a sensor, which allows the detecting of low analyte concentrations, a high sensitivity is indispensable.

The limit of detection (LOD) is a term used to describe the lowest analyte concentration that can be reliably measured and at which detection is feasible [93]. Each measurement method has limits in terms of the lowest quantity of a substance that can be determined. The fewer the substance that is detected, the lower the measured value is different from the value in absence of that substance (a blank value). But since both the blank value and the measured

value fluctuate from case to case (i.e. have a distribution), the correct assignment of the measured value becomes more uncertain the more the true analytical value approaches the blank value. The limit of detection, expressed as the concentration,  $c_A$ , is derived from the smallest measure,  $x_L$ , that can be detected with reasonable certainty for a given analytical procedure. The value of  $x_L$  is given by the equation [94]:

$$x_L = \bar{x}_{bi} + k s_{bi}, \quad (2.4)$$

where  $\bar{x}_{bi}$  is the mean of the blank measures,  $s_{bi}$  is the standard deviation of the blank measures, and  $k$  is a numerical factor chosen according to the confidence level desired. In practice, it is usually adequate to require in a first approximation that the useful signal has to exceed the mean value of the blank value  $\bar{x}_{bi}$  by three times ( $k = 3$ ) of the standard deviation of the background signal  $s_{bi}$ .

To receive a sensor output signal that can reliably be distinguished from the signal that is obtained in the absence of analyte, a sufficient analyte concentration must be present. The assumption of the above described simple and quick method is that if analyte is present, it will produce a signal greater than the analytical noise in the absence of analyte. This approach has the weakness that no objective evidence exists to prove that a low concentration of analyte will indeed produce a signal distinguishable from a blank value [93].

### 2.3.3 Selectivity

Selectivity is defined as the capability of a sensor to detect primarily one designated gas in the presence of other species [95]. Usually, it is desired that one sensor is sensitive to a particular gas, if possible, exclusively, even when interfering gases are present, which is expected in real conditions. An interfering gas is one, which causes a response of the sensor similarly to the desired analyte being detected. Interference can also lead to an increased or decreased sensing response to the analyte, or it can poison the sensor, resulting in an inoperable device. To reduce or avoid the effect of interference an array of various gas sensors with different sensitivities to gases as well as filters, which remove certain species of the sample before the exposure to the sensor, can be used. The selectivity of a sensor towards an analyzing gas is obtained by comparing the concentration of the corresponding interfering gas that leads to the same sensor signal [34]:

$$\text{Selectivity} = \frac{\text{Sensitivity of the sensor for interfering gas}}{\text{Sensitivity of the sensor towards the target gas}}. \quad (2.5)$$

The equation shows that a high selectivity means that the sensitivity towards the target gas dominates compared to the sensitivity towards interfering gases. In this case the sensor may be regarded as specific.

### **2.3.4 Long-term Stability**

Long-term stability is the ability of a sensor to maintain its properties when operated continuously over a long period. This is an important requirement of sensors, because in some application areas it is necessary that sensors stably operate without showing drift for long durations in harsh environments.

Up to now, no sensor technology has been reported that can satisfy all of the ideal characteristics described above. However, many improvements have been achieved during the last years, like enabling a high sensitivity [96] and selectivity [97]. A large contribution to those advances was made possible by understanding of gas-sensor interaction and incorporating microelectronics and nanocomponents to sensor devices, as will be outlined in the following section.

## **2.4 Nanoscale Gas Sensors**

The described sensor properties are mainly influenced by the material design used. This includes the selection and processing of the sensing materials, which is of central importance in research of gas sensors. In this context, nanomaterials received much attention in recent years as a way to achieve both ultra-sensitive sensing and small dimensions. Conventionally, chemical sensing of unknown substances is conducted in an analytical laboratory with complex tabletop instruments including, for example, mass spectrometry, chromatography, nuclear magnetic resonance, X-ray, and infrared technology [41]. On the one hand, these methods are very precise and allow identifying many species of unknown chemicals reliably. But on the other hand, the necessary equipment is often expensive and requires trained personnel. Therefore, considerable efforts have been made to accelerate the development of miniaturized low-cost sensing systems to address specific markets.

The systematic research of electronic devices based on nanostructures began with the discovery of CNTs in 1991 [98]. The well-known element carbon showed in a tubular structure mechanical and electrical properties that differ from those of the known configuration [99-101]. End of the nineties, the first electronic devices were demonstrated in the form of field-effect transistors (FETs) fabricated by SWCNTs [102, 103]. The first paper presenting nan-

owires as conductometric gas sensors was published in 2002 [60], since then much literature regarding this topic has been reported showing that impressive advances have been made. Many sensor systems are available at low cost, but these miniaturized devices mostly have difficulties with sensitivity, selectivity, baseline stability, and reproducibility.

Quasi one-dimensional nanostructures, i.e. structures with two dimensions below  $\sim 100$  nm, have different characteristics compared to their bulk counterpart, which influence the gas sensing properties of the devices. The main characteristics and advantages are presented below.

- a) A very large surface-to-volume ratio leads to dimensions comparable to the extension of surface charge region, which means that a large number of atoms act as surface atoms and thus participate in surface reactions [104]. For example, sensitivity values of an individual  $\text{In}_2\text{O}_3$  nanowire based sensor were reported, which are significantly higher than those for  $\text{NO}_2$  and  $\text{NH}_3$  sensing of comparable solid film devices [105].
- b) The high level of crystallinity results in a superior stability, because instabilities due to percolation or hopping conduction are reduced [106].
- c) In the literature relatively simple fabrication methods are reported [107, 108].
- d) The functionalization of the surface with a target-specific receptor enhances the selectivity of the device [109].
- e) A fast modulation of the operation temperature is ensured to adjust required reactions between the target gas and semiconductor.
- f) Catalyst deposition on the surface is possible for promotion or inhibition of specific reactions [110].
- g) It is possible to establish FET configurations that allow on the one hand the integration to conventional devices and device fabrication methods and on the other hand the use of gate potential to customize sensitivity and selectivity [111].
- h) It is expected that progressively more significant quantum effects become relevant owing to the reduction of the materials dimensions and material properties are modulated either along its radial or axial direction [112].
- i) The sensing response can be enhanced, when at least one of the structure dimensions is in the magnitude of the Debye length  $L_d$ , the characteristic length over which the electric potential of a local excess charge decreases to the  $1/e$ -fold [110]. For most semiconducting oxide nanowires  $L_d$  is comparable to their diameter over a wide temperature and doping range. Thus, the electronic properties are strongly influenced by surface processes, which allows to control the nanostructure's conductivity from non-



conductive to highly conductive based on the chemistry occurring at its surface. This leads to a significantly improved sensing performance, such as sensitivity and selectivity.

- j) The recovery and response times of nanostructure based sensors, which are determined by the adsorption-desorption, are significantly better than for thin film based semiconducting oxide sensors. The increased electron and hole diffusion rate to the surface of the nanostructures enables the analyte to be rapidly desorbed from the surface [105].

In general, process steps for the fabrication of nanostructure based devices can be divided in two methods. On the one hand, the so-called top-down methods with which smaller figures can be created via e.g. lithographic techniques from larger models and structures that are used as masks for patterning [113]. On the other hand, bottom-up methods that use physical-chemical principles of the atomic self-assembly to form magnified structures from smaller building blocks [114]. They are characterized by defined initial conditions, such as catalyst particles, and process conditions, such as gas, pressure and temperature, which are provided and through physical and chemical processes a structure assembly takes place. This enables a fabrication of nanostructures with less technological effort. A variety of morphologies can be fabricated by means of bottom-up techniques useful for sensing: microspheres, tubes, fibers, wires, rods, cables, ribbons, rings, sheets, diskettes, tetrapods, dendrites, walls, and so on [104, 115-121]. Beyond, it is possible to control the faceting, morphology, composition, doping level, stoichiometry, and crystallinity.

Conductometric sensors can be designed using either multiple or single nanowire arrangements. In the literature mostly the first configuration is reported owing to technological problems in electrically contact a single nanowire, although with latter devices a better understanding of the physical-chemical process governing its operation can be achieved. The majority of the publications mention the advantages in using single crystalline metal oxide nanowires as recognition element compared to their polycrystalline counterpart, but experimental studies of the influence of morphology of these materials are still limited [122].

## 2.5 Silicon Nanowire Based Gas Sensors

Among the different nanomaterials and morphologies, silicon nanowires (SiNWs) are very promising candidates for gas sensing applications due to several benefits they present. In 2001, the group of Lieber first introduced the use of SiNWs as building blocks in semiconductor nanodevices [123] and as sensors for biological and chemical species [124]. Since the pioneering work of Lieber, sensors based on SiNWs have been frequently reported due

to their ability of sensitive, label-free, and real-time detection of chemical species coupled with their uniformity, reproducibility, as well as excellent scalability [125]. Another crucial advantage of silicon is the enormous development efforts that have been put into microelectronics due to the growing importance. The thereby accumulated knowledge about silicon technology can for the most part be transferred to the gas sensor technology. SiNW based devices have a relatively large carrier mobility [126] and can be adjusted by controlling the doping level [127]. Compared to sensors fabricated from CNTs and organic materials like conductive polymeric nanowires [128], gas sensors based on SiNWs are more compatible for mass production owing to relatively simple preparation methods and mature fabrication technologies as well as complementary metal-oxide-semiconductor (CMOS) technologies [129, 130]. With regard to the fundamental sensor mechanism, devices made from SiNWs are better understood than metal oxide and polymer nanowires based devices [131]. The possibility of a chemical surface modification of SiNWs allows to chemical immobilize the selector material and influence the device performance [132, 133].

### 2.5.1 Fabrication Methods

Two main nano-fabrication approaches, bottom-up and top-down, have been reported to fabricate SiNWs sensors. A brief overview of the different growth methods is given, even though the focus of this work is on chemical vapor deposition (CVD) of silicon nanowires. CVD is the most widely used method, where the silicon source is a volatile gaseous silicon precursor, such as silane,  $\text{SiH}_4$ , or silicon tetrachloride,  $\text{SiCl}_4$ . The precursor is transported to the deposition surface, where it reacts and is cracked into its components [134]. Using this approach, it could be demonstrated that a broad range of NWs with homogeneous composition and single-crystal structures can be prepared. The NW diameter is controlled by the size of the catalyst nanoparticle and diameters of 3 nm can be realized. Lieber's group showed that the NW length is proportional to the growth time and specific dopants can be incorporated into NWs to control their electronic properties [135, 136].

Further SiNW growth techniques include annealing in reactive atmosphere [137], evaporation of  $\text{SiO}$  [138], molecular beam epitaxy (MBE) [139], laser ablation [140], and solution-based synthesis [141].

However, the technology has several shortcomings like it requires transfer and positioning of SiNWs, reliable contacts are hard to produce, significant device-to-device variation exists between NWs, and hybrid fabrication schemes are required to integrate NWs into electronic devices [142, 143].

The mentioned drawbacks coupled to the availability of high-quality ultrathin silicon-on-insulator (SOI) wafers [144], has pushed the research in the field of exclusively top-down processing based NW-like devices. Lithographic techniques, generally electron beam lithography, allow to precisely controlling sensor dimensions. A disadvantage of this direct writing method is the serial way of operation, which leads to a low throughput and it requires expensive devices. The narrow silicon wire is defined by removing the remainder of the SOI layer using either a wet chemical [145] or a dry reactive ion etching (RIE) [142, 146] method. Fabrication methods can also be distinguished between plane orientated and vertical standing SiNWs, i.e. nanowires are oriented more or less perpendicular to the substrate. To get vertical SiNWs a variety of nanostructuring techniques can be used, such as RIE, electron-beam lithography [147], nanosphere lithography [24], nanoimprint lithography [148], and block-copolymers [149]. In et al. fabricated vertically aligned, ordered arrays of SiNWs covered with a porous top electrode by means of polystyrene nanospheres in a two stage lithography process as shown in Fig. 2.9a [24]. SiNWs based resistors based on the growth of Au-catalyst vapor-liquid-solid (VLS) SiNWs by low pressure chemical vapor deposition (LPCVD) is reported by Demami et al. [150]. The first device fabrication step of the vertical SiNWs based resistors is the patterning of the interdigitated electrodes geometry on a  $\text{SiO}_2$  covered substrate followed by the lift-off and a thin film Au local deposition process. The local growth of long SiNWs ensures contacts between SiNWs resulting in the formation of resistors (Fig. 2.9b). Sensors based on vertical aligned SiNWs can also be fabricated by a uniform layer of Au induced NWs using plasma-enhanced chemical vapor deposition (PECVD) grown onto a defined area, over and between pre-patterned interdigitated metal electrodes on top of oxidized silicon wafers [151].

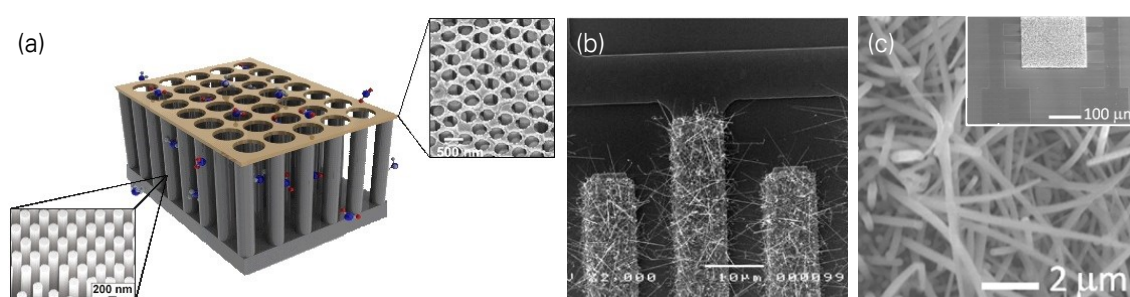


**Fig. 2.9:** Vertical standing SiNWs. (a) Vertically aligned, hexagonally ordered arrays of SiNWs topped by a porous electrode fabricated by nanosphere lithography [152]. (b) SiNWs based resistor synthesized following the VLS growth technique [150]. (c) SiNWs network detail with a SiNW chemiresistive sensor shown in the inset [151].

A major challenge in the technology of sensor systems is the contacting of the sensing element. The metal-semiconductor contact employed in this work is discussed in detail in the following.

## 2.5.2 Metal-Semiconductor Contact

For understanding the processes of the sensors fabricated in this work, the metal-semiconductor contact, Schottky contact, is described. This forms the basis of the functionality of the sensors due to the physical properties of the used materials. A Schottky barrier, named after Walter H. Schottky, is an energy barrier for charge carrier exchange formed at a metal-semiconductor junction [153]. The material specific energy level can be characterized in metals and semiconductors through the Fermi energy [153]. For metals, this results in the work function  $W_A$ , which describes the work that needs to be applied to extract an electron from the metal:

$$W_A = q \varphi_{me} = (E_{vac} - E_{F,me}), \quad (2.6)$$

where  $q$  describes the electrical charge,  $\varphi_{me}$  the potential difference between vacuum and Fermi potential,  $E_{vac}$  the vacuum energy level, and  $E_{F,me}$  the Fermi energy for the metal.

For non-degenerated semiconductors, the Fermi level is located within the band gap  $E_G$ . In the case of intrinsic semiconductors it is in the middle of the band gap at  $E_{F,sc,i} = E_i = E_G/2$ . For n-type doping the Fermi energy is shifted towards the conduction band with the energy  $E_C$ , and for p-type doping towards the valence band with the energy  $E_V$ . The work that is required to extract an electron from the conduction band is described by the relation of the charge  $q$  and the electron affinity  $\chi$ :

$$q \chi = (E_{vac} - E_C). \quad (2.7)$$

Fig. 2.10 shows these relations in the form of a simplified band diagram for the connection of a metal with an n-type doped semiconductor. After the connection of the materials an equilibrium state occurs through charge carrier motion in the direct contact area, whereby the Fermi energies align. Therefore, a band bending is formed, wherein the band is shifted towards lower electron energies  $E_n$ . The electron transport is determined by the potential barrier for electrons  $\varphi_{B,n}$ , which is referred to as Schottky barrier  $\varphi_{SB}$  and can be obtained from:

$$\varphi_{B,n} = \varphi_{me} - \chi. \quad (2.8)$$

In the case of p-type doped semiconductors, taking into account the band gap the Schottky barrier for holes  $\varphi_{B,p}$  results from equation (2.8):

$$\varphi_{B,p} = \frac{E_G}{q} - (\varphi_{me} - \chi). \quad (2.9)$$

Due to the material specific values of  $\varphi_{me}$ ,  $E_G$ ,  $E_F$ , and  $E_C$ , the values for  $\varphi_{B,n}$  and  $\varphi_{B,p}$  can be influenced by the choice of contact materials.

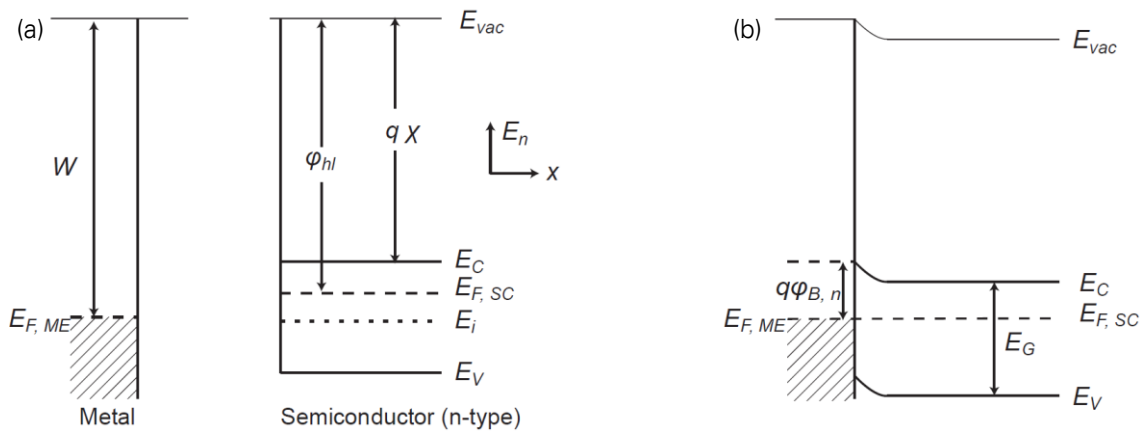


**Fig. 2.10:** The Schottky contact. Band diagram of the Schottky contact before (a) and after (b) junction of metal and n-type doped semiconductor.

Transport through a Schottky contact is assigned to different injection mechanisms depending on the energy location of the charge carrier. Thereby, they can go above the Schottky barrier, which is called thermionic emission, and they can go through the barrier, which is done by quantum mechanical tunneling and is referred to as charge carrier tunneling (see Fig. 2.11). Other possible mechanisms, such as trap assisted tunneling [153], are not discussed here. The total current density of the Schottky barrier  $J_{SB}$  results from the sum of the thermionic current density  $J_{Th}$  and the tunneling current density  $J_T$ :

$$J_{SB} = J_{Th} + J_T. \quad (2.10)$$

In the following, the transport of the electrons is considered in the case of band bending in the direction of lower energy electrons in an n-type doped semiconductor. The possible transport paths under the influence of a positive voltage from semiconductor towards metal are shown in Fig. 2.11. Since these describe the charge transport across a phase boundary, the process is referred to as injection. The injection comprises the processes of injection of

thermionic activated charge carriers as thermionic injection and the quantum mechanical tunneling as tunnel injection. Injection applies to both directions, whereby it includes the transport from the metal to the semiconductor and from the semiconductor to the metal.

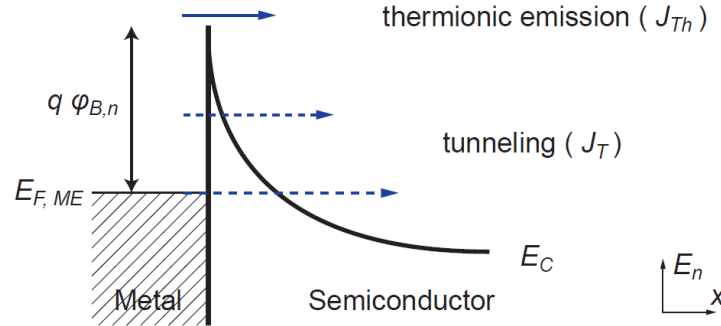


**Fig. 2.11:** Charge carrier injection mechanisms for electrons at a Schottky barrier. Thermionic injection over the barrier (blue arrow) and tunnel injection of electrons for two possible tunnel paths through the barrier (dashed blue arrows).

Thermionic emission can be described by the schematic conduction band diagrams such that at temperatures of  $T > 0$  K charge carriers having an energy  $E_{p,n} > q\phi_{SB}$  overcome the Schottky barrier. The number of charge carriers is determined by the temperature dependent Fermi distribution. The total current density of the thermionic emission of electrons results from the parts of the transport of thermally injected electrons in both directions [154]:

$$J_{Th} = J_{me \rightarrow sc} + J_{sc \rightarrow me}. \quad (2.11)$$

Tunneling is referred to a quantum mechanical tunneling process, in which charge carriers pass through a potential barrier. In Fig. 2.11 this process is schematically indicated for electrons by dashed arrows. The derivation will not be discussed in detail, but can be found in [155].

An empirical description of the total injection at the Schottky contact can be carried out by experimentally determined values, in which the parts of tunneling and thermionic currents are included:

$$J_{SB} = J_S \left[ \exp\left(\frac{qV}{\eta k_B T}\right) - 1 \right], \quad (2.12)$$

where  $J_S$  is the saturation current density, which can be extracted from the extrapolation of the saturation current of the characteristics of tunnel diodes and Schottky-barrier field-effect transistors (SBFETs) [153],  $V$  is the voltage,  $k_B$  is the Boltzmann constant,  $T$  is the tempera-

ture, and  $\eta$  is the ideality factor, which results from the characteristic curve slope and is defined as:

$$\eta = \frac{q}{k_B T} \frac{\delta V}{\delta(\ln J)}. \quad (2.13)$$

When a negligible tunneling takes place, the slope approaches to 1. For a dominant tunneling, for example by reducing the barrier width by high doping of the semiconductor,  $\eta$  and  $J_S$  increase.

A very vivid description is the method of the total injection of charge carriers through the effective barrier height  $\varphi_{eff}^*$  and the definition of a tunneling distance  $d_T$  from J. Knoch [156]. Thereby, a simplification is made, in which the injection mechanism is limited to the sole injection by thermionic emission. The missing part of the tunneling current is described by a larger thermionic current due to a reduced barrier height  $\varphi_{eff}^*$ . The thermionic current over this reduced barrier is the sum of thermionic and tunneling currents through the Schottky barrier:

$$J_{Th}(\varphi_{eff}^*) = J_{Th}(\varphi_{SB}) + J_T(\varphi_{SB}). \quad (2.14)$$

$\varphi_{eff}^*$  depends on the geometry and material parameters of the device. If the barrier at a certain energy is narrower than the tunneling distance in the unstrained bulk silicon with  $d_{T,Si} \approx 3.6$  nm, a tunneling probability of "1" is accepted, otherwise it is "0" [157].

### 2.5.3 Working Principle: Resistor versus Field Effect Transistor

The method of electrical characterization determines the working principle of SiNW based sensors. On the one hand, when changes in the device resistance, i.e. current, are measured, then it is referred to as resistor based sensors. On the other hand, field effect transistors (FETs) make use of an applied front-gate or back-gate electrode. It has to be considered that there is no relation between the fabrication method of the SiNWs (bottom-up or top-down) and the type of working principle. Though, it is noticed that nowadays most NW based FETs are prepared by top-down techniques [125].

In Fig. 2.12a a resistor based configuration is shown, where single SiNWs contact both electrodes to enable current flow. The adsorption of analyte molecules onto the SiNW surface is the basic principle of the resistor. This alters the surface status and changes the sensor resistance [158]. The gas concentration can be determined by measuring the amount of elec-

trical resistance change. Resistors belong to the most common configurations of NW based gas sensors.

The architecture of a typical top-down fabricated SiNWs based FET is depicted in Fig. 2.12b. In the case of FET sensors, the nanowire itself serves as conductive channel, connected by source and drain contacts, typically metallic or highly-doped semiconductor [124]. These elements are patterned on top of an insulating oxide film, which is above of a conducting (e.g. p-type Si) gate electrode [104]. The number of charge carriers can be influenced via a back or front gate. A NW FET sensor has the highest percentage conductance response in the sub-threshold regime [159]. This can be reached by applying a back-gate potential ( $V_{BG}$ ), which brings the nanowire into the depletion mode. When chemical species attach to the NW surface, the local electrical voltage experienced by the nanowire is influenced and changes the extent of depletion. If a fixed source-drain voltage ( $V_{DS}$ ) is applied, this leads to a variation of the number of majority charge carriers, which is detected as change in drain current ( $I_d$ ). A further possibility of registering the recognition event is by adapting the back-gate voltage  $\Delta V_{BG}$  in such a way that at fixed  $V_{DS}$ ,  $I_{DS}$  is kept constant. Thereby,  $\Delta V_{BG}$  reflects the change in boundary potential at the interface of the nanowire and its environment [125].

Devices based on SiNWs have high potential to increase sensitivity to the point of single-molecule detection owing to the large surface-to-volume ratio of nanowires and the gate effect of the amplifier configuration [160].

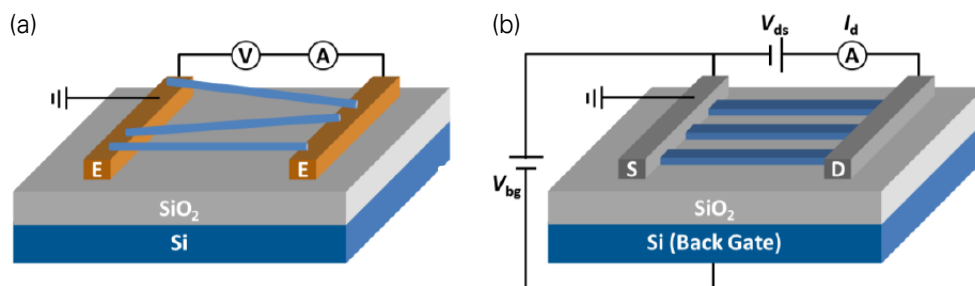


**Fig. 2.12:** Schematic illustration of SiNW based sensor principles. (a) Resistor and (b) FET schematics demonstrate the differences in the electrical configuration with respect to the electrodes (E), source (S), and drain (D) [125].

## 2.5.4 Sensing Mechanism

Here, the discussion will be limited to the sensing mechanism between SiNWs and NH<sub>3</sub>. The importance in sensing NH<sub>3</sub> is pointed out in section 2.6. Fig. 2.13a illustrates a model of reaction of NH<sub>3</sub> with p-type SiNWs. Li et al. proposes that two effects are important for the change of electrical resistance of SiNWs under NH<sub>3</sub> exposure [161]. Firstly, after the supply



of  $\text{NH}_3$ , it reacts with the hydroxyl groups ( $-\text{OH}$ ) at the nanowire surface, which breaks the O-H bond to form the energetically preferred  $\text{NH}_4^+$  group. An unstable electron pair on the O atom is left and an O-O bond is formed after two adjacent O atoms with unstable electron pairs combine. Two additional electrons are then released into the nanowire as free electrons (red dotted square). The adsorbed  $\text{NH}_3$  on the NW surface can also help the contribution of their lone pair electrons into NWs (blue dash dotted square) [162].

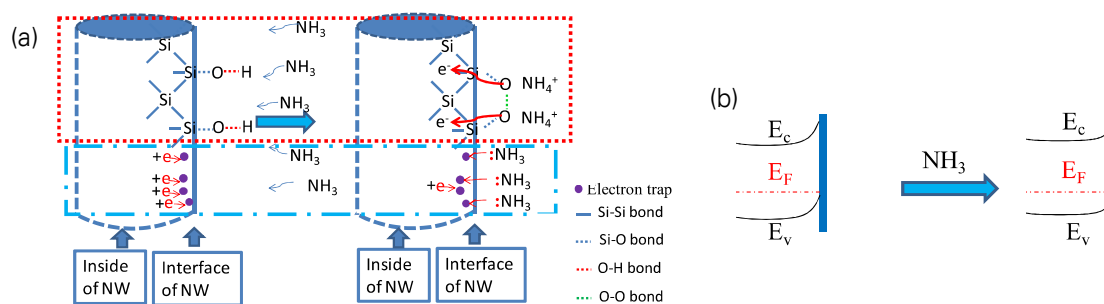


**Fig. 2.13:** P-type SiNW based sensing mechanism of  $\text{NH}_3$ . (a) The proposed model of chemical reaction of  $\text{NH}_3$  with SiNWs. (b) Band diagram of p-type SiNW at the interface [161].

The electron traps on the surface of p-doped nanowires are filled with the obtained electrons, as minority carriers, from both processes mentioned above. This reduces the depletion of the p-type nanowire surface, because the obtained electrons partly replace the electron filling from the inside of nanowire. Thus, the thickness of the positive charged layer is thinner and the resistance increases. Band bending is reduced, because electrons are donated from the  $\text{NH}_3$  rather than from the Si surface (Fig. 2.13b). These observations are supported by electrical measurements of n-type SiNWs, where the resistance of the NWs decreases in the presence of  $\text{NH}_3$ , which is the opposite response compared to p-type NWs [162].

## 2.6 Ammonia and its Sensing Applications

Ammonia is a naturally occurring gas that is present in the atmosphere, but above a certain concentration it is hazardous. Fig. 2.14 illustrates the global distributions of atmospheric  $\text{NH}_3$  concentrations according to the model of Dentener and Crutzen [163]. It can be seen that substantial spatial variability in gaseous  $\text{NH}_3$  concentrations exists. This section focusses on the properties of ammonia with respect to the influence on health and possible detection approaches in various application areas.

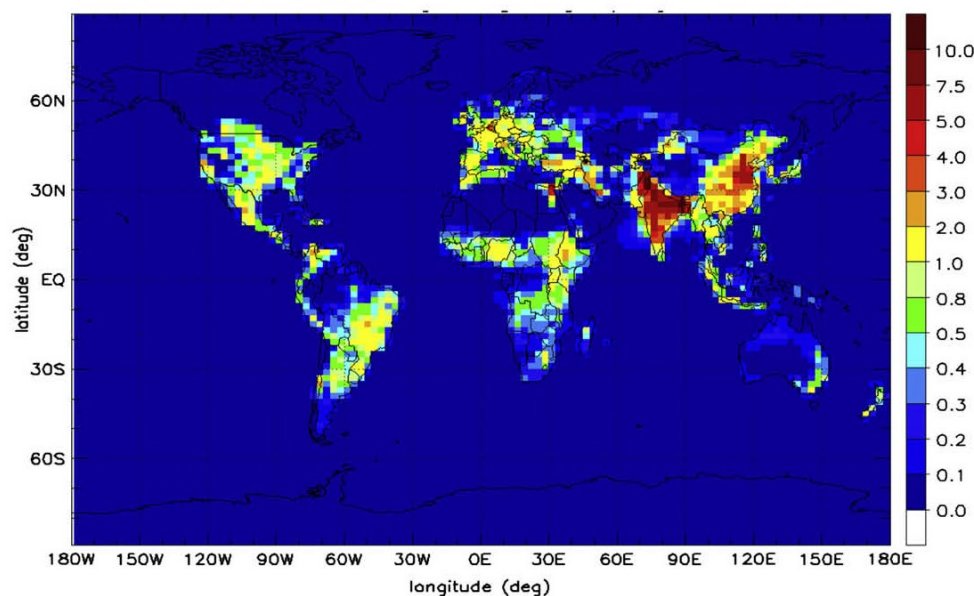


**Fig. 2.14:** Global ( $1^\circ \times 1^\circ$ ) estimates of atmospheric ammonia concentrations ( $\mu\text{g m}^{-3}$   $\text{NH}_3$ ) [164].

### 2.6.1 Chemical and Toxicological Properties

Ammonia ( $\text{NH}_3$ ) is one of the most abundant toxic chemicals [165]. It is a stable colorless gas at room temperature, lighter than air, highly soluble in water (forming ammonium hydroxide ( $\text{NH}_4\text{OH}$ )), and a strong alkaline with high corrosive properties. At high concentrations the unique penetrating odor of  $\text{NH}_3$  usually provides a simple detection. The odor threshold lies around 5 ppm (parts per million), which is low enough to allow warning of its presence, but  $\text{NH}_3$  causes olfactory fatigue or adaptation, making its presence difficult to notice at longer exposure. Thus, the odor threshold may increase up to 53 ppm [166]. The American Conference of Governmental Industrial Hygienists allowed an 8 h exposure limit of 25 ppm and a short-term exposure limit (15 min) of 35 ppm for  $\text{NH}_3$  in the workplace [167]. Even at those mentioned low concentrations,  $\text{NH}_3$  is irritating to the respiratory tract, skin and eyes [168]. Higher concentrations can lead to an immediate and severe irritation to the upper respiratory system and even to lung disorders, such as pulmonary edema. Extremely high concentrations in the range of 5000 to 10,000 ppm are suggested lethal within 5–10 min [169]. The relationship between concentration and the corresponding health complaints is shown in Table 2.1.

**Table 2.1:** Summary of potential occurring effects in dependence of the  $\text{NH}_3$  concentration [169, 170].

<b>Dose (ppm)</b>	<b>Signs and symptoms</b>
50	Irritation to eyes, nose and throat (2 h exposure)
100	Rapid eye and respiratory tract irritation
250	Tolerable by most persons (30–60 min exposure)
700	Immediately irritating to eyes and throat
>1500	Pulmonary edema, coughing, laryngospasm
2500–4500	Fatal (30 min)
5000–10,000	Rapidly fatal due to airway obstruction

## 2.6.2 Application Areas of Ammonia Sensors

Ammonia can be detected in many ways. Depending on the application,  $\text{NH}_3$  concentrations down to parts per billion (ppb) and with different required response times have to be measured. In the following, four major areas of interest for determining  $\text{NH}_3$  levels are introduced, namely environmental, automotive, chemical industry, and medical diagnostics, and the relevant concentrations are given.

### *Environmental gas analysis*

Ammonia concentrations in ambient air can go down to the sub-ppb range above the oceans. As an example, the average atmospheric  $\text{NH}_3$  level in the Netherlands is about 1.9 ppb [169]. For detecting such concentrations, sensors with a detection limit of 1 ppb or lower are necessary. Near intensive agricultural areas,  $\text{NH}_3$  concentrations can increase significantly, up to more than 10 ppm [171]. This is caused by the addition of large quantities of ammonium to cultivate farmland in the form of fertilizer. Another source is  $\text{NH}_3$  emission resulting from ammonification, a series of metabolic activities that decompose organic nitrogen like manure from agriculture performed by bacteria and fungi [172]. The necessary concentration range and time resolution of the analysis equipment depends on the specific application, but it does not require extremely fast detectors. Shorter response times in the order of a minute are preferred in stables to control venting systems.

### *Automotive industry*

Exhaust gasses are responsible for the major part of gaseous pollution in urban sites. In order to meet future emission standards, the automotive industry is interested in monitoring such gasses [173].  $\text{NH}_3$  emissions were measured to be up to 20 mg/s or up to 8 ppm in

exhaust gas [174]. Thus, an  $\text{NH}_3$  sensor is required to optimize the injected amount of urea and to ensure that no  $\text{NH}_3$  emissions appear [173]. Another reason for the usefulness of detectors for atmospheric pollution like  $\text{NH}_3$  is air quality control in the passenger cabin [175]. For such an application the detection limit should be around 50 ppm. Additionally, the sensor has to respond very fast in the order of seconds, so that the air inlet valve can be closed and prevent harmful gas from entering the car. A further application for  $\text{NH}_3$  sensors in the automotive industry is  $\text{NO}_x$  reduction in diesel engines. Modern diesel engines operate at high air-to-fuel ratios that give oxygen excess in the exhaust gas and thus makes it difficult to reduce the  $\text{NO}_x$  ( $\text{NO} + \text{NO}_2$ ) formed during the combustion [176].  $\text{NH}_3$  can act as a reducing agent for  $\text{NO}_x$  and lowers  $\text{NO}_x$  formation significantly. The use of  $\text{NH}_3$  to reduce  $\text{NO}_x$  is known as ammonia selective catalytic reduction ( $\text{NH}_3$  SCR) and belongs to the most promising methods for meeting the future legislation demands concerning  $\text{NO}_x$  emissions from diesel vehicles [177]. For this method, it is important that the injection of  $\text{NH}_3$  is precisely controlled by measuring the excess  $\text{NH}_3$  concentration in the exhaust system. Sensors should allow measuring very low  $\text{NH}_3$  concentrations within a few seconds. Currently used sensors have detection limits in the range of a few ppm [176] as well as a response time of around 1 min. Devices should be capable to withstand elevated temperatures, because measurements are carry out in exhaust pipes.

### *Chemical industry*

A widely used method for chemically producing  $\text{NH}_3$  is the so-called Haber-Bosch process, where  $\text{NH}_3$  is synthesized from nitrogen and hydrogen at an elevated temperature of about 500 °C and a pressure of about 300 kPa using a porous metal catalyst [169].  $\text{NH}_3$  was firstly needed as a cheap supply of nitrogen for the production of nitric acid, a key component of explosives. Nowadays, a large part of artificial  $\text{NH}_3$  is employed for fertilizers used in the agricultural sector, which contain ammonium salts, and chemical production. A further substantial part is used for refrigeration systems. These industrial sectors utilize almost pure  $\text{NH}_3$  with the result that leakage can lead to life-threatening situations for the involved people. An alarm system for high  $\text{NH}_3$  concentrations requires very fast response times, whereas concentrations less than the long-term maximum allowed workspace  $\text{NH}_3$  level do not require fast detectors. A response time in the order of minutes is adequate.

### *Medical applications*

Human breath normally contains  $\text{NH}_3$  at very low concentrations of 100-2000 ppb as part of a complex mixture of volatile organics in moist atmosphere, which makes detection difficult

[178]. Nevertheless, exhaled air has been analyzed extensively using gas chromatography and mass spectroscopy for the presence of a variety of molecules [179]. Several gases, among others  $\text{NH}_3$ , have been linked to certain diseases. Therefore, the medical community is considerably interested in detectors for measuring  $\text{NH}_3$  in exhaled air for the diagnosis of specific diseases [180]. Examples for such diseases are a disturbed urea balance, e.g. due to kidney disorder [17], and ulcers caused by *Helicobacter pylori* bacterial stomach infection [18]. Appropriate measuring devices should enable measuring down to 50 ppb  $\text{NH}_3$  in breath, including  $\text{CO}_2$  concentrations up to 3 % [180]. Additional requirements for measuring in exhaled air are a reasonable response time of not more than a few minutes as well as the ability to carry out measurements with only small volumes of target gas.

### 2.6.3 Ammonia Sensing Principles

In literature, many principles for measuring ammonia are demonstrated. The requirements of sensors for the different applications differ strongly. Another sensing device is used in the exhaust pipe of automobiles than for detecting ultra-low concentrations of ambient  $\text{NH}_3$  for environmental monitoring. Widely used types in commercial  $\text{NH}_3$  detectors are described in the following based on the basics that have been discussed in section 2.1.2. This includes metal oxide based sensing devices, catalytic  $\text{NH}_3$  sensors, conducting polymer detectors, optical gas analyzers, and indirect gas sensing systems using non-selective detectors. A comprehensive overview over the state of the art in SiNW based  $\text{NH}_3$  sensing is given in section 1.2.

Metal oxide based gas sensors are the most common used  $\text{NH}_3$  sensors, mostly  $\text{SnO}_2$  sensors. A variety of research activities have been done on these sensors, because they are rugged and inexpensive. Their functionality has been explained by many models [181]. By now, it is well established that they operate on the principle of conductance change due to chemisorption of gas molecules to the sensing layer [169]. The major drawback of these sensors is that they are not selective to one particular analyte. Diverse approaches were employed to develop selective devices, such as principle component analysis [182], artificial nose [183], conductance scanning at a periodically varied temperature [184], and metals or additives [185]. Lowest detectable concentrations are normally in the order from 0.5 to 1000 ppm [186]. Those sensors are commercial available and are used in the detection of combustion gasses [187] and leakage alarm systems, for example for  $\text{NH}_3$  leakage detection in cooling plants [184].

Catalytic  $\text{NH}_3$  sensors consist of catalytic metals, which are reactive to  $\text{NH}_3$ . A change of the  $\text{NH}_3$  level alters the charge carrier concentration in the catalytic metal, which can be detected by a field effect device, like a capacitor or a transistor [188]. Parameters like the catalytic metal, the morphology of the metal layer and the operating temperature can influence the selectivity and a detection limit of 1 ppm was achieved with this sensor type [169]. The catalytic sensor approach can be combined with a solid-state ion conducting material to form a gas-fuelled battery referred to as chemical cells. Such a cell for  $\text{NH}_3$  is demonstrated in literature based on an anion-exchange membrane with a Cu electrode and an Ag/AgCl counter electrode [189].

Conducting polymer based gas sensing devices make use of polymers, like polypyrrole [190] and polyaniline [191]. Polypyrrole irreversibly reacts with  $\text{NH}_3$  resulting in a reduction of the polymer film and an increase in mass in the polymer film, which causes a conductivity change or change in frequency of a resonator [190, 192]. Response times of about 4 min have been shown [193]. The major disadvantage of this sensor type, despite proposed regeneration mechanisms, is the irreversible reaction, which leads to a decreasing sensitivity over time under  $\text{NH}_3$  exposure [194]. Polyaniline is more stable and the conduction change is caused by the deprotonation through  $\text{NH}_3$  [195]. The detection limit of conducting polymer based sensors is about 1 ppm [195]. Alarm systems are commercially available with these sensors.

Optical gas analyzers can be classified into two main principles for the detection of  $\text{NH}_3$  discussed in literature. The spectrophotometric approach is based on a change in color when  $\text{NH}_3$  reacts with a reagent, whereas the second method applies optical absorption detection. Spectrophotometry is more used for dissolved  $\text{NH}_3$ , why it is not further described here. Optical adsorption spectroscopy is mostly used in sensitive and selective instruments for ambient  $\text{NH}_3$ . Mount et al. reported a system that has a detection limit of a few ppb in an integration time of 1 s using a laser and a spectrograph [196]. Those analyzers are commercially available, but are expensive. Furthermore, despite they are very sensitive and selective to  $\text{NH}_3$ , there are drawbacks for sensor systems measuring in small volumes. Firstly, the required equipment is very expensive. The attempt to overcome this by inexpensive diode-lasers led to reduced sensitivity [197]. Secondly, the gas volume between the light source and the detector determines the sensitivity limit requiring a large setup for an accurate measuring. Thus, miniaturization results in a decreased sensitivity, which makes this principle less suitable for miniaturized  $\text{NH}_3$  sensors like necessary for breath analyzers.

Finally, so-called indirect gas analyzers using a nonspecific detection principle can be applied for an enhanced selectivity towards  $\text{NH}_3$ . Thereby, the gas detection system has to include a

selection mechanism that enables only the analyte to influence the medium surrounding the detector, such as gas permeable membranes [198]. These systems also comprise gas samplers, like denuders or diffusion scrubbers to sample  $\text{NH}_3$  into a sample liquid [198]. Advantageous is the pre-concentrator effect by sampling a large volume of the analyte gas into a much smaller volume of liquid, where ammonium ions are formed [199]. Several ways to selectively measure  $\text{NH}_3$  concentrations in the low ppm range have been reported [200].

## **2.7 Summary**

In the present chapter, necessary basics for understanding this work were discussed and the following conclusions can be drawn. There is a broad variety of different sensor types, each having special capabilities for selected areas of application. Gas sensors have to meet diverse requirements in order to be used in practice. In comparison with bulk gas sensors, devices made of nanomaterials have many improved properties, which suggests that nanoscale devices have the potential to revolutionize many aspects of sensing in various fields of application. Silicon nanowire based sensors attracted much attention in recent years, and are recognized to be a promising instrument for fast and sensitive gas detection due to their unique characteristics. It was shown that the existing demands of the described application areas could not be fulfilled with the currently available sensor concepts. Consequently, there is a need that should be met by future developments.





### 3 Copper Nanowire Synthesis

In this chapter, the growth of high aspect ratio copper nanowires via directed electrochemical nanowire assembly (DNA) is presented. After the required materials and the setup for the synthesis are described, the influence of the metal salt solution concentration as well as the amplitude and frequency of the applied alternating voltage on the nanowire morphology is discussed. The impact of the process parameters on the nanowire growth is discussed on the basis of the Butler–Volmer equation. Finally, some guidelines for the formation of copper nanowires based on experimental and theoretical considerations are summarized.

#### 3.1 Directed Electrochemical Nanowire Assembly

Metal oxide based gas sensors are one of the most investigated groups of gas sensing devices due to the low cost and flexibility associated to their fabrication, simple use, as well as a broad variety of detectable gases and possible application fields [201]. The benefits of nanowire based sensors were demonstrated in paragraph 2.4. In the following, a method for preparing metal oxide nanowires as potential sensing elements is described. Copper was chosen as material, because it meets both requirements. On the one hand, copper oxide can be used as gas recognition element [202]. On the other hand, nanowires can be fabricated via DNA [203], which is a promising approach for the synthesis of nanowires with high aspect ratios as discussed in detail later.

Common methods for the fabrication of copper NWs include template-based techniques normally with polycarbonate membranes [204, 205] or alumina templates [206-209]. Wang et al. reported the synthesis of copper nanotubes by metal organic chemical vapor deposition (MOCVD) with silicon oxide nanowire templates [210]. A dense mat of entangled wires was fabricated with this method. Further approaches for the preparation of copper NWs comprise hydrothermal reduction [211, 212], vacuum vapor deposition [213], chemical vapor deposition [214], and electrodeposition [215]. These bottom-up methods have the drawback of the positioning and contacting of the NWs after their growth. Therefore, top-down approaches were developed to fabricate copper NWs, such as the damascene technology [216] and e-beam lithography [217]. However, those techniques usually involve multiple processing steps, which makes them complex and relatively expensive.

The use of NWs as recognition element in gas sensors requires the fabrication of thin and contacted wires. A capable method for this purpose is the synthesis of metal nanowires by

DENA [218]. This method has several advantages. It allows the fast growth of thin copper NWs with a high surface-to-volume ratio. Consequently, NWs are already in contact with the electrodes and no further processing is required. For this one-step procedure, an alternating voltage is applied across two electrodes in a metal salt solution. This induces the nucleation and growth of nanowires from one electrode to the other through the deposition of metal atoms at the growing nanowire tip. To the author's knowledge, detailed analyzes of DENA have been given for Pd from palladium acetate solution [219], and Pt from  $\text{H}_2\text{PtCl}_6$  or  $\text{K}_2\text{PtCl}_4$  [220]. Furthermore, DENA of Au from  $\text{HAuCl}_4$ , In from  $\text{In}(\text{CH}_3\text{COO})_3$ , Ni from  $\text{NiSO}_4$ , Co from  $\text{Co}(\text{CH}_3\text{COO})_2$ , Pb from  $\text{Pb}(\text{CH}_3\text{COO})_2$ , and Ag from  $\text{AgNO}_3$  was reported in reference [221]. It is surprising that copper NW growth by DENA has not been reported yet in the literature.

In this work, the impact of the most important process parameters on the resulting NW morphology and in particular on the NW diameter is investigated experimentally and discussed theoretically based on the Butler-Volmer equation. Theoretical considerations were supportive in understanding the processes occurring during nanowire growth and allowed establishing guidelines for achieving thin copper nanowires by the DENA synthesis method. The following three parameters were determined to be crucial: solution concentration of the metal salt as well as the amplitude and frequency of the applied alternating voltage. The so developed preparation route enabled to grow thin wires, which are well suited for gas sensing applications after their oxidation to get a semiconducting oxide. A resistive gas sensor configuration based on copper oxide nanowires is illustrated schematically in Fig. 3.1a.

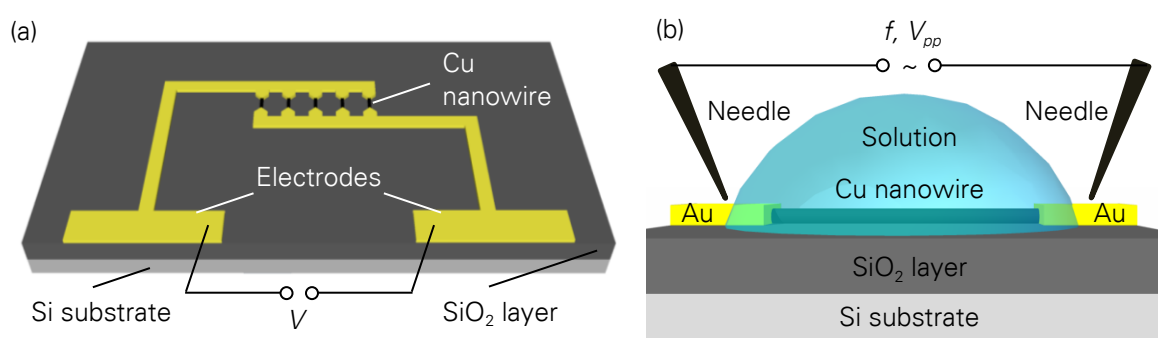


**Fig. 3.1:** Schematic representation of a sensor layout and copper nanowire synthesis. (a) Scheme of a resistive gas sensor based on copper nanowires grown via DENA. (b) Experimental setup for copper nanowire growth from aqueous solution (not drawn to scale) between gold microelectrodes at a specific frequency  $f$  of the applied AC peak-to-peak voltage  $V_{pp}$ .

### 3.2 Growth Process and Tip-Probe Station

The experimental setup for the nanowire growth is depicted in Fig. 3.1b. Silicon wafers cut into 15 mm x 15 mm pieces with a 400 nm oxide layer were used as isolating substrate for

the growth process. These substrates had a low degree of surface contaminations and thus are suitable to achieve full control over the nanowire growth morphology. It was crucial that the substrates were insulating, otherwise the leakage current through the substrate would be too high for electrochemical wire assembly to work [222]. The electrode structure was fabricated by laser lithography (wavelength 405 nm, DWL66fs, Heidelberg Instruments). For that a positive photoresist (AR-P 5350, Allresist) was spin-coated on the substrate with 6500 rpm for 40 s, followed by subsequent heating on a hotplate at 105 °C for 4 min. After the exposure, the structures were developed for 60 s in diluted developer (1 part developer, 2 parts water). In a subsequent deposition step, a 3 nm chromium layer (for improved gold adhesion) was thermally evaporated on the developed pattern, followed by 20 nm gold deposition. The lift-off was done in 1-Methyl-2-pyrrolidinone (NMP 99.5 %, Sigma Aldrich) at 55 °C for 30 min. Usually an electrode distance of 10  $\mu\text{m}$  was prepared, unless larger spacings of 40  $\mu\text{m}$  were used.

A drop of 2.0  $\mu\text{l}$  solution composed of aqueous copper(II)-nitrate ( $\text{Cu}(\text{NO}_3)_2$ , Sigma Aldrich) with concentrations of 0.05, 0.1, 0.5, 1.0, and 2.0 mM were put between two needles onto the electrode structure. The electrodes were contacted via the needles with a tip-probing station (Karl Suss). The tip-probing station comprised a microscope, a chuck with vacuum connection, and two needle holders at micropositioners (Karl Suss Microtec), see Fig. 3.2. Before the growth experiments were conducted, needles, chuck, and tweezers were rinsed with isopropanol to ensure a contaminant-free environment. Nanowire growth was initiated on the substrate between the electrodes through applying an alternating current (AC) voltage. A function generator (Tektronix AFG320) enabled to provide a rectangular voltage signal in the frequency range from 50 kHz to 750 kHz, monitored by an oscilloscope (Tektronix TDS3014), with one electrode grounded. Due to the use of highly diluted solutions, the resistance of the solution was far higher than the input impedance of the oscilloscope (1 M $\Omega$ ). This means that in good approximation the full output voltage of the function generator was applied to the solution during nanowire growth [223].

The morphology of the grown copper NWs was observed by SEM (Philips XL 30 ESEM-FEG). With the obtained top view images, the width of the NWs was measured. In the following, we refer to the width as nanowire diameter. Elemental analysis was also carried out with the Philips XL 30 ESEM-FEG system using energy dispersive X-ray spectrometry (EDX). The electrical properties of the copper NWs were characterized by a dual channel instrument (Keithley 2602 System SourceMeter).

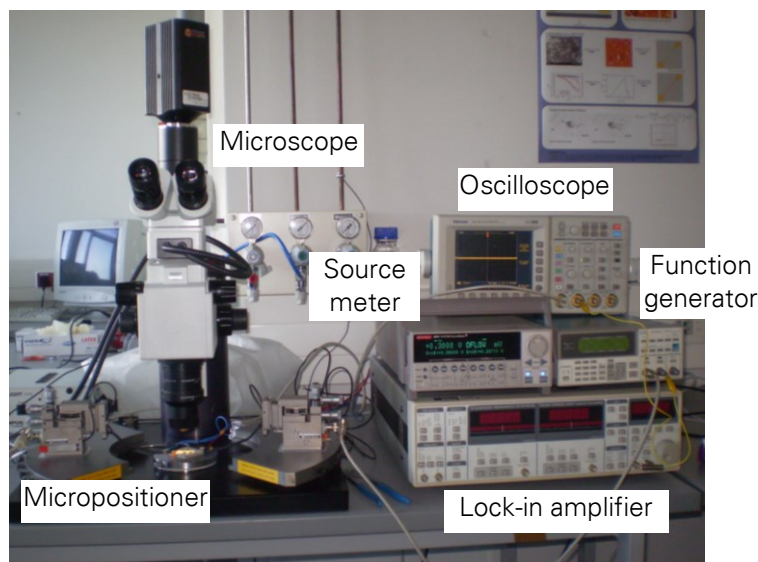


**Fig. 3.2:** Setup of copper nanowire growth experiments, which comprises the tip-probe station and electrical measuring equipment.

### 3.3 Theory

Copper NW assembly occurs due to the dissolution of copper(II)-nitrate to copper ions, which are reduced at the electrode surface



When the electrode is negatively charged during the negative half-cycle of the AC voltage, electrons are transferred. Reaction (3.1) is characterized by a standard electrode potential  $E_{eq}^{\circ}$  of +0.34 V [224]. The concentration dependence of the equilibrium potential  $E_{eq}$  can be estimated by the Nernst equation [224]

$$E_{eq} = E_{eq}^{\circ} + \frac{RT}{zF} \ln \frac{a_{+}}{a_{-}}, \quad (3.2)$$

which is about +0.21 V for the lowest considered cupric ion concentration of 0.05 mM (approximating the activity by the concentration,  $T$  – temperature,  $z$  – ion charge number,  $F$  – Faraday constant,  $R$  – universal gas constant,  $a_{+}$  – activity of the cation, and  $a_{-}$  – activity of the anion). Due to the applied AC voltage, also dissolution of copper can happen at sufficiently high positive electrode potential and thus need to be considered. But on average, deposition predominates.

As a further reaction, reduction of hydrogen ions can occur



At the anode, the following oxidation reactions happen



The standard electrode potentials for reactions (3.4) and (3.5) are +1.23 V and +1.5 V, respectively [224].

Wires start to grow after the formation of first copper precipitates, where copper is now the electrode material. In the following it is assumed, that the electron transfer at the electrode interface limits the reaction. The quantitative charge transfer at the electrode surfaces for the deposition reaction (3.1) is commonly described by the Butler–Volmer equation [225]

$$j = j_0 \left\{ \exp \left[ \frac{\alpha_a z F}{RT} (E - E_{eq.}) \right] - \exp \left[ - \frac{\alpha_c z F}{RT} (E - E_{eq.}) \right] \right\}, \quad (3.6)$$

$$j_0 \approx F k_0 \sqrt{c_{ox} c_{red}}, \quad (3.7)$$

where  $j$  is the charge current density across the electrode-electrolyte interface,  $j_0$  the exchange current density, and  $E$  the electrode potential.  $\alpha_a$  and  $\alpha_c$  are the anodic and cathodic transfer coefficients,  $k_0$  is the reaction rate constant, and  $c_{ox}$  and  $c_{red}$  are the concentrations of oxidant and reductive. The occurring material parameters, in particular  $k_0$  and  $E_{eq.}$ , are different for each of the partial reactions (3.1 and 3.3–3.5). Negative values of the current ( $j < 0$ ) correspond to copper deposition. According to equation (3.6), the copper deposition rate strongly increases with increasing negative over-potential  $E - E_{eq.}$ . The equilibrium potential  $E_{eq.}$  increases with the cupric ion concentration (*cf.* equation (3.2)), which facilitates copper deposition.

### 3.4 Nanowire Growth with DENA

This section deals with the experimental study on the growth of high aspect ratio copper nanowires with diameters of about 100 nm and a length of up to several micrometers. In the experiments, the concentration  $c$  of copper ions in solution as well as the peak-to-peak voltage  $V_{pp}$  and frequency  $f$  of the applied AC voltage were varied in order to elucidate their effect on the formation of copper nanowires. For these investigations a fixed electrode gap

size of 10  $\mu\text{m}$  was found out to be appropriate, because nanowire growth was observed for a high frequency range. When the NWs bridged the distance between the electrodes, the current suddenly increases. This was detected through the oscilloscope and the voltage was turned off. Occasionally, the high current caused wire disruption due to melting or electromigration [226]. Solutions to avoid this, are reported in the literature, like automatically switching off when the current exceeds a certain threshold or by using a resistor connected in series with the electrodes to limit the current flowing through completed nanowires [227, 228]. If no bridging was observed within 3 min, the voltage was also turned off.

This was an experimental manuscript on a new kind of nanowire, because to the author's knowledge, this was the first report of copper nanowires synthesis by DENA. Therefore, it was proved that the structures are really made of copper by carrying out elemental analysis using energy dispersive X-ray spectrometry (EDX, Philips XL 30 ESEMFEI). Fig. 3.3a shows a SEM image of a grown wire at a cupric ion concentration of 1.0 mM, a voltage amplitude  $V_{pp} = 20$  V and a frequency  $f = 750$  kHz bridging an electrode distance of 40  $\mu\text{m}$ . The average diameter of the wire was measured from SEM images and is around 600 nm. In the inset of Fig. 3.3a, the backscatter electron image of the morphology and surface composition of the surface including the electrode and wire is presented. EDX spectra of the different areas (electrode, wire, and substrate) are illustrated in Fig. 3.3b–d, respectively. The low peak of Au in the EDX spectrum in Fig. 3.3b identified in region (b) indicates small amounts of gold deposited as 20 nm electrode layer. Peaks of copper (Fig. 3.3c) were observed in the area of (c) and can be attributed to the grown wire. This reveals that the wire is made of copper. A sharp peak of Si and a low peak of O were found in all EDX spectra (Fig. 3.3b–d) and this is due to the Si/SiO<sub>2</sub> substrate.

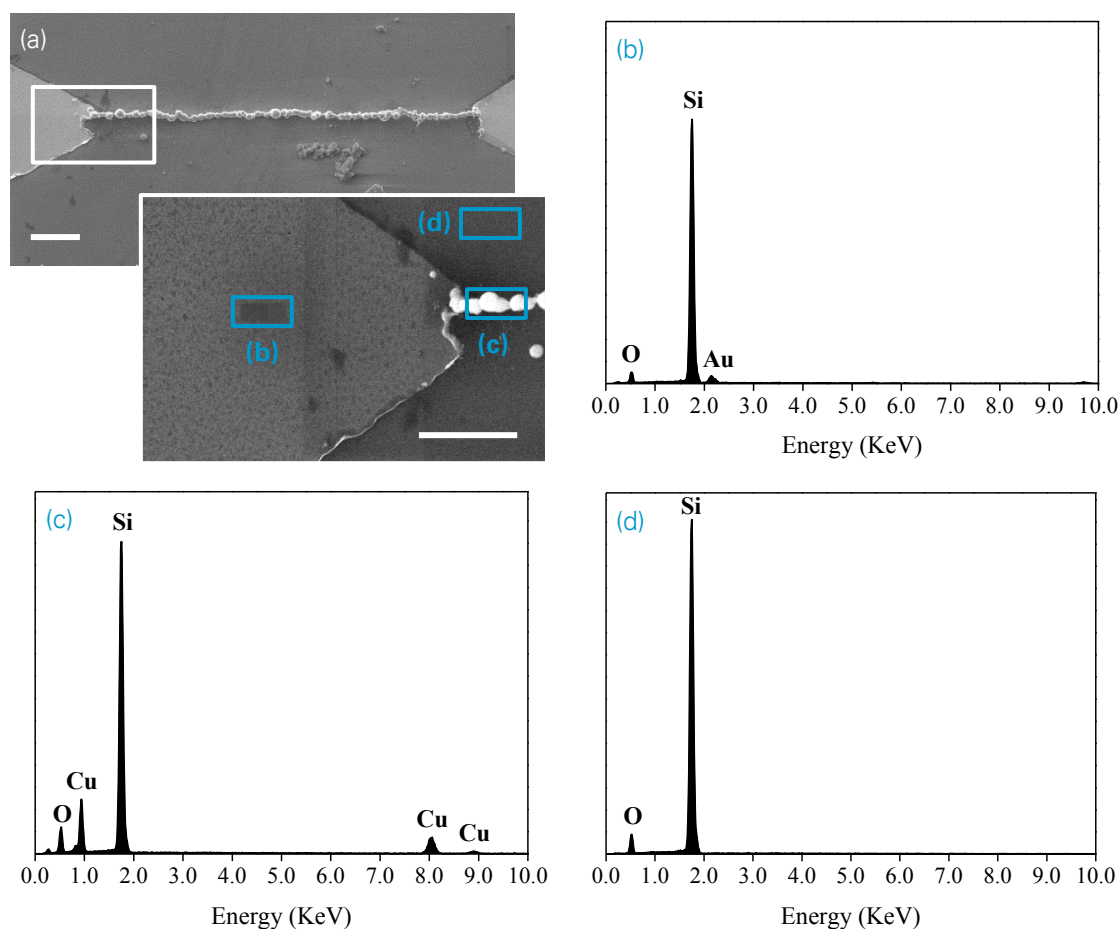


**Fig. 3.3:** EDX analysis of a grown nanowire. (a) SEM image of a synthesized nanowire with a  $\text{Cu}(\text{NO}_3)_2$  concentration of 1.0 mM, a voltage amplitude  $V_{pp} = 20$  V and a frequency  $f = 750$  kHz bridging an electrode distance of  $40 \mu\text{m}$  with a backscattered electron image of SEM in the inset and (b-d) corresponding EDX spectrum of the respective position. Scale bars  $5 \mu\text{m}$ . The areas indicated in blue in the inset of (a) correspond to the respective elemental analyses of (b-d). Si and O were detected at all three positions, which were expected since the growth was carried out on a silicon wafer with a 400 nm oxide layer substrate. The Au peak in (e) was attributed to the 20 nm thick gold layer of the electrode. The Cu peaks in (f) were due to the grown wire from aqueous copper(II)-nitrate solution revealing that the wire is made of copper.

In the following, the influence of (i) salt concentration, (ii) amplitude, and (iii) frequency of the applied voltage on the nanowire morphology is discussed.

### 3.4.1 Effect of Salt Concentration

To investigate the influence of the  $\text{Cu}(\text{NO}_3)_2$  concentration on the nanowire morphology, different cupric ion concentrations from 0.05 to 2.0 mM with a fixed voltage amplitude  $V_{pp} = 16$  V and frequency  $f = 250$  kHz were used. The SEM images are summarized in Fig. 3.4. As can be seen in Fig. 3.4a, concentrations below 0.1 mM did not result in nanowire growth. At a concentration of 0.1 mM, thin and highly branched nanowires grew with an average diameter of 65 nm (Fig. 3.4b). Further increase of the concentration led to the growth of thicker

nanowires as observed in Fig. 3.4d and e. At those high concentrations of 1.0 and 2.0 mM, the wires are considerably less branched compared to wires grown at 0.5 mM or less. For 2.0 mM the average diameter was 550 nm. The observed transition phenotypes from dendritic to more ordered patterns of wire morphology correlate well with previous reports in the literature of Sawada et al. studying the electro-deposition of Zn [229].

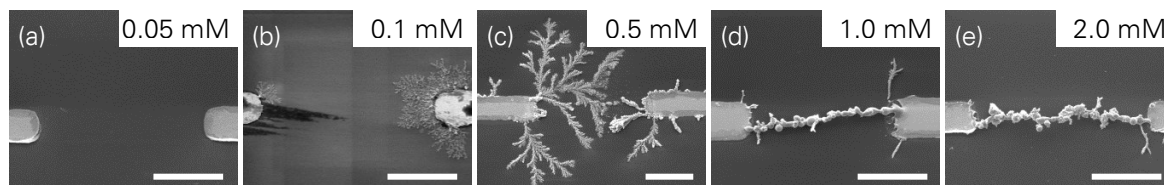


**Fig. 3.4:** SEM images of copper nanowires grown at concentrations of 0.05 (a), 0.1 (b), 0.5 (c), 1.0 (d), and 2.0 mM (e). Parameters:  $V_{pp} = 16$  V,  $f = 250$  kHz. With higher concentrations the wires become thicker and less branched. Scale bars 5  $\mu$ m.

### 3.4.2 Effect of voltage amplitude

Copper NWs were synthesized by applying peak-to-peak voltages of 6, 8, 10, and 20 V at a frequency of 250 kHz and a constant concentration of 1 mM (see Fig. 3.5). No bridging of the gap between the electrodes occurred at the lowest applied voltage of 6 V within an observation time of 3 min. The application of a higher voltage of 8 V led to the formation of a highly branched NW, which contacted both electrodes. Further increase of the voltage up to 10 and 20 V induced the growth of less branched wires. At the highest tested voltage of 20 V, short nanowires arising at the electrode sides were also observed. The bridging nanowire in Fig. 3.5d has a diameter of approximately 450 nm. Whereas, the shown wires grown at lower voltages (Fig. 3.5a–c) are significantly thinner with diameters of about 120 nm. It is worth noting that the gold electrodes considerably dissolved at the tips during wire growth at 20 V.

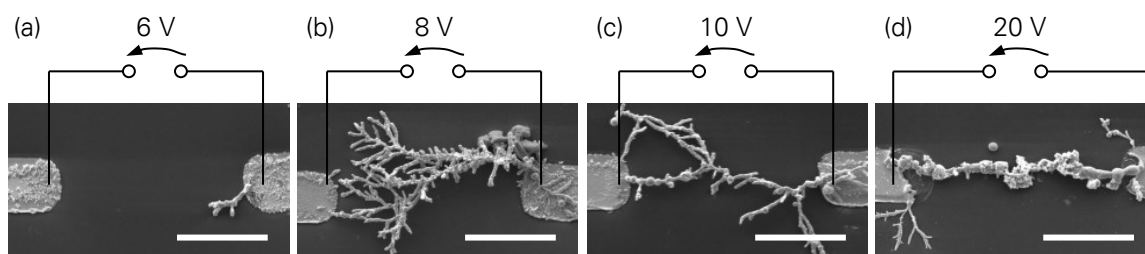


**Fig. 3.5:** SEM images of copper nanowires grown at peak-to-peak voltages  $V_{pp}$  of 6 (a), 8 (b), 10 (c), and 20 V (d), a concentration of 1 mM, and a frequency of 250 kHz. Scale bars 5  $\mu$ m. At a voltage of 6 V, the wire growth velocity is obviously too slow to connect the electrodes within 3 min observation time. At higher voltages the grown nanowire bridges the gap.



### 3.4.3 Effect of Frequency

Fig. 3.6 shows SEM images of copper NWs grown at different frequencies from 50 to 750 kHz of the applied AC voltage of 8 V or 10 V and a concentration of 1 mM. A voltage of 10 V for a frequency of 750 kHz had to be applied, because no wire growth occurred at this frequency and a voltage of 8 V within an observation time of 3 min. Therefore, the voltage was increased to 10 V for this frequency. Fig. 3.6a–f demonstrates the trend that the NW diameters decrease with increasing frequency. The corresponding mean values and standard deviations of the wire diameters for each frequency are presented in Fig. 3.6g. Each data point represents an average of 15 measurements on the respective SEM images. In the frequency range from 50 to 750 kHz, the mean diameters decrease from 310 to 110 nm. This trend is in accordance to previous reports on DENA of indium and gold wires [221] as well as platinum nanowires [230].

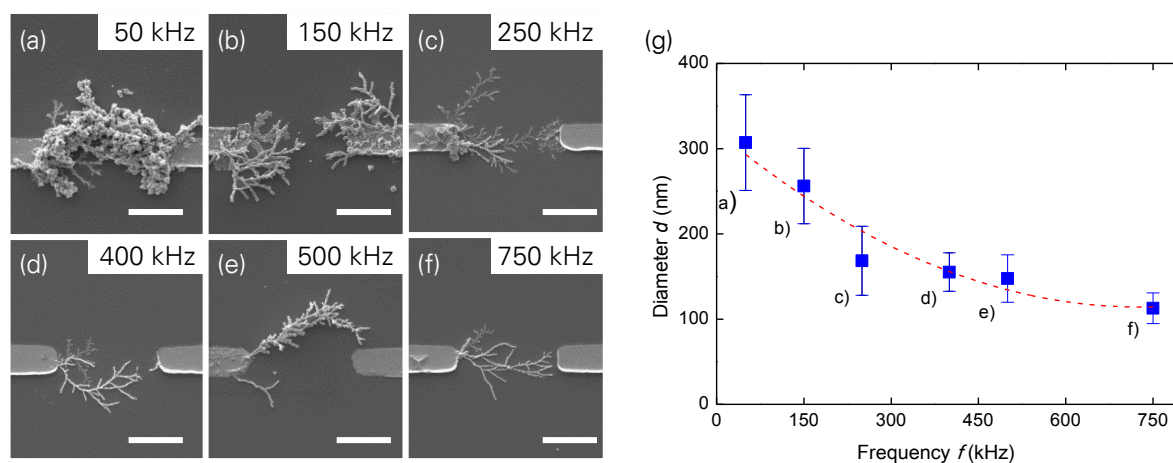


**Fig. 3.6:** SEM images of copper nanowires grown at frequencies of 50 (a), 150 (b), 250 (c), 400 (d), 500 (e), and 750 kHz (f). Parameters:  $c = 1$  mM and  $V_{pp} = 8$  V (a–e),  $V_{pp} = 10$  V (f). Scale bars 5  $\mu$ m. The diameter of the wires decreases with increasing frequency. (g) Wire diameter as a function of the frequency of the alternating voltage. The dashed line serves as a guide to the eye.

### 3.4.4 Electrical Properties

The  $I$ – $V$  measurement of a single nanowire with a diameter of approximately 500 nm shows a linear increase (Fig. 3.7), indicating an ohmic behavior at room temperature. The average resistance of this intact wire was measured as 110  $\Omega$ . This results in a wire conductivity of  $5 \times 10^6$  S  $m^{-1}$ , assuming a cylindrical wire shape with a length of 40  $\mu$ m and an average diameter of 300 nm. The value is approximately one order of magnitude lower than the conductivity of bulk copper of  $5.96 \times 10^7$  S  $m^{-1}$  at 20  $^{\circ}$ C showing that the contact resistance between the wire and the Au contacts is low. As mentioned before, a high contact re-

sistance is the prevalent problem of bottom-up approaches for depositing nanostructures between electrodes. A similar difference between nanosized and bulk materials was reported for Pd nanowires of about 200 nm diameter [218]. It is very probably that the conductivity is diminished due to a polycrystalline structure and surface roughness (slight diameter variations) of the wire. Furthermore, the wires have a granular morphology, which should decrease the wire conductivity by additional electron scattering at grain boundaries compared to monocrystalline nanowires. This effect could not be quantified since no successful growth of monocrystalline copper NWs of similar geometry for comparison was achieved.

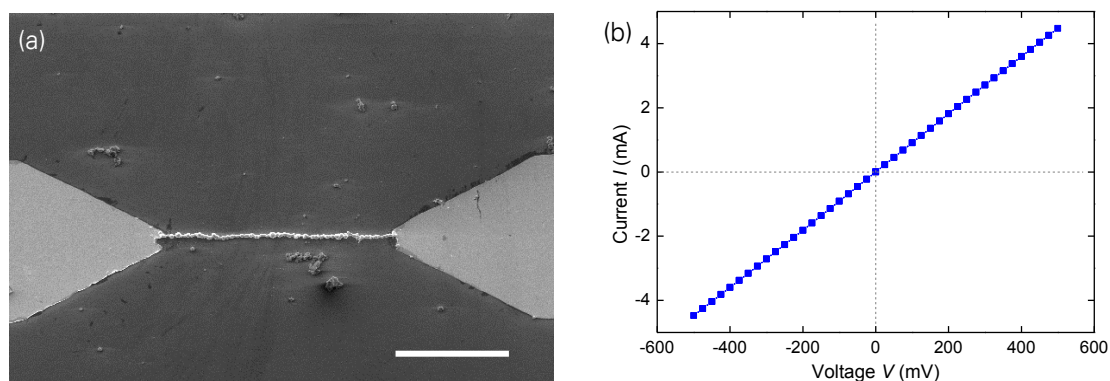


**Fig. 3.7:** Electrical characterization of a contacted copper nanowire with a diameter of around 500 nm. (a) SEM image of a grown nanowire with a length of 40 μm, a  $\text{Cu}(\text{NO}_3)_2$  concentration of 1.0 mM, a voltage amplitude  $V_{pp} = 20$  V, and a frequency  $f = 750$  kHz. Scale bar 20 μm. (b)  $I$ - $V$  characteristic of the grown copper nanowire in (a). The curve reveals ohmic behavior.

In terms of the use of grown and contacted nanowires in gas sensing applications, it is required to have semiconducting copper(II)oxide (CuO) nanowires instead of metallic copper nanowires. To find out, if the synthesized Cu wires convert to CuO nanowires in ambient air, the resistance was measured during three consecutive nights for 15 h, respectively. Fig. 3.8b gives an example of the resistance response of a copper nanowire fabricated by DENA. Due to the small variations in resistance, it is concluded that the wire did not oxidize, because the resistance remains approximately constant over time. Copper oxides are poor conductors and the determined wire conductivity in the range of  $10^6 \text{ S m}^{-1}$  is much higher compared to the electrical conductivity of CuO of  $10^{-1} \text{ S m}^{-1}$  at room temperature [273], which excludes that the wires oxidize to CuO at ambient conditions. The electrode design included an additional floating electrode (FE), which serves to reduce the Joule heating of the wire upon contact (Fig. 3.8a). This design is favorable, because the magnitude of the current and thus the Joule heating of the wire upon contact can be reduced by using floating electrodes. This electrode design should prevent the wires from burning when they contacted the electrode. The yield could be increased, but was still not satisfactory.

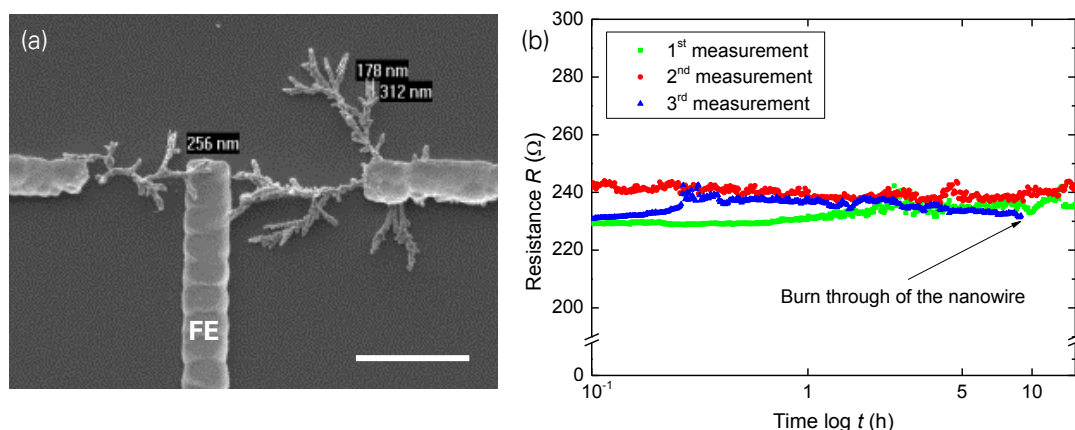


**Fig. 3.8:** Measurement of the resistance over time for an exemplary copper nanowire. (a) SEM image of the copper nanowire. Scale bar 5  $\mu\text{m}$ . (b) Measurement of resistance shows that no oxidation of the wire occurs.

For the application as gas sensor, it is also important that more than one wire is grown simultaneously. This enhances the sensor yield as well as the sensor-to-sensor reproducibility. An extensive analysis allowed to determine an optimized set of process parameters ( $V_{pp} = 20\text{ V}$ ,  $f = 250\text{ kHz}$ ,  $c = 1\text{ mM}$ ) to simultaneously grow single straight nanowires contacting one electrode tip to the other tip (Fig. 3.9). The distances between the electrodes were 40  $\mu\text{m}$ .

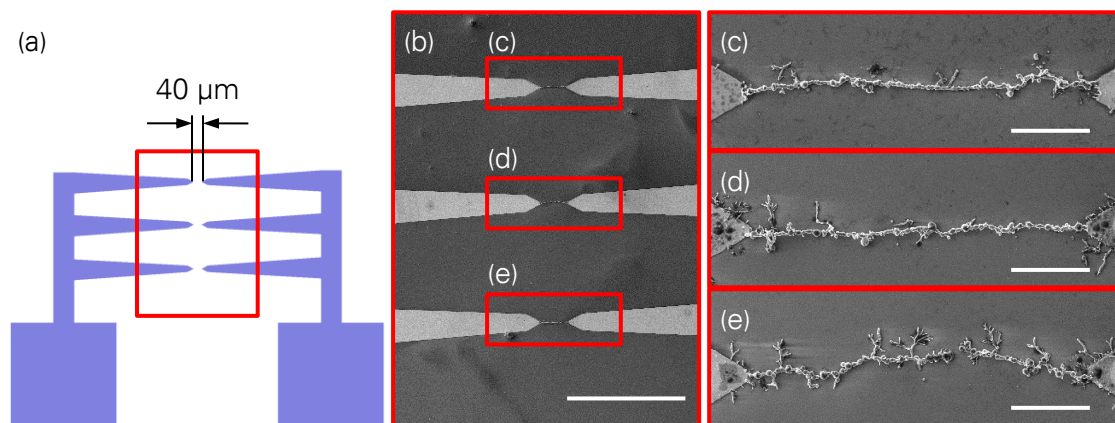


**Fig. 3.9:** Simultaneously grown copper nanowires. (a) Electrode layout with three parallel pairs of electrodes with a gap size of 40  $\mu\text{m}$ . (b) SEM image of the electrode tips with the grown wires in-between. Scale bars 200  $\mu\text{m}$ . (c-e) Grown wires with process parameters:  $V_{pp} = 20\text{ V}$ ,  $f = 250\text{ kHz}$ ,  $c = 1\text{ mM}$ . Scale bars 10  $\mu\text{m}$ .

### 3.5 Discussion

The copper NW growth was analyzed in dependence of experimental parameters (salt concentration, voltage, frequency). In the experiments, rectangular voltage signals were applied ( $V_{pp} \geq 6\text{ V}$ ). These are considerably larger than the characteristic electrode potentials men-

tioned in section 3.3. Fig. 3.5d gives a clear evidence for the dissolution of the gold electrodes at a high voltage of  $V_{pp} = 20$  V and to a less extent also in Fig. 3.4 at lower voltage. Dissolution of gold nano-dendrites was comprehensively studied in [231].

The nucleation of copper on the gold electrode surface obviously requires that the cupric ion concentration and the applied voltage amplitude exceed certain thresholds depending also on the frequency. So, for a low concentration of 0.05 mM ( $V_{pp} = 16$  V,  $f = 250$  kHz) and at a low voltage of  $V_{pp} = 8$  V ( $c = 1$  mM,  $f = 750$  kHz) no NW growth took place within three minutes. Such a so called voltage threshold was also described for the DENA technique of indium wires [232]. As a tendency, a high cupric ion concentration at the electrode surface supports the copper precipitation on gold for negative electrode polarity. This is due to the higher near-surface concentration with increasing bulk concentration. Moreover, the ion concentration is strongly enhanced owing to the cupric ion attraction during the negative half-wave of the voltage. In terms of the voltage, a higher voltage results in a larger electric field and accordingly to a larger attractive force. If the frequency is considered than at a lower frequency, the time for ion accumulation near the electrode surface is longer. Thus, a higher concentration can be reached during one half-wave. After the formation of copper nuclei, wires start to grow and subsequently copper becomes the electrode material. The Butler-Volmer equation (3.6) in section 3.3 describes the charge transfer at the electrode surfaces for the reduction of copper (3.1). With increasing charge transfer rate at the wire surface, ion transport from the bulk solution to the wire via diffusion and field-driven migration will become rate-determining. This transport limitation is apparently responsible for the formation of highly branched NWs [233] as depicted for instance in Fig. 3.4b and c. The obtained wire morphology is very similar to the fractal patterns realized by diffusion-limited aggregation as reported in literature [234, 235].

Ion transport caused by the electric field is particularly pronounced near the nanowire tip. At this point, the field strength can reach comparatively high values, because of the small tip radius. This can be determined by approximating the tip by a hemisphere of radius  $r_{tip}$  and assuming a counter electrode in large distance  $\gg r_{tip}$ . The electric field in vacuum is calculated from  $V/r_{tip}$  at the tip surface, where  $V$  is the applied voltage. In the solution, the ion accumulation near the surface also influences the electric field. This case is analyzed in more detail in [236]. The increased electric field at the nanowire tip leads to the favored copper deposition at this place.

In the case of lower frequencies, ions are attracted for a longer time during one voltage pulse resulting in a higher ion accumulation at the electrode surface, even in surface regions with lower electric field strength. This leads to a large number of thicker wires as shown in

Fig. 3.6a. Remarkably, wire growth can be observed at the whole electrode surface, not only at the electrode tip and also from both electrodes. With increasing frequency, the number of grown wires decreases and the wires are preferably formed at the electrode tips. Generally, ion accumulation at the electrode surface becomes less with shorter voltage pulses. Since ion accumulation at the wire tip is largest due to the higher electric field, wires nearly exclusively elongate as seen for example in Fig. 3.6f. Branching of wires takes place likely because of mass-transport limitation. The particularly fine dendritic structure in Fig. 3.4b implies that, at relatively low bulk concentration of 0.1 mM, only thin wires can grow since only sufficiently small tip radius ensures a high enough electric field strength for copper deposition.

After investigating the main parameters that influence the morphology of formed copper wires, the achieved findings were used to grow several wires simultaneously. Fig. 3.9 presents the controlled nucleation of nanowires at sharp electrode tips. In this case, the ion concentration of 1 mM and the frequency of 250 kHz were high enough to reduce the effect of mass-transport limitation as reason for wire branching. Thus, wires with only few short side branches and diameters of about 300 nm grew.

However, in Fig. 3.9 and also in Fig. 3.3a it can be seen that even though the structures are straight, they are rough dendrites, especially when compared to wires reported by others [218, 221, 230]. Applying an AC voltage to the electrodes, the direction of the electric-field-driven part of the particle transport is oscillating resulting in a periodic enrichment and depletion of the charged species near both electrode surfaces. It is assumed that two cases have to be distinguished, where the metal bearing species are metal cations (e.g.  $\text{Pd}^{2+}$ ) or anionic complexes (e.g.  $\text{AuCl}_4^-$  [231]) since anions are repelled from the electrode when electron charge transfer occurs during the negative half-cycle of the AC voltage, whereas cations are attracted. In a recent paper [233], it was demonstrated by computer simulations that the reduction of anionic complexes happens right after the polarity switch from positive to negative electrode potential. In the case of Pt and Au, it is speculated that the presence of  $\text{Cl}^-$  and the preferred adsorption of Cl on special crystal facets could promote special growth directions.

The present case of copper wire growth from  $\text{Cu}(\text{NO}_3)_2$  solution could be similar to the case of Ag from  $\text{AgNO}_3$ , where cations are attracted during reduction. From the thoroughly explored In wire growth [232], it is known that needle-like wires grow only in a very small voltage and concentration region with a constant frequency. Similarly, the voltage-concentration window for growing unbranched monocrystalline copper NWs could be extremely small or even missing. The tendency to branching seems larger for copper NWs compared to In

NWs. The reason for this difference is presently unknown. But it can be related to the different valence ( $\text{Cu}^{2+}$  and  $\text{In}^{3+}$ ). For instance, the solvation energy for  $\text{In}^{3+}$  should be considerably larger. It seems also likely that sufficient electron transfer for reduction of  $\text{Cu}^{2+}$  is easier than for  $\text{In}^{3+}$ , resulting possibly in a faster deposition and more unstable growth with nucleation of new grains.

To sum up, it is guessed that especially straight nanowires can be achieved exclusively in the cases of (a) growth of monocrystalline nanowires, e.g. shown in ref. [230], or (b) highly oriented growth with the preferred orientation of poly-crystallites within the nanowires, like shown in [233]. However, the nanowires shown in Fig. 3.9c-e represent neither case (a) nor case (b). The nanowires are polycrystalline and consist of multiple randomly oriented copper clusters, which can be easily distinguished in SEM image (e.g. in Fig. 3.5d or Fig. 3.9c-e). In this case, the straightness of the wire and its morphology is mostly caused by an electric field in solution and by mass-transport limitation, respectively.

### 3.6 Summary

In this chapter, the controlled electrochemical synthesis of copper nanowires from an aqueous  $\text{Cu}(\text{NO}_3)_2$  solution with diameters of about 100 nm and a length of up to several micrometers was demonstrated. The frequency was found to notably affect the nanowire diameter. This approach further enables the rapid growth of copper nanowires with distinct morphologies at predefined electrode locations. The following guidelines to obtain thin nanowires can be deduced from the experimental and theoretical investigations:

- Electrode structures should have sharp tips for controlled nucleation sites to initiate nanowires growth.
- The frequency has to be adjusted above a threshold as such that the copper ion concentration at the NW tip is sufficiently high to ensure wire growth at the tip, but to avoid copper deposition on the other wire surface. With increasing frequency the NW nucleation becomes harder at the initial gold electrode tips, resulting in a lower ion accumulation at the electrode surfaces. Thus, supporting the fact that the electrode tips should be as sharp as possible.
- Wire branching can be avoided by providing sufficiently large ion concentration, such that mass-transport limitation is not possible.
- It is crucial to properly limit the voltage amplitude to prevent dissolution of the gold electrodes.

The obtained results are of high interest for potential nanosensor configurations, particularly for developing highly sensitive gas sensors. However, despite the great progress, which has been achieved in the synthesis of copper nanowires via DENA, there are still a number of challenges to be solved in order to use this technology for gas detecting applications. Some of these issues are the relatively large width of the wires, low yield due to the regularly occurring burn through of the wires during the growth process, and the additional oxidation step. For these reasons and because of the higher sensitivity that can be reached by using silicon nanowires, this approach is not pursued further in this work. Furthermore, high operating temperatures are required for operating gas sensors based on metal oxide semiconductors as sensing materials. This is not needed for SiNW based devices. Therefore, further activities within this work focus on the use of silicon nanowires as gas sensing elements.





## 4 Technology for the Fabrication of Silicon Nanowire based Sensors

In the following chapter, developed and applied methods for the fabrication of gas sensors based on silicon nanowires in this work are described. The aim was to develop individual demonstrators enabling to investigate electrical characteristics under exposure to gases and verify new concepts, making it to a crucial part of the work on the topic. As introduced in section 2.4 there are two techniques for the fabrication of nanowire based devices. Both bottom-up and top-down methods were used to fabricate the devices in this work. The recognition element of the sensors was formed by the semiconductor silicon in the form of nanowires. The fabrication process was based on the nanowire growth, which belongs to the bottom-up methods. This method allows growing nominally undoped wires with diameters below 10 nm, a low edge roughness, and a constant diameter over several microns [237]. Comparable structures can be realized with top-down methods only at very great expense [238]. The patterning of the source and drain electrodes for the deposition of nickel were done by means of top-down methods. The combination of both methods led to improved electrical properties of the active elements of the fabricated devices through their high structural quality and they could be specifically structured for subsequent processes and measurements.

The fabrication steps of silicon nanowire based gas sensors used in this work can be divided into four main processes. Some process steps were done by colleagues as mentioned in the following:

1. Nanowire growth (done by Sebastian Pregel),
2. Nanowire transfer to the sample substrate (done by the author),
3. Contact of the wires (done by the author),
4. Silicidation (done by Andreas Gang).

A more detailed description of the different fabrication steps is shown in Fig. 4.1. The sensor fabrication process starts with the nanowire growth. The grown NWs need to be released from the substrate where growth took place and transferred onto another substrate for further processing. The NW transfer was enabled by a mechanical abrasion process called contact printing. After this procedure an array of SiNWs was obtained, which was etched in HCl / HNO<sub>3</sub> to remove the AuSi eutectic tips of the NWs. The following dry oxidation step was just carried out for those sensors having a low defect oxide shell. It was not done for

the sensors based on SiNWs with a native oxide shell. Optical lithography was used to pattern the electrode structure on top of the aligned NWs. A buffered hydrofluoric acid (BHF) etching step was performed for a local removal of the NW oxide shell, which would prevent the diffusion of nickel into the wire during silicidation. Afterwards, nickel was deposited as electrode material and the lift-off was conducted. After annealing in forming gas for further silicidation of the wires, NiSi<sub>2</sub>-Si interfaces were formed.

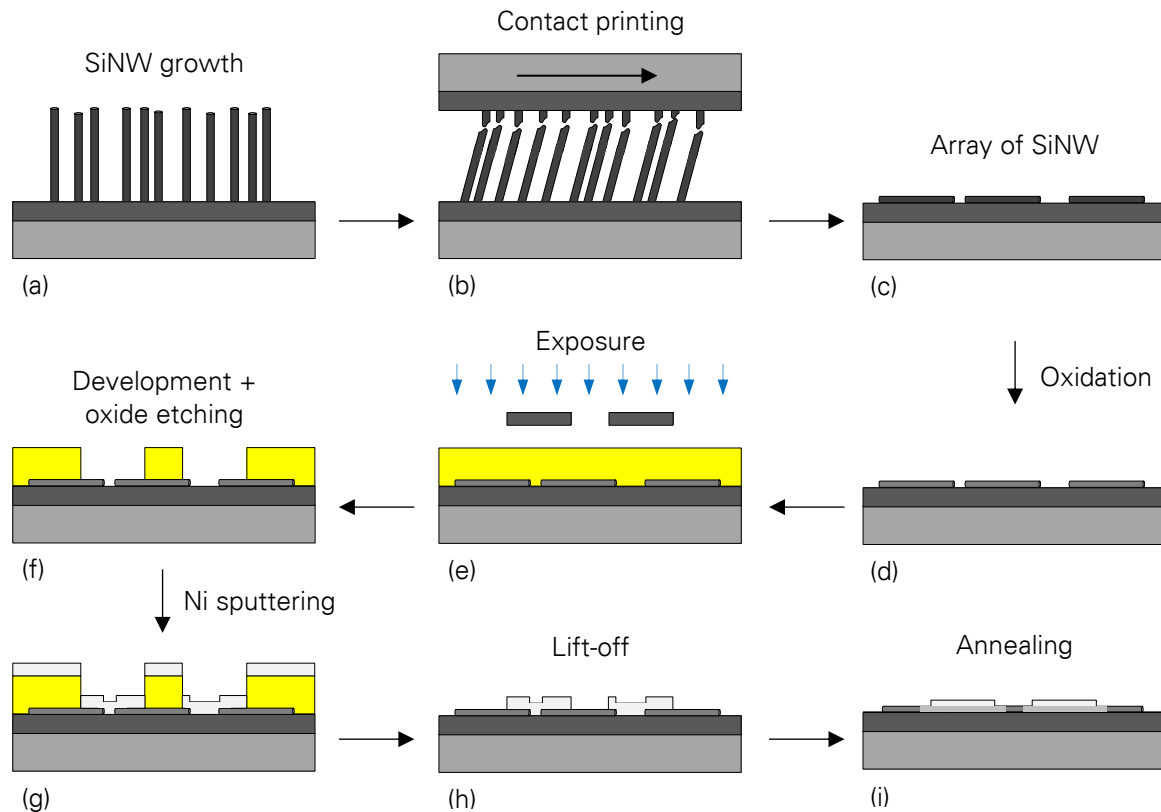


**Fig. 4.1:** Process steps for the silicon nanowire based sensor fabrication. (a) CVD synthesis of silicon nanowires, (b) contact printing transfer of grown nanowires to the chip substrate (Si/SiO<sub>2</sub>), (c) parallel array of silicon nanowires, (d) etching with HNO<sub>3</sub>+3 HCl and oxidation of the wires, (e) exposure with optical lithography, (f) development of the resist and local oxide etching by HF, (g) Ni deposition, (h) lift-off in a solvent, (i) annealing for the silicidation of nanowires forming NiSi<sub>2</sub>-Si interfaces. Dimensions and relations do not correspond to the actual values.

The individual process steps are described in detail in the following subchapters. Further development of the devices was basically carried out by changing the sensor design.

#### 4.1 Nanowire Synthesis

To fabricate a semiconductor area having a cylindrical structure, the nanowire growth was based on the vapor-liquid-solid process (VLS) [239]. It is one of the chemical vapor deposition methods (CVD). There, the material to be growing goes through various phase transitions

with means of a catalyst particle. The used nanowires were available from previous works of the group. These were grown in a CVD furnace using generated gold particles as a catalyst [240]. The material, structural, and geometric properties of the grown wires met the requirements of the sensors fabricated for this work, so that no additional growth experiments had to be performed. The nanowire growth for the wires used in this work can be divided into the following processes [237], depicted schematically in Fig. 4.2a:

- Surface coating of the catalyst by means of a 0.5-1.0 nm layer of Au on Si or  $\text{SiO}_2$ ,
- Coalescence of the Au layer,
- Influence of monosilane,
- Formation of a Si-Au mixed phase,
- Diffusion of Si,
- Formation of a eutectic (liquefaction),
- Supersaturation and formation of a solid Si-rich phase,
- Monolithic extension of Si.

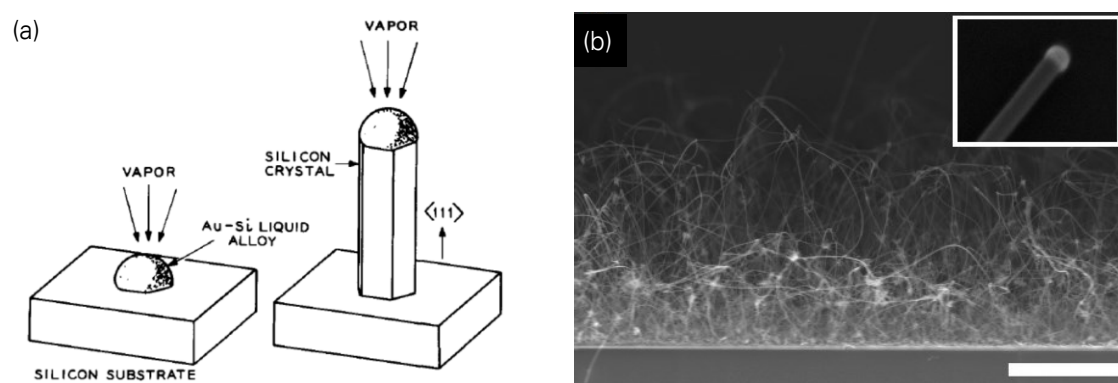


**Fig. 4.2:** Si nanowire synthesis. (a) Schematic representation of the procedure for VLS growth [239], (b) SEM side view image of the growth substrate after Si nanowire growth. Scale bar 10  $\mu\text{m}$ . Nanowire tip with AuSi eutectic droplet is shown in the inset [240].

Thus, SiNW were available, which were used as a semiconductor material for the fabrication of nanowire based gas sensors for this work. The application of dopants was suppressed in the fabrication and subsequent processes. However, the unintended placing of single dopant atoms cannot be excluded. The grown wires had a homogeneous diameter of  $22 \text{ nm} \pm 5 \text{ nm}$ , a length of approximately  $40 \mu\text{m}$ , and based on the number of wires a high density on the growth substrate ( $> 10 \mu\text{m}^{-1}$ ) [240, 241]. Transmission electron microscopy (TEM) investigations revealed a monocrystalline structure of the Si nanowires and an amorphous  $\text{SiO}_2$  shell [242]. Fig. 4.2b shows SiNWs on the growth substrate, which was the starting point of the experimental work.

## 4.2 Nanowire Transfer and Oxidation

The controlled and predictable assembly of well-ordered structures is essential to achieve the substantial potential of bottom-up synthesized nanowires in gas sensing applications. The wires connected to the growth substrate were not suitable for the fabrication of individual gas sensors, which required a detachment of the wires from the substrate. It is a major challenge in the development of nanomaterial based devices to controllably fabricate large areas having a high density of arrays with nanometer-scale structures. Diverse approaches for the hierarchical assembly of one-dimensional nanostructures can be found in literature. Nanowires are aligned in fluid flows [243], using the Langmuir-Blodgett technique [244, 245], and by electric-field directed assembly [246, 247]. However, solution based methods cause difficulties, such as contamination and nanowire bending during film densification [240].

In this work, a contact printing approach for the nanowire assembly over large areas was used. This dry deposition strategy enables the direct transfer and positioning of nanowires from a donor to a receiver substrate [248, 249]. Moreover, the technique has several advantages: it is simple and the transferred nanowires are highly aligned and dense with a high uniformity and reproducibility. The operating principle is schematically depicted in Fig. 4.3a. The growth substrate with the vertically arranged NWs, called donor substrate, was broken into smaller parts. Such a piece was attached to a steel cubic weight ( $1 \times 1 \times 1 \text{ cm}^3$ ) with double-sided adhesive tape after it was held under a nitrogen stream to remove dust and silicon grains. The weight ensured a defined pressure between the donor and receiver substrate (Si/SiO<sub>2</sub>, degenerately p-doped/400 nm). Before the nanowire transfer process, the receiver substrate was cleaned with acetone, isopropanol, and purged with nitrogen. The donor substrate was placed upside down on top of the device substrate such that the NWs were in contact with the chip. A gentle manual pressure to the side of the wafer piece was then applied, leading to a sliding of the growth substrate of a few millimeters. In order to avoid leakage currents through scratches in the later Ni deposited areas, the growth substrate was placed in the region where the contact pads were not located. During the printing process NWs are well aligned by shear forces and a controlled transfer of NWs is enabled through chemical binding interactions between NWs and the surface of the receiver substrate (Fig. 4.3b). It is assumed that NWs stick to the receiver substrate even by covalent bonding [240], which is probably, because NWs adhere to the surface during the remaining fabrication process. Finally, the donor substrate was carefully removed and devices were then fabricated on the printed NW array using conventional top-down lithography. For the contact printing process no lubricant or chemical surface treatments were applied, like suggested in some

literature [248], to reduce contamination risk. Surface contamination cannot only lead to an accumulation of NWs (Fig. 4.3c), but also damage the SiO<sub>2</sub> layer, which later results in gate leakage and degraded sensor behavior. Therefore, a thick SiO<sub>2</sub> back gate oxide was used.

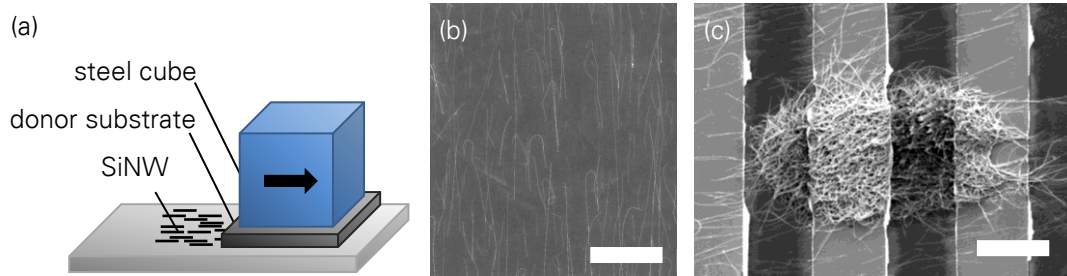


**Fig. 4.3:** Contact printing of NWs. (a) Schematic of the process for contact printing of a NW array. (b) SEM image of SiNWs printed on a Si/SiO<sub>2</sub> substrate showing highly dense and aligned monolayer of NWs. (c) A contaminated substrate surface can lead to a nanowire accumulation. Scale bar 5 μm.

Additionally to the Si nanowires with a native oxide shell, Si nanowires with thermally grown SiO<sub>2</sub> were fabricated. For this an additional process step was introduced, which is described in the following. The high temperature step of the oxidation increases the diffusion of the Au catalyst particles connected to the wires. These can generate deep charge carrier traps that affect the electrical behavior [250]. In addition, the diffusion of oxygen through a native oxide is not constant, resulting in a non-uniform thermal oxidation and thus an inhomogeneous oxide thickness [251]. To reduce the charge carrier traps and increase the homogeneity of the SiO<sub>2</sub> layer, the substrate was etched for 2 h in aqua regia (HNO<sub>3</sub> 25 %, HCL 75 %). Through the strong adhesion of the nanowires on the sensor chip due to contact printing no detachment of the nanowires was observed. For the oxidation of the wires a rapid thermal processing (RTP) furnace (SHS 2800, AST Electronic GmbH) was used. After purging the chamber with N<sub>2</sub>, the sample was heated with about 45 K·s<sup>-1</sup> at 875 °C under a flow rate of 10 slm O<sub>2</sub> at 1 bar. This temperature was maintained for 6 min and then lowered below 60 °C without interrupting the oxygen supply. Directly afterwards a passivation was carried out under forming gas with 90 % N<sub>2</sub> and 10 % H<sub>2</sub> at 450 °C for 10 min to saturate remaining dangling bonds at the Si/SiO<sub>x</sub> interfaces [252, 253]. By this temperature treatment no metallic pre-structured substrates could be used.

### 4.3 Sensor Design

The basis of the sensor devices were 4 inch wafers with 400 nm thermally grown front oxide from which the substrates were separated by laser cutting to a size with a width of 1 cm and a length of 2 cm, determined by the dimension of the sample holder in the gas detec-

tion system (see chapter 5). The upper 50 mm<sup>2</sup> of the sensor surface had to remain unprocessed, since this area was needed to attach the substrate by means of a contact pin inside the gas detection system. Contact pads for electrical connection of the devices were located at the lower edge (Fig. 4.4a). Long electrode leads were necessary to minimize local oxide rupturing through the contact printing technique. This could result in scratches along the printing direction leading to gate leakage. Previous experiments showed that long leads of the electrode layout have to be oriented in the direction of the printed nanowires. A width of 50  $\mu\text{m}$  and length of 6 mm was chosen.

To realize highly sensitive resistive gas sensors, the arrangement of the metal electrodes and the sensing element is one of the key issues. An interdigitated electrode array was designed and fabricated to increase the surface area as depicted in Fig. 4.4b and c. With this design a large amount of nanowires was connected in parallel, which led to an increased sensor reproducibility compared to sensors based on single nanowires. The electrode distance was 6  $\mu\text{m}$ , the electrode width 4  $\mu\text{m}$ , the length of an individual electrode was 500  $\mu\text{m}$ , and the length of the interdigitated array 1.5 mm, resulting in a number of 150 electrode gaps per chip.

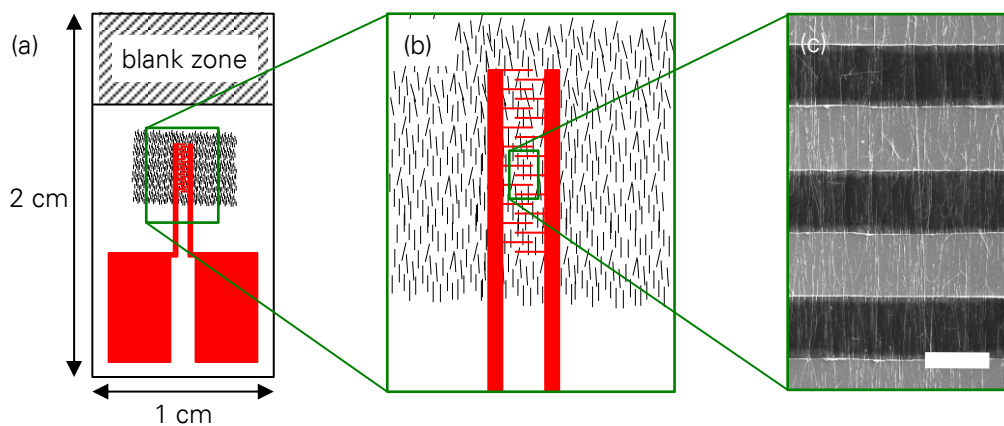


**Fig. 4.4:** Sensor design. (a) Schematic illustration of the sensor layout with contact pads, electrodes and a blank zone for the sample attachment. (b) Microstructure of an interdigitated electrode array with a perpendicular nanowire orientation. (c) SEM image of contacted nanowires. Scale bar 5  $\mu\text{m}$ .

#### 4.4 Fabrication of Contact Electrodes

Through contact electrodes, the nanowires can be mechanically fixed and electrically contacted. Metal contacts are established in the semiconductor fabrication, because of their low electrical resistance, mechanical, thermal, and chemical stability as well as the simple fabrication [254]. In this work the contact to the nominally undoped semiconductor was produced by using electrodes made of Ni. This was the diffusion source for the nickel silicide

formation, which was a crucial basis for the function of the SiNW based gas sensors [255]. One method of the Ni contact fabrication is conventional top-down lithography.

#### 4.4.1 Lithography

Two different kinds of lithography were used for the fabrication of microelectrodes. Laser lithography was applied for the structuring of photomasks, which were subsequently utilized for optical lithography. Photoresists are materials that undergo photochemical reactions when exposed to light [256]. In optical lithography a specific pattern is accomplished by the imaging of a mask. In contrast, in laser lithography a scanned, focused laser beam is used to directly write patterns in photoresist in a serial fashion.

The used photomasks from Rose Fotomasken GmbH were deposited with layers of chromium and positive photoresist (LRC-chromium, AZ 1500 resist). Structuring was done by laser lithography (DWL 66fs, Heidelberg Instruments) using a 4 mm write head at  $\lambda = 405$  nm followed by 60 s development (AZ 351B, Microchemicals) and subsequent etching for 60 s (Chromium etch No. 1, Microchemicals). Afterwards, the mask was ready for use in optical lithography.

Mask alignment and exposure was carried out with a MJB4 Mask Aligner from SÜSS MicroTec. An adhesion promoter (TI Prime, Microchemicals) prior to the coating step was deposited by spin-coating and then tempered at 120 °C for 2 min before the resist was applied to improve the adhesive effect of the photoresist. The image reversal photoresist (AZ 5214E, Microchemicals) was used to achieve a negative wall profile ideally suited for lift-off. It was spin-coated on the substrate with 3400 rpm for 60 s to reach a thickness of 1  $\mu\text{m}$ , followed by subsequent heating on a hotplate at 110 °C for 1 min. The exposure with optical lithography was performed with a mercury lamp as ultraviolet (UV) source at a wavelength of  $\lambda = 365$  nm for 1 s followed by a bake step for 2 min at 120 °C. The exposed areas of the resist became almost insoluble (in developer) and no longer light sensitive due to a special cross linking agent together with the exposed photoactive compound. The pre baked photoresist was flood exposed (no mask) for 30 s to generate some exposed photoactive compounds at the surface. The structures were developed for 60 s in undiluted AZ 760 MIF, where the (during the first exposure) unexposed areas are dissolved and the cross linked areas remain, resulting in a negative pattern of the mask. Finally, the reversal-bake step at 120 °C for 4 min was performed to partially crosslink this top areas. Thereby, a top layer with a lowered dissolution rate compared to the bulk material was generated. Due to the lower dissolution rate in the top layer a T-shaped profile with overhanging lips was the result.

#### 4.4.2 Oxide Etching

Silicon forms a native oxide upon contact with ambient air [257]. This acts as a diffusion barrier for Ni, whereby a formation of nickel silicide is prevented in the bulk at temperatures below 800 °C (see subchapter 3.5) [258]. A passivation is used to prevent oxide formation, where free Si bonds are saturated with hydrogen. This passivation prevents the adsorption of molecular oxygen up to 380 °C [259] and can be achieved by means of surface treatment by HF or BHF. These etching solutions remove the native silicon oxide and passivate the bare silicon [260]. The passivation decreases at room temperature (RT) in the air after a few minutes, resulting in the formation of a new native oxide.

In this work, a 1 % BHF solution was used for etching, which in contrast to HF has a temporally constant etch rate through the excess of F-ions and does not damage the resist even after long etching durations. Chips based on NWs with a native oxide shell were immersed for 30 s and substrates with thermally grown oxide shells were etched for 80 s. The AZ5214e resist layer protects the covered areas from the acid for several minutes.

#### 4.4.3 Nickel Deposition

After the etching process, a 50 nm Ni stack was deposited. The selected method was physical vapor deposition (PVD). Among the various PVD-techniques sputtering was available and appropriate, because the period between etching and deposition could be kept very short, thus preventing the reoxidation of the Si nanowire surface. The sputtering chamber (High Resolution Ion Beam Coater Model 681, Gatan) used in this work had a load lock allowing the main chamber to permanently operate in vacuum conditions.

Ion beam sputtering utilizes an ion beam, which is accelerated towards the target with adjustable kinetic energies between 2 keV and 10 keV. The highly energetic argon ions from the injected argon gas lead to a release of Ni atoms from the target by means of their kinetic energy. The resulting ion beam impinges upon a target material and this results in a material beam directed towards the substrate. With a film-thickness monitor the deposition rate is continuously measured and the film thickness can be controlled.

The lift-off was then carried out by dipping the substrate in acetone for 30 min with a short (5 s) ultrasonic agitation. After rinsing in isopropanol and drying in a nitrogen stream the device was ready for the silicidation procedure.



#### 4.5 Fabrication of Schottky Contacts within a Nanowire

In general, through the chemical reaction of metals with silicon, referred to as silicidation, intermetallic phases can be formed [261]. The resulting silicides have a low electrical resistance and high temperature stability, therefore Co-, W-, Pt-, and Ni-silicide are used in semiconductor technology [254]. Compared to the reaction in bulk material, the activation temperatures and at certain temperatures formed phases of the nanowire silicidation differ [262]. The silicide formation is primarily determined by the interfacial reaction, whereby the silicidation rate does not depend on the contact distance [237]. Due to the chemical conversion of the single-crystalline Si into single-crystalline  $\text{NiSi}_x$ , a semiconductor-metal-contact with an abrupt interface and a low interfacial density is formed [263, 264].

In this work Ni was used as contact metal. Diffusion of Ni atoms is required to form a nickel silicide within a Si nanowire. For the silicidation an annealing process in forming gas ( $\text{H}_2/\text{N}_2$  20/1 v/v) in a RTP furnace designated SHS 2800 of the company AST Electronic GmbH was carried out. Devices with a native oxide shell were annealed at 450 °C for 20 s, whereas the silicidation rate for thermally grown nanowire oxide shell is smaller with 500 °C for 30 s. The annealing in forming gas leads to an additional hydrogen passivation of dangling bonds at the Si/SiO<sub>2</sub> interface improving electrical characteristics [252]. Upon annealing, Ni diffuses axially into the SiO<sub>2</sub> coated SiNW and transforms the Si regions into metallic, single-crystalline  $\text{NiSi}_2$  NW segments (Fig. 4.5) [255]. Thus,  $\text{NiSi}_2$ /intrinsic-Si/ $\text{NiSi}_2$  NW axial heterostructures surrounded by a SiO<sub>2</sub> shell are formed [265]. Contacted NWs with  $\text{NiSi}_2$ /Si Schottky junctions are shown by SEM in Fig. 4.5.

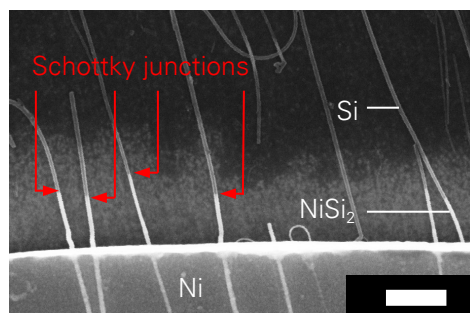


**Fig. 4.5:** SEM image of contacted NWs with  $\text{NiSi}_2$  interfaces. The red arrows indicate the location of the Schottky junctions. Scale bar 100 nm.

#### 4.6 Summary

This chapter described the developed and used methods for the fabrication of SiNW based gas sensors. It was based on grown, nominally undoped Si nanowires with diameters

around 20 nm. By transferring the nanowires to a parallel dense array, the electrode fabrication by lithography on a substrate with 400 nm SiO<sub>2</sub>, the deposition of Ni, and the silicidation of the wires, the fabrication procedure of the devices used in this work was demonstrated. The nanowire growth as well as the silicidation are processes, by which the high structural quality of the monocrystalline nanowires with abrupt metal-semiconductor interfaces can be achieved. The so formed NiSi<sub>2</sub>-Ni-NiSi<sub>2</sub> nanowire heterostructure formed one important prerequisite of the sensor operation. An equivalent structuring can be realized with top-down processes only with very high effort. An essential step in improving the electrical properties represent gas sensors based on nanowires with a thermally grown oxide shell.

## 5 Measurement Setup and Implementation

This chapter deals with the developed gas measurement setup, which was used to carry out  $\text{NH}_3$  detection experiments in this work. The test and measurement system has a significant impact on the successful development of gas sensor systems. Due to the growing application of gas sensing, like in the breath gas analysis, there is a rising interest in multisensor systems and pattern recognition techniques leading to increased specifications for such measurement systems. The following chapter describes the experimental setup, beginning with a brief overview of the state of the art and requirements of a gas test system. Furthermore, this section gives a comprehensive view on the gas measurement procedure used in this thesis.

### 5.1 State of the Art

At present, various gas measurement systems are known, which ensure a defined gas flow over sensors at certain temperatures during the measurement. In the following, only the literature relative to gas measurement chambers is considered, because this work focuses on the development of such a system and it belongs to the most important parts of the whole gas flow apparatus.

H.-E. Endres et al. presented a test system for gas sensors in 1995 [266]. Two chambers were developed, which ensured a small volume and a well-defined gas flow. These test chambers contained simultaneously up to ten different types of sensors (semiconductor, dielectric, micro-scale, etc.) and enabled measurements of the gas temperature and pressure. A 1999 by P. Pérez Ballesta et al. developed gas measurement chamber consisted of a 20.7 l comprehensive cylindrical glass chamber, which was divided longitudinally by a glass shell [267]. This enabled the physical recirculation of the air inside the chamber and the generation of a controlled wind speed by a small fan, which was installed inside the chamber. A gas measurement chamber with a small volume in which a sensor was installed, was published by Kida et al. in 2008 [268]. The dead volume of the chamber was  $0.6 \text{ cm}^3$ . The diameter of the gas inlet and outlet was 0.5 and 2 mm, respectively. This size difference reduced the pressure drop in the chamber by facilitating the gas outlet. A ceramic heating element was attached to the bottom of the chamber, while three heat insulating plates out of mullite were disposed directly below the heater to allow maximum heating of  $450 \text{ }^\circ\text{C}$ . In a further publication, a system was described in which the substrate was located in a gas flow cham-

ber of Teflon [269]. The electrodes of one sensor were connected to a potentiostat. During measurement, a continuous stream of gas with a constant flow rate, which could be switched between nitrogen and the analyte-nitrogen mixture, was directed over the substrate. In another embodiment, the measurements of the test gas flow occurred in the sensor chamber made from stainless steel, which had to be readjusted for different sensor types and models [270]. In 2014, a stainless steel gas measurement chamber is demonstrated with a total of 104 integrated electrical feedthroughs [271]. The chamber consists of a base plate containing the electrical feedthroughs, a stainless steel ring, and a top cover. Inside the chamber custom-made printed circuit boards (PCB) distribute electronic connections to allow adjusting for different pin-layouts of the microchips.

## 5.2 Requirements of a Test System for Gas Sensors

The main task of a gas measurement system is to regulate all the conditions that are essential for the sensor's behavior to achieve a qualified performance of the measurements. In this way sensor properties and behavior can be investigated under the influence of gases, which is indispensable for the understanding, development and optimization of sensors. To examine the full capability of sensors, it is necessary to provide on the one hand concentrations that cover all desired concentration ranges and on the other hand a high accuracy of the gas combinations. Parameters that influence thermodynamic processes on the sensor surface, like temperature and pressure, must be controlled and stable. Furthermore, the design of the exposure chamber has to ensure a fast gas exchange and a homogeneous gas flow. Today's sensor applications call for selective gas detections. Hence, it is essential that test systems can measure several gas sensors simultaneously. To guarantee a precise control of the environmental conditions and allow the storage and evaluation of the large amount of measurement data, only computer-controlled measurement units are applicable. Thus, the main requirements for a laboratory-based apparatus to characterize nanomaterial based gas sensors can be summarized as follows:

- Control of the analyte gas concentration in the ppm to ppb range,
- Fast measurement and read-out of the sensor signal (near-real-time),
- Precise control of the sensor temperature,
- Possibility of reuse of the sensors by non-fixed bonds,
- Simultaneous measurement of multiple sensors,
- Uniform gas flow over all sensors.

From these requirements and considering needs for a laboratory-based system, a novel set-up was designed. Accordingly, the presented apparatus is capable of reading-out up to four sensor responses quasi-simultaneously. The possibility of simultaneous measurements allows on the one hand determining the reproducibility of the fabricated sensors and on the other hand comparative studies of different sensing materials. In the following, the implementation of the mentioned requirements in the system developed in this work is described.

### 5.3 Apparatus

The complete apparatus is schematically depicted in Fig. 5.1. It comprises four subsystems: the gas delivery system to control the gas composition and concentration inside the measurement chamber, the gas exposure chamber for a specific attachment of the samples, the read-out electronics to determine the resistivity of the sensors, and the temperature control for the sensor chips. The subsystems can be controlled via a single computer by integrated programs with graphical user interfaces. All of the gas feedthroughs are implemented through a 2-tube system. Stainless steel tubes with diameters of 6 mm (Swagelok) for the gas inlet and outlet are connected with adapters to a standardized clamp flange (KF-) system (VACOM Vakuum Komponenten & Messtechnik GmbH). This is further described in the following sections. The whole system was designed using the 3D-computer-aided design (CAD)-software solution Inventor® Professional (Autodesk).

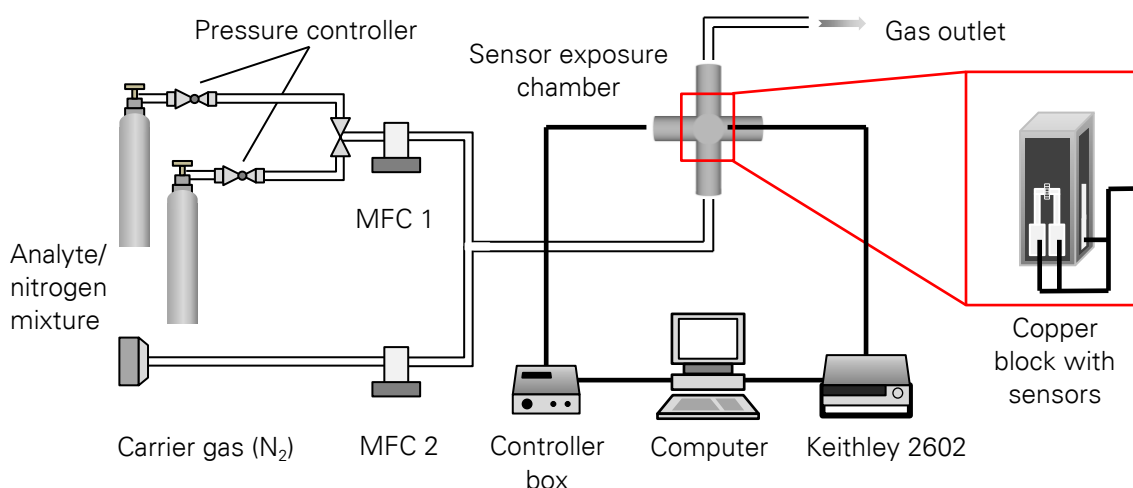


**Fig. 5.1:** Schematic configuration of the developed gas flow apparatus with a small volume gas chamber equipped with read-out electronics for the sensor measurements.

### 5.3.1 Gas Delivery System

The gas delivery system is made up of two individual channels. Each channel is connected via tubes to pressure reduced gas cylinders or to the nitrogen connection. The two bottles contain the analytes diluted in  $N_2$  and one tube is directly connected to the pure nitrogen supply. The flow rates of  $N_2$  and sample gases are precisely controlled to a setpoint value independent of pressure and flow resistance variations by SLA5850 (Brooks Instrument GmbH) mass flow controllers (MFC). Flow control is done by computer software (Brooks Smart DDE) through a RS232/RS485 converter and a specially developed Microsoft Excel user interface. With it setpoint values can be transferred to the MFCs. The maximum flow rate of the MFC for the  $N_2$  flow is 2 l/min. For the analyte/ $N_2$  mixture a flow rate of 20 ml/min can be achieved. By changing the flow rate of the latter, the concentration is varied. Both gas flows of the individual channels are merged after the MFCs and then guided to the measurement chamber. The exhaust of the chamber is extracted via an evacuation system.

### 5.3.2 Exposure Chamber

Test chambers for gas sensors are an important issue of every gas measurement system. Those have to be optimally planned concerning the gas flow, in order to get reproducible flow at the sensor surfaces. The chamber designed in this work is optimized with regard to a small volume for short gas exchange times and a highly laminar gas flow. Furthermore, the whole apparatus is hermetically sealed using vacuum components, because harmful gases were used for the experiments. Standard connection is a small vacuum flange KF40. The material is stainless steel with only two integrated electrical feedthroughs, which makes the system gas-tight and decreases costs, because complicated and expensive gas-tight feedthroughs are reduced (Fig. 5.2). Stainless steel was chosen as material for the chamber since it is inert to most chemical reactions. The core of the gas measurement system is a stainless steel KF-DN40 6-way-cross (1, VACOM Vakuum Komponenten & Messtechnik GmbH), in which the sensors are located. Each of the six ports has its own function, which is discussed later in more detail. The dead volume of the chamber is very low with about 0.8 cm<sup>3</sup>, whereby a fast gas exchange is ensured.

The 6-way-cross is seated on two fork mounts (2), which enable its rotation. This ensures a facilitated installation of the sensors and through hose clips the 6-way-cross is secured against accidental tilting. The holders are attached to a mounting profile (3, ITEM Industrietechnik GmbH). This is designed in L-shape to guarantee a stable position. At the two ends

rocker bases made out of nylon (4) are mounted, which allow a lying down of the whole apparatus. This constitutes an alternative way to the rotatable holders, but was not used for reasons of space within the fume hood. Two stainless steel pipes with a diameter of 6 mm (Swagelok) are used for gas inlet (5) and outlet (6) to suppress a back diffusion of gases.

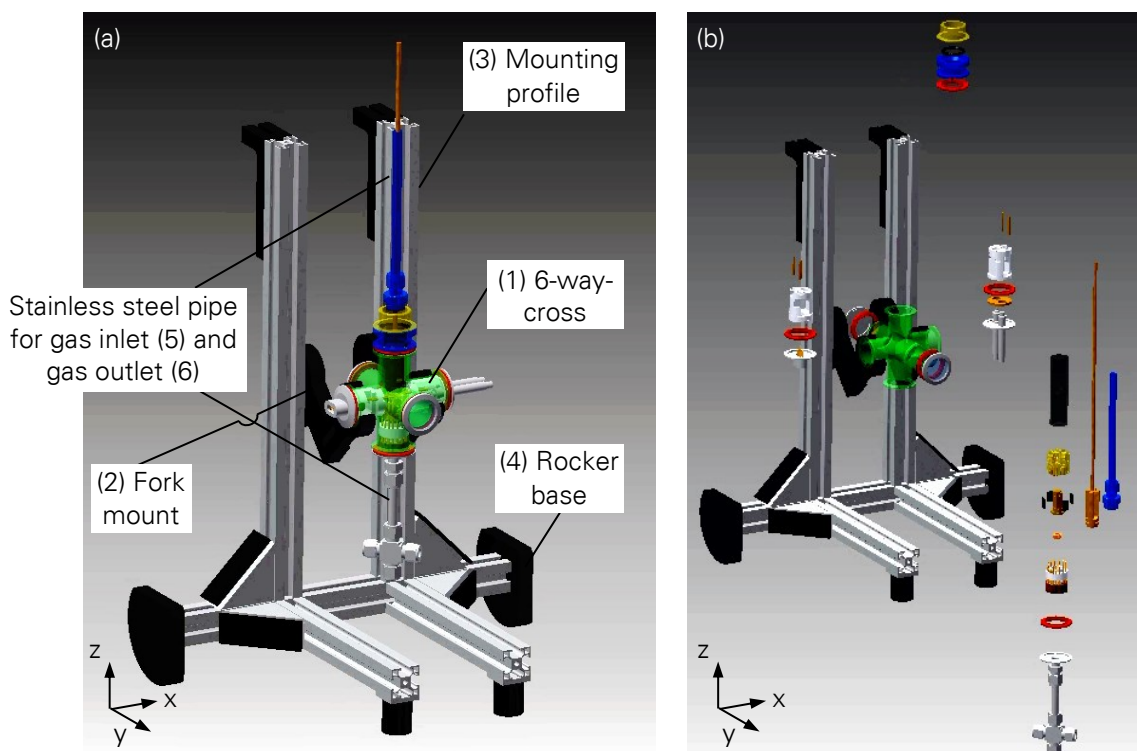


**Fig. 5.2:** CAD model of the gas measurement chamber, which is gas-tight and rotatably mounted on a holder. This holder is attached to a mounting profile in a stable L-shape. (a) Assembled measuring system and (b) individual components of the system.

The double cross piece comprises six ports with an inner diameter of 40 mm, respectively (Fig. 5.3). Within the chamber a gold coated copper block (10x10x20 mm) is located, which serves as thermal controlled sample holder. A 5  $\mu\text{m}$  Ni layer was chemically deposited as diffusion barrier and subsequently a 1  $\mu\text{m}$  Au layer to avoid oxidation and scale of the Cu was electrodeposited. Three spring contact pins per chip, which are high temperature resistant, allow both the contacting of sensors to measure the resistance signal and the chip fixation. Around the Cu block with the sensors four parts out of Macor ceramics or Teflon are fixed with sleeve nuts. Macor was chosen, because it is an efficient insulator of heat and electricity and is stable up to about 1000  $^{\circ}\text{C}$ . The processing of the Macor elements was carried out using mechanical machining methods. The attachment of the sensors is done via the contact pressure of the three high-temperature spring contact pins, which are pressed into the Macor ceramics as well as through the Macor ceramics itself, which is bolted to the Cu block. The whole chip changing process can be carried out with just a small screwdriver.

All six ports of the 6-way-cross are airtight using seals (KF standard). A seal is positioned between the two flanges (KF40) and consists of a centering ring and the acrylonitrile butadiene rubber (NBR, high chemical resistance) O-ring (7) stretched upon fixed by clamp chains (VACOM Vakuum Komponenten & Messtechnik GmbH). They enable a quick and easy assembly without any tools. Two of the double cross piece ports (front and rear) are viewports out of borosilicate glass (8) with removable O-ring seals (VACOM Vakuum Komponenten & Messtechnik GmbH) for adjusting the contact pins during the sensor installation, as they provide an insight into the measuring chamber.

The multiplexer electronics is located inside the lower arm of the chamber (z-). This includes a custom-made PCB via surface-mount technology (SMT), where the four relays are mounted, which are responsible for switching between the chips. Relays with AgPd contacts are used having a contact resistance less than  $100\text{ m}\Omega$ . Each closer of a relay thus operates one chip. Furthermore, an ATtiny24 microcontroller (Atmel) is molded in epoxy resin, which is used to switch the relays randomly and multiplex the signal. In section 5.3.3 the sensor control is discussed in more detail. The sensors are connected via spring contact pins with the control electronics. Thereby, no cohesive connection takes place and the chips are therefore reusable. In the middle of the control electronics, the stainless steel pipe is located, leading the gas mixture to the chips.

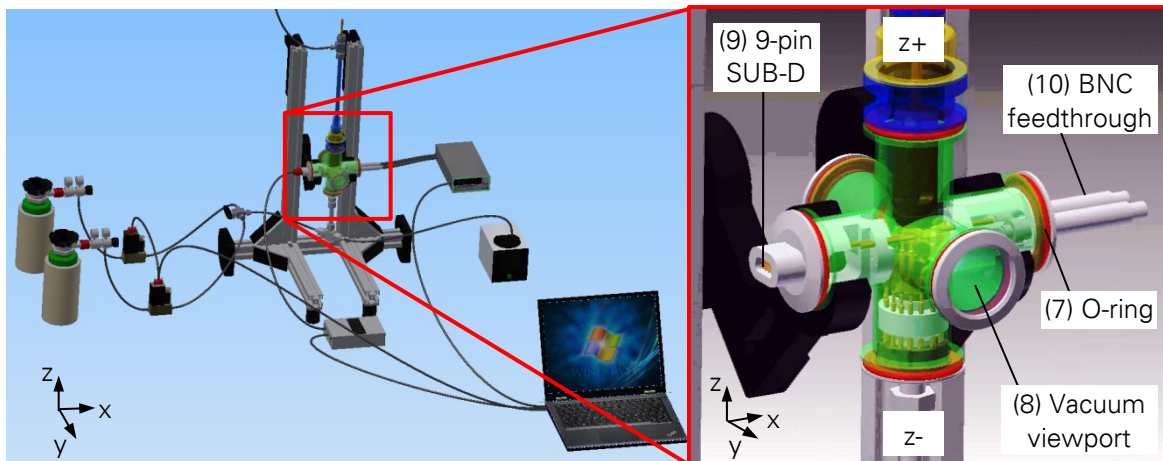


**Fig. 5.3:** Apparatus with exposure chamber (left). Stainless steel 6-way-cross with six ports, with different functions, like gas inlet, gas outlet, and viewports, respectively (right). Two electrical feedthroughs, one for the connection to the controller and the other one to the measuring instrument, ensure to read out the resistance of up to four sensors.

The stainless steel pipe has four holes as can be seen in Fig. 5.4a, where the gas flows to the sensors bounded by the Macor ceramics. Fig. 5.4a shows the assembled PCB board with the relays, sealing ring, Macor ceramics, and 13 contact pins. The 13 contact pins are composed of 8 pieces for the sensor connection, two for the operating voltage, two for the



BNC connector and one for the clock signal. The chips, sheathed with Macor ceramics, are shown in Fig. 5.4b. The ceramics with the attached contact pins is fixed to the Cu block by means of a screw. The distance between the sensors and the ceramics is 1 mm.

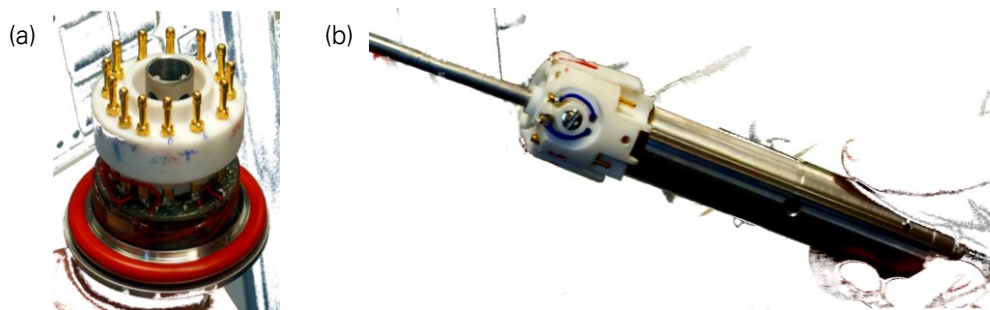


**Fig. 5.4:** Components inside the gas exposure chamber. (a) Lower part with the relays, PCB board sealing ring, Macor ceramics, and 13 contact pins, (b) Macor ceramics covering the sensors.

The upper cylinder (z+) includes the gas outlet and the connection to the heating device, which is controlled using a power head. The heating control is discussed in detail in section 5.3.4. Via a 9 pin SUB-D feedthrough (9) the system is connected to the controller box, thus the operating voltage is provided as well as the signal for the control of the sensors. The right port contains a Bayonet Neill–Concelman (BNC) feedthrough (10) for the connection to a measuring instrument. The electrical feedthroughs on the airside are connected via cables to the controller and measuring instrument, respectively. To avoid empty spaces, where gas diffusion can take place, all electronic components are embedded in epoxy resin. As much as possible of the electronic layout is placed within the chamber, so that the number of electrical feedthroughs is minimized. This reduces the costs of expensive feedthrough components and ensures the gas tightness of the system.

### 5.3.3 Control and Read-out Electronics

The resistance of each sensor is determined using a Keithley 2602 System SourceMeter connected with two coaxial cables and a BNC connector to the chamber. The electronic layout was designed that it ensures the quasi-simultaneously time-resolved determination of the resistance of up to four gas sensitive materials independently of each other. For this a voltage between 100 nV and 40 V can be applied to the devices and the measurement range can be adjusted allowing for setting ideal parameters for each sensing material. Since the measurement chamber provides means to read-out four sensors, the switching between the sensors is arranged through the control of the relays by the controller. The four chips are

exposed and heated simultaneously, but only one resistance value can be read out at a time. A relay pointer multiplexes the four sources of current.

The Keithley SourceMeter is connected to the computer via a RS-232 interface and a custom made program implemented in MATLAB (The MathWorks) controls the read-out. The proceeding of reading out the different sensor responses and the data acquisition are illustrated in Fig. 5.5. The measurement speed can be controlled by the MATLAB software to realize different measurement tasks, such as short-term investigations of surface reaction dynamics and long-term measurements for drift and saturation studies. The switch between the sensors is limited by the relay switching time, which is 10 ms. So, all four devices can be measured per second, which was sufficient for the applications in this work. In each measurement, the most important data are preserved, such as applied voltage, measured current, and time.

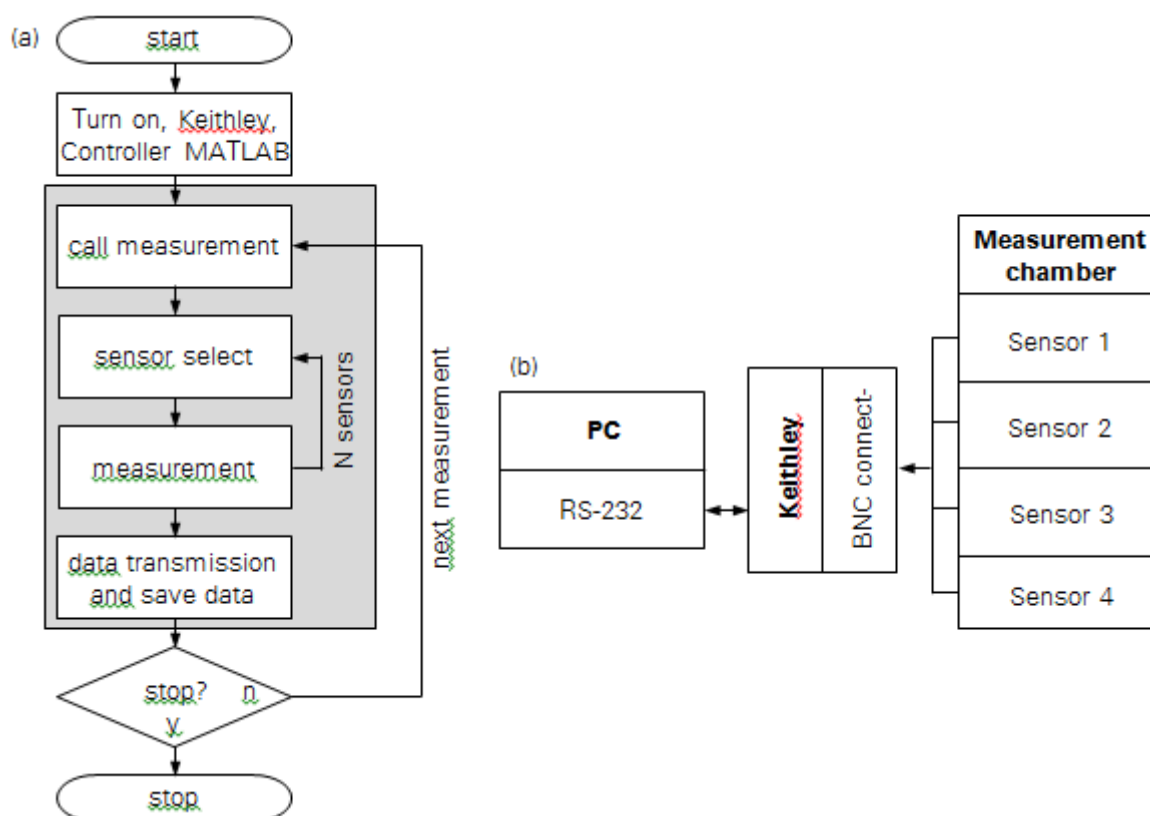


**Fig. 5.5:** Proceeding of the data readout. (a) Flow chart of the data acquisition process. The grey square specifies the steps executed by means of the MATLAB program. (b) Illustration of the working principle of the data acquisition system. The Keithley is controlled by MATLAB via a RS-232 connection. The four sensors are connected to the Keithley using a BNC connector and contact pins for contacting the sensors.

The controller box, which was custom made, is an important instrument of the gas measurement system. It includes the thermocouple module, SBC360 board, and liquid crystal

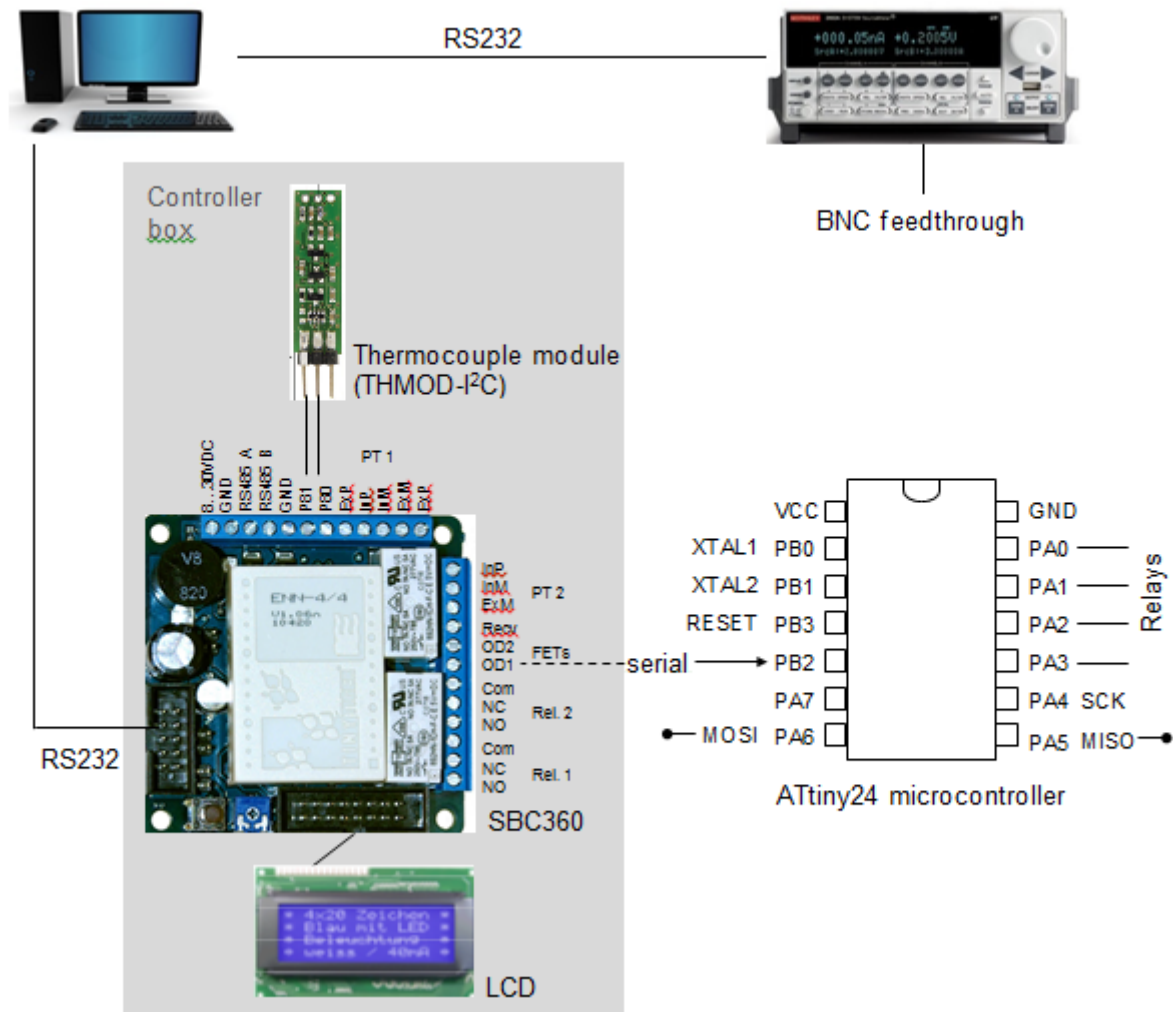
display (LCD) and takes over the control of the switching between the sensors and the temperature control. Fig. 5.6 illustrates the structure of the controller box as well as the control and read-out electronics. A RS232 serial interface connects the computer with the SBC360 board. The thermocouple module serves to monitor and control the temperature and is connected to the SBC360 board. The exact working principle is explained in section 5.3.4. A LCD display shows the respective sensor, which is measured, and is plugged in the SBC360 board.

In a first approach, a sequential switching between the sensors by means of a Johnson counter (decade counter) was used. In order to enable a random access to any of the four chips this technology was replaced by an ATtiny24 microcontroller through SMT. One power output of the SBC360 board inside the controller box is used to transmit one byte addresses serial to the ATtiny24 microcontroller. A one-wire serial write-only connection was used, because the number of feedthroughs to the chamber is limited. The former feedthrough for the counter was used to control the microcontroller. This microcontroller multiplexes the signals and transmits single byte addresses via a universal serial interface (USI) to control the four digital outputs. Since all digital inputs and outputs (I/O) of the controller board are in use, a power metal-oxide-semiconductor field-effect transistor (MOSFET) output pin is used to transmit the one byte addresses to the controller universal asynchronous receiver/transmitter (UART) register.

### 5.3.4 Temperature Control

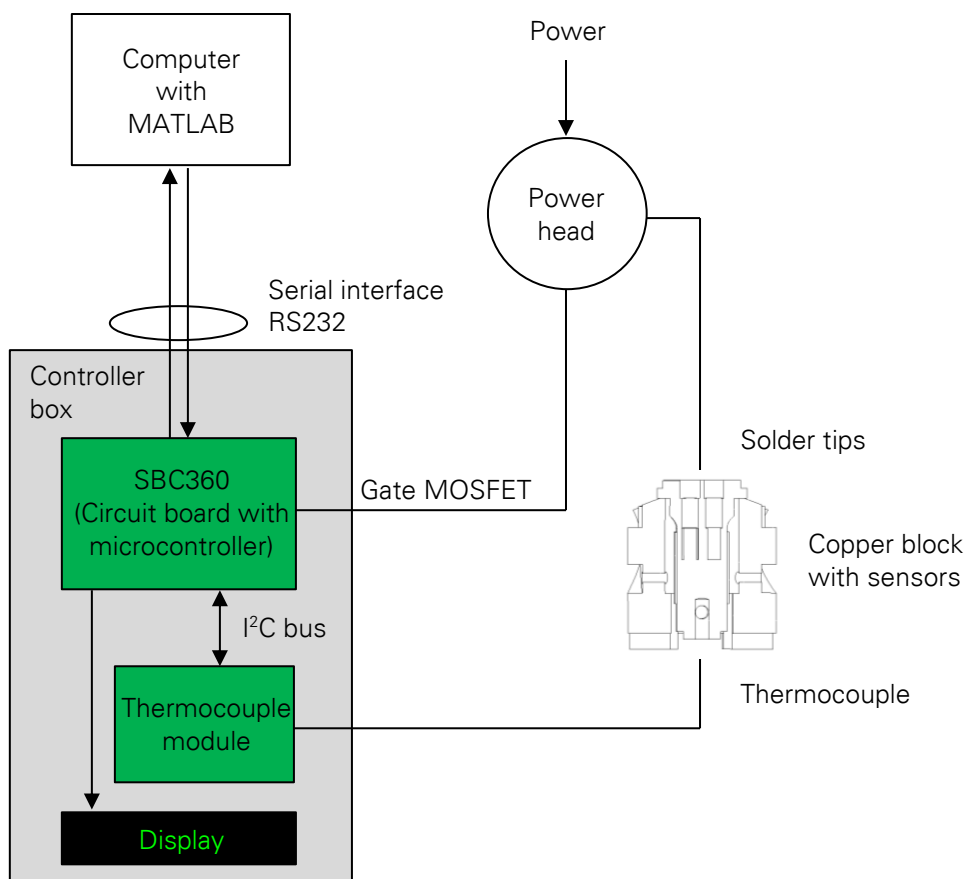
The temperature of nanomaterial based gas sensors is a key factor, since those sensors react very sensitively to temperature changes. Moreover, selectivity towards specific gases is very important for gas sensor applications and can be increased by temperature variations [272]. The entire copper block, on which the sensors are located, is uniformly heated. Therefore, all four sensors are equally heated and it is not possible to control each sensor chip's temperature individually.

Fig. 5.7 shows the schematic temperature controlling of the system. A software subroutine implemented in MATLAB manages the temperature control electronics, which allows for adjusting the sensor temperature. Via a serial interface (RS232) the computer is connected with the controller box. Temperature is monitored and controlled by a thermocouple type K via an inter-integrated circuit (I<sup>2</sup>C) bus module, which is controlled by the microcontroller board. This was chosen due to its two independent Pt1000 receiver circuits.



**Fig. 5.6:** Schematic representation of the control and read-out electronics.

But even the smallest Pt1000 sensors could not be integrated into the double cross piece, because the dimensions are too big for the needed temperature range. Therefore, a mantle thermocouple is used instead enabling a temperature range from 0 to +1100 °C. The thermocouple module THMOD-I<sup>2</sup>C-800 (B & B Thermotechnik) is read out via an I<sup>2</sup>C bus, compares the actual temperature with the setpoint value, and controls the MOSFET, which controls the solder tips and is placed inside the power head. The power head consists of an acrylic glass drum, which includes a light-emitting diode (LED) shining blue when the samples are heated, and the MOSFET for controlling the heating of the copper block, which is done by four serially connected solder tips. The power for the MOSFET is supplied by the SBC360 board.



**Fig. 5.7:** Schematics of the temperature control. Via the RS232 interface the time ticks and the temperature values of the sample holder are transferred from the SBC360 board to MATLAB. MATLAB in turn uses the American Standard Code for Information Interchange (ASCII) format for data transmission.

## 5.4 Measurement Procedure

The importance of the operational procedure lies in the reduction of uncertainties that affect the composition and value of the final concentration of the gas in the chamber. Gas mixing is a main factor involved in the process since it determines the gas flows and thus the gas concentrations. Another important issue is the measurement cycle, because it ensures the quality and comparability of several measurements. In the following, these aspects are explained more in detail.

### 5.4.1 Gas Mixing

The gas composition in the measurement chamber determines the dynamics of the sensor reaction. In the following, the prefabricated mixture of the analyte diluted in the carrier gas (nitrogen) is referred to as test gas. Prefabricated gas mixtures in bottles were purchased from Air Liquide for a smaller degree of dilution and laboratory security.

The adjustment of a certain gas concentration is carried out by assembling the volume part of the test gas to the whole gas flow, see Fig. 5.8. One test gas flow  $\dot{V}_{test\ gas}$  is mixed with one carrier gas flow for dilution  $\dot{V}_{carrier\ gas}$  resulting in a constant total flow  $\dot{V}_{total}$ , which is the sum flow through the sensor chamber.

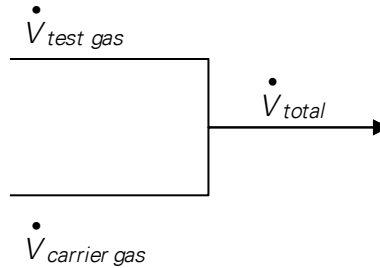


**Fig. 5.8:** Schema of the gas mixing method. The combination of two single gas flows leads to one total gas flow.

The gas is diluted with the carrier gas (nitrogen). Using the concentration of the test gas in the bottle  $C_{test\ gas}$ , the concentration set-point of the analyte  $C_{Analyte}$  of the total gas flow can be achieved using the following formula [266]:

$$C_{Analyte} = C_{test\ gas} \frac{\dot{V}_{test\ gas}}{\dot{V}_{total}}. \quad (5.1)$$

For varying the analyte concentration, the flow rate of the test gas has to be adjusted according to equation 5.1. This is done by MFCs, which keep the required gas flow at a constant level. Aiming at high accuracy in the attainable gas concentrations, two different calibrated MFCs were used. The MFC for the carrier gas has a maximum flow rate of 2 l/min. The second MFC for the test gas covers a flow range of 0.2-20 ml/min. The accuracy of the MFCs is specified to be better than 1% related to the maximum flow and are calibrated and certified by the manufacturer. During the measurement a constant total flow rate with a desired analyte concentration is preferable. A constant gas flow prevents any distortion of the measurement due to changing time constants for gas exchange, forced cooling of heated sensors, and other flow-dependent effects [266]. For experiments in this work a constant carrier gas flow of 2 l/min is used. The flow rate of the test gas was varied according to the required analyte concentration. For example, if the test gas has an analyte concentration of 1% and the sensor response to a concentration of 10 ppm is investigated, then a test gas

flow rate of 2 ml/min must be adjusted. The total flow is thus slightly higher than the carrier gas flow, but this does not affect the sensor reaction (see section 6.3).

Using a constant total flow rate  $\dot{V}$  of 2 l/min, the chamber volume  $V_{chamber}$  being 0.8 cm<sup>3</sup>, and a security factor of three, the purging time can be calculated with [266]:

$$t_{purge} = 3 \frac{V_{chamber}}{\dot{V}_{total}}. \quad (5.2)$$

Thus, it takes less than 1 s until a new steady-state gas concentration is established after a change has been set, which is very fast compared to systems known from the literature [266, 271]. Taking into account the whole volume between the two MFCs and the chamber, the purging time is ~2 s.

#### 5.4.2 Gas Measurement Protocol

Measurements of different analyte concentrations are carried out in the sensor chamber with the following sensor operating mode. A constant voltage and gas flow are applied to the sensors and the sensor signal (current) is measured by a Keithley SourceMeter. Measurements are controlled by a PC that sends the set-points to the peripheral components and receives the measured data. At the beginning of a new measurement cycle, purging processes are necessary for the MFCs and tube cleaning, which need at least 20 min. Each measurement run proceeds in a similar way. Firstly, purging with nitrogen of variable duration is conducted before each measurement and after each concentration ramp to ensure stable experimental conditions. A normal measurement cycle includes many concentration repetitions and variations with rising and decreasing gas concentrations in order to investigate recovery effects and the reproducibility (Fig. 5.9). The duration of each concentration step depends on the sensor and the sensor properties to be measured.

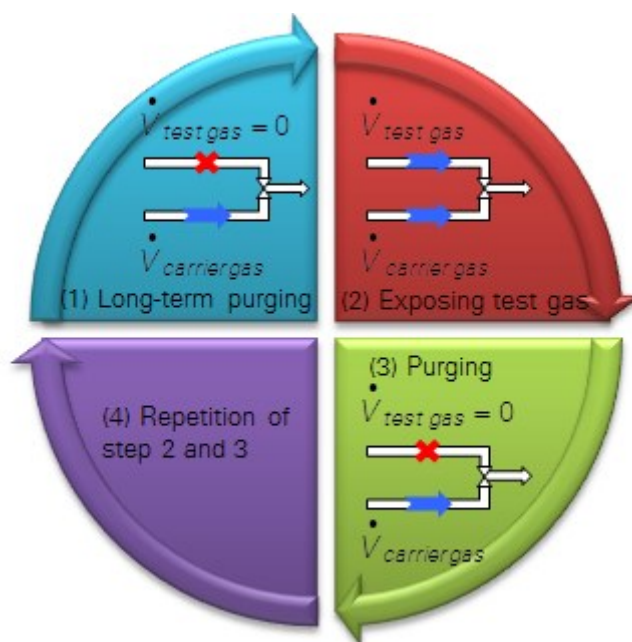


**Fig. 5.9:** Characteristic process steps of gas measurements with several measurement cycles.

## 5.5 Summary

This chapter began with an overview over the state of the art of gas measurement chambers. The subsequent elaborated requirements for such systems formed the basis for the design of the gas measurement system. The developed apparatus is composed of four parts: the gas delivery system, the gas exposure chamber, the read-out electronics, and the temperature control, which are described in detail. The advantages of the designed measurement system can be summarized as follows. Up to four sensors can be measured quasi-simultaneously. The apparatus enables the heating of the sensors and moreover the sensors are heated uniformly over the entire surface. As a result a temperature gradient is avoided. The gas flow is uniform over all sensors. A low dead volume of the chamber (approximately  $0.8 \text{ cm}^3$ ) ensures a fast gas exchange. The back diffusion of gases in the chamber is prevented by a long pipe used for the gas outlet. The sensor installation and removal is easily performed, because the system can move in a horizontal position and through the spring contact pins no material integrated bond is necessary. The system is suitable for low gas concentrations, as a diffusion of the gas in the environment is prevented through the stainless steel construction. The last part of this chapter discussed the realization of the concentration variation, which is achieved via the flow rate adjustment of the test gas, whereas the carrier gas flow remains constant. This is implemented through MFCs. The established gas measurement protocol shows that purging and several measurement cycles are necessary to study the behavior of the sensors.



## 6 Characterization of Silicon Nanowire based Sensors

Silicon nanowires are unique candidates for the fabrication of gas sensing devices due to their high surface-to-volume ratio, well wettability and chemisorption properties as well as established growth techniques, biocompatibility and controllable physical and electrical properties [274]. Here, the performance of SiNW based devices for the detection of ammonia is investigated. At the beginning, the fabricated devices are electrical characterized. Subsequently, requirements on gas sensors are defined, which hereinafter serve as basis for conducted measurements. For that, the most important sensor characteristics are selected with respect to the application area and the current status of research. The investigated sensors can be classified into devices based on silicon nanowires with a native oxide shell and those with a thermally grown oxide layer. Firstly, the sensing behavior of native oxide shell SiNW sensors is studied towards ammonia under the following aspects: drift, response and recovery time, repeatability, calibration curve, limit of detection, effect of humidity, influence of temperature, selectivity, sensor-to-sensor reproducibility, and long-term stability. Secondly, investigations on devices with thermally grown oxide shell SiNWs are carried out including  $\text{NH}_3$  detection measurements as well as relative humidity and temperature variations. Finally, the results of the two types of sensors are compared and summarized in order to derive possible future research activities.

### 6.1 Electrical Characterization of the Sensors

Before gas measurements were carried out, the electrical properties of the fabricated SiNW based FETs were measured in ambient air. The measurements were conducted at the tip-probe station described in section 3.2. Measuring needles of tungsten were used for contacting and applying the drain-source voltage  $V_{DS}$  to the substrates, which could be positioned with micropositioners. The needles and the electrically contactable sample holder (chuck) were connected by triaxial cables with a measuring system from Keithley (2604B SourceMeter). The chips were vacuum force fitted to the chuck, which was used to regulate the back gate potential  $V_G$  during measurements. The measuring needles were connected to the source and drain contact pads of the sensors for measurements.

The substrates were degenerately doped (p/boron  $< 0.005 \text{ } \Omega\text{cm}$ ) to minimize the space charge region under the back gate oxide and resulting serial capacitance. The 400 nm thermal  $\text{SiO}_2$  layer acted as gate dielectric. All sensors were used as back gate (G) devices with

an electrode distance of 6  $\mu\text{m}$ , which was found out in a previous work to show best results [240]. Such a sensor with source (S)-drain (D)-contacts is schematically illustrated in Fig. 6.1.

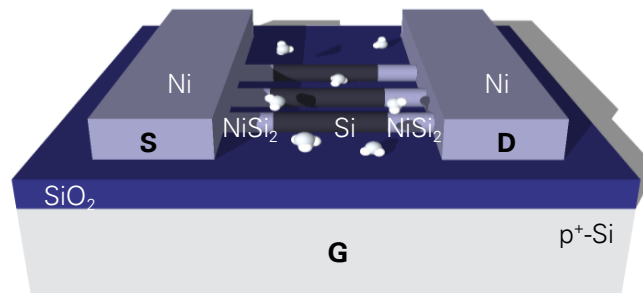


**Fig. 6.1:** Schematic representation of a nanowire sensor with nickel silicide contacts.

To determine the electrical characteristics, the measurement of the transfer characteristic was performed. In a transistor, the electric field can be generated by applying a voltage across an active region between the source and drain electrode, whereby a directed charge carrier motion and thus a drain-source current  $I_{DS}$  is created. Due to the influence of a gate potential to the channel region, the electric field can be varied along the channel direction, thereby changing the current density. By keeping the voltage between the source and drain electrode constant, in this way the current flow between the contacts is changed. In a transistor, this correlation is described by the transfer characteristic. With the dependence of the current flow between source and drain electrode on the gate voltage, as  $I_{DS} = f(V_G)$ , this represents the most important characteristic for the characterization of a FET. Fig. 6.2 shows the transfer characteristic ( $I_{DS}-V_G$ ) at  $V_{DS} = 0.25$  V in semi logarithmic representation of a nanowire transistor with back gate. Voltages were always applied in step functions and corresponding gate currents were recorded during measurements. The drain-source current was measured by sweeping the back gate voltage from -20 V to 20 V and back to -20 V. The course of the characteristic curves is illustrated by arrows.

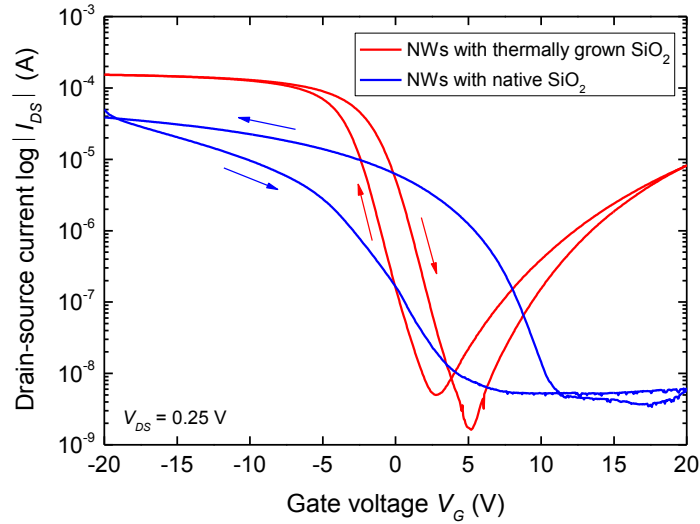


**Fig. 6.2:** Transfer characteristics of typical SiNW based sensors (recorded for  $V_{DS} = 0.25$  V). Source-drain current  $I_{DS}$  versus gate voltage  $V_g$  of thermally grown oxide shell nanowire parallel array devices on 400 nm  $\text{SiO}_2$  back gate oxide (red) and nanowire parallel arrays with native oxide on 400 nm  $\text{SiO}_2$  back gate oxide (blue). The course of the curve is indicated by arrows.

First, the transfer characteristic of the device based on nanowires with a native  $\text{SiO}_2$  shell is discussed. The characteristic curve shows hysteresis. The reason of this hysteresis is the presence of charge carrier traps on the wire surface, in the native oxide, and at the Si / oxide interface. While the drain-source current increases for negative voltages, it is not incremented for positive voltages. Thus, the sensor exhibits unipolar p-type behavior. This is typically for intrinsic nanowires with a native oxide shell as already observed for single nanowire devices [255].

The characteristic curve of the device with thermally grown  $\text{SiO}_2$  shell nanowires shows an ambipolar behavior. For the current transport both electrons and holes are thus involved. The higher current level at negative gate voltages is mainly due to a lower barrier height for holes with  $\varphi_{B,p} = 0.46$  eV compared to  $\varphi_{B,n} = 0.66$  eV in the contact of  $\text{NiSi}_2$  with Si [275], resulting in higher thermionic and tunneling currents according to the charge carrier transport through the Schottky barriers (see section 2.5.2).

Gate-source current ( $I_g$ ), equivalent to gate leakage current, was also measured as shown in Fig. 6.3. Gate leakage currents were in the order of  $10^{-10}$  A for NWs with a native  $\text{SiO}_2$  shell and  $10^{-9}$  A for NWs with a thermally grown  $\text{SiO}_2$  shell, respectively. From these results, it was verified that  $I_{DS}$  of the FETs is controllable using the back gate at a gate voltage below 20 V.

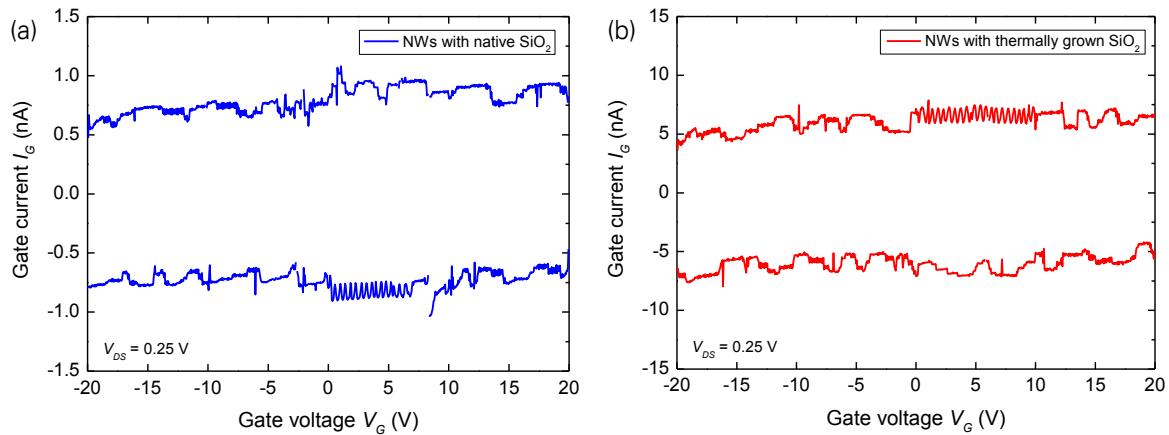


**Fig. 6.3:** Gate current  $I_G$  in dependence of gate voltage  $V_G$  for devices based on (a) NWs with a native  $\text{SiO}_2$  shell and (b) NWs with a thermally grown  $\text{SiO}_2$  shell.

## 6.2 Sensor Requirements and Typical Diagrams of Gas Sensing

A gas sensor must meet certain requirements in order to determine its quality. Those requirements are very differentiated. The wide variety of applications (see also section 2.6.2), according to the respective conditions of use, requires solutions tailored to the measuring task. Gas detectors for industrial use as security products have to fulfill further requirements in addition to the legal requirements (explosion protection, electromagnetic compatibility) so that even under harsh conditions the sensor quality and the reliability is ensured. Table 6.1 gives an overview of requirements that determine the quality of a sensor. Aspects highlighted in green are relevant for the sensors studied in this work. The subsequent analysis is based on these requirements, which are explained in the respective evaluation paragraph. The most important sensor properties were discussed in detail in section 2.3.

The listed requirements describe both the static and the dynamic behavior of a sensor. The static behavior shows the relationship between the input variable and the output variable in the steady state. The dynamic behavior describes the relationship between an input variable change and the output variable change as a function of time. Most of the mentioned characteristics are static: limit of detection, linearity, measurement range dynamics, precision, sensitivity, accuracy, repeatability, reproducibility, resolution, cross sensitivity, air pressure, selectivity, temperature, humidity, contamination, hysteresis, overflow, but there are also dynamic properties that are investigated within this work: drift (span, zero), response time, recovery time, warm-up period, and lifetime.

**Table 6.1:** Requirements on gas sensors.

<b>Sensor quality</b>	<b>Requirements</b>
Use	Continuous/ discontinuous measurement, analyte diversity, multi gas measurement, matrix
Qualitative measurement	Molecule identification, identification of functional groups
Quantitative measurement	Limit of detection, linearity, measurement range dynamics, precision, sensitivity, accuracy, drift (span, zero), repeatability, reproducibility
Measuring time	Response time, recovery time, warm-up period
Operation	Maintenance, calibration, haptics, handling, cleaning
On-site measurement	Size, weight, energy demand, auxiliary material
Safety	Damage protection, irradiation, hygiene, material
Robustness	Wind speed, light, chemical/mechanical stability, electromagnetic radiation, dust, salt test, temperature, splash water
Reliability	Resolution, cross sensitivity, air pressure, selectivity, temperature, humidity, contamination, hysteresis, overflow, lifetime
Protectability (IP)	Licenses, exclusive market rights
Integrability	Size, interface, energy demand, auxiliary material
Costs	Purchase price, operating costs, usage costs, recycling

IP: intellectual property

In order to analyze the different sensor characteristics, experiments must be conducted that examine both types of behaviors and appropriate diagrams have to be recorded. Therefore, different types of charts are used in this work. Fig. 6.4 shows the two modes in which the sensors were operated. In order to get a first impression of the sensing behavior, the resistance change of the devices under  $\text{NH}_3$  exposure was determined by applying a constant voltage and measuring the current (Fig. 6.4a and b). Additionally, the samples were operated as FETs, so the sensing mechanism could be examined in more detail (Fig. 6.4c–e). Diagrams, where the drain-source current in dependence of the gate voltage is shown, allow conclusions on the static sensor behavior, whereas the threshold voltage shift versus time diagrams were used for dynamic sensor investigations.

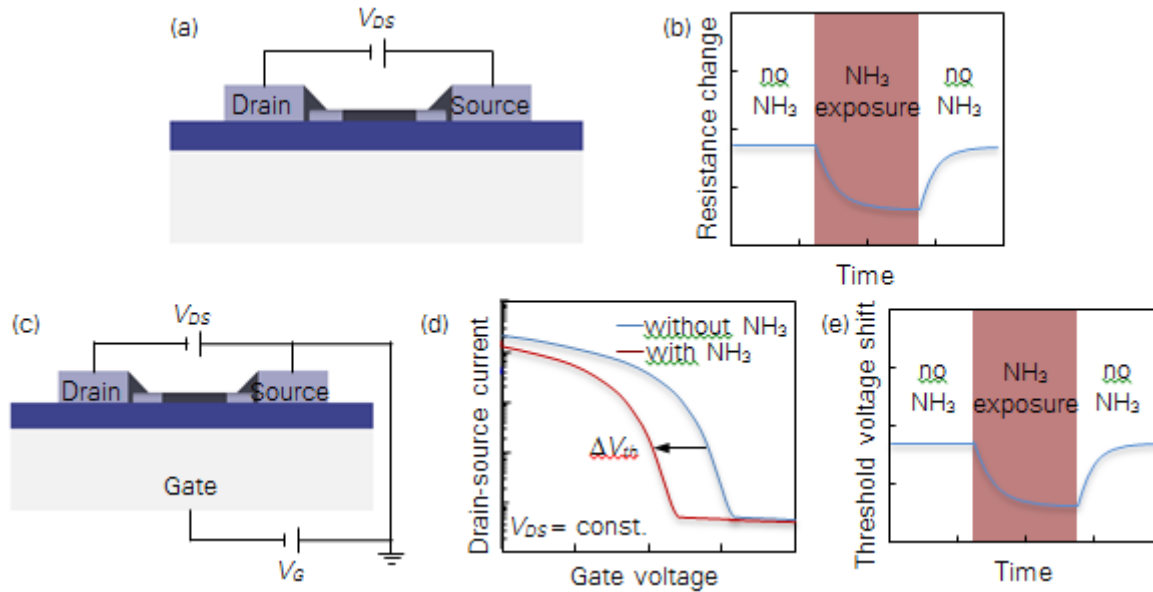


**Fig. 6.4:** Operating principles for SiNW based gas sensors and recorded sensor signals. (a) Electrical circuit for measuring the sensor resistance. (b)  $\Delta R/R_0-t$  diagram for measuring the resistance change under  $\text{NH}_3$  exposure. (c) Electrical circuit for driving the nanowire FET. (d)  $I_{DS}-V_G$  diagram for observing the influences of  $\text{NH}_3$  on the transfer characteristic (static sensor behavior). (e)  $\Delta V_{th}-t$  diagram for investigating the changes of the threshold voltage  $V_{th}$  under  $\text{NH}_3$  exposure (dynamic sensor behavior).

### 6.3 Resistance Response of the Devices towards Ammonia

The sensing performances of native oxide SiNWs based resistors were evaluated by applying a constant voltage of 0.1 V across the electrodes and monitoring the change in current upon exposure to  $\text{NH}_3$  using a Keithley 2602. Resistance values were then reported as function of time for devices under exposure to  $\text{NH}_3$ . The sensing response  $\Delta R/R_0$  (%) was calculated by observing the normalized difference in current before ( $I_0$ ) and after ( $I$ ) the exposure to the analyte:  $\Delta R/R_0$  (%) =  $[(I - I_0) / I_0] \times 100$ . The measurements were carried out at room temperature. The devices were put inside the chamber through which the gas flowed, as shown in Fig. 5.1. Prior to measurements, the influence of flow rate variations on the sensor signal was investigated (Fig. 6.5a). This was necessary, because small changes of the total flow rate could not be avoided when  $\text{NH}_3$  was introduced to the carrier gas flow. In order to find out if these flow rate differences affect the signal, the resistance response in dependence of the flow rate variation of  $\text{N}_2$  was recorded. For that the total flow rate was changed by 2, 1, and 0.2 l/min for 60 s followed by 60 s recovery under a constant flow of  $\text{N}_2$  for five times. Each response represents the average change in resistance from one device for five repetitions (Fig. 6.5b). With an increasing change of the flow rate the response increased. This is attributed to the corresponding temperature change of the sensor environment, which affects the signal, see section 6.5.6. For the minimum flow variation of 0.2 l/min a mean value of the response of just 0.007 % was determined. The maximum total

flow rate variation in this work was 0.01 l/min for a  $\text{NH}_3$  concentration of 50 ppm. This value was more than one order of magnitude lower than the minimum flow rate change of 0.2 l/min proving that the flow rate variation under exposure to  $\text{NH}_3$  had no influence on the sensor signal.

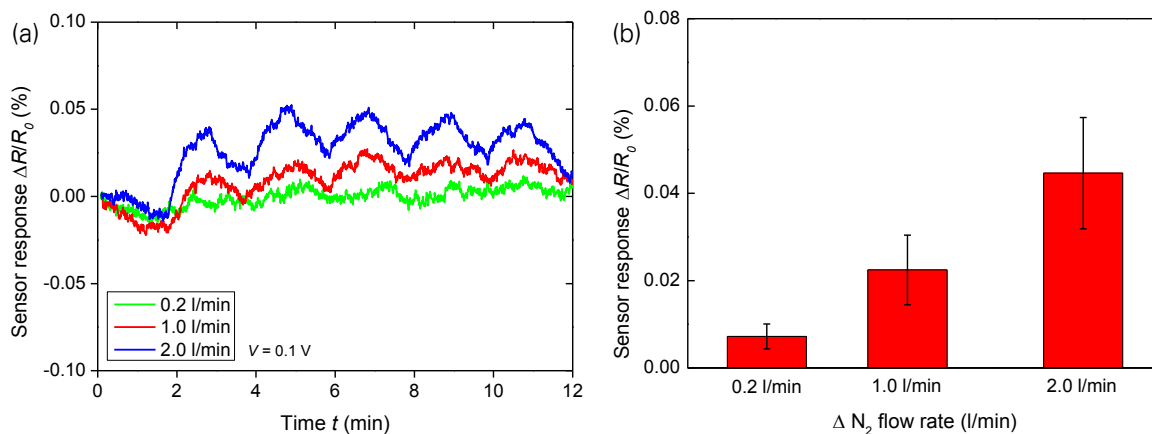


**Fig. 6.5:** Response towards  $\text{N}_2$  flow rate change of 2, 1, and 0.2 l/min. (a) Change in resistance with time of a device to which flow rate variations were applied. (b) Quantitative comparison of the sensor response towards flow rate changes. Vertical error bars represent standard deviation from the mean value based on five cycles.

All sensors were exposed to different  $\text{NH}_3$  concentrations of 20, 10, 5, 2.5, 1, and 0.5 ppm diluted by  $\text{N}_2$  for 90 s followed by 210 s recovery under a constant flow of  $\text{N}_2$ . This was done five times for each concentration, respectively. The concentrations of  $\text{NH}_3$  for this experiment were chosen to be sufficiently high to obtain a measurable response from the SiNW devices. The sensing responses of these resistors to  $\text{NH}_3$  exposure are presented in function of time in Fig. 6.6a. For each  $\text{NH}_3$  concentration sensing response values of four different devices are summed up in Fig. 6.6b. The electrical resistance decreased under  $\text{NH}_3$  exposure and with increasing concentrations this effect increased.

Upon exposure to  $\text{NH}_3$  cycling tests, time dependence change of the electrical resistance is found to indicate a quasi-reversible trend. The resistance decreases, because  $\text{NH}_3$  species act as donor of electrons at the SiNWs surface [20]. The adsorbed  $\text{NH}_3$  molecules transfer electrons to the SiNWs crystal core. This induces significant changes in the carriers transport along the NWs and thus in the electrical resistance of the SiNWs. It is known that the SiNWs conductance can be modulated by an applied voltage [20]. Positively charged gas molecules (electron donors) bound to the SiNWs surface can modulate their conductance by changing the volume of the conductive layer. In this case,  $\text{NH}_3$  may act as chemical gate. This means that the Fermi level of the SiNWs is shifted reducing the sample electrical re-

sistance. In order to investigate the  $\text{NH}_3$  sensing mechanism of the SiNW based sensors in more detail, the devices were operated in the following as FETs.

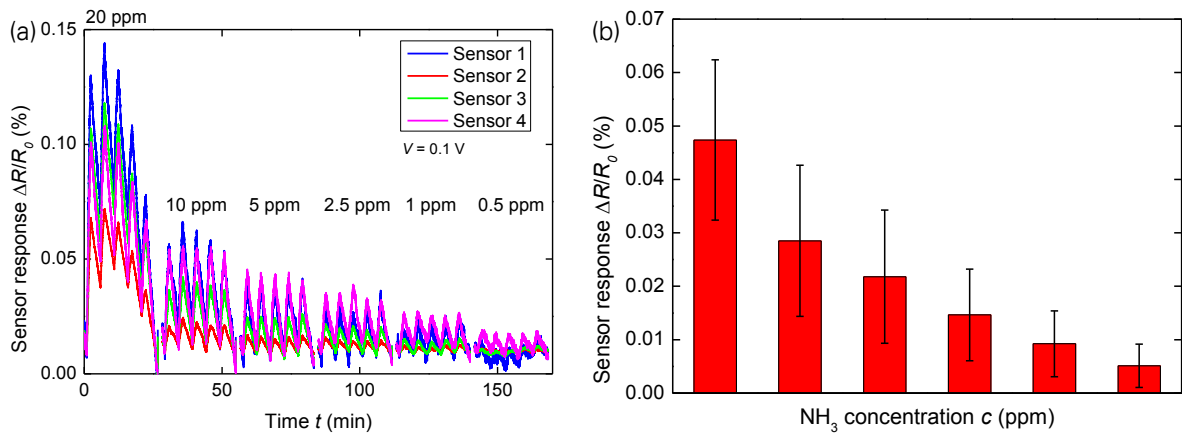


**Fig. 6.6:** Sensing response of SiNW based resistors to 20, 10, 5, 2.5, 1, and 0.5 ppm  $\text{NH}_3$ . (a) Resistance variations versus time under  $\text{NH}_3$  exposure for concentrations from 20–0.5 ppm and five cycles for each concentration. (b) Average responses from four different devices each.

#### 6.4 Measurements at the Drägerwerk AG & Co. KGaA

The designed measurement system did not allow operating the SiNW based sensors as FETs. This was however required to find out more about the detection mechanism and the influence of  $\text{NH}_3$  on the sensor. Thus, a measuring apparatus of the Drägerwerk AG & Co. KGaA in Lübeck was used. This setup additionally enabled measurements with varied humidity and temperature conditions as well as interference measurements. The structure of the system is schematically shown in Fig. 6.7. The read-out electronics included a Keithley and a computer with a custom made program implemented in MATLAB as introduced in section 5.3.3. Instead of nitrogen as carrier gas, dried ambient air was used with a composition as shown in Fig. 1.2 making the measurements closer to reality. Ammonium carbonate ( $(\text{NH}_4)_2\text{CO}_3$ ) was placed within a permeation tube and heated up to 50 °C inside a permeation chamber. Ammonia was released according to the following reactive formula:



The present concentration was determined by a Chip Measurement System (CMS, Dräger), which was connected to the three-way valve before the gas outlet. The total flow to the sensor consisted of two flows (moistened air and dry air flow), when the sensor was not exposed to  $\text{NH}_3$ , and three flows (moistened air, dry air, and  $\text{NH}_3$  containing dry air) when the sensor was exposed to  $\text{NH}_3$ . Each flow rate was regulated by a MFC. The total flow rate was



always kept constant by reducing the flow rate of the dry air flow by a certain value, when the  $\text{NH}_3$  containing flow was supplied with same flow rate. This ensured that the sensor signal was not influenced by flow variations. The flow including  $\text{NH}_3$  from the permeation chamber to the sensor was always kept constant at 200 ml/min.  $\text{NH}_3$  concentrations were changed by adjusting the flow rate of the total flow. After applying another total flow rate, the signal had to become stable again before measurements were conducted. For a concentration of 680 ppb  $\text{NH}_3$ , the total flow was 1000 ml/min. The relative humidity (RH) level was varied by the ratio between the volumetric humid carrier gas flow and total flow. The humid carrier gas was saturated with water vapor in a glass bubbler, which was temperature regulated. Through a Dew Master chilled mirror hygrometer (Edgetech Instruments), the relative humidity was controlled. Temperature changes were realized through the furnace, which had an integrated temperature control.

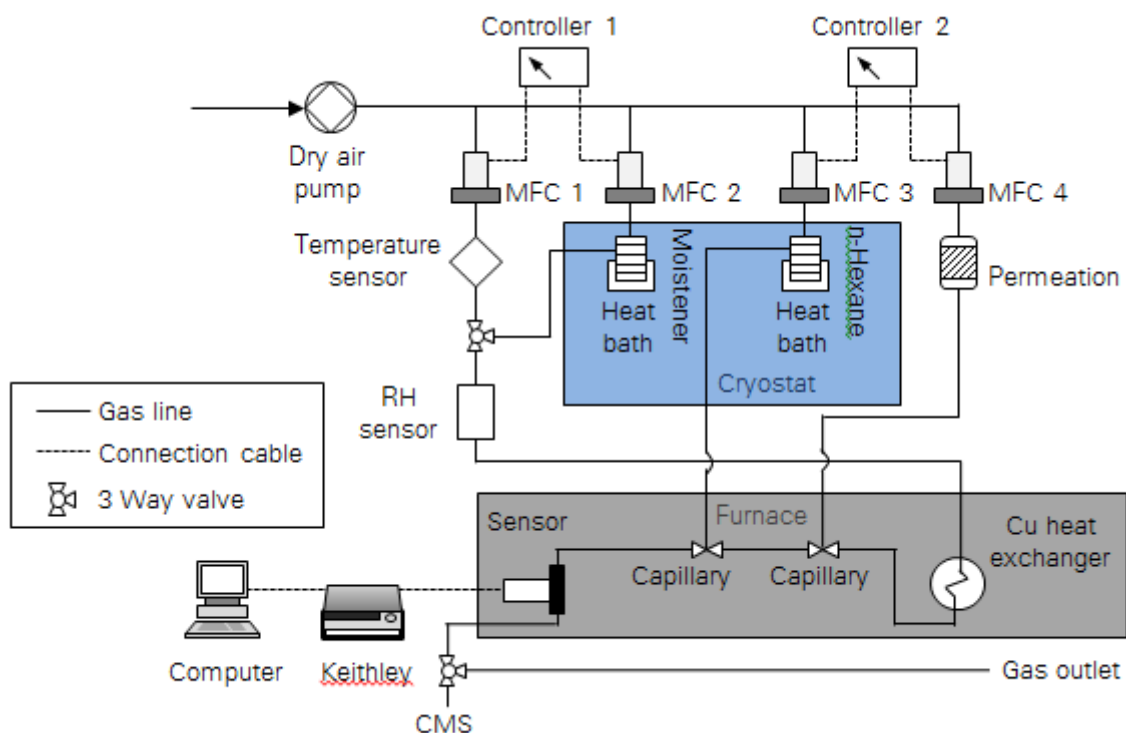


**Fig. 6.7:** Schematic structure of the measuring apparatus at the Drägerwerk AG & Co. KGaA.

The chips were mounted into the furnace by means of a specially constructed device, which is depicted in Fig. 6.8. So, the same sensor design as presented in section 4.3 could be used and only the blank zone had to be removed. The cylinder with a diameter of 2 cm served as the sample holder and was made of poly(methyl methacrylate) (PMMA). Via three contact pins, which were connected with BNC cables to the Keithley, the electrical contacting of the

sensors was carried out. To ensure a good electrical connection, the contact pins were additionally glued to the substrate by conductive silver lacquer.

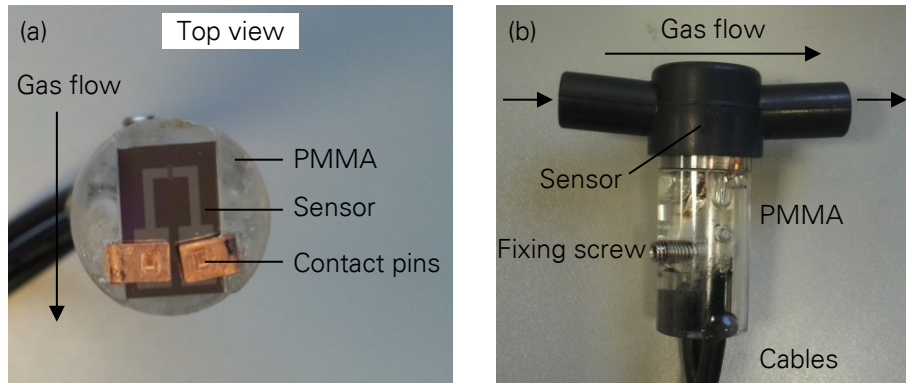


**Fig. 6.8:** PMMA adapter and sample holder (a) Top view of the sensor inside the sample holder. (b) Side view of the PMMA adapter connected to the component through which the gas flow took place.

## 6.5 Gas Sensing Performance of Native Oxide Shell Silicon Nanowires

A FET based structure with back gate was used to evaluate the sensing performance of SiNWs with a native grown oxide shell. Layer-by-layer growth of native oxide occurred on the SiNWs surface in air, which produced a rough native oxide film surface with a thickness of around 1 nm [162, 257]. The  $I_{DS}-V_G$  characteristics and hysteresis of the devices was investigated under the influence of ammonia. The drain-source current was measured at  $V_{DS} = 0.25$  V by sweeping  $V_G$  from -4 to +4 V at a controlled temperature of 25 °C and a relative humidity of 17.5 %, if not stated otherwise. The gate voltage was swept from 0 V to +4 V to -4 V and back to 0 V. The concentration of  $\text{NH}_3$  was kept constant at 680 ppb except for investigations of the limit of detection and calibration curve, where a variation of the concentration was required.

The threshold voltage shift  $\Delta V_{th}$ , as the measured quantity, is defined as sensor signal. The change of  $V_{th}$  allows getting information about the dynamic sensor behavior over a specific period of time. If the curves are shifted on the gate voltage axis, the shape of the graphs can be assumed to be equal. The shift  $I_{DS}(V_G, t_i)$  and  $I_{DS}(V_G, t_j)$  can be found by fitting the mean squared displacement of the shifted curves  $\text{MSD}_{ij}(\Delta) = \langle [I_{DS}(V_G, t_j) - I_{DS}(V_G, t_i)]^2 \rangle$  using a parabolic function [276]. The minimum of the fitted function determines the shift of the threshold voltage between the curves,  $\Delta V_{th}$ . The hysteresis is defined as  $V_{th,up} - V_{th,down}$ , where  $V_{th,up}$  is  $V_{th}$  in the gate voltage range from -4 V to +4 V and  $V_{th,down}$  is  $V_{th}$  in the gate voltage range from +4 V to -4 V.

### 6.5.1 Drift Investigation

Sensor drift is often referred to as currently the most challenging problem in gas sensing [277, 278]. This phenomenon is one of the most serious impairments of the application of electronic noses. Drift is an undesired change in output that is not a function of the measurement and over a specified time with fixed input and operation conditions. It can be classified into two types: zero drift and span drift. The signal level may vary from its starting value (zero value) when the sensor works. This is referred to as zero drift. Thus, it introduces an error into the measurement equal to the amount of variation. Zero drift may result from changes of temperature, electronics stabilizing, and aging of the transducer or electronic components. Span drift refers to degradation of sensor output over time with respect to a continuous, constant concentration of target gas.

#### Zero drift

Zero drift was determined by exposing the sensor only to the carrier gas without  $\text{NH}_3$ , which was dry air, and measuring the threshold voltage drift  $\Delta V_{th}$  for 3 h.  $V_{th}$  drift was recorded by applying a constant drain-source voltage of 0.25 V and a gate voltage of  $-4 - +4$  V.  $I_{DS}$  was continuously recorded. It was observed that the threshold voltage is continuously shifted towards positive  $V_G$ . The signal drift value was measured to be 23 mV/h in average, which is consistent with drift values of other silicon nanowire based sensors [279].  $V_{th}$  drift is stable for a continuous flow of dry air as can be seen in Fig. 6.9.

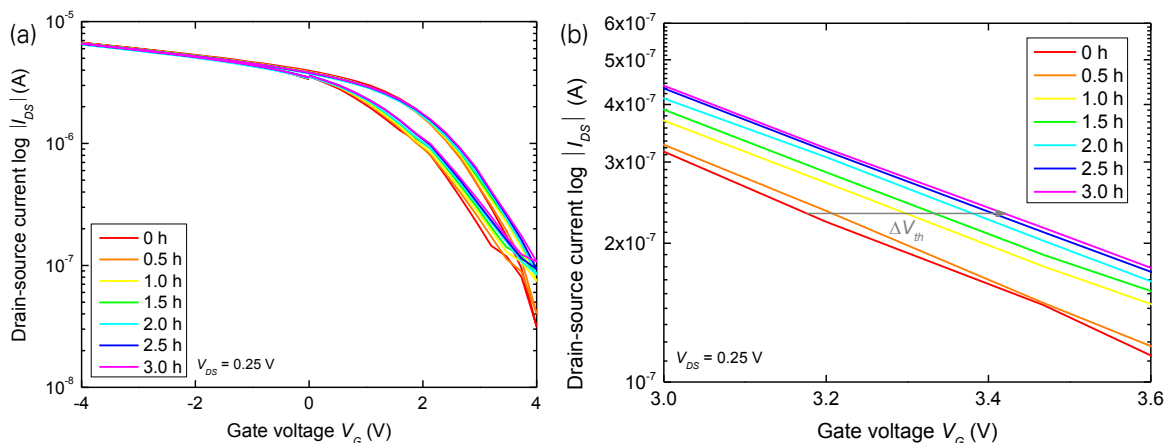


**Fig. 6.9:** Threshold voltage drift over a period of 3 h. (a) Drain-source current in dependence of the gate voltage in the range of  $-4 - +4$  V. The curves are shifted to positive  $V_G$  over time and the hysteresis does not change. (b) Magnified detail of the  $V_G-I_{DS}$  curves in the range of 3.0–3.6 V. For reasons of clarity the  $I_{DS,up}$  and  $I_{DS,down}$  values were averaged. The grey arrow indicates the shift direction of  $V_{th}$ .

It is difficult to identify the cause of drift, which could be either a surface, a bulk effect, or both. The phenomenon can be caused by local heating of the sensor element and surrounding air at the surface due to power dissipation. The temperature dependency of the devices will be discussed in section 6.5.6 and supports this assumption. Several further mechanisms for the drifting phenomenon have been proposed in the literature, like slow surface effects, such as hydration of the  $\text{SiO}_2$  surface [280], variation of the surface state density at the Si /  $\text{SiO}_2$  interface [281], surface exchange reaction and chemical diffusion of oxygen leading to changes in oxygen defect concentration [282], and field-induced migration, which appears due to changes in the space charge potential upon gas adsorption. This causes the charged oxygen vacancies to redistribute in the space charge region and thus affect the conductivity [283].

#### *Span drift*

Span drift was investigated after the sensor response reached saturation during exposure to a continuous, constant concentration of  $\text{NH}_3$ . It was observed that the signal shows the same drift behavior as for zero drift.

### **6.5.2 Response and Recovery Time**

The response time  $\tau_{90}$  is defined as the time required for the signal to reach 90 % of the equilibrium value after  $\text{NH}_3$  was injected. The recovery time is the time interval over which the sensor signal reduces to a certain percentage of the saturation value when the sensor is exposed to a specific concentration of  $\text{NH}_3$  and then purged with dry air. In this work for all investigations related to  $\text{NH}_3$  a recovery time referred to as  $\tau_{50}$  is used, which means that the signal recovers to 50 % of the reached saturation value upon  $\text{NH}_3$ . The reason is that the recovery time of the sensors after  $\text{NH}_3$  exposure was very long. For all other analyses, which comprise humidity and temperature studies without  $\text{NH}_3$  influence, a recovery time referred to  $\tau_{10}$  is used, which means that the signal reduces to 10 % of the response. This was enabled through the much faster recovery after those interfering influences. So the results remain comparable.

To determine the response and recovery time, a sensor based on undoped SiNWs was exposed to 680 ppb  $\text{NH}_3$  at room temperature with a relative humidity of 17.5 % and its threshold voltage shift  $\Delta V_{th}$  as a function of time was recorded and is shown in Fig. 6.10a. The response and recovery time of the sensing response towards other  $\text{NH}_3$  concentrations are shown in section 6.5.4. When a sensor was exposed to  $\text{NH}_3$ , the threshold voltage ab-

ruptly decreased and then slowly reached a relatively stable value. The response time of the devices upon exposure to  $\text{NH}_3$  was around 44 min. When the gas flow was switched to air, the threshold voltage promptly increased and very slowly reached a relatively stable value. It is assumed that the signal recovers completely, which can be seen in Fig. 6.11a. The recovery time of the sensor with  $\text{NH}_3$  was about 73 min. This suggests slow molecular desorption from the nanowire sample and that the sensor can be reversibly used. The results are comparable to other published response and recovery times of SiNW based  $\text{NH}_3$  sensors, where a recovery time of 5 h was reported [19]. For sensors based on Te-modified SiNWs much shorter response and recovery times are demonstrated in the literature with 5 and 8 s, respectively [27].

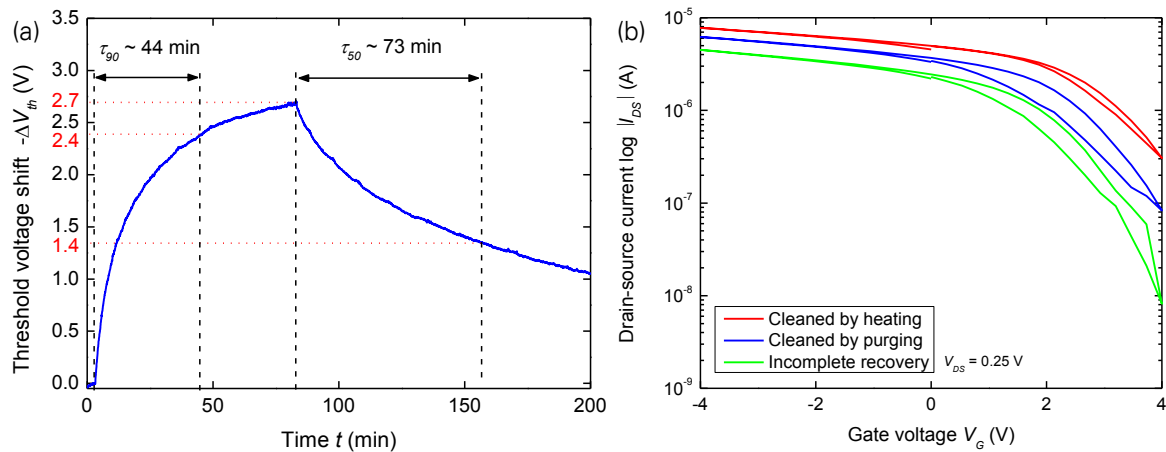


**Fig. 6.10:** Response and recovery time of the sensors for different  $\text{NH}_3$  concentrations. (a) Exemplary determination of the response and recovery time of a sensor with a  $\text{NH}_3$  exposure of 680 ppb. (b)  $V_G$ – $I_{DS}$  characteristics after  $\text{NH}_3$  exposure with an incomplete recovery in comparison to the curves after purging with air for 15 h and after heating at 60 °C for 30 min.

The slow response time of the sensor can be attributed to the hydrogen bond between  $\text{NH}_3$  and the SiNW surface (section 2.5.4) [21, 161]. Due to the long response and recovery period, a strong hydrogen bond is assumed. This type of bond is an electrostatic dipole-dipole interaction, which is directional. Therefore, molecules must be positioned at a certain angle to each other, so that an interaction between the gas molecules and the surface occurs. The probability that the molecules impinge at the correct angle is small. This explains the long response time. The strong bonding between  $\text{NH}_3$  molecules and the SiNWs requires a long time to desorb and it causes the slow recovery of the SiNW based sensor. The interaction time  $\tau$  of given species strongly depends on the interaction energy between the gaseous molecule and the surface material via

$$\tau = \tau_0 e^{\frac{Q}{RT}} \quad (6.2)$$

with  $R$  being the universal gas constant,  $T$  the temperature, and  $\tau_0$  a constant. This formula is referred to as Frenkel equation.

As known, chemical sensing at room temperature is hardly reversible, because the thermal energy is usually lower than the activation energy for desorption. This leads to a long recovery time, which can be seen from Fig. 6.10a, where the threshold voltage of the sensor after the exposure to  $\text{NH}_3$  does not recover (or it takes several hours) to the initial value due to the presence of adsorbed gas molecules on the surface of silicon nanowires. The dependence of the interaction of gas-solid type is usually analyzed as function of temperature, since the interaction time is strongly depending on this parameter, see equation (6.2). That is why, the heating of the sensor was tested to desorb the gas species from the surface. The sensor was placed inside a furnace (Fig. 6.7) and therefore could be heated easily. However, according to previous experiments, it was required to avoid operating the sensors at elevated temperatures ( $\geq 60^\circ\text{C}$ ), since the electrical contacting was not designed for that. When the sensor was heated up to  $60^\circ\text{C}$ , the signal became very noisy. This was attributed to the different thermal expansion coefficients of the used materials. The contact pins were made of copper, where a piece of silver was attached. This was connected to the nickel electrodes by silver conductive paint (Fig. 6.8). Thus, the heating of the sensor was carried out without electrical connection. To avoid the destruction of the electrics inside the furnace, the sensors were only heated up to  $60^\circ\text{C}$ .

Fig. 6.10b shows three different  $I_{DS}-V_G$  curves after exposure to  $\text{NH}_3$  with a concentration of 680 ppb for 80 min. The green one was recorded after 2 h of purging with dry air. The blue graph was measured after purging the sensor overnight and the red curve illustrates the drain-source current after heating up the sensor at  $60^\circ\text{C}$  for 30 min. A comparison of the three  $I_{DS}-V_G$  curves shows that the curve after heating of the sensor is most shifted to a positive voltage and the hysteresis is reduced compared to the signals without heating. The drastically reduction of the hysteresis by heating is discussed in detail in section 6.5.6. Thus, subsequent heating up the exposed sample in air to a temperature of  $60^\circ\text{C}$  for 30 min led to a full recovery of the signal and the recovery time can be reduced by several hours.

The adsorption or desorption rate of gas molecules on solid surface can be expressed as follows [284]:

$$r_a = K f(\theta) \exp\left(-\frac{E_a}{RT}\right), \quad (6.3)$$

$$r_d = K' f'(\theta) \exp\left(-\frac{E_d}{RT}\right), \quad (6.4)$$

where  $r_a$  and  $r_d$  are the rate of adsorption and desorption, respectively;  $K$  and  $K'$  are the adsorption or desorption rate constant, respectively;  $\theta$  is the fraction of the surface occupancy; and  $E_a$  and  $E_d$  are the activation energy of adsorption and desorption, respectively.  $f(\theta)$  is a function related to the surface vacancy ( $1-\theta$ ).  $f'(\theta)$  on the other hand is a function of the surface occupancy ( $\theta$ ). Based on the above equations,  $r_a$  increases with a higher gaseous pressure and fraction of the surface vacancy and reduces with increasing adsorption activation energy.  $r_d$  increases with an increase of the temperature and an increase of the fraction of the surface covered, whereas it reduces with increasing desorption activation energy. As a result, heating is favorable for desorption, thus enhancing the recovery of the sensors.

The response and recovery time of the SiNW based sensors were very long at room temperature and a relative humidity of 17.5 %. A long response time until a saturation value is reached and long recovery period needed after each  $\text{NH}_3$  exposure are not practical for some sensing devices like e-noses, and severely restricts their usage in applications where the gas concentrations may change rapidly or a fast signal is required, like for disease diagnosis or gas alarm in occupational health and safety applications. It was shown that the recovery time can be enhanced by heating the sensor, but this required additional power consumption, which is particularly adversely in small and portable devices, where no space for a large battery exists and a low weight is essential.

The response and recovery time with and without exposure to  $\text{NH}_3$  are not only influenced by the temperature, but also by the relative humidity in the ambient environment. This is discussed in detail in sections 6.5.5 and 6.5.6. Another common method to enhance the response and recovery time of nanowire based sensors is to implement a UV irradiation procedure to facilitate desorption of gas species on the surface. It was reported in the literature that the recovery time of UV radiated nanosensors is much shorter than that of nonradiated sensors [285]. This can be explained by equation (6.4). Irradiation with UV light reduces the desorption activation energy, which is plausible for recovery of the gas sensors. Fan et al. demonstrated the refresh of nanowire  $\text{NH}_3$  sensors using a large gate voltage [286]. The minimum gate "refresh" voltage was determined to be concentration dependent. For instance, the "refresh" voltage for 1 %  $\text{NH}_3$  is -30 V for a pulse duration of 60 s. However, the concrete recovery times are not reported. The two additional described approaches for faster signal recovery were not pursued in this work.

### 6.5.3 Repeatability

Repeatability is the sensor's ability to exhibit the same response for successive measurements of the same gas at a consistent concentration, when all operating and environmental conditions remain constant. Fig. 6.11 shows the sensor repeatability characteristic curves in  $\text{NH}_3$ . Three measurements at room temperature with a  $\text{NH}_3$  concentration of 680 ppb and a relative humidity of 17.5 % were carried out. The sensor was exposed for 80 min and the recovery was recorded for 2 h. The first measurement started from the baseline, which is referred to as ① air in Fig. 6.11a. After signal saturation the curve named ② 680 ppb  $\text{NH}_3$  was measured. The  $I_{DS}-V_G$  characteristics of the recovery after 2 h (③) is also depicted. The second measurement began immediately after the 2 h recovery of the first measurement. It can be seen that after the 80 min of  $\text{NH}_3$  exposure, the graph is very close to the curve of the first measurement. The third measurement was conducted after the full recovery of the signal. For this, the sensor was purged overnight with dry air. The respective graphs are very close to the previous ones, i.e. the sensor has a good repeatability (Fig. 6.11a).

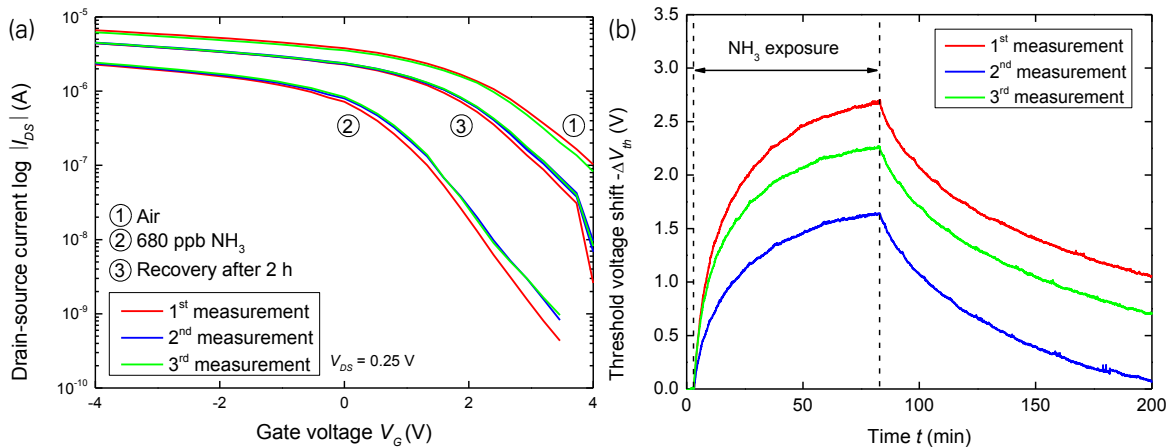


**Fig. 6.11:** Sensor repeatability. (a) Output characteristics of a SiNW based sensor before, during and after 680 ppb  $\text{NH}_3$  exposure. (b)  $\Delta V_{th}$  over time of the measurements in (a).

The threshold voltage shift versus time is shown in Fig. 6.11b. The lower sensing response of the second measurement compared to the other two measurements is attributed to the incomplete recovery of the sensor after the first exposure to  $\text{NH}_3$ . To compare the maximum signal change, the  $V_{th}$  value of the first measurement at 200 s has to be added, since this is the missing recovery.

Repeatability is determined by calculating the standard deviation of the three consecutive averaging sensing responses. A standard deviation of  $\pm 0.25$  V is determined, which corresponds to a repeatability of around  $\pm 10$  % for a mean value of  $\Delta V_{th} = -2.55$  V (Fig. 6.12a).



This is a good value for concentrations in the ppb range. A repeatability of  $\pm 30\%$  is permitted for measurements of hazardous workplace atmospheres according to TRGS 402 and DIN EN 482. For response  $\tau_{90}$  and recovery time  $\tau_{50}$ , values of  $44 \text{ min} \pm 0.01 \text{ min}$  and  $66 \text{ min} \pm 10 \text{ min}$  were determined, respectively (Fig. 6.12b and c). For this, only the values of the first and third measurement were used.

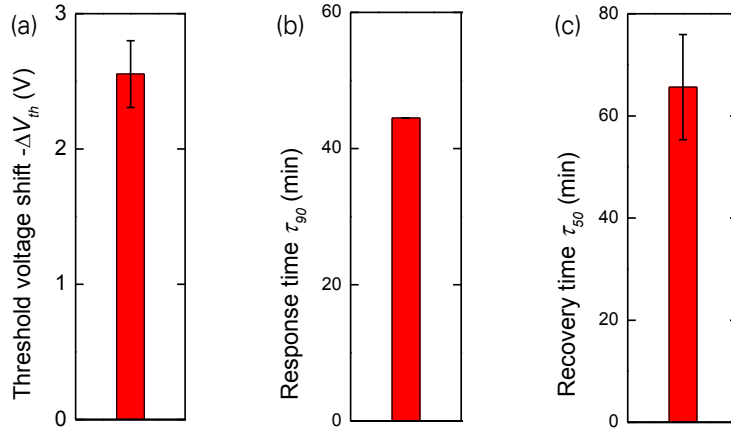


**Fig. 6.12:** Sensor repeatability determined from three consecutive measurements of 680 ppb  $\text{NH}_3$ . (a) Repeatability of the threshold voltage shift. (b) Repeatability of the response time, which is very high, so that no error bar is visible. (c) Repeatability of the recovery time.

#### 6.5.4 Calibration Curve and Limit of Detection

A sequence of  $\text{NH}_3$  exposures of the SiNW based sensor is shown in Fig. 6.13. The diagram of  $\Delta V_{th}$  over time can be found in Fig. A.1 in the appendix. During the exposures to  $\text{NH}_3$  in the concentration range from 680 ppb to 170 ppb, the relative humidity and the temperature were kept constant at 57 % and 25 °C, respectively. The higher relative humidity was chosen, because it is closer to reality and the response time is faster (see section 6.5.5). However, it should be noted that the signal intensity decreases with increasing relative humidity and that with a lower relative humidity even higher sensor responses can be achieved. This effect is investigated and analyzed in section 6.5.5. It was found that the response of the sensor was 165 % when exposing to 170 ppb  $\text{NH}_3$ .

The measured  $I_{DS}-V_G$  characteristics in Fig. 6.13 shows that in the case of  $\text{NH}_3$  the  $I_{DS}$  value at -4 V and 4 V in  $V_G$  were  $4.44 \cdot 10^{-4} \text{ A}$  and  $2.63 \cdot 10^{-4} \text{ A}$ , respectively, whereas  $3.37 \cdot 10^{-4} \text{ A}$  and  $2.56 \cdot 10^{-4} \text{ A}$  in 680 ppb of  $\text{NH}_3$ . As the concentration increased, the drain-source current decreased in lower voltage than the  $V_G$  for the minimum value of the  $I_{DS}$ . In other words, the unipolar  $I_{DS}-V_G$  curve shifted negatively. Moreover, another effect was observed. The  $I_{DS}-V_G$  graph additionally decreased over the entire voltage range according to the concentration increase of  $\text{NH}_3$ .

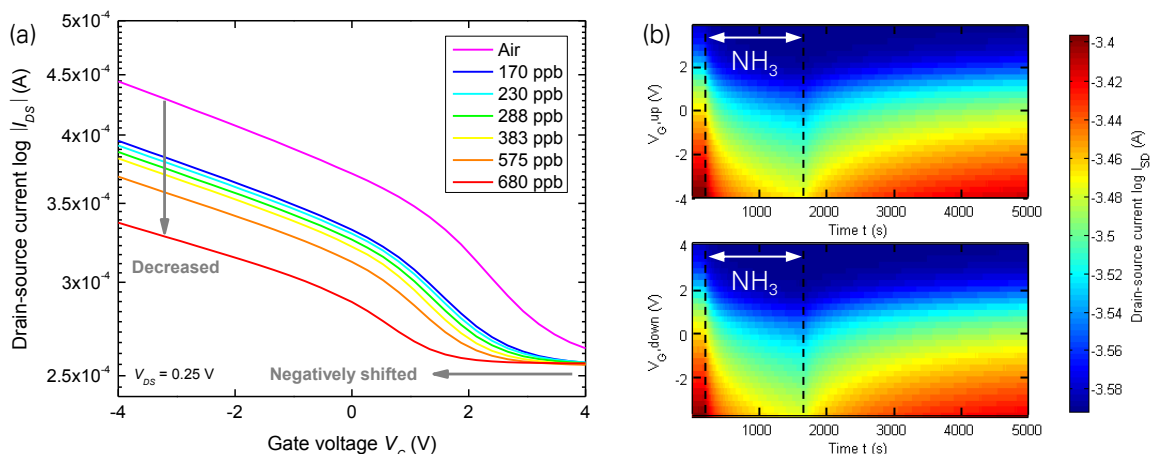


**Fig. 6.13:** Change of the  $I_{DS}-V_G$  characteristics under exposure to different  $\text{NH}_3$  concentrations at 57 % RH and 25 °C. (a)  $I_{DS}-V_G$  characteristics in various concentrations of  $\text{NH}_3$ . With higher concentrations, the transfer characteristic is negatively shifted and decreased indicated by arrows. (b) Drain-source currents for a  $\text{NH}_3$  concentration of 680 ppb in a gate sweep measurement as a function of gate voltage and time.

The negative shift caused by  $\text{NH}_3$  gas can be attributed to changes in the presence of charge carrier traps. Charge can be captured during device operation. This phenomenon is referred to as charge trapping and may shift  $V_{th}$  permanently or for a limited period. The common types of charge traps comprise  $\text{SiO}_2/\text{Si}$  interface trapped charges due to the interruption of the periodic Si lattice structure and oxide-trapped space charge associated with defects in  $\text{SiO}_2$  [287]. Charge traps due to water are reported in section 6.5.5 and in literature for MOSFETs without passivation [288]. Charge can be injected into localized energy states via tunneling or thermally. The occupation/vacation rate of trap states depends on the tunneling distance and the activation energy [289]. Charge can be trapped either deeply in the oxide, which is often not easily released and exhibits a large retention time, or directly at the Si /  $\text{SiO}_2$  interface, where charge carriers are easily trapped and released making this trapping reversible. Latter are called interface trap charges and can reduce device performance. Their impact on  $V_{th}$  is large, since they are close to the conduction channel.

In the absence of  $\text{NH}_3$ , traps are filled by electrons from SiNWs. The electron transfer from the NWs into the oxide traps leads to a depletion of mobile electrons at the surface of SiNWs. As shown in Fig. 6.2, the sensor based on NWs with a native oxide shell exhibits unipolar p-type behavior, which leads to a hole enhancement in the NW and the energy band at the Si /  $\text{SiO}_2$  interface bends upwards (Fig. 2.13b). Upon adsorption of  $\text{NH}_3$  an electron is donated to the system. This is due to the Lewis structure of  $\text{NH}_3$ , which shows an electron lone pair [162]. Thus, an additional way of providing electrons is established. Consequently, electrons are donated from the  $\text{NH}_3$  molecules rather than from the Si surface resulting in a decrease of the energy band bending at the Si /  $\text{SiO}_2$  interface (Fig. 2.13b). For the p-type

transfer characteristics this indicates that  $\text{NH}_3$  molecules transfer negative charge to SiNWs leading to the negative shift of  $\Delta V_{th}$  (Fig. 6.13a).

It was already mentioned that the reason of hysteresis is the presence of charge carrier traps and that those are affected by  $\text{NH}_3$  adsorption. This can be clearly seen in Fig. 6.14a, where exemplary hysteresis curves as function of time are plotted under influence of three different  $\text{NH}_3$  concentrations. When  $\text{NH}_3$  was turned on and thus adsorbed on the SiNW surface, an abrupt increase in hysteresis took place. Such a sudden change in hysteresis also appeared, when  $\text{NH}_3$  was switched off. Fig. 6.14b shows that the magnitude of hysteresis change for all six measured  $\text{NH}_3$  concentrations between 680 and 170 ppb, when  $\text{NH}_3$  was turned on and off. With increasing concentration, the change of the hysteresis increased (except the values for 680 ppb  $\text{NH}_3$ ). This change happened very quickly within a few seconds, so that this results in a completely new possibility of fast  $\text{NH}_3$  detection by measuring the change in hysteresis. However, for a  $\text{NH}_3$  concentration of 170 ppb the limit of detection was almost reached, so that this method would be less sensitive compared to measuring the threshold voltage shift.

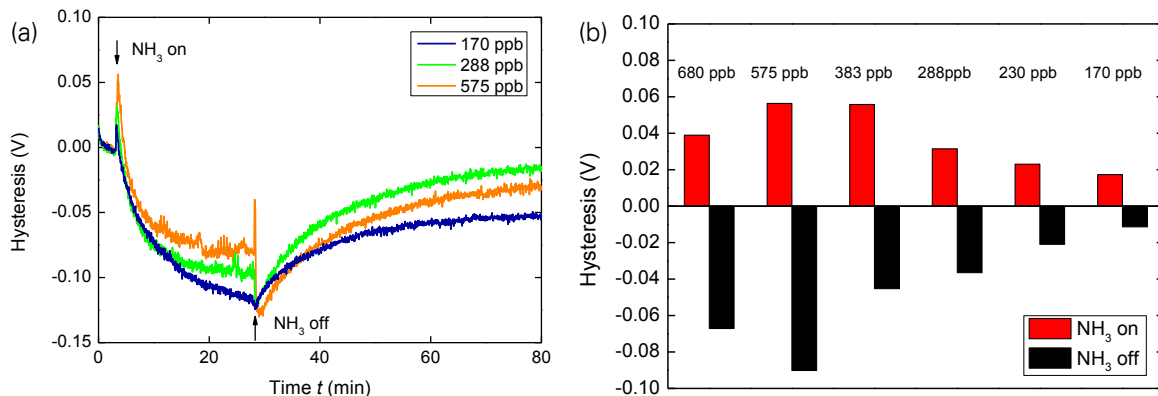


**Fig. 6.14:** Influence of  $\text{NH}_3$  on the hysteresis of the signal. (a) Hysteresis of the signal as function of time for 170, 288, and 575 ppb  $\text{NH}_3$ . For reasons of clarity only three curves are shown. (b) Magnitude of the hysteresis change when  $\text{NH}_3$  is turned on and off for all measured  $\text{NH}_3$  concentrations in the range of 680–170 ppb.

It has to be considered that the change in hysteresis over time, except the jumps, was low and was also affected by other influences, since the entire sensor characteristic changed and not just a shift of the  $I_{DS}-V_G$  graph occurred. The decrease in  $I_{DS}$  over the entire voltage range caused by  $\text{NH}_3$  is shown in Fig. 6.13a and denotes that not only oxide-trapped space charge but also interface traps are influenced since the  $I_{DS}-V_G$  curve became flatter. Plots of the drain-source current versus gate voltage  $V_G$  and time  $t$  during the course of a 680 ppb  $\text{NH}_3$  sensing experiment are demonstrated in Fig. 6.13b. In order to visualize the modulation of the current upon  $\text{NH}_3$  and gate voltage changes, color mapping of the recorded signal was

employed. In this diagram, the change of the entire sensor characteristic and not only shift of  $\Delta V_{th}$  may very well be recognized by the fact that if two different courses of drain-source current over time are compared (e.g.  $I_{DS} = 3.52$  A (light blue) and  $I_{DS} = 3.47$  A (yellow)), those are not only shifted, but also the signal shape changes. This can be particularly well observed during the period when the sensor was exposed to  $\text{NH}_3$ .

The relationship between the  $\text{NH}_3$  concentration and  $\Delta V_{th}$  is referred to as calibration curve and is shown in Fig. 6.15b. This was determined on the basis of the collected data upon exposure to  $\text{NH}_3$  at different concentrations, such as those presented in Fig. 6.13. It was not possible to apply concentrations below 170 ppb. In order to obtain the threshold voltage shift values for these sub ppb concentrations, a fit of the measured data was carried out by using a logarithmic function ( $y = a \ln(x) + b$ ). The fit parameters are  $a = -0.7161$  and  $b = 2.0864$ . Therefore the equation relating the  $\text{NH}_3$  concentration to the sensor response is:  $\Delta V_{th} = -0.7161 \ln(x) + 2.0864$ , where  $x$  is the  $\text{NH}_3$  concentration expressed in ppb units. With this fit, the signal of the concentrations below the 170 ppb level down to the limit of detection (LOD) can be evaluated. Thus, the equation allows finding the  $\text{NH}_3$  concentration corresponding to a threshold voltage variation of  $\Delta V_{th} = 3\sigma$ , where  $\sigma$  is the standard deviation and represents noise fluctuations. This  $\text{NH}_3$  value is consistently referred to as LOD. The detection limit for solid-state gas sensors is usually defined as the minimal concentration that causes a signal exceeding the sensors' intrinsic noise [290], see also section 2.3.2. Indeed, according to the equation  $3\sigma = -0.7161 \ln(\text{LOD}) + 2.0864$ , by assuming a typical fluctuation  $\sigma = 0.002$  V (Fig. 6.15a), the detection limit is approximately 20 ppb. This is illustrated by a red square in Fig. 6.15b.

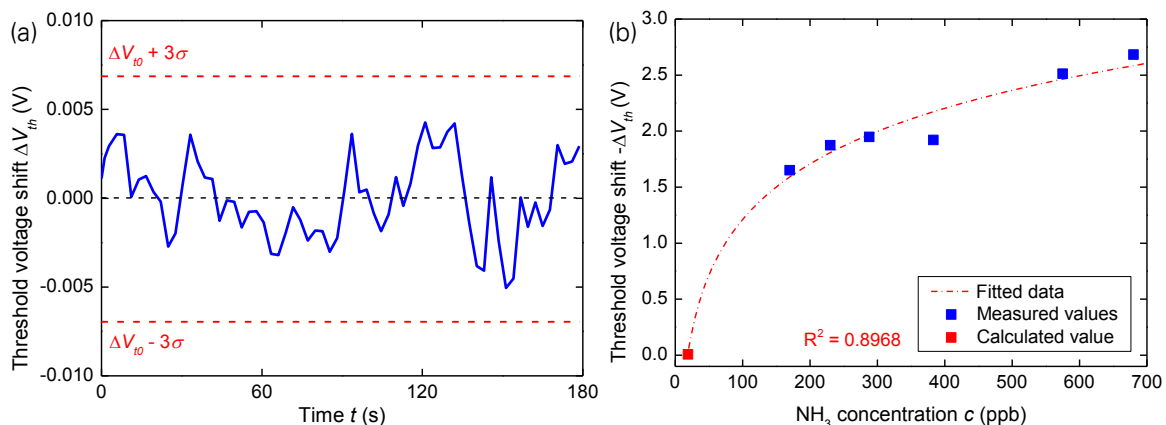


**Fig. 6.15:** Calibration curve of the SiNW based  $\text{NH}_3$  sensor. (a) Noise of the sensor. (b)  $\Delta V_{th}$  in dependence of the  $\text{NH}_3$  concentration. A higher threshold voltage shift occurs with higher  $\text{NH}_3$  concentrations. The dot-dash line is the fit of the measured values.

A detection of 500 ppb  $\text{NH}_3$  diluted in clean air was reported for top-down fabricated vertically aligned SiNWs, while the measurement of a concentration of 10 ppm  $\text{NH}_3$  in air was achieved with bottom-up grown tellurium-modified SiNWs [24, 27]. To the best of the author's knowledge, the present results demonstrate the lowest  $\text{NH}_3$  concentration so far measured in air with a sensor based on SiNWs. The data also shows that lower detection limits can be expected by doping or functionalization of the SiNWs to enhance the amount of OH-groups on the nanowire surface for more interactions in the form of hydrogen bonds between  $\text{NH}_3$  and the SiNW surface.

Due to the small variations of the tested  $\text{NH}_3$  concentrations, the standard deviation was determined for a concentration of 575 ppb for two measurements. The coefficient of variance between different measurements was  $2.23 \text{ V} \pm 0.25 \text{ V}$ . Response times for different concentrations were also determined and are shown in Fig. A.2a in the appendix. It can be seen that the response time slightly increased with increasing concentrations. Owing to the very long recovery time of the sensor, the recovery time was calculated after 50 % of the signal intensity was reached (Fig. A.2b). The recovery time remained approximately constant in dependence of the concentration. However, the coefficients of determination are very low and thus further investigations on response and recovery time have to be done in order to determine the exact correlation between those times and the  $\text{NH}_3$  concentration.

### 6.5.5 Effect of Humidity

Moisture is present in various concentrations in most surroundings. Therefore, the influence of humidity on the sensor response is crucial to know. The sensor was installed in the chamber and the relative humidity was varied, whereas the temperature was kept constant at 25 °C. Sweeping of  $V_G$  was changed for subsequent measurements from -4→+4 to -2→+4, because no change in the  $I_{DS}$ - $V_G$  characteristic occurred for  $V_G < -2$ . This behavior was caused by the low quality of native oxide on the nanowire surface. SiNWs with a natively grown oxide shell have a bad dielectric layer between the gate dielectric and Si channel including charge trapping sites and possible water incorporations. This deficient dielectric layer possesses a serial capacitance degrading the oxide capacitance and gate coupling [240]. The transfer characteristic is shifted to the right (positive  $V_G$ ), on/off ratio is low, and n-conduction cannot be reached (Fig. 6.9a). This charge trapping related hysteresis is discussed in detail in the following and in section 6.5.6.

Dry air was used as carrier gas. The humidity-controlled air was prepared by varying the mixing ratio of a dry air and water-saturated air, which was prepared by bubbling the air through

water. A constant total flow of 1000 ml/min was ensured and RH was at 17.5, 34.5, 52.5, and 69.5 %, respectively. During the measurement, no  $\text{NH}_3$  was introduced to the chamber. The temperature in the furnace was stabilized at 25 °C. As an illustration, Fig. 6.16 displays the effects of changing humidity. Similar to many gas sensors, the SiNW based gas sensor also responded to humidity [291].

The influence of the relative humidity to the transfer characteristics of SiNWs is shown in Fig. 6.16a. The  $I_{DS}-V_G$  curve shifts were examined during the stabilization of the relative humidity in sensor chamber. Under a constant relative humidity,  $\text{H}_2\text{O}$  molecules were pre-sorbed in the nanowires, resulting in a negatively shift of the  $I_{DS}-V_G$  characteristic. Fig. 6.16b shows the threshold voltage shifts over time at various relative humidity. The sensor linearly responded to humidity over the range investigated 17.5–69.5 % RH at 25 °C (Fig. 6.16c). The threshold voltages were shifted from 0 to -0.19 V on increasing the relative humidity from 17.5 to 69.5 %, because  $\text{H}_2\text{O}$  molecules were absorbed by the large amount of hydroxyl groups at the surface of the SiNWs [161]. The values for the relative humidity were 17.5, 34.5, 52.5, and 69.5 % converted into absolute humidity values results in 4, 8, 12, and 16 ppm, respectively. In comparison to the applied  $\text{NH}_3$  concentrations, the  $\text{H}_2\text{O}$  concentrations were many times larger, but the sensor signal change was lower showing that the sensitivity of the sensor to  $\text{NH}_3$  was much higher than to moisture. The threshold voltage shift for the lowest applied  $\text{NH}_3$  concentration of 170 ppb was -1.7 V compared to -0.2 V for 16 ppm  $\text{H}_2\text{O}$ . Nevertheless, the humidity changes detected by the sensor are obvious. The reasons for this are capacitance changes, which can be attributed to the adsorption/desorption process of water molecules on the surface of the SiNWs [274].

The response time  $\tau_{90}$  and recovery time  $\tau_{10}$  showed a linear dependency to the relative humidity. With increasing humidity the response and recovery time decreased (Fig. 6.16c). It was observed that the response time was in the range of 55–92 s and the recovery time was 28–112 s. Consequently, the response time for humidity changes was much faster than the response time towards  $\text{NH}_3$ . So, the response time to 170 ppb  $\text{NH}_3$  was 15 min, whereas the sensor reached saturation after only 55 s for 16 ppm  $\text{H}_2\text{O}$  (34.5 % RH). A total recovery of the signal occurred after a few seconds to minutes, whereas it took several hours for the signal to recover after exposure to  $\text{NH}_3$ . The surface of SiNWs is normally covered by many Si-OH chemical bonds [292]. The existence of these hydroxyls enables the hydrophilic surface, which leads to the fast response time. It was also found that the recovery time is longer than the response time at low RH ( $\leq 52.5$  %), but vice versa at high RH (69.5 %). This characteristic was also reported in the literature and is mainly attributed to the sensing process of SiNWs [292]. The adsorption process of water molecules on a solid surface can be

classified into chemisorption and physisorption. At low RH, firstly a molecule layer adsorbs by chemisorption and with RH increasing gradually layer by layer adsorbs by physisorption. Thus, at low RH the process is dominated by chemisorption, with the result that water molecules are usually doubly bonded to two hydroxyls of the surface and cannot move freely. This leads to the longer recovery time. However, at high RH, the adsorption process is dominated by physisorption rather than chemisorption, because the van der Waals interaction leading to physisorption is much weaker than the chemical bonding interactions leading to chemisorption [293]. Consequently, the recovery time can be much shorter than the response time.

As a result, the developed SiNW based sensor has the possibility to be used as a humidity sensor. Humidity measurement and control is vital in many areas, such as manufacturing processes, automobile industry, packaging, cryogenic processes, environmental monitoring, meteorology, flood-warning systems, agriculture, medical field, and domestic applications, because of water's unique properties that greatly influences both living organisms and materials [45].

As shown in Fig. 6.16a, for SiNW based sensors exposed to the ambient environment with different RH, hysteresis appeared in the current ( $I_{DS}$ ) versus gate voltage ( $V_G$ ) characteristics (recorded under constant S/D bias  $V_{DS}$ ) when  $V_G$  was swept from 0 V to +4 V to -4 V and back to 0 V. It is known that the width of the hysteresis in  $V_G$  is dependent on the sweeping rate of the gate voltage,  $dV_G/dt$  and that the hysteresis is caused by slow charge traps that discharge on a time scale longer than several seconds [294]. This effect was not investigated within this work and the sweeping rate of  $V_G$  was kept constant. That water induces hysteresis and charging effects, was reported on all kinds of back gated nanostructure devices [294–298]. The results suggest that charge trapping by water is an important cause of the hysteresis in SiNW FETs exposed to the ambient environment besides the existence of  $\text{SiO}_2$ /Si-related charge traps (Fig. 6.16d). Native oxide is known to be porous, hygroscopic and be able to swell by water incorporation [299]. Therefore, water from the environment can diffuse into the amorphous  $\text{SiO}_2$ . It is assumed that there are two different types of water charge traps. The first one involves water molecules that are weakly adsorbed on the SiNW surface. These molecules can be easily removed by exposing to dry air. The second type includes  $\text{SiO}_2$  surface-bound water in close proximity to the nanowires. SiNW based FET was fabricated on thermally grown  $\text{SiO}_2$  substrate, which has a surface chemistry that is similar to that of silica [300]. When exposed to and stored in ambient air, the thermally grown  $\text{SiO}_2$  surface consists of Si-OH silanol groups and is hydrated by a network of water molecules that are hydrogen bonded to the silanols [300]. Due to the hydrogen bonding

among water molecules, a multilayer of surface-bound water can be present in ambient air (RH 40–50%) [294]. Native oxide shell SiNWs also have O-H bonds at the surface [161].

Fig. 6.16a shows that after exposure to dry air with 0 % RH there was still a hysteresis. This is due to a monolayer or submonolayer of hydrogen-bonded water, which remains on  $\text{SiO}_2$  and cannot be removed even by pumping in vacuum over extended periods of time at room temperature [300]. From the literature it is known that water bound to silanols on  $\text{SiO}_2$  can be removed by heating in dry environments [300]. This agrees well with the result that hysteresis was drastically reduced after heating to 60 °C in air for 30 min (Fig. 6.10b).

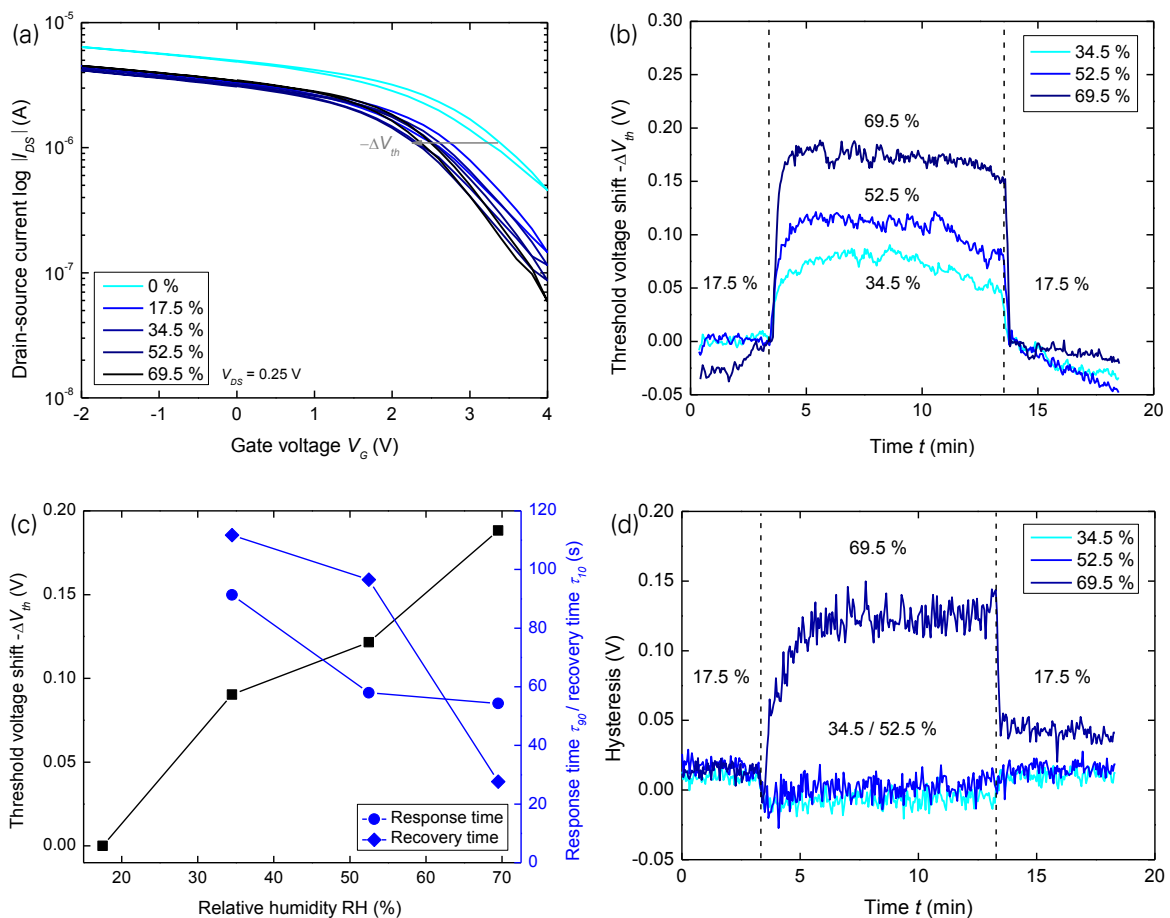


**Fig. 6.16:** Sensor response towards relative humidity changes in the range 17.5–69.5 %. (a)  $I_{DS}-V_G$  characteristics for relative humidity between 17.5 and 69.5 %. (b)  $\Delta V_{th}$  over time for 34.5, 52.5, and 69.5 % RH. (c) Threshold voltage shift, response, and recovery time in dependence of the humidity change. The lines serve as guides to the eye. (d) Hysteresis over time for 34.5, 52.5, and 69.5 % RH.

All of the described hysteresis occurrences correlate well with the  $\text{H}_2\text{O}-\text{SiO}_2$  surface chemistry. This correlation, plus the fact that water is known to act as slow charge traps (removable by annealing in dry conditions) in conventional metal oxide-semiconductor devices [301] leads to the conclusion that surface water is largely responsible for the hysteresis in the SiNW sensor.



When investigating hysteresis versus humidity for the device, it was observed that with increasing relative humidity and thus water adsorption resulted in increased hysteresis, especially for 69.9 % RH (Fig. 6.16d). This is likely due to a higher concentration of permeated  $\text{H}_2\text{O}$  molecules in the native  $\text{SiO}_2$  layer. Moreover, after changing the RH back to 17.5 %, hysteresis decreased. It is assumed that this recovery is due to detrapping of trapped electrons in the gate oxide. This effect is reported for MOSFETs and is generally more successful for p-type MOSFETs [302] than for n-type MOSFETs [303], because nMOSFET degradation is normally due to interface trap generation [304], while pMOSFET degradation is dominated by electron trapping in the gate oxide [302]. The trapped charge in the oxide can be partly detrapped, but generated interface traps are hard to remove. This is also supported by the fact that interface traps lead to a flattening of the  $I_{DS}-V_G$  characteristic, which cannot be observed (Fig. 6.16a). In summary, the increase of the hysteresis is caused by water induced charge trapping in the native oxide on the surface of SiNWs.

Through a control experiment by changing the relative humidity from 17.5 % to 0 %, it was assumed that a noticeable decrease in hysteresis takes place. Surprisingly, the hysteresis increased even though much lower than in comparison to 69.5 % RH (Fig. 6.17b). This can be due to the existence of  $\text{SiO}_2/\text{Si}$ -related charge traps [305] and the above mentioned monolayer of hydrogen-bonded water, which cannot be removed by exposing to dry air. By reducing the RH from 17.5 to 0 %, a positive threshold voltage shift occurred compared to a negative shift for increasing RH.

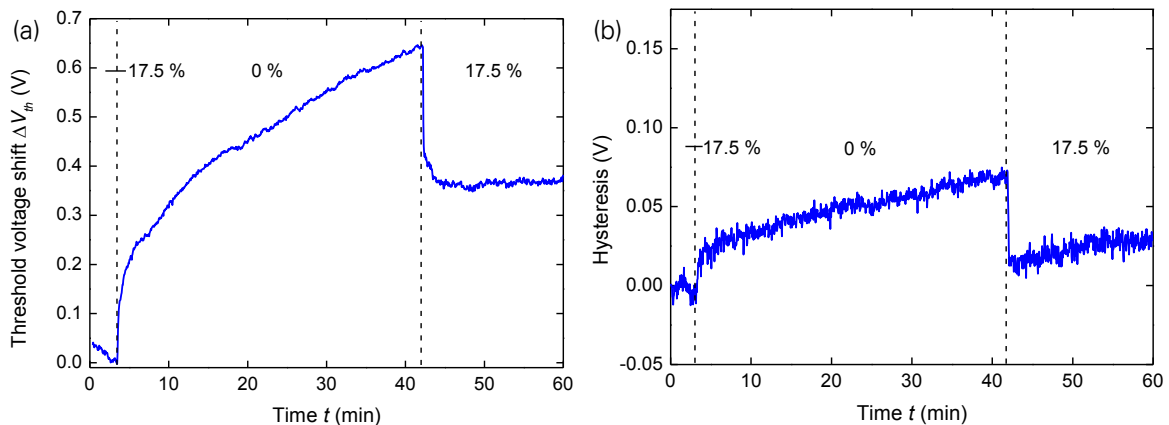


**Fig. 6.17:** Sensor response towards 0 % RH. (a)  $\Delta V_{th}$  over time for RH = 0 %. (b) Hysteresis change over time for RH = 0 %.

In the following,  $\text{NH}_3$  sensing characteristics of devices based on SiNWs with a native oxide shell in dependence of the relative humidity in the atmosphere was investigated. The influence of the relative humidity in the range of 0–52.5 % on the sensing properties towards

$\text{NH}_3$  of SiNWs is shown in Fig. 6.18. During the measurement, the concentration of  $\text{NH}_3$  was regulated at 680 ppb and the temperature remained constant at 25 °C. The flow rate of dry air had to be minimum 200 ml/min, because the gas flow with  $\text{NH}_3$  is connected to that flow with a constant flow rate of 200 ml/min. The total flow for a  $\text{NH}_3$  concentration of 680 ppb was 1000 ml/min and included also the water-saturated air flow. As already mentioned, the relative humidity was controlled by varying the mixing ratio of dry air and water-saturated air. Therefore, it was not possible to adjust a relative humidity of 69.5 % at a  $\text{NH}_3$  concentration of 680 ppb. The dry air flow would be 0 ml/min in that case. The concentration of  $\text{NH}_3$  gas in the measuring atmosphere was varied between pure air and 680 ppb by mixing  $\text{NH}_3$  and the humidity-controlled air. The  $I_{DS}-V_G$  curve shifts were examined under a constant relative humidity before introducing  $\text{NH}_3$  and after exposure to  $\text{NH}_3$ . The responses of the sensor exposed to 680 ppb of  $\text{NH}_3$  at various relative humidity are illustrated in Fig. 6.18a. The humidity had a significant effect on the performance of the sensor when detecting the low concentration of  $\text{NH}_3$ . The threshold voltage shifts stabilized at a relative humidity of 0, 17.5, 34.5, and 52.5 % and reached values of -3.0, -2.3, -1.7, and -1.4 V, respectively. The diagram with the  $\Delta V_{th}$  shift over time is shown in the appendix (Fig. A.3).

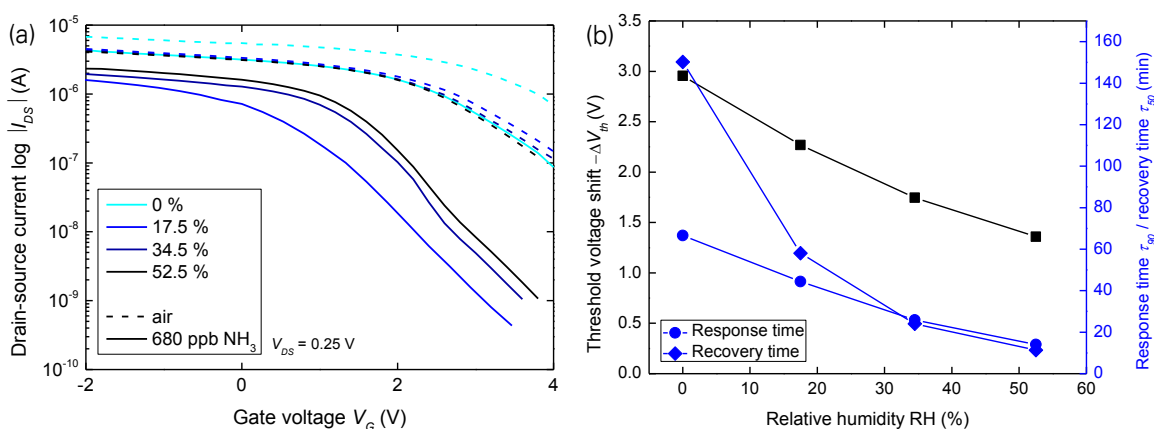


**Fig. 6.18:** Sensing responses of the SiNWs based sensor upon exposure to 680 ppb  $\text{NH}_3$  at different humidity. (a)  $I_{DS}-V_G$  characteristics for a humidity range of 0–52.5 % upon exposure to  $\text{NH}_3$ . (b) Threshold voltage shift, response, and recovery time towards  $\text{NH}_3$  in dependence of the humidity. The lines serve as guides to the eye.

It can be observed that the responses decreased with increasing the relative humidity after introducing  $\text{NH}_3$  (Fig. 6.18b). This is consistent with results found in the literature [306]. The decrease in sensitivity with increasing water vapor concentration can be explained by the reduction of the number of available sites for  $\text{NH}_3$  adsorption caused by water molecules, which decreases the  $\text{NH}_3$  dissociation rates given that the active site density has been decreased [306].

However, with a higher relative humidity the response time was reduced from 67 min at 0 % RH to 14 min at 52.5 % RH. The reason can be due to the amount of H<sub>2</sub>O molecules absorbed on hydrophilic OH-groups on nanowire surfaces were increased by increasing the relative humidity. NH<sub>3</sub> molecules are easy to be absorbed by H<sub>2</sub>O molecules. The formation of hydrogen bond between NH<sub>3</sub> and H<sub>2</sub>O molecules was confirmed by the coadsorption study of NH<sub>3</sub> and H<sub>2</sub>O [307]. Therefore, the type of bonding is changed resulting in faster response and recovery times.

Due to the linear dependency of sensing response and RH, the effect of humidity on the sensor signal can be eliminated by independently measuring humidity and performing a humidity calibration.

### 6.5.6 Influence of Temperature

A reasonable sensor operation with a stable signal baseline under ambient conditions requires that the temperature has no influence on the signal. This can be achieved in two ways. Either by keeping the operational temperature of the device constant at an elevated level above room temperature by means of an external temperature controlled heater, or by avoiding the influence of temperature to the device as much as possible. In practice, both methods are applied [308]. For the second approach it is first necessary to carry out a good comprehension of the temperature influence to the SiNW based sensor, which is done in the following.

Measurements were performed under a dry air purge and the space including the sensor inside the furnace was heated to temperatures between 25 °C and 50 °C. The threshold voltage shift over time is illustrated in Fig. 6.19b. The starting temperature (reference temperature) was 25 °C for all measurements. After a stable baseline of the signal was reached, the temperature of the furnace was increased to 30, 40, and 50 °C, respectively. This took a few seconds. After 2000 s (~33 min) the furnace was cooled down to 25 °C again, which took 5–10 min. It was observed that a linear dependency between sensor signal, response/recovery time and temperature exists (Fig. 6.19c). In contrast to the signal and sensing times towards humidity variations, with increasing temperature the sensing response increased as well as response and recovery time. The response time was between 13 and 16 min, which was higher compared to the time needed to reach a stable baseline after a humidity change, but lower than the response time towards 680 ppb NH<sub>3</sub> at 17.5 % RH.

Fig. 6.19a shows the  $I_{DS}-V_G$  characteristics of the SiNW based FET recorded at four different temperatures of 25, 30, 40 and 50 °C. With increasing temperature,  $\Delta V_{th}$  was shifted posi-

tively with a value of  $0.04 \text{ V}/^\circ\text{C}$ . This can be attributed on the one hand to the decrease in relative humidity and thus less water at the SiNW surface due to the rising temperature, which is consistent with the positive shift of  $\Delta V_{th}$  with reducing RH (Fig. 6.16a). On the other hand, with increasing temperature more charge carriers have sufficient energy to overcome the energetic barrier via thermionic emission. The increase of on current is caused by the enhanced generation of charge carriers in the semiconductor, but also from the modified Fermi distribution in the metal leading to a higher tunneling rate.

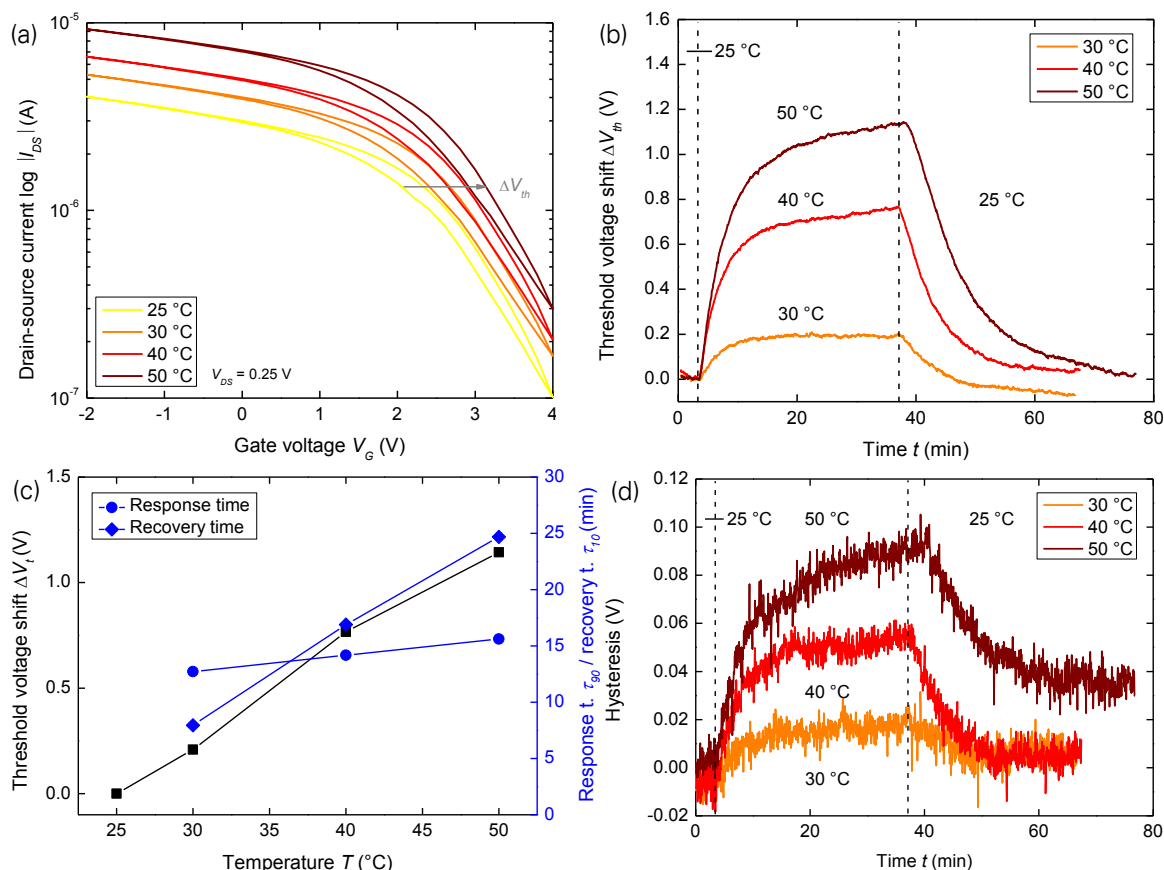


**Fig. 6.19:** Sensor response towards temperature changes in the range 30–50 °C. (a)  $I_{DS}-V_G$  characteristics for temperatures between 25 and 50 °C. (b)  $\Delta V_{th}$  over time for 30, 40, and 50 °C. (c) Threshold voltage shift, response, and recovery time in dependence of the temperature. The lines serve as guides to the eye. (d) Hysteresis over time for 30, 40, and 50 °C.

The hysteresis showed temperature dependence as well. Fig. 6.19d demonstrates that the hysteresis increased with higher temperatures. This was also reported in previous works and possible reasons were described, such as a higher probability of chemical surface reactions, increased ion mobility, or excess energy for charge carriers to tunnel into deep traps [240]. In a simplified model, it can be assumed that traps below the Fermi level are filled. According to the Fermi Dirac distribution for a higher temperature more charge carriers at high energy levels are available, which can fill traps and cause hysteresis. In Fig. 6.19a, only

a shift of the  $I_{DS}-V_G$  curve and no flattening is observed revealing that just charge trapping in the oxide occurs and no  $\text{SiO}_2/\text{Si}$  interface trapped charges.

It is well-known that temperature has an influence on the adsorption processes at the sensitive surface. Both the quantity of adsorbed species and the adsorption dynamics are affected. Thus, the sensitivity of semiconducting gas sensors is greatly dependent on the operating temperature and exhibits a peak value at a certain operating temperature. In order to obtain the optimum operating temperature, the sensitivity of the sensor was measured in the temperature range of 25–50 °C with 17.5 % RH at a fixed concentration of  $\text{NH}_3$  (680 ppb). The results are shown in Fig. 6.20. Before exposing to  $\text{NH}_3$ , the sensor was heated up to the respective temperature and then it was waited until the signal was stable, i.e. at the earliest after 16 min, which was found out to be the highest response time (Fig. 6.19c).

In general, the sensitivity of the sensor upon exposure to  $\text{NH}_3$  decreased with increasing temperature (Fig. 6.20b). This trend is consistent with previous reports on  $\text{NH}_3$  detection with SiNWs [27]. The diagram with  $\Delta V_{th}$  as a function of time is shown in the appendix (Fig. A.4). Maximum sensitivity of the sensor was found at 25 °C in the experimental range. Therefore, this optimal operating temperature was applied in all the investigations in this work.

The response time slightly decreases with increasing temperature. The recovery time was determined, when the sensor signal reduced to 50 % of the saturation value under  $\text{NH}_3$  exposure. The recovery time also decreases with higher temperatures. This is attributed to the temperature dependence of the desorption rate of gas molecules on solid surfaces, see equation 6.4. Above a temperature of 40 °C the recovery time remains approximately the same (Fig. 6.20b).

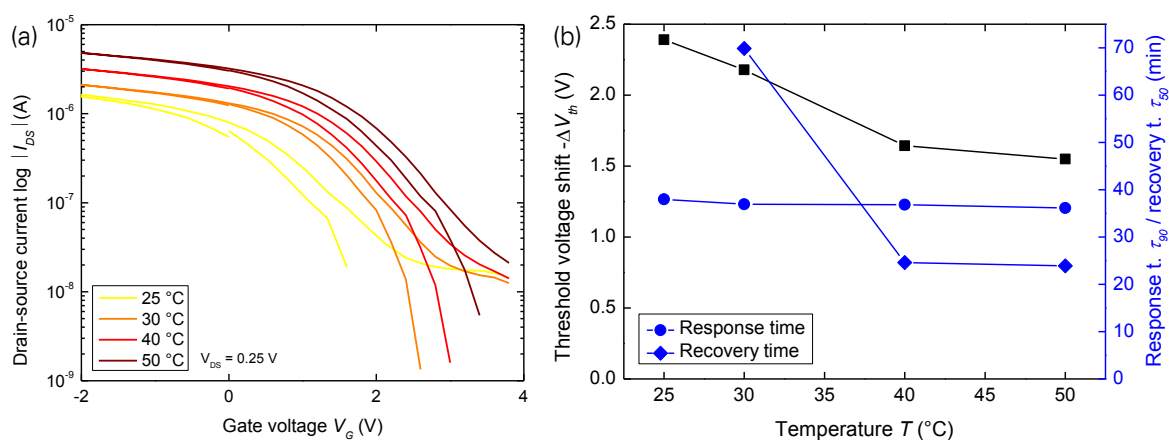


**Fig. 6.20:** Sensing responses of the SiNWs based sensor device at different temperatures upon exposure to 680 ppb  $\text{NH}_3$ . (a)  $I_{DS}-V_G$  characteristics for a temperature range of 25–50 °C upon exposure to  $\text{NH}_3$ . (b) Threshold voltage shift, response, and recovery time towards  $\text{NH}_3$  in dependence of the temperature. The lines serve as guides to the eye.

### 6.5.7 Selectivity

One of the most challenging issues for the realization of an effective gas sensor is to achieve selectivity with high sensitivity. The substances used in this work to study the selectivity of SiNW based sensors are typically found in residential environments and are representative for a number of substance classes, respectively. For the measurements six substances, namely acetone ( $C_3H_6O$ ), acetonitrile ( $C_2H_3N$ ), chloroform ( $CHCl_3$ ), ethanol ( $C_2H_6O$ ), ethyl acetate ( $C_4H_8O_2$ ), and toluene ( $C_7H_8$ ) diluted in air were applied to the sensor. These substances are the most common solvents in living areas that cannot only be found in the building substance but also in furniture, wallpaper, paint, flooring, and varnishes. The flow over the sensor was kept constant at 1000 ml/min and the exposure duration was 300 s.

In Germany, statutory occupational exposure limits (Arbeitsplatzgrenzwerte AGW) exist, which are the time-weighted average concentrations of substances in the workplace air in which an acute or chronic damage to the health of employees is not expected. These thresholds are published in the "Technische Regeln für Gefahrstoffe 900" (TRGS 900 Arbeitsplatzgrenzwerte) [309] and given for the applied substances in Table 6.2. The concentrations of the tested substances were chosen to be much higher than the allowed occupational exposure limits (Table 6.2). The corresponding response amplitudes detected at 17.5 % RH and a temperature of 25 °C are summarized in Fig. 6.21a for one specific sensor device. It can be observed that there is no correlation between the applied substances and the sensor signal. These results clearly demonstrate the high selectivity of SiNW based sensors for  $NH_3$  and, especially, ketones, nitriles, halogens, alcohols, esters, and aromatics.

**Table 6.2:** Tested substances with corresponding concentrations and occupational exposure limits.

Substance class	Representative	Concentration	Exposure limit <sup>1</sup>
Ketones	Acetone	1200 ppm	500 ppm
Nitriles	Acetonitrile	900 ppm	20 ppm
Halogens	Chloroform	2000 ppm	0.5 ppm
Alcohols	Ethanol	4000 ppm	500 ppm
Esters	Ethyl acetate	5000 ppm	400 ppm
Aromatics	Toluene	2000 ppm	50 ppm

<sup>1</sup> Values from TRGS 900 Arbeitsplatzgrenzwerte [309]

To exclude the possibility that the sensor broke before selectivity measurements were carried out, the sensor was exposed to  $NH_3$  again after those measurements. For this, a concentration of 680 ppb was used in 17.5 % RH and 25 °C for 20 min. The response was

compared to the one before selectivity measurements. The same characteristic trend and magnitude of the signal change was observed (Fig. 6.21b) with a standard deviation value of  $\pm 0.48$  V, which is consistent with the value of repeatability to 680 ppb  $\text{NH}_3$  determined in section 6.5.3 ( $\pm 0.25$  V). This confirms the assumption that the sensor was able to selectively detect  $\text{NH}_3$ .

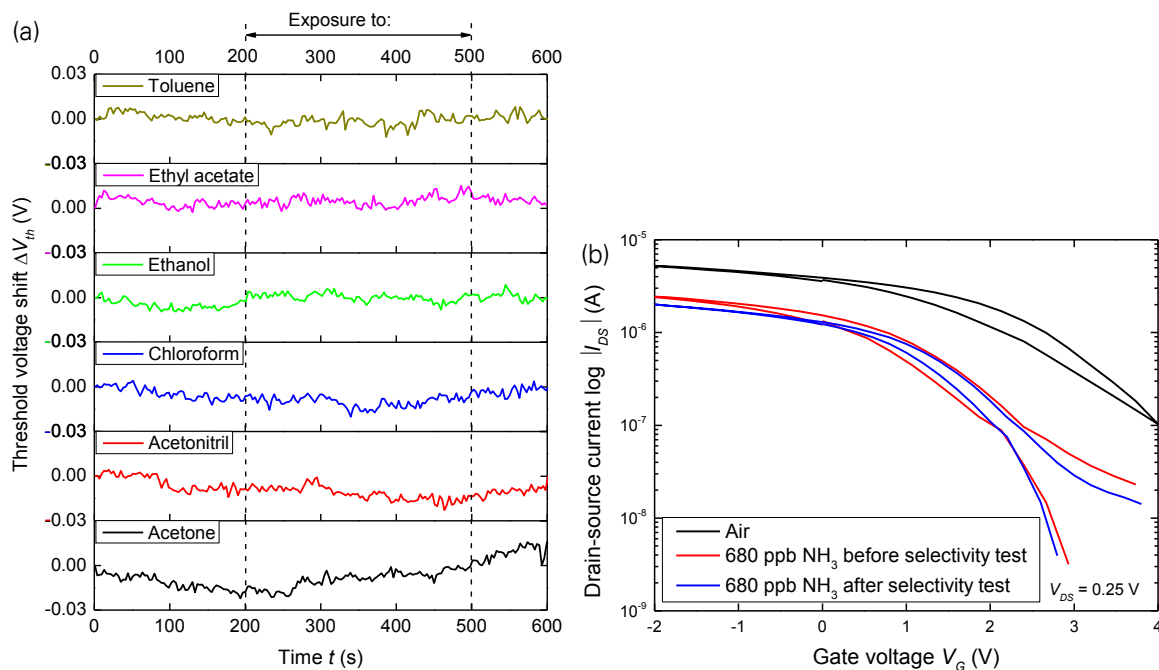


**Fig. 6.21:** Sensing properties of a SiNW sensor for various substances. (a) Comparative plots of the resulting dynamic sensing responses to six different vapors at diverse concentration levels: acetone (1200 ppm), acetonitrile (900 ppm), chloroform (2000 ppm), ethanol (4000 ppm), ethyl acetate (5000 ppm), and toluene (2000 ppm). (b) Comparison of the signal intensity before and after selectivity measurements.  $\text{NH}_3$  was still detected with the same sensitivity.

### 6.5.8 Sensor-to-Sensor Reproducibility

To test the reproducibility of measurements between different devices, three devices were exposed to 680 ppb  $\text{NH}_3$  at 17.5 % RH and 25 °C for 80 min followed by recovery of devices facilitated by purging with air for 2 h. Fig. 6.22 summarizes the results of these studies for three devices. Fig. 6.22a shows the responses of three sensors over one cycle of exposure towards  $\text{NH}_3$ . The coefficient of variance between devices was  $4.8 \text{ V} \pm 1.8 \text{ V}$  for the exposure to 680 ppb  $\text{NH}_3$ . Thus, a reproducibility of 37.5 % was determined. The average value of the response time was  $46 \text{ min} \pm 6 \text{ min}$  and for the recovery time  $265 \text{ min} \pm 168 \text{ min}$ . The recovery time was determined by exponential fitting of the recovery curve and is thus just an approximated value.

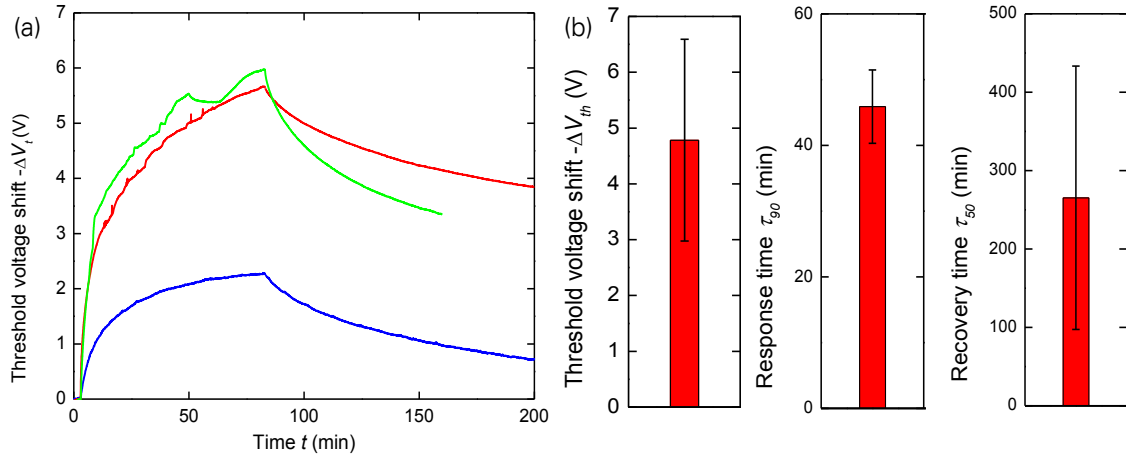


**Fig. 6.22:** Response towards  $\text{NH}_3$  gas of three SiNW based sensors prepared according to the same fabrication procedure. (a) The change in  $\Delta V_t$  in response to  $\text{NH}_3$  (exposed for 80 min) at 680 ppb. (b) Average values of response, response time, and recovery time of the three sensors. Vertical error bars represent standard deviations from the mean response, response time, or recovery time for three devices.

It was assumed that with increasing sensing response the response and recovery time are faster, because more oxygen is found on the SiNW surface and thus more binding sites. Surprisingly, this was not confirmed by the measurements. Instead the recovery time increased with increasing sensor response. The standard deviation of the sensing response of the different sensors was quite high due to the individual fabrication of the devices. The improvement of the sensor-to-sensor reproducibility can be realized technologically, e.g. by fabricating a single chip containing many devices.

### 6.5.9 Long-term Stability

Stability is the ability of a sensor to retain its performance characteristics, like sensitivity, selectivity, response, and recovery time, for a certain period of time. To speed up the investigation of the long-term stability, the gas sensor was aged in air at 60 °C for 3 days. This corresponds to approximately one year of continuous operation, which is a value of experience used of the Drägerwerk AG and can be calculated by the Arrhenius equation:

$$k = A e^{-\frac{E_A}{RT}}, \quad (6.5)$$

where  $k$  is the rate constant of a chemical reaction on the absolute temperature  $T$ ,  $A$  is the pre-exponential factor,  $E_A$  is the activation energy, and  $R$  is the universal gas constant.

At normal temperature  $T_1$  ( $T_1 = 293$  K) a chemical decomposition reaction with  $E_A$  and corresponding  $k_1$  is assumed:



$$k_1 = A e^{-\frac{E_A}{RT_1}}. \quad (6.6)$$

At an elevated temperature  $T_2$  ( $T_2 = 333$  K),  $k_2$  is accordingly:

$$k_2 = A e^{-\frac{E_A}{RT_2}}. \quad (6.7)$$

If the first Arrhenius equation (6.6) is divided by the second (6.7), the following ratio is obtained:

$$\frac{k_1}{k_2} = e^{\frac{E_A}{R} \left( \frac{1}{T_2} - \frac{1}{T_1} \right)}. \quad (6.8)$$

If an  $E_A$  of 90 kJ is assumed, a ratio of  $k_2/k_1 = 100$  with  $R = 8.3144621$  J·mol<sup>-1</sup>·K<sup>-1</sup> is determined. This means that reaction 2 is 100 times faster than reaction 1, because of the temperature increase. This procedure is mainly dependent on  $E_A$ , which is in the gas phase usually between 30 and 100 kJ.

After the aging, the sensor was measured with 680 ppb NH<sub>3</sub> exposure under the same conditions as before with 17.5 % RH and 25 °C. Fresh means that the sensor was stored in air at room temperature for several months before usage. The sensing responses of the fresh and aged sensor are compared in Fig. 6.23a. The sensing response of the aged sensor is 19 % of the response of the fresh sensor. This means that the signal intensity decreased by 81 % for a period of one year of continuous operation. The response time of around 54 min is higher than that one of the fresh sensor (44 min). It can also be seen that no recovery of the signal takes place. Therefore, no recovery time could be determined.

The  $I_{DS}-V_G$  curves of the fresh and aged SiNW sensors are shown in Fig. 6.23b. Here, number ① represents the curves before exposure to NH<sub>3</sub>, number ② stands for the graphs under 680 ppb NH<sub>3</sub> exposure, and number ③ shows the sensor recovery after 2 h. The hysteresis of the  $I_{DS}-V_G$  curves was reduced after aging of the sensor. This effect was discussed in detail in section 6.5.6. Additionally, the graphs are shifted comparable to the shift reported in section 6.5.2.

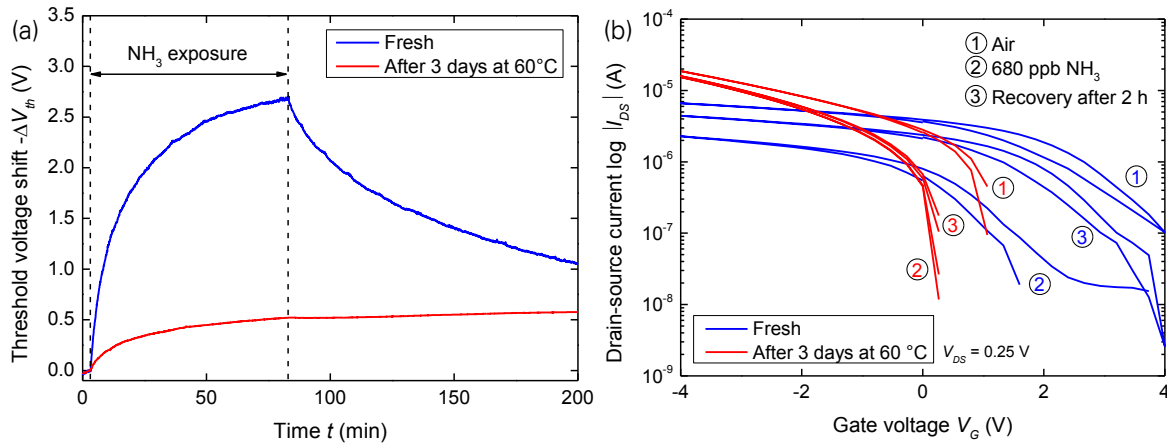


**Fig. 6.23:** Comparison of the 680 ppb  $NH_3$  detection of a fresh and an aged sensor. (a) The responses of the fresh and aged sensor as a function of sensing time to 680 ppb  $NH_3$ . (b) The  $I_{DS}-V_G$  curves of the fresh and aged SiNW based sensor.

It is reported in literature that semiconductors do not guarantee high stability of gas sensor parameters [45]. In an oxygen atmosphere, surface oxidation takes place. This inevitably leads to the change of electronic, adsorption, and catalytic properties of the semiconductor surface [257]. Ihokura and Watson [310] attribute the aging process to a progressive increase in surface coverage by chemisorbed oxygen with corresponding changes in both grain-boundary resistance and capacitance, which indicates the corresponding changes in the grain-boundary barrier height and the width of depletion layer. However, the stability of SiNW based  $NH_3$  sensors after long-term storage has not been reported yet in the literature. After  $NH_3$  measurements, the sensors were studied by SEM, but no changes in the structure or of the surface could be observed.

One of the principal limitations of silicon nanowires with a native oxide shell is its high surface activity leading to adsorption of moisture, oxygen and other contaminants in the ambient which subsequently change the composition of the native  $SiO_2$  and cause its degradation by aging. Oxidizing of the SiNWs is one approach for improving its stability, which can be carried out by thermal oxidation (see section 4.2). This was done in this work and the results of the study of SiNWs with a thermally grown  $SiO_2$  shell are presented in the following.

## 6.6 Sensors based on Silicon Nanowires with a Thermally Grown Oxide Shell

The electric characteristic of FETs is largely dependent on the properties of the dielectric and the interfaces to the semiconductor [250]. The requirement for unshifted characteristics without hysteresis and for the fabrication of high electron and hole current densities is a charge poor, wire surrounding dielectric. On the one hand, an improved gate coupling due to

lower electrical fields perpendicular to the current direction leads to a lower probability of forming trapped charges. On the other hand, a reasonable dielectric forms less trapped charge states. In the modern semiconductor industry, gate oxides with a permittivity of  $\epsilon_r > \epsilon_{SiO_2} = 3.9$  are established [311]. For that, a coating of the wires with the dielectric is required. Owing to the resulting intermediate layer through the native wire oxide, a high interface state density is expected. An alternative to the coating is the thermal oxidation of the wires. The interface grows into the wire during oxidation. In bulk silicon, the material system of thermally grown  $SiO_2$  on Si was used as standard gate oxide used in MOSFET technology for several decades, because of low interface traps [312] and the simple fabrication procedure [313].

In this work, the described approach was implemented by removing the native oxide shell and subsequent thermal growth of the  $SiO_2$  layer (see section 4.2). Applied to the sensor principle used here, it means that above mentioned effects of hysteresis caused by charge trapping can be reduced. It was shown that hysteresis leads to a change of  $V_{th}$  over time. Since  $V_{th}$  is the analyzed sensor response, which indicates the presence and concentration of the analyte, measurements can be falsified. Additionally, the influences of humidity and temperature on the sensor response, which are promoted by charge trapping, will be reduced by SiNWs with thermally grown  $SiO_2$ . Also, the amount of oxygen (possible binding sites) is increased due to the higher homogeneity of the  $SiO_2$  shell on the surface of the nanowires, which can lead to an enhanced sensitivity.

The  $I_{DS}-V_G$  characteristics and threshold voltage shift  $\Delta V_{th}$  of those devices were studied under the influence of ammonia, humidity change, and temperature variations. The drain-source current was measured at  $V_{DS} = 0.25$  V by sweeping  $V_G$  from -8 to +15 V. The gate voltage was swept in the same way as for the native oxide shell SiNWs from 0 V to +15 V to -8 V and back to 0 V.

### 6.6.1 Drift Investigation

Zero drift was determined by exposing the sensor only to the carrier gas without  $NH_3$ , which was dry air, and measuring the threshold voltage drift  $\Delta V_{th}$  for 1 h.  $V_{th}$  drift was recorded by applying a constant drain-source voltage of 0.25 V and a gate voltage of -8 – +15 V (Fig. 6.24).  $I_{DS}$  was continuously recorded. It was observed that the threshold voltage was continuously shifted towards negative  $V_G$ , whereas the  $\Delta V_{th}$  drift of the sensor based on natively grown oxide SiNWs was towards positive  $V_G$ . This can be due to the various reasons that exist for the occurring of shift (section 6.5.1). Moreover, the signal drift value was measured

to be 350 mV/h in average, which is approximately one order of magnitude higher than the zero drift value of native oxide shell SiNWs. This can be attributed to the shorter measurement period of 1 h compared to 3 h. As can be seen in Fig. 6.24b the drift decreased over time.

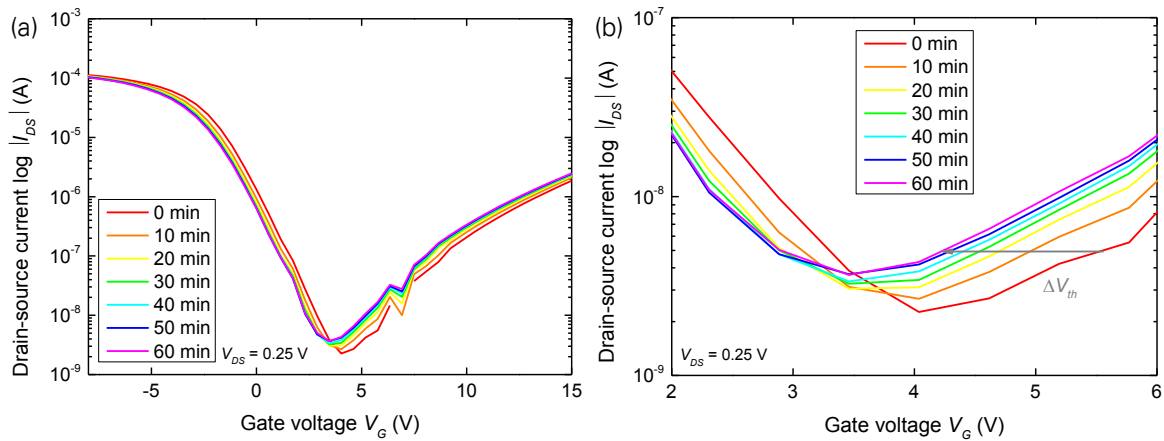


**Fig. 6.24:** Threshold voltage drift over a period of 3 h. (a) Drain-source current in dependence of the gate voltage in the range of -8 – +15 V. The curves are shifted to positive  $V_G$  over time and the hysteresis does not change. (b) Magnified detail of the  $I_{DS}$ – $V_G$  curves in the range of 2–6 V. For reasons of clarity the  $I_{DS,up}$  and  $I_{DS,down}$  values were averaged. The grey arrow indicates the shift direction of  $V_{th}$ .

## 6.6.2 Influence of Ammonia, Humidity, and Temperature

In order to compare the sensing performance of thermally grown  $\text{SiO}_2$  shell nanowires with native oxide SiNWs, former were first exposed to  $\text{NH}_3$  and then the effect of humidity and temperature on the sensors was investigated.

### Ammonia

Signals are collected by 10 min under flowing  $\text{NH}_3$  with preceding and subsequent air flow at 17.5 % RH and 25 °C. Source-drain current ( $I_{DS}$ ) versus  $V_G$  curves (at  $V_{DS} = 0.25$  V) were carried out during the exposure experiment ( $V_G$  ranged from -8 to +15 V). The results from exposing SiNW devices to different concentrations of  $\text{NH}_3$  are shown in Fig. 6.25. Devices made from thermally grown oxide shell SiNWs showed no response to the same concentrations of  $\text{NH}_3$  as used for exposures to native grown oxide shell SiNWs (Fig. 6.13a). Further controls, in which 1.36 ppm of  $\text{NH}_3$  was applied instead of 680 ppb, showed no signal response to  $\text{NH}_3$  either. The small variation between  $I_{DS}$ – $V_G$  curves of 680 ppb and 1.36 ppm are attributed to normal drift. The value of  $\Delta V_{th}$  is -0.4 V for 10 min  $\text{NH}_3$  exposure to 1.36 ppm compared to a value of 1.8 V for natively grown  $\text{SiO}_2$  shell SiNW based devices.

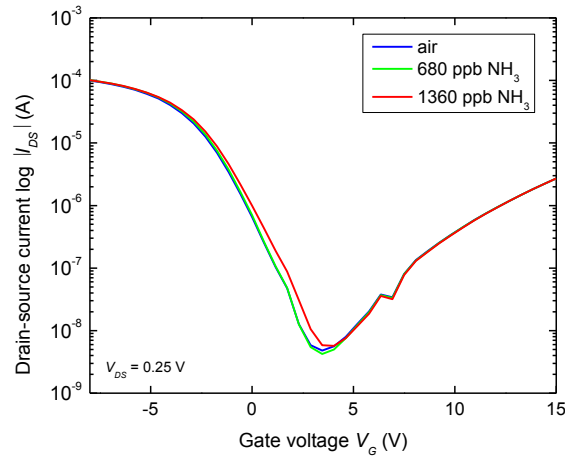


**Fig. 6.25:**  $I_{DS}-V_G$  characteristics before and after exposure to  $\text{NH}_3$  with concentrations of 680 ppb and 1.36 ppm at 17.5 % RH at 25 °C for 10 min, respectively.

The isolating thermally grown  $\text{SiO}_2$  layer with a thickness of 6 nm, which corresponds to 60 Å and thus 60 atomic layers, seems to be too thick, so that no interaction with the semiconductor can take place. Possible oxide surface charges on the outside have a reduced influence on the potential in the active region through the increased distance from the active region. This results in a lower influence by adsorbates from the ambient air [314].

### Humidity

The relative humidity in the ambient environment of the sensor was changed from 17.5 % to 69.5 % for 10 min and then back to 17.5 % in order to investigate the influence of humidity on the device. Temperature was kept constant at 25 °C and the transfer characteristic of the FET was measured (Fig. 6.26a). A threshold voltage shift under 69.5 % RH was not detectable in comparison to a shift of 0.2 V for natively grown  $\text{SiO}_2$  shell nanowire based sensors. In contrast, a change in the hysteresis could be measured (Fig. 6.26b). The average value of the hysteresis change from 69.5 % RH compared to 17.5 % RH was 0.11 V. For the native oxide based sensor it was slightly higher with approximately 0.12 V. This result shows that the hysteresis is affected by humidity, but no shift of the threshold voltage was observed. When the humidity is increased, water diffuses into the thermal  $\text{SiO}_2$  film. This results in the production of negative bulk oxide charge and positive interface charge by an avalanche-injected electron flux [315], which increases the hysteresis. As discussed in section 6.5.5, trapped charge in the oxide can be detrapped. This is observed in Fig. 6.26b, where the hysteresis decreases after the relative humidity is reduced.

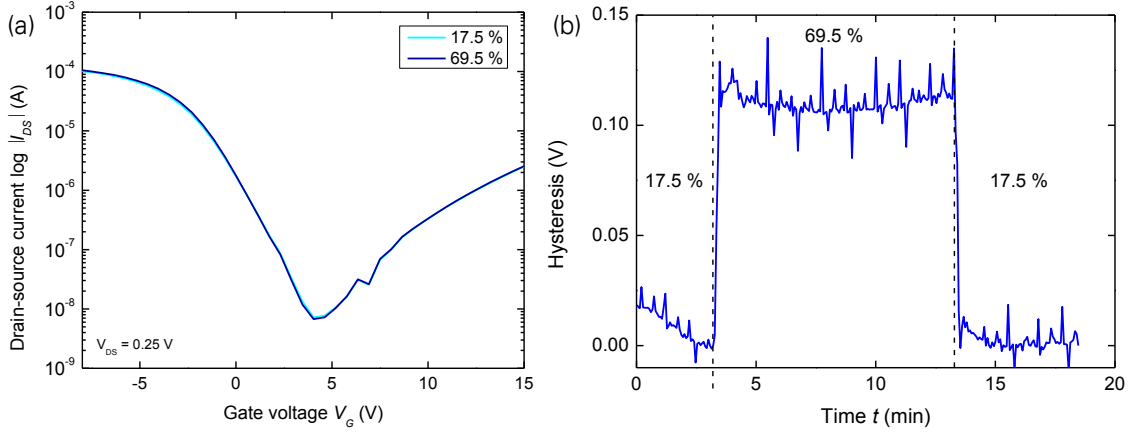


**Fig. 6.26:** Influence of humidity on the devices based on thermally grown  $\text{SiO}_2$  shell nanowires. (a) Transfer characteristics for humidity of 17.5 % and 69.5 %. (b) Hysteresis over time for 17.5 and 69.5 % RH.

### Temperature

The starting temperature inside the furnace was 25 °C and the drain-source voltage was  $V_{DS} = 0.25$  V. Subsequently, the temperature was increased to 30, 40, and 50 °C at 17.5 % RH for 2000 s (~33 min). The time of 2000 s was chosen in order to compare the results with those of the native oxide based sensor. The determined values for response and recovery time are not comparable with those from the native oxide SiNW based sensor, because no new baseline of the signal was reached within the time of increased temperature. In general, the same effects were apparent as for the native oxide SiNWs.  $\Delta V_{th}$  and hysteresis increased with increasing temperature (Fig. 6.27c and d). As the temperature increased, the drain-source current increased in higher voltage than the  $V_G$  for the minimum value of the  $I_{DS}$  (Fig. 6.27a). This means, the ambipolar  $I_{DS}-V_G$  curve shifted negatively. However, for the  $I_{DS}$  in lower voltage than the  $V_G$  for the minimum value of the  $I_{DS}$ , no negative shift could be seen. Instead the  $I_{DS}-V_G$  curves of the sensor recorded at four different temperatures between 25 and 50 °C intersect in one point at  $V_G = 0$  V. This point is called the isothermic point and in this point the influence of temperature on  $I_{DS}$  is minimal [308]. This effect was also described for a FET using a gas sensitive film [308] and can be qualitatively, but not quantitatively applied to a FET with nanowires. The temperature concerning a transducer FET affects both the mobility  $\mu$  of charge carriers and the level of the Fermi energy  $e\Psi_F$ . The following temperature dependence for the linear regime of the  $I_{DS}-V_G$  characteristics can be derived from [153]:

$$\frac{dI_{DS}}{dT} = \frac{W}{L} C_{Tot} (V_G - V_{th}) V_{DS} \frac{d\mu}{dT} - \mu \frac{W}{L} C_{Tot} V_{DS} \left( 2 - \frac{1}{C_{Tot}} \frac{Q_D}{2\Psi_F} \right) \frac{d\Psi_F}{dT}, \quad (6.9)$$

where  $L$  is the effective channel length,  $W$  the effective channel width,  $C_{Tot}$  the total capacitance across the insulator,  $V_{th}$  the threshold voltage,  $V_{DS}$  the drain-source voltage,  $\mu$  the inversion charge carrier mobility,  $Q_D$  the charge of depletion layer. Owing to the counteracting behavior of both contributions (subtraction) a point can be found with  $dI_{DS}/dT$  being minimal. This point can be chosen by variation of the gate voltage  $V_G$ .

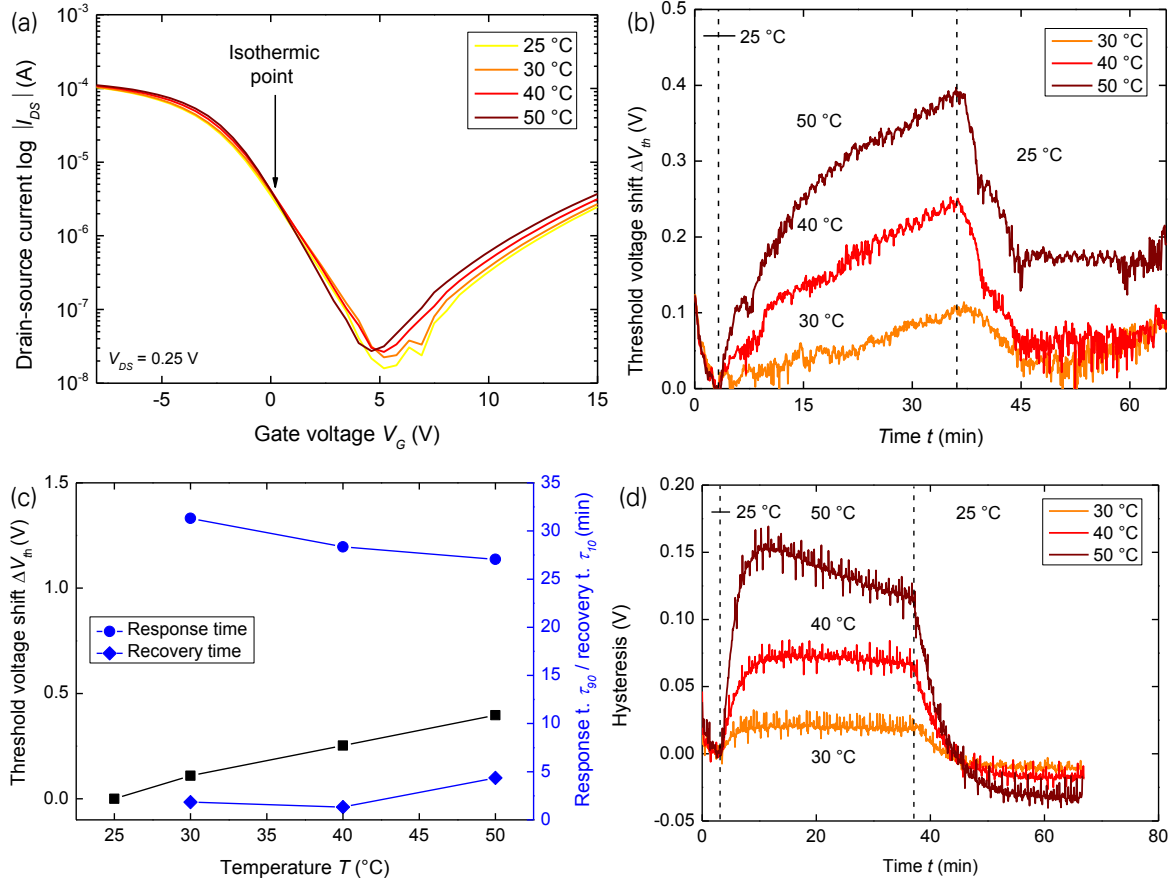


**Fig. 6.27:** Sensor response of a thermally grown oxide SiNW based device towards temperature changes in the range 30–50 °C. (a)  $I_{DS}$ – $V_G$  characteristics of a SiNW FET at temperatures between 25 and 50 °C. (b)  $\Delta V_{th}$  over time for 30, 40, and 50 °C. (c) Threshold voltage shift, response, and recovery time in dependence of the temperature change. The lines serve as guides to the eye. (d) Hysteresis over time for 30, 40, and 50 °C.

## 6.7 Comparison of the Performances of Native and Thermal Oxide Shell Silicon Nanowire based Sensors

In order to compare the sensing properties of natively and thermally grown oxide SiNWs, the results are summarized in Table 6.3. It can be seen that the respective values for the threshold voltage shifts, which were used in this work as sensor response, were all higher for native oxide SiNW based devices than for thermal oxide SiNW based sensors. Especially for the detection of  $\text{NH}_3$ , native grown oxide shell sensors showed a high sensing response of

175 % after 10 min of 1.36 ppm  $\text{NH}_3$  exposure at 17.5 % RH and 25 °C, whereas thermal oxide SiNWs did not respond. A similar behavior was observed for humidity changes, where just natively grown  $\text{SiO}_2$  shell SiNWs showed a  $V_{th}$  shift owing to a RH variation from 17.5 % to 69.5 % at 25 °C. This is a great advantage of the thermal oxide SiNWs sensors compared to the native oxide devices, because if they do not react to moisture changes, those sensors can be used in an environment with humidity variations (which is the case in almost any application) without further electronics for considering one of the major interfering influences. However, a change in the hysteresis as a result of the humidity variation was observed for both sensor types. That the device with natively grown oxide showed a larger hysteresis than the device with thermally grown oxide is because of the presence of charge carrier traps in the native oxide, which leads to charge trapping by water (section 6.5.5). The positive  $V_{th}$  shift as a result of temperature variations is also higher for native than for thermal oxide shell SiNWs. It was not expected that the hysteresis increases more with increasing temperatures for thermal oxide shell SiNWs than for native oxide shell SiNWs.

**Table 6.3:** Comparison between sensing performances of natively and thermally grown oxide SiNW based devices.

Influences	Native oxide SiNWs		Thermal oxide SiNWs	
	$\Delta V_{th}$ (V)	Hysteresis (V)	$\Delta V_{th}$ (V)	Hysteresis (V)
<b><math>\text{NH}_3</math>: 1.36 ppm</b>	-1.75		-0.38	
<b>RH = 69.5 %</b>	-0.19	0.12	0.00	0.11
<b>T = 30 °C</b>	0.21	0.02	0.11	0.02
<b>T = 40 °C</b>	0.77	0.06	0.25	0.07
<b>T = 50 °C</b>	1.14	0.09	0.40	0.14

To conclude, it was demonstrated that sensors based on SiNWs with a natively grown  $\text{SiO}_2$  shell show a better sensing performance towards  $\text{NH}_3$  than devices with thermally grown oxide shell SiNWs. This is attributed to the lower amount of charge carrier traps in the oxide layer of the later mentioned, which also affects the influence of humidity and temperature variations. Due to the benefits of the use of thermal oxide, such as less shifted transfer characteristics with lower hysteresis and enhanced sensitivity owing to more possible binding sites through the higher homogeneity of the  $\text{SiO}_2$  shell, further research activities should focus on the growth and subsequent investigation of thinner thermal  $\text{SiO}_2$  layers on the surface of SiNWs.



## 6.8 Summary

In chapter 6, sensors based on natively and thermally grown SiO<sub>2</sub> shell SiNWs were electrically characterized, their sensing performance towards ammonia was investigated, and finally the results were compared. The electrical characterization revealed that devices based on native SiO<sub>2</sub> shell SiNWs exhibit unipolar behavior with a transfer characteristic shifted to positive  $V_G$  and hysteresis. Thermally grown oxide shell SiNW sensors however, show an ambipolar  $I_{DS}-V_G$  characteristics with a lower hysteresis. Introductory, the most important requirements on gas sensors were described and served as basis for subsequent measurements. The sensor properties can be classified into static and dynamic behavioral characteristics and their analysis requires appropriate diagrams, which were presented.

Firstly, sensors based on SiNWs with native oxide were investigated. It was observed that those devices had a zero drift of 23 mV/h, which can be caused by local heating of the sensor element and further yet unexplained mechanisms. The response and recovery time were measured to be 44 min and 73 min, respectively. It has to be considered that after 73 min only 50 % of the saturation value was reached and that a full recovery of the signal took several hours. Therefore, a subsequent heating step was introduced, where the sensor was heated up to 60 °C for 30 min resulting in a full recovery and hysteresis was drastically reduced. The repeatability was determined to be  $\pm 10\%$ , which is a good value considering a allowed repeatability of  $\pm 30\%$  for measurements of hazardous workplace atmospheres according to TRGS 402 and DIN EN 482. A sequence of NH<sub>3</sub> exposures in the concentration range from 680 ppb to 170 ppb were carried out and indicated that the sensors were able to highly sensitively detect NH<sub>3</sub>. The response of the sensor was 165 % when exposing to 170 ppb NH<sub>3</sub> and the theoretically calculated limit of detection was 20 ppb. It was found out that the  $I_{DS}-V_G$  curve was not only shifted negatively, but also decreased over the entire voltage range according to the concentration increase of NH<sub>3</sub>. This was attributed to the transfer of negative charge of NH<sub>3</sub> molecules to silicon nanowires. Afterwards, the influence of humidity and temperature on the sensor and sensing performance towards NH<sub>3</sub> was studied. Both kinds of interferences affected the sensor behavior, wherein the device turned out to be a suitable humidity sensor due to the fast response and recovery time in the range of seconds. For increasing values of humidity and temperature, the signal intensity towards NH<sub>3</sub> was reduced, whereas the response and recovery time was decreased. This result is advantageous regarding the energy consumption of the devices, because no heating is required to achieve maximum sensitivity. The selectivity of the sensors was examined towards six different substances typically found in residential environments and representative

for a number of substance classes. Acetone ( $C_3H_6O$ ), acetonitrile ( $C_2H_3N$ ), chloroform ( $CHCl_3$ ), ethanol ( $C_2H_6O$ ), ethyl acetate ( $C_4H_8O_2$ ), and toluene ( $C_7H_8$ ) were applied to a device with concentrations much higher than the allowed occupational exposure limits according to TRGS 900 Arbeitsplatzgrenzwerte. No cross sensitivity to all of the substances was observed making the sensor highly selective to  $NH_3$ . A sensor-to-sensor reproducibility of 37.5 % was determined, which was attributed to the fact that the devices were fabricated individually. Processes for industry-oriented manufacturing, such as top-down processes, can enhance this value, but their application was not the aim of this work. The long-term stability of the sensor was investigated by storing the device in 60 °C for 3 days and subsequent exposure to  $NH_3$ . This corresponds to approximately one year of continuous operation and it was observed that the signal intensity decreased by 81 %.

Secondly, devices with thermally grown  $SiO_2$  shell SiNWs were studied. Those showed no response towards  $NH_3$  and humidity. The influence of temperature on the sensors was observed, but lower compared to the preceding sensors.

To conclude, the results of the devices with native oxide SiNWs show clearly that the sensor principle is promising with respect to an application for disease diagnosis by breath analysis. For this, it is particularly important that the sensor has a linear dependence to water vapor and no cross sensitivity to ethanol, which is a metabolite typically found in the ppm range in human breath samples [316]. In this application area, the temperature remains approximately constant, a high sensitivity is required, and a small size of the sensor favorable. Only the response time has to be enhanced and is a possible starting point for further research activities.

## 7 Conclusions and Outlook

### 7.1 Conclusions

Sensor systems must meet stringent requirements for durability, reliability, and energy efficiency. Based on that, there are a lot of reasons that speak for a miniaturization of sensors. Especially in industrial applications the following needs play an increasingly significant role: small construction size, easy integration into systems, low power consumption, low weight, and significant cost advantages in the mass production of sensors. This work aimed at developing a nanowire based sensor for highly sensitive and selective ammonia detection having the potential to be used in portable instruments with low power consumption.

After a short introduction, semiconductor materials were motivated as recognition elements for gas sensors. Derived from important gas sensing properties, significant advantages of nanowires compared to conventional materials were demonstrated. The correlation between large surface-to-volume ratio and high sensitivity was described, which is the basis for detecting very low analyte concentrations. Bottom-up and top-down methods, which are the two basic approaches for the fabrication of nanostructure based devices, were introduced. These two techniques were also used in this work to fabricate devices. Bottom-up methods enabled nanosensor fabrication with less technological efforts compared to top-down approaches paying the price of a lower reproducibility. Among the different nanomaterials, silicon nanowires were found to be particularly suitable, because of their uniformity, reproducibility, as well as excellent scalability to name just a few. A peculiarity of the sensors prepared in this work is the Schottky contact, which enables low electrical resistance between nanowires and electrodes. The significance of the detection of ammonia was illustrated by the versatile application areas of ammonia sensors and known sensing principles are shown with their advantages and drawbacks.

The controlled electrochemical synthesis of copper nanowires from an aqueous  $\text{Cu}(\text{NO}_3)_2$  solution allowed analyzing this method for the fabrication of nanowires for gas sensor applications. This approach was presented in chapter 3 and enabled the rapid growth of copper nanowires with distinct morphologies at predefined electrode locations. The growth of high aspect ratio copper nanowires with diameters of about 100 nm and a length of up to several micrometers via directed electrochemical nanowire assembly was achieved. It was found out that the nanowire morphology was controlled by the metal salt solution concentration

and by the amplitude and frequency of the applied alternating voltage. The frequency further notably affected the nanowire diameter. The impact of the process parameters on the nanowire growth was discussed on the basis of the Butler–Volmer equation. Despite the many advantages of the fabrication procedure, some drawbacks, mainly the high operating temperatures and lower expected sensitivity, led to the use of silicon nanowires in the further course of the work.

In chapter 4, the fabrication of silicon nanowire based gas sensors was described. Starting from bottom-up grown silicon nanowires with diameters around 20 nm, those were transferred via contact printing method to the device substrate. The following process step of etching the native oxide and then thermally grow an oxide shell distinguished the sensors with native oxide shell SiNWs from those with a thermally grown oxide shell. As sensor layout an interdigitated electrode structure contacting the parallel aligned SiNWs was fabricated by lithography. The realization of Schottky contacts within the nanowires was done by partial oxide etching, Ni sputtering, lift-off, and subsequent annealing for silicidation.

Chapter 5 dealt with the designed gas measurement setup. After introducing the state of the art and requirements of test systems for nanomaterial based gas sensors, the developed apparatus was introduced. It comprised four main parts: the gas delivery system to control the gas composition and concentration inside the measurement chamber, the gas exposure chamber for an attachment of the samples in the gas flow, the read-out electronics to determine the sensing response of the sensors, and the temperature control for the substrates. A measurement protocol was prepared for the testing of sensors in defined gas atmospheres.

The fabricated sensors based on SiNWs with a native or thermally grown oxide shell were electrically characterized and analyzed in chapter 6. As basis for the measurements, main sensor requirements were defined. Firstly, SiNWs with a native SiO<sub>2</sub> shell were studied, starting with resistance measurements and determining the drift of those devices, which was comparable with drift values of SiNW based sensors reported in literature. Subsequently, the response and recovery time was determined by exposing to 680 ppb NH<sub>3</sub>. The response time of the device was around 44 min and the recovery time to reach 50 % of the sensing response was approximately 73 min, whereas a full recovery took several hours. It was observed that the recovery can be enhanced by heating up the sensor to 60 °C for 30 min. A novel mechanism to detect NH<sub>3</sub> was demonstrated by measuring the change of the hysteresis under NH<sub>3</sub> exposure. This was found to decrease the response time to a few seconds, but led to a reduction of the sensor sensitivity. The repeatability to NH<sub>3</sub> was measured to be ±10 %, which is a good value for concentrations in the ppb range and taking into

account that a repeatability value of  $\pm 30\%$  is permitted for measurements of hazardous workplace atmospheres according to TRGS 402 and DIN EN 482.  $\text{NH}_3$  concentrations down to 170 ppb were measured and a theoretical limit of detection of 20 ppb was calculated. These results demonstrated the lowest  $\text{NH}_3$  concentration measured so far in air with a sensor based on SiNWs. It was found out that the device is an excellent sensor for humidity, because of the very fast response and recovery times in the range of a few seconds. As expected, with increasing humidity the signal intensity towards  $\text{NH}_3$  decreases, but the response and recovery time also reduces. The influence of the temperature on  $\text{NH}_3$  measurements was investigated and it was discovered that the maximum sensitivity of the sensor is at 25 °C in the experimental range. This is a great advantage, since no additional energy consumption for heating of the sensor is needed. In contrast to metal oxide semiconductors, which are the most common sensing materials and require high operating temperatures. To demonstrate the selective sensing properties of SiNW based sensors, six different substances, belonging to the most common solvents in living areas and each representative of another substance class, were applied to the sensor. The developed sensors clearly showed no cross sensitivity. The sensor-to-sensor reproducibility was low with a coefficient of variance between devices of  $4.8 \text{ V} \pm 1.8 \text{ V}$  for the exposure to 680 ppb  $\text{NH}_3$ . The long-term stability was investigated by storing a sensor in air at 60 °C for 3 days. This corresponds to a year of continuous operation and after this aging process, signal intensity decreased by 81 %. Finally, SiNWs with a thermally grown oxide shell were studied in terms of  $\text{NH}_3$  detection as well as humidity and temperature influence on the sensors. It was found that those sensors neither responded to  $\text{NH}_3$  exposure nor to humidity changes. Merely a temperature dependence was observed. This was attributed to fewer charge carrier traps in the oxide compared to SiNWs with a native oxide.

## 7.2 Outlook

Developing a nanosensor requires competences confined in not related disciplines. Major efforts will be needed to further engineer such devices. Regarding the use of copper nanowires synthesized by DENA, further investigations should involve oxidation processes to transform grown copper nanowires into semiconducting CuO nanowires for gas sensor applications. The scope of functions of the gas measuring apparatus can be further enhanced by integrating a humidity variation, which requires additional mass flow controllers for defined gas flows. It was shown that the developed sensors are suitable for respiratory gas analyses, since they work despite high humidity values in the right concentration range of

50–2000 ppb and temperature range of 20–40 °C as well as showed no cross sensitivity to ethanol, which is typically found in the ppm range in human breath samples. Electronics can be used to calculate out the linear humidity dependence of the sensor by including a commercial available humidity sensor and the temperature is approximately constant in the breath analysis. Apart from the high sensitivity and selectivity of the developed sensors, the response and recovery time have to be reduced in order to use these devices for applications where fast responses are required, such as respiratory gas analysis (response time < 1 min). This can be realized by e.g. fabricating thinner thermally grown oxide layers (more oxygen binding sites) with a thickness of 1–2 nm comparable with the native SiO<sub>2</sub> shell or surface functionalization of the SiNWs. Further works should include considerations to achieve a better sensor-to-sensor reproducibility. One approach can be to find an alternative method to align SiNWs on the device substrate to prevent damaging of the SiO<sub>2</sub> layer, which later results in gate leakage and degraded sensor behavior. The alignment of nanowires with microfluidics may represent a solution. In order to bring the sensor in the direction to be ready for the market, not only the requirements studied in this work are necessary, but further investigations must be carried out such as accuracy, calibration, and robustness tests. Market studies foresee a huge need for cheap, accurate, and selective molecular sensors for applications as diverse as life technologies, environmental monitoring, and security. Investment in this field will be essential in playing a leading role in the next massively interconnected sensorics area.

---

## Bibliography

- [1] M. J. Thorpe, D. Balslev-Clausen, M. S. Kirchner, and J. Ye. Cavity-enhanced optical frequency comb spectroscopy: application to human breath analysis, *Optics Express*, 2008, 16, 2387–2397.
- [2] H. Haick, Y. Broza, P. Mochalski, V. Ruzsanyi, and A. Amann. Assessment, origin, and implementation of breath volatile cancer markers, *Chem. Soc. Rev.*, 2014, 43, 1423–1449.
- [3] A. Manolis. The Diagnostic Potential of Breath Analysis, *Clin. Chem.*, 1983, 29, 5–15.
- [4] A. Amann, W. Miekisch, J. Schubert, B. Buszewski, T. Ligor, T. Jezierski, J. Pleil, and T. Risby. Analysis of Exhaled Breath for Disease Detection, *Annu. Rev. Anal. Chem.*, 2014, 7, 455–482.
- [5] C. M. Willis, S. M. Church, C. M. Guest, W. A. Cook, N. McCarthy, A. J. Bransbury, M. R. T. Church, and J. C. T. Church. Olfactory detection of human bladder cancer by dogs: proof of principle study, *BMJ*, 2004, 329, 712.
- [6] A. M. Rouhi. Detecting Illegal Substances, *Chemical & Engineering News*, 1997.
- [7] D. M. Stoddart. The Scented Ape: The Biology and Culture of Human Odour, Cambridge University Press, Cambridge, 1st ed., 1990.
- [8] R. R. Reed. Signaling pathways in odorant detection, *Neuron*, 1992, 8, 205–209.
- [9] Y. Dan, S. Evoy, and A. T. C. Johnson. Chemical gas sensors based on nanowires, *Nanowire Research Progress*, Chapter 3, Nova Science Publisher, 2008.
- [10] K. Persaud, and G. Dodd. Analysis of discrimination mechanisms in the mammalian olfactory system using a model nose, *Nature*, 1982, 299, 352–355.
- [11] R. H. Wright. The Science of Smell, Allen & Unwin, London, 1st ed., 1964.
- [12] P. Gründler. Chemical Sensors: An Introduction for Scientists and Engineers, Springer Science & Business Media, Berlin, Heidelberg, 2007.
- [13] N. Yamazoe. Toward innovations of gas sensor technology, *Sensors and Actuators B*, 2005, 108, 2–14.
- [14] Occupational Safety and Health Administration. Occupational Safety and Health Act of 1970, 1970.

- 
- [15] Directive 2008/50/EC of the European Parliament and of the Council on ambient air quality and cleaner air for Europe, *Official Journal of the European Union*, 2008, L 152, 1–44.
- [16] Global Markets and Technologies for Sensors, BCC Research Report, IAS006E, 2013.
- [17] L. R. Narasimhan, W. Goodman, C. Kumar, and N. Patel. Correlation of breath ammonia with blood urea nitrogen and creatine during hemodialysis, *PNAS*, 2001, 98, 4617–4621.
- [18] D. J. Kearney, T. Hubbard, and D. Putnam. Breath ammonia measurement in Helicobacter pylori infection, *Digest. Dis. Sci.*, 2002, 47, 2523–2530.
- [19] X. T. Zhou, J. Q. Hu, C. P. Li, D. D. D. Ma, C. S. Lee, and S. T. Lee. Silicon nanowires as chemical sensors, *Chem. Phys. Lett.*, 2003, 369, 220–224.
- [20] A. A. Talin, L. L. Hunter, F. Léonard, and B. Rokad. Large area, dense silicon nanowire array chemical sensors, *Appl. Phys. Lett.*, 2006, 89, 153102.
- [21] T. I. Kamins, S. Sharma, A. A. Yasserli, Z. Li, and J. Straznicki. Metal-catalysed, bridging nanowires as vapour sensors and concept for their use in a sensor system, *Nanotechnology*, 2006, 17, S291–S297.
- [22] M. C. McAlpine, H. D. Agnew, R. D. Rohde, M. Blanco, H. Ahmad, A. D. Stuparu, W. A. Goddard, and J. R. Heath. Peptide-nanowire hybrid materials for selective sensing of small molecules, *J. Am. Chem. Soc.*, 2008, 130, 9583–9589.
- [23] J. Wan, S. Deng, R. Yang, Z. Shu, B. Lu, S. Xie, Y. Chen, E. Huq, R. Liu, and X. Qu. Silicon nanowire sensor for gas detection fabricated by nanoimprint on SU8/SiO<sub>2</sub>/PMMA trilayer, *Microelectron. Eng.*, 2009, 86, 1238–1242.
- [24] H. J. In, C. R. Field, and P. E. Pehrsson. Periodically porous top electrodes on vertical nanowire arrays for highly sensitive gas detection, *Nanotechnology*, 2011, 22, 355501.
- [25] F. Demami, L. Ni, R. Rogel, A. C. Salaun, and L. Pichon. Silicon nanowires based resistors as gas sensors, *Sensors and Actuators B*, 2012, 170, 158–162.
- [26] L. Ni, E. Jacques, R. Rogel, A. C. Salaun, L. Pichon, and G. Wenga. VLS silicon nanowires based resistors for chemical sensor applications, *Proced. Eng.*, 2012, 47, 240–243.



- [27] L. Yang, H. Y. Lin, Z. S. Zhang, L. Cheng, S. Y. Ye, and M. W. Shao. Gas sensing of tellurium-modified silicon nanowires to ammonia and propylamine, *Sensors and Actuators B*, 2013, 177, 260–264.
- [28] O. S. Wolfbeis. Chemical sensors - survey and trends, *Fresenius J Anal Chem*, 1990, 337, 522–527.
- [29] J. Riegel, H. Neumann, and H.-M. Wiedenmann. Exhaust gas sensors for automotive emission control, *Solid State Ionics*, 2002, 152–153, 783–800.
- [30] O. S. Wolfbeis, B. Kovács, K. Goswami, and S. M. Klainer. Fiber-Optic Fluorescence Carbon Dioxide Sensor for Environmental Monitoring, *Mikrochim. Acta*, 1998, 129, 181–188.
- [31] C. Di Natale, A. Macagnano, E. Martinelli, R. Paolesse, G. D’Arcangelo, C. Roscioni, A. Finazzi-Agró, and A. D’Amico. Lung cancer identification by the analysis of breath by means of an array of non-selective gas sensors, *Biosensors and Bioelectronics*, 2003, 18, 1209–1218.
- [32] U. Kehse. Digitale Spürnasen, *Pictures of the Future*, 2004, autumn, 81–84.
- [33] K. Todd. Canary in the old growth, *High Country News*, 2009, Paonia, Colorado, February 16.
- [34] D. K. Aswal, and S. K. Gupta. Science and Technology of Chemiresistor Gas Sensors, Nova Science Publishers Inc., New York, 1st ed., 2007.
- [35] J. Vetelino, and A. Reghu. Introduction to Sensors, CRC Press, Boca Raton, 1st ed., 2010.
- [36] W. H. Brattain, and J. Bardeen. Surface Properties of Germanium, *Bell System Tech. J.*, 1953, 32, 1–41.
- [37] T. Seiyama, A. Kato, K. Fujishi, and M. Nagatani. A New Detector for Gaseous Components Using Semiconductive Thin Films, *Anal. Chem.*, 1962, 34, 1502–1503.
- [38] N. Taguchi. A metal oxide gas sensor, Japanese Patent, 1962, No. 45-38200.
- [39] S. Yamauchi. Chemical Sensor Technology, Elsevier, Amsterdam, 4th ed., 1992.
- [40] A. Hulanicki, S. Glab, and F. Ingman. Chemical Sensors: Definitions and Classification, *Pure & Appl. Chem.*, 1991, 63, 1247–1250.
- [41] J. Fraden. Handbook of Modern Sensors: Physics, Designs, and Applications, Springer Science & Business Media, New York, 4th ed., 2010.

- 
- [42] Y. L. Hoo, W. Jin, C. Shi, H. L. Ho, D. N. Wang, and S. C. Ruan. Design and modeling of a photonic crystal fiber gas sensor, *Applied Optics*, 2003, 42, 3509–3515.
- [43] S. Miwa, and T. Arakawa. Selective gas detection by means of surface plasmon resonance sensors, *Thin Solid Films*, 1996, 281-282, 466–468.
- [44] G. Freitag. Entwicklung eines neuen Feldeffekt-Gassensors mit hybridem Gate-Aufbau und vertikalem Transistordesign, Cuvillier Verlag, Göttingen, 1st ed., 2005.
- [45] G. Korotcenkov. Handbook of Gas Sensor Materials: Properties, Advantages and Shortcomings for Applications Volume 1: Conventional Approaches, Springer Science & Business Media, New York, 1st ed., 2013.
- [46] S. Fanget, S. Hentz, P. Puget, J. Arcamone, M. Matheron, E. Colinet, P. Andreucci, L. Duraffourg, Ed. Myers, and M.L. Roukes. Gas sensors based on gravimetric detection—A review, *Sensors and Actuators B*, 2011, 160, 804–821.
- [47] F. M. Battiston, J.-P. Ramseyer, H. P. Lang, M. K. Baller, C. Gerber, J. K. Gimzewski, E. Meyer, and H.-J. Güntherodt. A chemical sensor based on a microfabricated cantilever array with simultaneous resonance-frequency and bending readout, *Sensors and Actuators B*, 2001, 77, 122–131.
- [48] G. Sauerbrey. Verwendung von Schwingquarzen zur Wägung dünner Schichten und zur Mikrowägung, *Zeitschrift für Physik*, 1959, 155, 206–222.
- [49] M. A. Ryan, A. V. Shevade, C. J. Taylor, M. L. Homer, M. Blanco, and J. R. Stetter. Computational Methods for Sensor Material Selection, Springer Science & Business Media, Dordrecht, 1st ed., 2009.
- [50] M. Otto. Analytische Chemie, John Wiley & Sons, Weinheim, 4th ed., 2011.
- [51] P. T. Meriläinen. A differential paramagnetic sensor for breath-by-breath oximetry, *J. Clin. Monit.*, 1990, 6, 65–73.
- [52] J.-H. Lee, C.-L. Tsai, C.-S. Fann, and S.-H. Wang. Design of an Acousto-Magnetic Oxygen Sensor, *Journal of Medical and Biological Engineering*, 2002, 22, 193–198.
- [53] J. B. Miller. Catalytic Sensors for Monitoring Explosive Atmospheres, *IEEE Sensors Journal*, 2001, 1, 88–93.
- [54] S. J. Gentry. Catalytic devices, In: T. E. Edmonds, Chemical sensors, Springer Science+Business Media B.V., New York, 1988.

- 
- [55] M. J. Madou, and S. R. Morrison. Chemical Sensing with Solid State Devices, Academic Press Inc, San Diego, 1st ed., 1989.
- [56] X. Liu, S. Cheng, H. Liu, S. Hu, D. Zhang, and H. Ning. A Survey on Gas Sensing Technology, *Sensors*, 2012, 12, 9635–9665.
- [57] M. Mittal, and A. Kumar. Carbon nanotube (CNT) gas sensors for emissions from fossil fuel burning, *Sensors and Actuators B*, 2014, 203, 349–362.
- [58] F. C. Tompkins. Chemisorption of gases on metals, *J. Vac. Sci. Technol.*, 1979, 16, 1077.
- [59] T. Sahm, A. Gurlo, N. Barsan, and U. Weimar. Basics of oxygen and SnO<sub>2</sub> interaction; work function change and conductivity measurements, *Sensors and Actuators B*, 2006, 118, 78–83.
- [60] E. Comini, G. Faglia, G. Sberveglieri, Z. Pan, and Z. L. Wang. Stable and highly sensitive gas sensors based on semiconducting oxide nanobelts, *Appl. Phys. Lett.*, 2002, 81, 1869.
- [61] S. R. Morrison. Mechanism of Semiconductor Gas Sensor Operation, *Sensors and Actuators*, 1987, 11, 283–287.
- [62] M. Ippommatsu, H. Sasaki, and H. Yanagida. Sensing mechanism of SnO<sub>2</sub> gas sensors, *Journal of Materials Science*, 1990, 25, 259–262.
- [63] S. Maeng, S.-W. Kim, D.-H. Lee, S.-E. Moon, K.-C. Kim, and A. Maiti. SnO<sub>2</sub> Nanoslab as NO<sub>2</sub> Sensor: Identification of the NO<sub>2</sub> Sensing Mechanism on a SnO<sub>2</sub> Surface, *ACS Appl. Mater. Interfaces*, 2014, 6, 357–363.
- [64] T. Seiyama, and S. Kagawa. Study on a Detector for Gaseous Components Using Semiconductive Thin Films, *Anal. Chem.*, 1966, 38, 1069–1073.
- [65] N. Barsan, and U. Weimar. Understanding the fundamental principles of metal oxide based gas sensors; the example of CO sensing with SnO<sub>2</sub> sensors in the presence of humidity, *J. Phys.: Condens. Matter*, 2003, 15, R813–R839.
- [66] J. Kong, N. R. Franklin, C. Zhou, M. G. Chapline, S. Peng, K. Cho, and H. Dai. Nanotube Molecular Wires as Chemical Sensors, *Science*, 2000, 287, 622–625.
- [67] K. G. Ong, and C. A. Grimes. A Carbon Nanotube-based Sensor for CO<sub>2</sub> Monitoring, *Sensors*, 2001, 1, 193–205.

- [68] L. Valentini, C. Cantalini, I. Armentano, J. M. Kenny, L. Lozzi, and S. Santucci. Investigation of the NO<sub>2</sub> sensitivity properties of multiwalled carbon nanotubes prepared by plasma enhanced chemical vapor deposition, *J. Vac. Sci. Technol. B*, 2003, 21, 1996–2000.
- [69] T. Ueda, H. Norimatsu, Md. M. H. Bhuiyan, T. Ikegami, and K. Ebihara. NO Sensing Property of Carbon Nanotube Based Thin Film Gas Sensors Prepared by Chemical Vapor Deposition Techniques, *Japanese Journal of Applied Physics*, 2006, 45, 8393–8397.
- [70] B. Esser, J. M. Schnorr, and T. M. Swager. Selective Detection of Ethylene Gas Using Carbon Nanotube-based Devices: Utility in Determination of Fruit Ripeness, *Angew. Chem. Int. Ed.*, 2012, 51, 5752–5756.
- [71] J. K. Abraham, B. Philip, A. Witchurch, V. K. Varadan, and C. C. Reddy. A compact wireless gas sensor using a carbon nanotube/PMMA thin film chemiresistor, *Smart Mater. Struct.*, 2004, 13, 1045–1049.
- [72] E. S. Snow, F. K. Perkins, E. J. Houser, S. C. Badescu, and T. L. Reinecke. Chemical detection with single-walled carbon nanotube capacitor, *Science*, 2005, 307, 1942–1945.
- [73] M. E. Roberts, M. C. LeMieux, and Z. Bao. Sorted and aligned single-walled carbon nanotube networks for transistor-based aqueous chemical sensors, *ACS Nano*, 2009, 3, 3287–3293.
- [74] D. R. Kauffman, and A. Star. Electronically monitoring biological interactions with carbon nanotube field-effect transistors, *Chem. Soc. Rev.*, 2008, 37, 1197–1206.
- [75] Y. Wang, and J. T. W. Yeow. A Review of Carbon Nanotubes-Based Gas Sensors, *Journal of Sensors*, 2009, 2009, 1–24.
- [76] C. Dekker. Carbon nanotubes as molecular quantum wires, *Phys. Today*, 1999, 52, 22–28.
- [77] P. G. Collins, K. Bradley, M. Ishigami, and A. Zettl. Extreme oxygen sensitivity of electronic properties of carbon nanotubes, *Science*, 2000, 287, 1801–1804.
- [78] A. Bachtold, C. Strunk, J.-P. Salvetat, J.-M. Bonard, L. Forró, T. Nussbaumer, and C. Schönberger. Aharonov-Bohm oscillations in carbon nanotubes, *Nature*, 1999, 397, 673–675.

- [79] J. Vavro, M. C. Llaguno, and J. E. Fischer. Thermoelectric Power of p-Doped Single-Wall Carbon Nanotubes and the Role of Phonon Drag, *Phys. Rev. Lett.*, 2003, 90, 065503.
- [80] J. Zhao, A. Buldum, J. Han, and J. P. Lu. Gas molecule adsorption in carbon nanotubes and nanotube bundles, *Nanotechnology*, 2002, 13, 195–200.
- [81] H. Y. Jung, S. M. Jung, J. R. Kim, and J. S. Suh. Chemical sensors for sensing gas adsorbed on the inner surface of carbon nanotube channels, *Appl. Phys. Lett.*, 2007, 90, 153114.
- [82] J. M. Schnorr, D. van der Zwaag, J. J. Walish, Y. Weizmann, and Timothy M. Swager. Sensory Arrays of Covalently Functionalized Single-Walled Carbon Nanotubes for Explosive Detection, *Adv. Funct. Mater.*, 2013, 23, 5285–5291.
- [83] A. Hirsch. Functionalization of Single-Walled Carbon Nanotubes, *Angew. Chem. Int. Ed.*, 2002, 41, 1853–1859.
- [84] X. Zhang, B. Yang, Z. Dai, and C. Luo. The gas response of hydroxyl modified SWCNTs and carboxyl modified SWCNTs to H<sub>2</sub>S and SO<sub>2</sub>, *Electrical Review*, 2012, 88, 311–314.
- [85] P. He, and L. Dai. Aligned carbon nanotube–DNA electrochemical sensors, *Chem. Commun.*, 2004, 3, 348–349.
- [86] R. Leghrib, E. Llobet, A. Felten, J. J. Pireaux, Z. Zanolli, J. C. Charlier, I. Suárez, and C. Ewels. NO<sub>2</sub> and CO interaction with plasma treated Au-decorated MWCNTs: Detection pathways, *Procedia Chemistry*, 2009, 1, 931–934.
- [87] C.-S. Lee, S. E. Baker, M. S. Marcus, W. Yang, M. A. Eriksson, and R. J. Hamers. Electrically addressable biomolecular functionalization of carbon nanotube and carbon nanofiber electrodes, *Nano Lett.*, 2004, 4, 1713–1716.
- [88] S. Dag, Y. Ozturk, S. Ciraci, and T. Yildirim. Adsorption and dissociation of hydrogen molecules on bare and functionalized carbon nanotubes, *Physical Review B*, 2005, 72, 1–8.
- [89] J. Kong, M. G. Chapline, and H. Dai. Functionalized carbon nanotubes for molecular hydrogen sensors, *Adv. Mater.*, 2001, 13, 1384–1386.
- [90] S. J. Kim. The effect on the gas selectivity of CNT-based gas sensors by binder in SWNT/silane sol solution. *IEEE Sens. J.*, 2010, 10, 173–177.

- 
- [91] F. Schedin, A. K. Geim, S. V. Morozov, E. W. Hill, P. Blake, M. I. Katsnelson, and K. S. Novoselov, Detection of individual gas molecules adsorbed on graphene, *Nat. Mater.*, 2007, 6, 652–655.
- [92] R. Jaaniso, and O. K. Tan. Semiconductor Gas Sensors, Elsevier Science & Technology, 1st ed., 2013.
- [93] D. A. Armbruster, and T. Pry. Limit of Blank, Limit of Detection and Limit of Quantitation, *Clin. Biochem. Rev.*, 2008, 29, 49–52.
- [94] IUPAC. Compendium of Chemical Terminology Gold Book, Version 2.3.3, 2014.
- [95] A. C. Pike. Design of Chemoresistive Silicon Sensors for Application in Gas Monitoring, Ph.D. Thesis, University of Warwick, 1996.
- [96] L. Zhou, F. Shen, X. Tian, D. Wang, T. Zhang, and W. Chen. Stable Cu<sub>2</sub>O nanocrystals grown on functionalized graphene sheets and room temperature H<sub>2</sub>S gas sensing with ultrahigh sensitivity, *Nanoscale*, 2013, 5, 1564–1569.
- [97] B. Wang, J. C. Cancilla, J. S. Torrecilla, and H. Haick. Artificial Sensing Intelligence with Silicon Nanowires for Ultraselective Detection in the Gas Phase, *Nano Lett.*, 2014, 14, 933–938.
- [98] S. Iijima. Helical microtubules of graphitic carbon, *Nature*, 1991, 354, 56–58.
- [99] D. H. Robertson, D. W. Brenner, and J. W. Mintmire. Energetics of nanoscale graphitic tubules, *Physical Review B*, 1992, 45, 12592.
- [100] S. Iijima, and T. Ichihashi. Single-shell carbon nanotubes of 1-nm diameter, *Nature*, 1993, 363, 603–605.
- [101] S. J. Tans, M. H. Devoret, H. Dai, A. Thess, R. E. Smalley, L. J. Geerligs, and C. Dekker. Individual single-wall carbon nanotubes as quantum wires, *Nature*, 1997, 386, 474–477.
- [102] S. J. Tans, A. R. Verschueren, and C. Dekker. Room-temperature transistor based on a single carbon nanotube, *Nature*, 1998, 393, 49–52.
- [103] R. a. Martel, T. Schmidt, H. R. Shea, T. Hertel, and P. Avouris. Single-and multi-wall carbon nanotube field-effect transistors, *Appl. Phys. Lett.*, 1998, 73, 2447–2449.
- [104] A. Kolmakov, and M. Moskovits. Chemical sensing and catalysis by one-dimensional metal-oxide nanostructures, *Annu. Rev. Mater. Res.*, 2004, 34, 151–180.

- 
- [105] C. Li, D. Zhang, X. Liu, S. Han, T. Tang, J. Han, and C. Zhou. In<sub>2</sub>O<sub>3</sub> nanowires as chemical sensors, *Appl. Phys. Lett.*, 2003, 82, 1613–1615.
- [106] Z. L. Wang. Characterizing the Structure and Properties of Individual Wire-Like Nanoentities, *Adv. Mater.*, 2000, 12, 1295–1298.
- [107] S. C. Lyu, Y. Zhang, and C. J. Lee. Low-Temperature Growth of ZnO Nanowire Array by a Simple Physical Vapor-Deposition Method, *Chem. Mater.*, 2003, 15, 3294–3299.
- [108] Y. T. Cheng, Y. H. Cho, N. Takama, P. Löw, C. Bergaud, and B. J. Kim. Simple fabrication of Si nanowire and its biological application, *J. Phys.: Conf. Ser.*, 2009, 152, 012048.
- [109] A. Kolmakov. The effect of morphology and surface doping on sensitization of quasi-1D metal oxide nanowire gas sensors, *Proceedings of SPIE*, 2006, 6370, 63700X.
- [110] E. Comini, and G. Sberveglieri. Metal oxide nanowires as chemical sensors, *Materials Today*, 2010, 13, 36–44.
- [111] M. Law, H. Kind, B. Messer, F. Kim, and P. Yang. *Angew. Chem. Int. Ed.*, 2002, 41, 2405–2408.
- [112] W. I. Park, G.-C. Yi, M. Kim, and S. J. Pennycook. Quantum confinement observed in ZnO/ZnMgO nanorod heterostructures, *Adv. Mater.*, 2003, 15, 526–529.
- [113] P. Bhattacharya, R. Fornari, and H. Kamimura. *Comprehensive Semiconductor Science, Six-Volume Set*, Elsevier Science, 1st ed., 2011.
- [114] S. A. Dayeh. *Semiconductor Nanowires for Future Electronics: Growth, Characterization, Device Fabrication, and Integration*, Ph.D. Thesis, University of California, San Diego, 2008.
- [115] R. W. J. Scott, S. M. Yang, G. Chabanis, N. Coombs, D. E. Williams, and G. A. Ozin. *Adv. Mater.*, 2001, 13, 1468–1472.
- [116] C. J. Martinez, B. Hockey, C. B. Montgomery, and S. Semancik. Porous Tin Oxide Nanostructured Microspheres for Sensor Applications, *Langmuir*, 2005, 21, 7937–7944.
- [117] H. T. Ng, J. Li, M. K. Smith, P. Nguyen, A. Cassell, J. Han, and M. Meyyappan. Growth of Epitaxial Nanowires at the Junctions of Nanowalls, *Science*, 2003, 300, 1249.

- [118] F. Hernandez-Ramirez, J. D. Prades, A. Tarancon, S. Barth, O. Casals, R. Jimenez-Diaz, E. Pellicer, J. Rodriguez, J. R. Morante, M. A. Juli, S. Mathur, and A. Romano-Rodriguez. Insight into the Role of Oxygen Diffusion in the Sensing Mechanisms of SnO<sub>2</sub> Nanowires, *Adv. Funct. Mater.*, 2008, 18, 2990–2994.
- [119] Y. J. Hong, H. S. Jung, J. Yoo, Y.-J. Kim, C.-H. Lee, M. Kim, and G.-C. Yi. Shape-Controlled Nanoarchitectures Using Nanowalls, *Adv. Mater.*, 2009, 21, 222–226.
- [120] D. Barreca, E. Comini, A. Gasparotto, C. Maccato, C. Sada, G. Sberveglieri, and E. Tondello. Chemical vapor deposition of copper oxide films and entangled quasi-1D nanoarchitectures as innovative gas sensors, *Sensors and Actuators B*, 2009, 141, 270–275.
- [121] D. Barreca, A. Gasparotto, C. Maccato, C. Maragno, E. Tondello, E. Comini, and G. Sberveglieri., Columnar CeO<sub>2</sub> nanostructures for sensor application, *Nanotechnology*, 2007, 18, 125502.
- [122] G. Korotcenkov. The role of morphology and crystallographic structure of metal oxides in response of conductometric-type gas sensors, *Mater. Sci. Eng. R*, 2008, 61, 1–39.
- [123] Y. Cui, and C. M. Lieber. Functional nanoscale electronic devices assembled using silicon nanowire building blocks, *Science*, 2001, 291, 851–853.
- [124] Y. Cui, Q. Wei, H. Park, and C. M. Lieber. Nanowire nanosensors for highly sensitive and selective detection of biological and chemical species, *Science*, 2001, 293, 1289–1292.
- [125] A. Cao, E. J.R. Sudhölter, and L. C.P.M. de Smet. Silicon Nanowire-Based Devices for Gas-Phase Sensing, *Sensors*, 2014, 14, 245–271.
- [126] Y. Cui, Z. Zhong, D. Wang, W. U. Wang, and C. M. Lieber. High performance silicon nanowire field effect transistors, *Nano Lett.*, 2003, 3, 149–152.
- [127] Y. Cui , X. Duan , J. Hu, and C. M. Lieber. Doping and electrical transport in silicon nanowires, *J. Phys. Chem. B*, 2000, 104, 5213–5216.
- [128] J. Janata, and M. Josowicz. Conducting polymers in electronic chemical sensors, *Nature Materials*, 2003, 2, 19–24.



- [129] M. Mescher, L. C. P. M. de Smet, E. J. R. Sudholter, and J. H. Klootwijk. Robust fabrication method for silicon nanowire field effect transistors for sensing applications, *J. Nanosci. Nanotechnol.*, 2013, 13, 5649–5653.
- [130] E. Stern, J. F. Klemic, D. A. Routenberg, P. N. Wyrembak, D. B. Turner-Evans, A. D. Hamilton, D. A. LaVan, T. M. Fahmy, and M. A. Reed. Label-free immunodetection with CMOS-compatible semiconducting nanowires, *Nature*, 2007, 445, 519–522.
- [131] R. M. Penner. Chemical sensing with nanowires, *Annu. Rev. Anal. Chem.*, 2012, 5, 461–485.
- [132] M. Y. Bashouti, K. Sardashti, S. W. Schmitt, M. Pietsch, J. Ristein, H. Haick, and S. H. Christiansen. Oxide-free hybrid silicon nanowires: From fundamentals to applied nanotechnology, *Prog. Surf. Sci.*, 2013, 88, 39–60.
- [133] L. C. P. M. de Smet, D. Ullien, M. Mescher, and E. J. R. Sudhölter. Organic Surface Modification of Silicon Nanowire-Based Sensor Devices. In: *Nanowires-Implementations and Applications*, A. Hashim, InTech, Rijeka, 1st ed., 2011.
- [134] V. Schmidt, J. V. Wittemann, S. Senz, and U. Gösele. Silicon Nanowires: A Review on Aspects of their Growth and their Electrical Properties, *Adv. Mater.*, 2009, 21, 2681–2702.
- [135] Y. Li, F. Qian, J. Xiang, and C. M. Lieber. Nanowire electronic and optoelectronic devices, *Mater. Today*, 2006, 9, 18–27.
- [136] F. Patolsky, G. Zheng, C. M. Lieber. Nanowire-based biosensors, *Anal. Chem.*, 2006, 78, 4260–4269.
- [137] A. V. Sandulova, P. S. Bogoyavlenskii, and M. I. Dronyum. Preparation and some properties of whisker and needle-shaped single crystals of germanium, silicon and their solid solutions, *Sov. Phys. Solid State*, 1964, 5, 1883.
- [138] Z. W. Pan, Z. R. Dai, L. Xu, S. T. Lee, and Z. L. Wang. Temperature-Controlled Growth of Silicon-Based Nanostructures by Thermal Evaporation of SiO Powders, *J. Phys. Chem. B*, 2001, 105, 2507–2514.
- [139] P. Werner, N. D. Zakharov, G. Gerth, L. Schubert, and U. Gösele. On the formation of Si nanowires by molecular beam epitaxy, *Int. J. Mater. Res.*, 2006, 97, 1008–1015.

- 
- [140] Y. F. Zhang, Y. F. Tang, N. Wang, C. S. Lee, I. Bello, and S. T. Lee. Silicon nanowires prepared by laser ablation at high temperature, *Appl. Phys. Lett.*, 1998, 72, 1835–1837.
- [141] J. D. Holmes, K. P. Johnston, R. C. Doty, and B. A. Korgel. Control of thickness and orientation of solution-grown silicon nanowires, *Science*, 2000, 287, 1471–1473.
- [142] Z. Li, Y. Chen, X. Li, T. I. Kamins, K. Nauka, and R. S. Williams. Sequence-Specific Label-Free DNA Sensors Based on Silicon Nanowires, *Nano Lett.*, 2004, 4, 245–247.
- [143] E. Stern, A. Vacic, and M. A. Reed. Semiconducting nanowire field-effect transistor. *IEEE Trans. Electron. Devices*, 2008, 55, 3119–3130.
- [144] G. K. Celler, and S. Cristoloveanu. Frontiers of silicon-on-insulator, *J. Appl. Phys.*, 2003, 93, 4955–4978.
- [145] R. Rogel, E. Jacques, L. Pichon, and A. C. Salaun. Polycrystalline Silicon Nanowires Synthesis Compatible With CMOS Technology for Integrated Gas Sensing Applications, *IEEE Trans. Electron. Devices*, 2014, 61, 598–604.
- [146] M. Saitoh, T. Murakami, and T. Hiramoto. Large Coulomb blockade oscillations at room temperature in ultranarrow wire channel MOSFETs formed by slight oxidation process, *IEEE Trans. Nanotechnol.*, 2003, 2, 241–245.
- [147] H.I. Liu, D. K. Biegelsen, N. M. Johnson, F. A. Ponce, and R. F. W. Pease. Self-limiting oxidation of Si nanowires, *J. Vac. Sci. Technol. B*, 1993, 11, 2532–2537.
- [148] K. J. Morton, G. Nieberg, S. Bai, and S. Y. Chou. Wafer-scale patterning of sub-40 nm diameter and high aspect ratio (>50:1) silicon pillar arrays by nanoimprint and etching, *Nanotechnology*, 2008, 19, 345301.
- [149] D. Zschech, D. H. Kim, A. P. Milenin, R. Scholz, R. Hillebrand, C. J. Hawker, T. P. Russell, M. Steinhart, and U. Gösele. Ordered arrays of <100>-oriented silicon nanorods by CMOS-compatible block copolymer lithography, *Nano Lett.*, 2007, 7, 1516–1520.
- [150] F. Demami, L. Ni, R. Rogel, A.C. Salaun, and L. Pichon. Silicon nanowires based resistors as gas sensors, *Sensors and Actuators B*, 2012, 170, 158–162.
- [151] M. Cuscunà, A. Convertino, E. Zampetti, A. Macagnano, A. Pecora, G. Fortunato, L. Felisari, G. Nicotra, C. Spinella, and F. Martelli. On-chip fabrication of ultrasensitive NO<sub>2</sub> sensors based on silicon nanowires, *Appl. Phys. Lett.*, 2012, 101, 103101.

- 
- [152] C. R. Field, H. J. In, N. J. Begue, and P. E. Pehrsson. Vapor Detection Performance of Vertically Aligned, Ordered Arrays of Silicon Nanowires with a Porous Electrode, *Anal. Chem.*, 2011, 83, 4724–4728.
- [153] S. M. Sze, and K. K. Ng. Physics of semiconductor devices, John Wiley & Sons, Hoboken, 3rd ed., 2006.
- [154] K. Shenai, and R. W. Dutton. Current transport mechanisms in atomically abrupt metal-semiconductor interfaces, *IEEE Transactions on Electron Devices*, 1988, 35, 468–482.
- [155] C. Y. Chang, and S. M. Sze. Carrier transport across metal-semiconductor barriers, *Solid-State Electronics*, 1970, 13, 727–740.
- [156] J. Knoch, M. Zhang, S. Mantl, and J. Appenzeller. On the performance of single-gated ultrathin-body SOI Schottky-barrier MOSFETs, *IEEE Transactions on Electron Devices*, 2006, 53, 1669–1674.
- [157] J. Knoch, M. Zhang, J. Appenzeller, and S. Mantl. Physics of ultrathin-body silicon-on-insulator Schottky-barrier field-effect transistors, *Appl. Phys. A*, 2007, 87, 351–357.
- [158] X. Chen, C. K. Y. Wong, C. A. Yuan, and G. Zhang. Nanowire-based gas sensors, *Sensors and Actuators B*, 2013, 177, 178–195.
- [159] X. P. A. Gao, G. F. Zheng, and C. M. Lieber. Subthreshold regime has the optimal sensitivity for nanowire FET biosensors, *Nano Lett.*, 2010, 10, 547–552.
- [160] F. Patolsky, and C. M. Lieber. Nanowire nanosensors, *Mater. Today*, 2005, 8, 20–28.
- [161] C. Li, C. Zhang, K. Fobelets, J. Zheng, C. Xue, Y. Zuo, B. Cheng, and Q. Wang. Impact of ammonia on the electrical properties of p-type Si nanowire arrays, *J. Appl. Phys.*, 2013, 114, 173702.
- [162] C. Li, E. Krali, K. Fobelets, B. Cheng, and Q. Wang. Conductance modulation of Si nanowire arrays, *Appl. Phys. Lett.*, 2012, 101, 222101.
- [163] F. J. Dentener, and P. J. Crutzen. A three-dimensional model of the global ammonia cycle, *J. Atmos. Chem.*, 1994, 19, 331–369.
- [164] M. A. Sutton, J. W. Erisman, F. Dentener, and D. Möller. Ammonia in the environment: From ancient times to the present, *Environmental Pollution*, 2008, 156, 583–604.

- [165] I. Makarovskiy, G. Markel, T. Dushnitsky, and A. Eisenkraft. Ammonia – When Something Smells Wrong, *IMAJ*, 2008, 10, 537–543.
- [166] J. E. Amoores, and E. Hautala. Odor as an aid to chemical safety: odor thresholds compared with threshold limit values and volatilities for 214 industrial chemicals in air and water dilution, *J. Appl. Toxicol.*, 1983, 3, 272–290.
- [167] American Conference of Governmental Industrial Hygienists. Threshold limit values for chemical substances and physical agents and biological exposure indices, ACGIH® Worldwide, Cincinnati, 7th ed., 2001.
- [168] L. G. Close, F. I. Catlin, and A. M. Cohn. Acute and chronic effects of ammonia burns on the respiratory tract, *Arch. Otolaryngol.*, 1980, 106, 151–158.
- [169] B. Timmer, W. Olthuis, and A. van den Berg. Ammonia sensors and their applications – a review, *Sensors and Actuators B*, 2005, 107, 666–677.
- [170] C. E. Amshel, M. H. Fealk, B. J. Phillips, and D. M. Caruso. Anhydrous ammonia burns: case report and review of the literature, *Burns*, 2000, 26, 493–497.
- [171] G. H. Mount, B. Rumburg, J. Havig, B. Lamb, H. Westberg, D. Yonge, K. Johnson, and R. Kincaid. Measurement of atmospheric ammonia at a dairy using differential optical absorption spectroscopy in the mid-ultraviolet, *Atmos. Environ.*, 2002, 36, 1799–1810.
- [172] N. A. Campbell, and J. B. Reece. *Biology*, Pearson Education Inc., San Francisco, 6th ed., 2002.
- [173] R. Moos, R. Müller, C. Plog, A. Knezevic, H. Leye, E. Irion, T. Braun, K.-J. Marquardt, and K. Binder. Selective ammonia exhaust gas sensor for automotive applications, *Sensors and Actuators B*, 2002, 83, 181–189.
- [174] T. D. Durbin, R. D. Wilson, J. M. Norbeck, J. W. Miller, T. Huai, and S. H. Rhee. Estimates of the emission rates of ammonia from light-duty vehicles using standard chassis dynamometer test cycles, *Atmos. Environ.*, 2002, 36, 1475–1482.
- [175] C. Pijolat, C. Pupier, M. Sauvan, G. Tournier, and R. Lalauze. Gas detection for automotive pollution control, *Sensors and Actuators B*, 1999, 59, 195–202.
- [176] M. Wallin, C.-J. Karlsson, M. Skoglundh, and A. Palmqvist. Selective catalytic reduction of NO<sub>x</sub> with NH<sub>3</sub> over zeolite H-ZSM-5: influence of transient ammonia supply, *J. Catal.*, 2003, 218, 354–364.

- [177] M. Koebel, M. Elsener, and M. Kleemann. Urea-SCR: a promising technique to reduce  $\text{NO}_x$  emissions from automotive diesel engines, *Catal. Today*, 2000, 59, 335–345.
- [178] P. Spanel, S. Davies, and D. Smith. Quantification of ammonia in human breath by the selected ion flow tube analytical method using  $\text{H}_3\text{O}^+$  and  $\text{O}_2^+$  precursor ions, *Rapid Commun. Mass. Spectrom.*, 1998, 12, 763–766.
- [179] M. Phillips, J. Herrera, S. Krishnan, M. Zain, J. Greenberg, and R. N. Cataneo. *J. Chromatogr. B*, 1999, 729, 75–88.
- [180] W. Ament, J. R. Huizenga, T. W. van der Mark, R. G. Grevink, and G. J. Verkerke. Respiratory Ammonia Output and Blood Ammonia Concentration During Incremental Exercise, *Int. J. Sports Med.*, 1999, 20, 71–77.
- [181] P. K. Clifford, and D. T. Tuma. Characteristics of semiconductor gas sensors I. Steady state gas response, *Sens. Actuators*, 1983, 3, 233–254.
- [182] C. Delpha, M. Siadat, and M. Lumbreras. Discrimination of a refrigerant gas in a humidity controlled atmosphere by using modeling parameters, *Sensors and Actuators B*, 2000, 62, 226–232.
- [183] C. Di Natale, F. Davide, and A. D’Amico. Pattern recognition in gas sensing: well-stated techniques and advances, *Sensors and Actuators B*, 1995, 23, 111–118.
- [184] A. Jerger, H. Kohler, F. Becker, H. B. Keller, and R. Seifert. New applications of tin oxide gas sensors. II: Intelligent sensor system for reliable monitoring of ammonia leakage, *Sensors and Actuators B*, 2002, 81, 301–307.
- [185] X. Wang, N. Miura, and N. Yamazoe. Study of  $\text{WO}_3$ -based sensing material for  $\text{NH}_3$  and  $\text{NO}$  detection, *Sensors and Actuators B*, 2000, 66, 74–76.
- [186] N. Ramgir, N. Datta, M. Kaur, S. Kailasaganapathi, A. K. Debnath, D. K. Aswal, and S. K. Gupta. Metal oxide nanowires for chemiresistive gas sensors: Issues, challenges and prospects, *Colloids and Surfaces A: Physicochem. Eng. Aspects*, 2013, 439, 101–116.
- [187] A. A. Tomchenko, G. P. Harmer, B. T. Marquis, and J. W. Allen. Semiconducting metal oxide sensor array for the selective detection of combustion gases, *Sensors and Actuators B*, 2003, 93, 126–134.

- [188] I. Lundström, A. Spetz, F. Winqvist, U. Ackelid, and H. Sundgren. Catalytic metals and field-effect devices – a useful combination, *Sensors and Actuators B*, 1990, 1, 15–20.
- [189] N. Mayo, R. Harth, U. Mor, D. Marouani, J. Hayon, and A. Bettelheim. Electrochemical response to H<sub>2</sub>, O<sub>2</sub>, CO<sub>2</sub> and NH<sub>3</sub> of a solid-state cell based on a cation- or anion-exchange membrane serving as a polymer electrolyte, *Anal. Chim. Acta*, 1995, 310, 139–144.
- [190] I. Lähdesmäki, A. Lewenstam, and A. Ivaska. A polypyrrole-based amperometric ammonia sensor, *Talanta*, 1996, 43, 125–134.
- [191] A. L. Kukla, Y. M. Shirshov, and S. A. Piletsky. Ammonia sensors based on sensitive polyaniline films, *Sensors and Actuators B*, 1996, 37, 135–140.
- [192] Q. Y. Cai, M. K. Jain, and C. A. Grimes. A wireless, remote query ammonia sensor, *Sensors and Actuators B*, 2001, 77, 614–619.
- [193] A. L. Kukla, Y. M. Shirshov, and S. A. Piletsky. Ammonia sensors based on sensitive polyaniline films, *Sensors and Actuators B*, 1996, 37, 135–140.
- [194] I. Lähdesmäki, W. W. Kubiak, A. Lewenstam, and A. Ivaska. Interference in a polypyrrole-based amperometric ammonia sensor, *Talanta*, 2000, 52, 269–275.
- [195] V. V. Chabukswar, S. Pethkar, and A. A. Athawale. Acrylic acid doped polyaniline as an ammonia sensor, *Sensors and Actuators B*, 2001, 77, 657–663.
- [196] G.H. Mount, B. Rumberg, J. Havig, B. Lamb, H. Westberg, D. Yonge, K. Johson, and R. Kincaid. Measurement of atmospheric ammonia at a dairy using differential optical absorption spectroscopy in the mid-ultraviolet, *Atmos. Environ.*, 2002, 36, 1799–1810.
- [197] M. Fehér, P. A. Martin, A. Rohrbacher, A. M. Soliva, and J. P. Maier. Inexpensive near-infrared diode-laser-based detection system for ammonia, *Appl. Opt.*, 1993, 32, 2028–2030.
- [198] S.-I. Ohira, K. Toda, S.-I. Ikebe, and P. K. Dasgupta. Hybrid microfabricated device for field measurement of atmospheric sulfur dioxide, *Anal. Chem.*, 2002, 74, 5890–5896.
- [199] C. B. Boring, R. Al-Horr, Z. Genfa, and P. K. Dasgupta. Field measurement of acid gases and soluble anions in atmospheric particulate matter using a parallel plate wet

- denuder and an alternating filter based automatic analysis system, *Anal. Chem.*, 2002, 74, 1256–1268.
- [200] B. H. Timmer, K. M. v. Delft, R. P. Otjes, W. Olthuis, and A. v. d. Berg. A miniaturized measurement system for ammonia in air, *Anal. Chim. Acta*, 2004, 507, 139–145.
- [201] N. Barsan, D. Koziej, and U. Weimar. Metal oxide-based gas sensor research: How to?, *Sensors and Actuators B*, 2007, 121, 18–35.
- [202] J. Hennemann, T. Sauerwald, C.-D. Kohl, T. Wagner, M. Bognitzki, and A. Greiner. Electrospun copper oxide nanofibers for H<sub>2</sub>S dosimetry, *Phys. Status Solidi A*, 2012, 209, 911–916.
- [203] C. Schmädicke, M. Poetschke, L. D. Renner, L. Baraban, M. Bobeth, and G. Cuniberti. Copper nanowire synthesis by directed electrochemical nanowire assembly, *RSC Adv.*, 2014, 4, 46363–46368.
- [204] M. Motoyama, Y. Fukunaka, T. Sakka, Y. H. Ogata, and S. Kikuchi. Electrochemical processing of Cu and Ni nanowire arrays, *J. Electroanal. Chem.*, 2005, 584, 84–91.
- [205] J.-L. Duan, J. Liu, H.-J. Yao, D. Moa, M.-D. Houa, Y.-M. Suna, Y.-F. Chena, and L. Zhang. Controlled synthesis and diameter-dependent optical properties of Cu nanowire arrays, *Mater. Sci. Eng. B*, 2008, 147, 57–62.
- [206] Y. T. Pang, G. W. Meng, Y. Zhang, Q. Fang, and L. D. Zhang. Copper nanowire arrays for infrared polarizer, *Appl. Phys. A*, 2003, 76, 533–536.
- [207] G. A. Gelves, Z. T. M. Murakami, M. J. Krantz, and J. A. Haber. Multigram synthesis of copper nanowires using ac electrodeposition into porous aluminium oxide templates, *J. Mater. Chem.*, 2006, 16, 3075–3083.
- [208] H. Cao, L. Wang, Y. Qiu, and L. Zhang. Synthesis and I–V properties of aligned copper nanowires, *Nanotechnology*, 2006, 17, 1736–1739.
- [209] G. Sharma, V. Kripesh, M. C. Simb, and C. H. Sow. Synthesis and characterization of patterned and nonpatterned copper and nickel nanowire arrays on silicon substrate, *Sens. Actuators A*, 2007, 139, 272–280.
- [210] J. H. Wang, P. Y. Su, M. Y. Lu, L. J. Chen, C. H. Chen, and C. J. Chu. Synthesis of Cu Nanotubes with Silicon Oxide Nanowire Templates by MOCVD, *Electrochem. Solid-State Lett.*, 2005, 8, C9–C11.

- 
- [211] A. R. Rathmell, S. M. Bergin, Y.-L. Hua, Z.-Y. Li, and B. J. Wiley. The Growth Mechanism of Copper Nanowires and Their Properties in Flexible, Transparent Conducting Films, *Adv. Mater.*, 2010, 22, 3558–3563.
- [212] M. Mohl, P. Pusztai, A. Kukovecz, and Z. Konya. Low-Temperature Large-Scale Synthesis and Electrical Testing of Ultralong Copper Nanowires, *Langmuir*, 2010, 26, 16496–16502.
- [213] Z. Liu, and Y. Bando. A Novel Method for Preparing Copper Nanorods and Nanowires, *Adv. Mater.*, 2003, 15, 303–305.
- [214] H. Choi, and S.-H. Park. Seedless Growth of Free-Standing Copper Nanowires by Chemical Vapor Deposition, *J. Am. Chem. Soc.*, 2004, 126, 6248–6249.
- [215] E. C. Walter, M. P. Zach, F. Favier, B. J. Murray, K. Inazu, J. C. Hemminger, and R. M. Penner. Metal Nanowire Arrays by Electrodeposition, *ChemPhysChem*, 2003, 4, 131–138.
- [216] W. Steinhögl, G. Schindler, G. Steinlesberger, M. Traving, and M. Engelhardt. Comprehensive study of the resistivity of copper wires with lateral dimensions of 100 nm and smaller, *J. Appl. Phys.*, 2005, 97, 023706.
- [217] Q. Huang, C. M. Lilley, M. Bode, and R. Divan. Surface and size effects on the electrical properties of Cu nanowires, *J. Appl. Phys.*, 2008, 104, 023709.
- [218] C. Cheng, R. K. Gonela, Q. Gu, and D. T. Haynie. Self-Assembly of Metallic Nanowires from Aqueous Solution, *Nano Lett.*, 2005, 5, 175–178.
- [219] C. Cheng, R. K. Gonela, Q. Gu, and D. T. Haynie. Self-Assembly of Metallic Nanowires from Aqueous Solution, *Nano Lett.*, 2005, 5, 175–178.
- [220] A. Nerowski, J. Opitz, L. Baraban, and G. Cuniberti. Bottom-up synthesis of ultrathin straight platinum nanowires: Electric field impact, *Nano Research*, 2013, 6, 303–311.
- [221] B. Ozturk, I. Talukdar, and B. N. Flanders. Directed growth of diameter-tunable nanowires, *Nanotechnology*, 2007, 18, 365302.
- [222] N. Ranjan. Dielectrophoretic Formation of Nanowires and Devices. Ph.D. Thesis, Technische Universität Dresden, 2009.
- [223] A. Nerowski. Electrochemical Metal Nanowire Growth from Solution, Ph.D. Thesis, Technische Universität Dresden, 2013.



- 
- [224] W. M. Haynes. CRC Handbook of Chemistry and Physics, Taylor and Francis Group, Boca Raton, 94th ed., 2014.
- [225] W. Schmickler, and E. Santos. Interfacial Electrochemistry, Springer Science & Business Media, Heidelberg, 2nd ed., 2010.
- [226] D. R. Strachan, D. E. Smith, M. D. Fischbein, D. E. Johnston, B. S. Gupton, M. Drndić, D. A. Bonnell, and A. T. Johnson, Jr. Clean Electromigrated Nanogaps Imaged by Transmission Electron Microscopy, *Nano Lett.*, 2006, 6, 441–444.
- [227] A. Nerowski, M. Poetschke, M. Bobeth, J. Opitz, and G. Cuniberti. Dielectrophoretic Growth of Platinum Nanowires: Concentration and Temperature Dependence of the Growth Velocity, *Langmuir*, 2012, 28, 7498–7504.
- [228] B. C. Gierhart, D. G. Howitt, S. J. Chen, R. L. Smith, and S. D. Collins. Frequency dependence of gold nanoparticle superassembly by dielectrophoresis. *Langmuir*, 2007, 23, 12450–12456.
- [229] Y. Sawada, A. Dougherty, and J. P. Gollub. Dendritic and fractal patterns in electrolytic metal deposits, *Phys. Rev. Lett.*, 1986, 56, 1260–1263.
- [230] J. K. Kawasaki, and C. B. Arnold. Synthesis of Platinum Dendrites and Nanowires Via Directed Electrochemical Nanowire Assembly, *Nano Lett.*, 2011, 11, 781–785.
- [231] G. Paneru, and B. N. Flanders. Complete reconfiguration of dendritic gold, *Nanoscale*, 2014, 6, 833–841.
- [232] I. Talukdar, B. Ozturk, B. N. Flanders, and T. D. Mishima. Directed growth of single-crystal indium wires, *Appl. Phys. Lett.*, 2006, 88, 221907.
- [233] A. Nerowski, M. Poetschke, U. Wiesenhuetter, J. Nikolai, U. Cikalova, A. Dianat, A. Erbe, J. Opitz, M. Bobeth, L. Baraban, and G. Cuniberti. Effect of waveform of ac voltage on the morphology and crystallinity of electrochemically assembled platinum nanowires, *Langmuir*, 2014, 30, 5655–5661.
- [234] T. A. Witten, and L. M. Sander. Diffusion-Limited Aggregation, a Kinetic Critical Phenomenon, *Phys. Rev. Lett.*, 1981, 47, 1400–1403.
- [235] R. M. Brady, and R. C. Ball. Fractal growth of copper electrodeposits, *Nature*, 1984, 309, 225–229.

- [236] M. Poetschke, M. Bobeth, and G. Cuniberti. Ion Fluxes and Electro-osmotic Fluid Flow in Electrolytes around a Metallic Nanowire Tip under Large Applied ac Voltage, *Langmuir*, 2013, 29, 11525–11534.
- [237] W. M. Weber. Silicon to Nickel Silicide Longitudinal Nanowire Heterostructures: Synthesis, Electrical Characterization and Novel Devices, Ph.D. Thesis, Technische Universität München, 2008.
- [238] R. G. Hobbs, N. Petkov, and J. D. Holmes. Semiconductor Nanowire Fabrication by Bottom-Up and Top-Down Paradigms, *Chemistry of Materials*, 2012, 24, 1975–1991.
- [239] R. S. Wagner, and W. C. Ellis. Vapor-liquid-solid mechanism of single crystal growth, *Appl. Phys. Lett.*, 1964, 4, 89–90.
- [240] S. Pregl. Fabrication and characterization of a nanowire based Schottky-barrier field effect transistor platform for functional electronics and biosensor applications, Ph.D. Thesis, Technische Universität Dresden, 2014.
- [241] W. M. Weber, G. S. Duesberg, A. P. Graham, M. Liebau, E. Unger, C. Cheze, L. Geelhaar, P. Lugli, H. Riechert, and F. Kreupl. Silicon nanowires: catalytic growth and electrical characterization, *physica status solidi (b)*, 2006, 243, 3340–3345.
- [242] E. Baek, S. Pregl, M. Shaygan, L. Römhildt, W. M. Weber, T. Mikolajick, D. A. Ryndyk, L. Baraban, and G. Cuniberti. Optoelectronic Switching of Nanowire-based Hybrid Organic/Oxide/Semiconductor Field-Effect Transistor, *Nano Research*, 2014, accepted.
- [243] Y. Huang, X. Duan, Q. Wei, and C. M. Lieber. Directed assembly of one-dimensional nanostructures into functional networks, *Science*, 2001, 291, 630–633.
- [244] D. Whang, S. Jin, Y. Wu, and C. M. Lieber. Large-scale hierarchical organization of nanowire arrays for integrated nanosystems, *Nano Lett.*, 2003, 3, 1255–1259.
- [245] S. Acharya, A. B. Panda, N. Belman, S. Efrima, and Yuval Golan. A Semiconductor-Nanowire Assembly of Ultrahigh Junction Density by the Langmuir–Blodgett Technique, *Adv. Mater.*, 2006, 18, 210–213.
- [246] P. A. Smith, C. D. Nordquist, T. N. Jackson, and T. S. Mayer. Electric-field assisted assembly and alignment of metallic nanowires, *Appl. Phys. Lett.*, 2000, 77, 1399–1401.

- [247] S. Raychaudhuri, S. A. Dayeh, D. Wang, and E. T. Yu. Precise semiconductor nanowire placement through dielectrophoresis, *Nano Lett.*, 2009, 9, 2260–2266.
- [248] Z. Fan, J. C. Ho, Z. A. Jacobson, R. Yerushalmi, R. L. Alley, H. Razavi, and A. Javey. Wafer-Scale Assembly of Highly Ordered Semiconductor Nanowire Arrays by Contact Printing, *Nano Lett.*, 2008, 8, 20–25.
- [249] A. Javey, S. W. Nam, R. S. Friedman, H. Yan, and C. M. Lieber. Layer-by layer assembly of nanowires for three-dimensional, multifunctional electronics, *Nano Lett.*, 2007, 7, 773–777.
- [250] S. M. Sze, and K. K. Ng. *Physics of Semiconductor Devices*, John Wiley & Sons, Hoboken, 2006.
- [251] H. Kageshima, M. Uematsu, K. Akagi, S. Tsuneyuki, T. Akiyama, and K. Shiraishi. Mechanism of oxide deformation during silicon thermal oxidation, *Physica B: Condensed Matter*, 2006, 376, 407–410.
- [252] M. L. Reed, and J. D. Plummer. Chemistry of Si-SiO<sub>2</sub> interface trap annealing, *Journal of Applied Physics*, 1988, 63, 5776–5793.
- [253] L. D. Thanh, and P. Balk. Elimination and Generation of Si-SiO<sub>2</sub> Interface Traps by Low Temperature Hydrogen Annealing, *Journal of The Electrochemical Society*, 1988, 135, 1797–1801.
- [254] U. Hilleringmann. *Silizium-Halbleitertechnologie. Grundlagen mikroelektronischer Integrationstechnik*, Vieweg +Teubner, Wiesbaden, 5th ed., 2008.
- [255] W. M. Weber, L. Geelhaar, A. P. Graham, E. Unger, G. S. Duesberg, M. Liebau, W. Pamler, C. Chèze, H. Riechert, and P. Lugli. Silicon-nanowire transistors with intruded nickel-silicide contacts, *Nano Lett.*, 2006, 6, 2660–2666.
- [256] H. J. Levinson, “Principles of Lithography”, SPIE Press, Washington, 3rd ed., 2011.
- [257] M. Morita, T. Ohmi, E. Hasegawa, M. Kawakami, and M. Ohwada. Growth of native oxide on a silicon surface, *Journal of Applied Physics*, 1990, 68, 1272–1281.
- [258] P. S. Lee, D. Mangelinck, K. L. Pey, J. Ding, J. Y. Dai, C. S. Ho, and A. See. On the Ni-Si phase transformation with/without native oxide, *Microelectronic Engineering*, 2000, 51, 583–594.

- [259] H. Ikeda, K. Hotta, T. Yamada, S. Zaima, H. Iwano, and Y. Yasuda. Oxidation of H-terminated Si(100) surfaces studied by high-resolution electron energy loss spectroscopy, *Journal of Applied Physics*, 1995, 77, 5125–5129.
- [260] H. S. Nalwa. Handbook of Surfaces and Interfaces of Materials, Academic Press, London, 2001.
- [261] K. Maex, and M. Van Rossum. Properties of Metal Silicides, INSPEC, London, 1st ed., 1995.
- [262] Y. E. Yaish, A. Katsman, G. M. Cohen, and M. Beregovsky. Kinetics of nickel silicide growth in silicon nanowires: From linear to square root growth, *Journal of Applied Physics*, 2011, 109, 094303.
- [263] Y. Wu, J. Xiang, C. Yang, W. Lu, and C. M. Lieber. Single-crystal metallic nanowires and metal/semiconductor nanowire heterostructures, *Nature*, 2004, 430, 61–65.
- [264] K.-C. Lu, W.-W. Wu, H.-W. Wu, C. M. Tanner, J. P. Chang, L. J. Chen, and K. N. Tu. In situ Control of Atomic-Scale Si Layer with Huge Strain in the Nanoheterostructure NiSi/Si/NiSi through Point Contact Reaction, *Nano Lett.*, 2007, 7, 2389–2394.
- [265] A. Heinzig, S. Slesazeck, F. Kreupl, T. Mikolajick, and W. M. Weber. Reconfigurable Silicon Nanowire Transistors, *Nano Lett.*, 2012, 12, 119–124.
- [266] H.-E. Endres, H. D. Jander, and W. Göttler. A test system for gas sensors, *Sensors and Actuators B*, 1995, 23, 163–172.
- [267] P. Pérez Ballesta, A. Baldan, and J. Cancelinha. Atmosphere Generation System for the Preparation of Ambient Air Volatile Organic Compound Standard Mixtures, *Anal. Chem.*, 1999, 71, 2241–2245.
- [268] T. Kida, T. Kuroiwa, M. Yuasa, K. Shimanoe, and N. Yamazoe. Study on the response and recovery properties of semiconductor gas sensors using a high-speed gas-switching system, *Sensors and Actuators B*, 2008, 134, 928–933.
- [269] B. Esser, J. M. Schnorr, and T. M. Swager. Selective Detection of Ethylene Gas Using Carbon Nanotube-based Devices: Utility in Determination of Fruit Ripeness, *Angew. Chem. Int. Ed.*, 2012, 51, 5752–5756.
- [270] N. Helwig, M. Schüler, C. Bur, A. Schütze, and T. Sauerwald. Gas mixing apparatus for automated gas sensor characterization, *Meas. Sci. Technol.*, 2014, 25, 055903-1–9.

- [271] J. Kneer, A. Eberhardt, P. Walden, A. Ortiz Pérez, J. Wöllenstein, and S. Palzer. Apparatus to characterize gas sensor response under real-world conditions in the lab, *Rev. Sci. Instrum.*, 2014, 85, 055006-1–7.
- [272] C. Bur, P. Reimann, M. Andersson, A. Schütze, and A. Lloyd Spetz. Increasing the Selectivity of Pt-Gate SiC Field Effect Gas Sensors by Dynamic Temperature Modulation, *IEEE Sensors Journal*, 2012, 12, 6, 1906–1913.
- [273] A. A. Samokhvalov, N. A. Viglin, B. A. Gizhevskii, N. N. Loshkareva, V. V. Osipov, N. I. Solin, and Y. P. Sukhorukov. Low-mobility charge carriers in CuO, *Journal of Experimental and Theoretical Physics*, 1993, 76, 463–468.
- [274] H. Taghinejad, M. Taghinejad, M. Abdolahad, A. Saeidi, and S. Mohajerzadeh. Fabrication and modeling of high sensitivity humidity sensors based on doped silicon nanowires, *Sensors and Actuators B*, 2013, 176, 413–419.
- [275] R. T. Tung, A. Levi, J. P. Sullivan, and F. Schrey. Schottky-barrier inhomogeneity at epitaxial NiSi<sub>2</sub> interfaces on Si (100), *Physical Review Letters*, 1991, 66, 72.
- [276] F. M. Zörgiebel, S. Pregl, L. Römhildt, J. Opitz, W. Weber, T. Mikolajick, L. Baraban, and G. Cuniberti. Schottky barrier-based silicon nanowire pH sensor with live sensitivity control, *Nano Research*, 2014, 7, 263–271.
- [277] A. Vergara, S. Vembua, T. Ayhan, M. A. Ryan, M. L. Homer, and R. Huerta. Chemical gas sensor drift compensation using classifier ensembles, *Sensors and Actuators B*, 2012, 166–167, 320–329.
- [278] H. Liu, and Z. Tang. Metal Oxide Gas Sensor Drift Compensation Using a Dynamic Classifier Ensemble Based on Fitting, *Sensors*, 2013, 13, 9160–9173.
- [279] J.-H. Ahn, J.-Y. Kim, M.-L. Seol, D. J. Baek, Z. Guo, C.-H. Kim, S.-J. Choi, and Y.-K. Choi. A pH sensor with a double-gate silicon nanowire field-effect transistor, *Appl. Phys. Lett.*, 2013, 102, 083701.
- [280] R. K. Iler. *The Chemistry of Silica*, John Wiley & Sons, New York, 1st ed., 1979.
- [281] L. Bousse, and P. Bergveld. The role of buried OH sites in the response mechanism of inorganic-gate pH-sensitive ISFETs, *Sensors and Actuators*, 1984, 6, 65–78.
- [282] W. Göpel, K. Schierbaum, H.-D. Wiemhöfer, and J. Maier. Defect Chemistry of Tin(IV)-Oxide in Bulk and Boundary Layers, *Solid State Ionics*, 1989, 32/33, 440–443.

- [283] B. Kamp, R. Merkle, R. Lauck, and J. Maier. Chemical diffusion of oxygen in tin dioxide: Effects of dopants and oxygen partial pressure, *Journal of Solid State Chemistry*, 2005, 178, 3027–3039.
- [284] W.-D. Zhang, and W.-H. Zhang. Carbon Nanotubes as Active Components for Gas Sensors, *Journal of Sensors*, 2009, 2009, 160698.
- [285] O. Lupan, V.V. Ursaki, G. Chai, L. Chow, G.A. Emelchenko, I.M. Tiginyanu, A.N. Gruzintsev, and A.N. Redkin. Selective hydrogen gas nanosensor using individual ZnO nanowire with fast response at room temperature, *Sensors and Actuators B*, 2010, 144, 56–66.
- [286] Z. Fan, and J. G. Lu. Gate-refreshable nanowire chemical sensors, *Appl. Phys. Lett.*, 2005, 86, 123510.
- [287] R. F. Pierret. Semiconductor Device Fundamentals, Addison-Wesley, Reading, 2nd ed., 1996.
- [288] J. F. Zhang, and B. Eccleston. Donor-Like Interface Trap Generation in pMOSFET's at Room Temperature, *IEEE Transactions on Electron Devices*, 1994, 41, 740–744.
- [289] I. Lundströms, S. Christensson, and C. Svensson. Carrier Trapping Hysteresis in MOS Transistors, *phys. stat. sol. (a)*, 1970, 1, 395–407.
- [290] F. Schedin, A. K. Geim, S. V. Morozov, E. W. Hill, P. Blake, M. I. Katsnelson, and K. S. Novoselov. Detection of individual gas molecules adsorbed on graphene, *Nature Materials*, 2007, 6, 652–655.
- [291] K. G. Ong, K. Zeng, and C. A. Grimes. A Wireless, Passive Carbon Nanotube-Based Gas Sensor, *IEEE Sensors Journal*, 2002, 2 82–88.
- [292] X. Chen, J. Zhang, Z. Wang, Q. Yan, and S. Hui. Humidity sensing behavior of silicon nanowires with hexamethyldisilazane modification, *Sensors and Actuators B*, 2011, 156, 631–636.
- [293] L. Y. Li, Y. F. Dong, W. F. Jiang, H. F. Ji, and X. J. Li. High-performance capacitive humidity sensor based on silicon nanoporous pillar array, *Thin Solid Films*, 2008, 517, 948–951.
- [294] W. Kim, A. Javey, O. Vermesh, Q. Wang, Y. Li, and H. Dai. Hysteresis caused by water molecules in carbon nanotube field-effect transistors, *Nano Lett.*, 2003, 3, 193–198.

- 
- [295] P. Hu, C. Zhang, A. Fasoli, V. Scardaci, S. Pisana, T. Hasan, J. Robertson, W.I. Milne, and A.C. Ferrari. Hysteresis suppression in self-assembled single-wall nanotube field effect transistors, *Physica E*, 2008, 40, 2278–2282.
- [296] H. Wang, Y. Wu, C. Cong, J. Shang, and T. Yu. Hysteresis of electronic transport in graphene transistors, *ACS Nano*, 2010, 4, 7221–7228.
- [297] G. Gu, and M. G. Kane. Moisture induced electron traps and hysteresis in pentacene based organic thin-film transistors, *Appl. Phys. Lett.*, 2008, 92, 053305.
- [298] D. Wang, Y.-L. Chang, Q. Wang, J. Cao, D. B. Farmer, R. G. Gordon, and H. Dai. Surface chemistry and electrical properties of germanium nanowires, *Journal of the American Chemical Society*, 2004, 126, 11602–11611.
- [299] H. Tanaka, T. Yazawa, K. Eguchi, H. Nagasawa, N. Matsuda, and T. Einishi. Precipitation of colloidal silica and pore size distribution in high silica porous glass, *Journal of noncrystalline solids*, 1984, 65, 301–309.
- [300] L.T. Zhuravlev. The surface chemistry of amorphous silica. Zhuravlev model, *Colloids and Surfaces A*, 2000, 173, 1–38.
- [301] M. O. Andersson, K. R. Farmer, and O. J. Engstrom. Negative charging in ultrathin metal-oxide-silicon tunnel diodes, *Journal of Applied Physics*, 1992, 71, 1846-1852.
- [302] R. Woltjer, A. Hamada, and E. Takeda. Time dependence of p-MOSFET hot-carrier degradation measured and interpreted consistently over ten orders of magnitude, *IEEE Trans. Electron Devices*, 1993, 40, 392–401.
- [303] M. Bourcerie, B. S. Doyle, J. C. Marchetaux, J. C. Soret, and A. Boudou. Relaxable damage in hot-carrier stressing of n-MOS transistors-oxide traps in the near interfacial region of the gate oxide, *IEEE Trans. Electron Devices*, 1990, 37, 708–717.
- [304] C. Hu, S. C. Tam, F. C. Hsu, P. K. KO, T. Y. Chan, and K. W. Terrill. Hot-electron-induced MOSFET degradation-model, monitor, and improvement, *IEEE J. Solid-State Circuits*, 1985, 32, 375–385.
- [305] M. S. Fuhrer, B. M. Kim, T. Dürkop, and T. Brintlinger. High-Mobility Nanotube Transistor Memory, *Nano Lett.*, 2002, 2, 755-759.
- [306] D.S. Vlachos, P.D. Skafidas, and J.N. Avaritsiotis. The effect of humidity on tin-oxide thick-film gas sensors in the presence of reducing and combustible gases, *Sensors and Actuators B*, 1995, 24–25, 491–494.

- 
- [307] Y. Shingaya, H. Kubo, and M. Ito. Coadsorption of ammonia and electrolyte anions on a Pt(111) electrode, *Surface Science*, 1999, 427–428, 173–178.
- [308] M. Burgmair, M. Zimmer, and I. Eisele. Humidity and temperature compensation in work function gas sensor FETs, *Sensors and Actuators B*, 2003, 93, 271–275.
- [309] Bundesministerium für Arbeit und Soziales. Technische Regeln für Gefahrstoffe 900, *BArBl Heft*, 2006, 1, 41–55.
- [310] K. Ihokura, and J. Watson. The Stannic Oxide Gas Sensor, CRC Press, Boca Raton, 1994.
- [311] M. Wu, Y. I. Alivov, and H. Morkoç. High- $\kappa$  dielectrics and advanced channel concepts for Si MOSFET, *Journal of Materials Science: Materials in Electronics*, 2008, 19, pp. 915–951.
- [312] B. E. Deal, M. Sklar, A. S. Grove, and E. H. Snow. Characteristics of the Surface-State Charge ( $Q_{ss}$ ) of Thermally Oxidized Silicon, *Journal of The Electrochemical Society*, 1967, 114, 266–274.
- [313] J. Schulze. Konzepte siliziumbasierter MOS-Bauelemente, Springer, Berlin, 1st ed., 2006.
- [314] A. Heinzig. Entwicklung und Herstellung rekonfigurierbarer Nanodraht-Transistoren und Schaltungen, Ph.D. Thesis, Technische Universität Dresden, 2014.
- [315] F. J. Feigl, D. R. Young, D. J. DiMaria, S. Lai, and J. Calise. The effects of water on oxide and interface trapped charge generation in thermal  $\text{SiO}_2$  films, *Journal of Applied Physics*, 1981, 52, 5665–5682.
- [316] M. Fleischer, E. Simon, E. Rumpel, H. Ulmer, M. Harbeck, M. Wandel, C. Fietzek, U. Weimar, and H. Meixner. Detection of volatile compounds correlated to human diseases through breath analysis with chemical sensors, *Sensors and Actuators B*, 2002, 83, 245–249.



## Appendix

### A.1 Threshold Voltage Shift as Function of Time for Different NH<sub>3</sub> Concentrations

A sensor based on native oxide SiNWs was exposed to NH<sub>3</sub> in the concentration range from 680 ppb to 170 ppb, the relative humidity and the temperature were kept constant at 57 % and 25 °C, respectively. The diagram of the threshold voltage shift over time shows that with increasing NH<sub>3</sub> concentrations the sensing response increases.

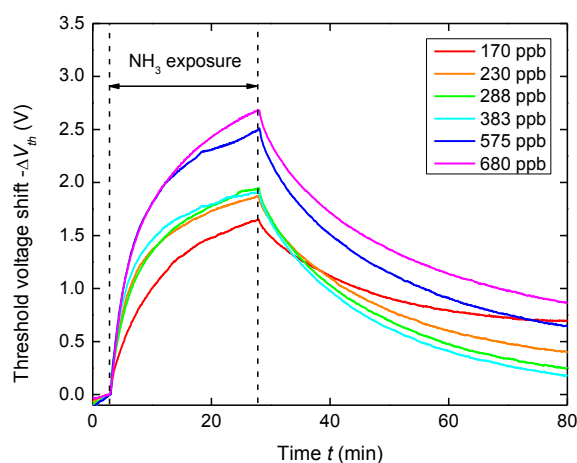


**Fig. A.1:** Threshold voltage shift over time for different NH<sub>3</sub> concentrations at 25 °C and a relative humidity of 57 %.

### A.2 Response and Recovery Time in Dependence of NH<sub>3</sub> Concentration

Response and recovery times of native oxide SiNW sensors were determined for different NH<sub>3</sub> concentrations in the range of 680–170 ppb at 57 % RH and 25 °C. With increasing concentrations the response time slightly increases, but the recovery time remains approximately constant.

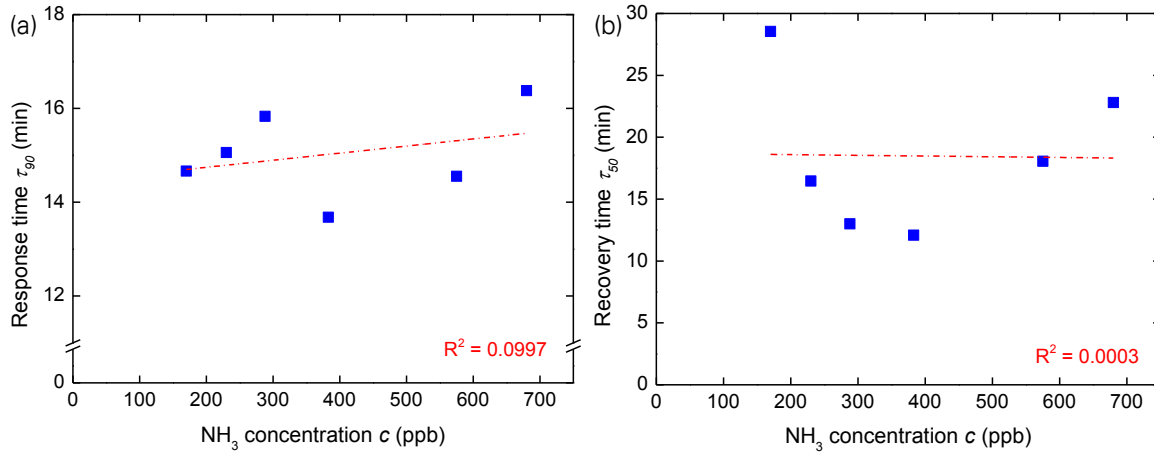


**Fig. A.2:** Investigation of response and recovery of the sensor for different NH<sub>3</sub> concentrations. (a) Response time in dependence of the NH<sub>3</sub> concentration. (b) Recovery time of the signal towards various NH<sub>3</sub> concentrations. The dot-dash lines serve as guides to the eye.

### A.3 Humidity Influence

The influence of the relative humidity on the sensing response of native oxide SiNWs towards NH<sub>3</sub> shows that with increasing humidity the signal intensity decreases in the range of 0–52.5 % RH. During the measurement, the concentration of NH<sub>3</sub> was regulated at 680 ppb and the temperature remained constant at 25 °C.

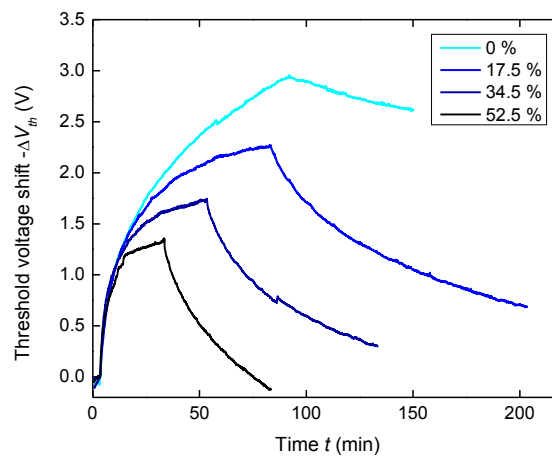


**Fig. A.3:** Threshold voltage shift over time at different humidity upon exposure to 680 ppb NH<sub>3</sub> and at 25 °C.

### A.4 Temperature Influence

The sensing response of the sensor was measured in the temperature range of 25–50 °C with 17.5 % RH at a fixed NH<sub>3</sub> concentration of 680 ppb. The threshold voltage shift as function of time reveals that with higher temperatures  $\Delta V_{th}$  decreases.

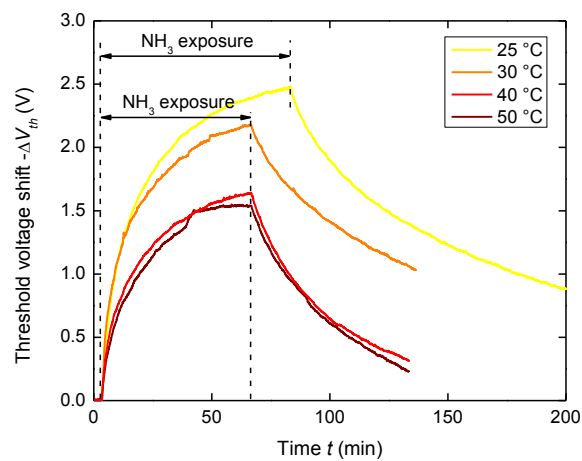


**Fig. A.4:** Threshold voltage shift over time at different temperatures upon exposure to 680 ppb NH<sub>3</sub> at 17.5 % RH.



## Publications and Conferences

### Publications and Peer-Review Proceedings as a Direct Result of this Thesis

- 1 **C. Schmädicke**, S. Pregl, A. Gang, L. Baraban, and G. Cuniberti.  
Silicon Nanowire based Sensor for Ammonia Detection, in preparation.
- 2 **C. Schmädicke**, M. Pötschke, L. D. Renner, L. Baraban, M. Bobeth, and G. Cuniberti.  
Copper Nanowires Synthesis by Directed Electrochemical Nanowire Assembly, *RSC Advances*, 2014, 4, 46363–46368.
- 3 **C. Schmädicke**, M. Pötschke, L. D. Renner, and G. Cuniberti.  
A Novel Electrochemical Synthesis Route for Copper Nanowire Formation, Proceedings of the IEEE Sensors, 2013, Baltimore, USA.
- 4 **C. Schmädicke**, A. Nerowski, L. Baraban, L. D. Renner, and G. Cuniberti.  
Fabrication of Copper Nanowires from Aqueous Solution, Proceedings of the AMA Conferences, 2013, Nürnberg, Germany.

### Conference Contributions

- 1 **C. Schmädicke**, S. Pregl, J. Voigt, L. Baraban, and G. Cuniberti.  
Gas Measurement System and Silicon Nanowire based Sensor for the Detection of Ammonia, MRS Spring Meeting 2014, Lille, France, May 2014, oral presentation.
- 2 **C. Schmädicke**, M. Pötschke, L. D. Renner, and G. Cuniberti.  
A Novel Electrochemical Synthesis Route for Copper Nanowire Formation, IEEE Sensors 2013, Baltimore, USA, November 2013, poster.
- 3 **C. Schmädicke**, A. Nerowski, L. Baraban, L. D. Renner, and G. Cuniberti.  
Fabrication of Copper Nanowires from Aqueous Solution. AMA Conferences 2013, Nürnberg, Germany, May 2013, poster.



## Patent Filing

- 1 G. Cuniberti, **C. Schmädicke**, J. Voigt, and L. Baraban.  
Vorrichtung zum Messen von mikro- und nanostrukturierten Sensoren unter definierter Gasatmosphäre, Deutsches Patent- und Markenamt, 10 2014 218 205, 12.09.2014.
- 2 T. M. Swager, J. Im, J. M. Schnorr, A. R. Petty, and **C. Schmädicke**.  
Devices and methods including a preconcentrator material for detection of analytes, United States Patent and Trademark Office, WO 2015/035243 A1, 12.03.2015.





## Acknowledgements

Firstly, I would like to thank my supervisor Prof. Gianaurelio Cuniberti to give me the opportunity to carry out this thesis in his chair. He gave me not only the freedom to think independently and grow personally but also the chance to work on a challenging and exciting project, gain experience abroad, and manage students, which will be invaluable benefits throughout my career.

A special thanks to Prof. Timothy Swager for the possibility to gain both a wonderful experience and support for my thesis in Boston. I am very grateful that I got you as a helpful advisor and as a second reviewer for my thesis. I would like to express my appreciation to Prof. Andrés Lasagni for being the third reviewer of my thesis.

I would like to thank Dr. Lars Renner and Dr. Larysa Baraban for fruitful discussions, guidance through this thesis, and correcting drafts as well as Dr. Francesca Moresco for reading and editing this dissertation.

I could always count on the support by Linda Deutscher, Andreas Gang, Marcin Meyer, Sebastian Pregl, and Felix Zörgiebel, who were both professionally and personally an important assistance in the realization of my work. I would specifically like to thank Jan Voigt and Gero Wiemann for their work helping me construct the gas sensor testing facility. I would also like to thank the many other colleagues, who have accompanied me during my doctoral phase and gave me great advice and assistance.

I also want to express my gratitude to Dr. Wolfgang Bäther, Dr. Jens Zosel, and my colleagues at the MIT, in particular Dr. Jan Schnorr. Their valuable knowledge from their experiences had greatly contributed to the thesis. I hope that we meet again in the future.

Ein ganz besonderer Dank gilt meiner Familie für ihre Liebe und dass sie mich stets unterstützt, aufgebaut und ermutigt haben.

Mein lieber André, mit deiner Gutmütigkeit, Besonnenheit und deinem unersättlichen Wissensdurst warst und bist du die wichtigste Stütze in meinem Leben.

I wish to thank my friends, who have enriched my life besides the dissertation.

Finally, I am grateful for all mentioned and not mentioned people, who supported me during the years of my Ph.D.